TABLE OF CONTENTS

LIST OF TABLES

LIST OF FIGURES

LIST OF ABREVIATIONS

ASTM	American Society for Testing Material
CA	Cellular Automaton
CPU	Central Processing Unit
DDD	Discrete Dislocation Dynamic
DIC	Digital Image Correlation
EBSD	Electron Backscatter Diffraction
EIM	Equivalent Inclusion Method
Esh	Eshelby's inclusion problem solution
FE/FEM	Finite Element (Method)
FCC	Face-Centered Cubic
FFT	Fast Fourier Transform
HCF	High Cycle Fatigue
HCP	Hexagonal Closest Packed
KUBC	Kinematic Uniform Boundary Conditions
LEFM	Linear Elastic Fracture Mechanics
MC	Méric-Cailletaud model
NTFA	Nonuniform Transformation Field Analysis
PBC	Periodic Boundary Conditions
REV	Representative Elementary Volume

RSS	Resolved Shear Stress
SC	Self-Consistent (model)
VHCF	Very High Cycle Fatigue

LIST OF SYMBOLS AND UNITS OF MEASUREMENTS

x, $\vec{\boldsymbol{x}}$, $\boldsymbol{X}$, $\mathbb{X}$	These notations correspond to a scalar, a vector, a second-order and a fourth-order tensors respectively. Their respective component notations are expressed as follows: x, x_i, X_{ij}, $\mathbb{X}_{ijkl}$.
$\bigotimes$	Tensor product
$:$	Double tensor contraction
$\dot{x}$	Time derivative
$\lvert \bullet \rvert$	Absolute value of the argument
$(\bullet)^+$	Positive operator: takes the positive part of its argument.
$\langle \bullet \rangle_X$	Average the argument values over the set X. As example, $\langle \boldsymbol{\varepsilon}(\vec{\boldsymbol{x}}) \rangle_{\forall \vec{\boldsymbol{x}} \in g} = \boldsymbol{\varepsilon}^g$ and $\left\langle \tau_s^g \right\rangle_s = \frac{1}{n_s} \sum_{s=1}^{n_s} \tau_s^g$ (each grain g are of identical volume).
$max\,(\bullet)_X$	Maximum value of the argument over the set X.
$\bullet_{FE}$ / $\bullet_{CA}$ / $\bullet_{Esh}$	Variable prediction obtained from FE, CA or Eshelby models respectively.
$\mathbb{C}^{cry}$ / $\mathbb{S}^{cry}$	Stiffness / compliance tensors of the crystal expressed in the crystal axis system.
$\mathbb{C}^g$ / $\mathbb{S}^g$	Stiffness / compliance tensors of a grain g expressed in the global axis system depending on the grain g crystallographic orientation.
$\mathbb{C}^{eff}$ / $\mathbb{S}^{eff}$	Stiffness / compliance tensors of the polycrystalline aggregate obtained after homogenization.
$\boldsymbol{\varepsilon}^g$, $\boldsymbol{\varepsilon_e}^g$, $\boldsymbol{\varepsilon_p}^g$	Grain g total, elastic and plastic mean strain tensors.
$\boldsymbol{\sigma}^g$, τ_s^g, ν_s^g	Grain g mean stress tensor, mean resolved shear stress over the slip system s and mean cumulative viscoplastic slip of the slip system s.

$\boldsymbol{E}^{eff}, \boldsymbol{\Sigma}^{eff}$	Effective strain and stress tensor of the aggregate such as $\boldsymbol{E}^{eff} = \langle \boldsymbol{\varepsilon}^{g} \rangle_{g}$ and $\boldsymbol{\Sigma}^{eff} = \langle \boldsymbol{\sigma}^{g} \rangle_{g}$.
$\boldsymbol{\Delta \bullet}^{A}_{X}$	Variable variation induced in grain A by a specific neighborhood X. An exponent eff over the exponent A, such as $\boldsymbol{\Delta \bullet}^{A^{eff}}_{X}$, is added when $\mathbb{C}^{A} = \mathbb{C}^{eff}$.
$\mathbb{U}^{\overrightarrow{AB}}$	CA model parameter depending on the vector $\overrightarrow{AB}$ formed by grains A and B centroids, and obtained for a specific aggregate morphology and $\mathbb{C}^{eff}$.
$\mathbb{A}^{\overrightarrow{AB}}$	Influence tensor $\mathbb{A}^{\overrightarrow{AB}}$ (determining grain B influence over grain A strain tensor depending on grain B stiffness tensor $\mathbb{C}^{B}$ and $\mathbb{A}^{\overrightarrow{AB}}$.
σ^{g}_{eq}	The von Mises equivalent stress such as $\sigma^{g}_{eq} = \sqrt{\frac{3}{2}\boldsymbol{s}^{g} : \boldsymbol{s}^{g}}$, where $\boldsymbol{s}^{g}$ is the deviatoric stress.
$\varepsilon^{g}_{p\ eq}$	The von Mises equivalent viscoplastic strain such as $\varepsilon^{g}_{p\ eq} = \sqrt{\frac{2}{3}\boldsymbol{\varepsilon_{p}}^{g} : \boldsymbol{\varepsilon_{p}}^{g}}$.
ν^{g}_{Σ}	The total cumulative viscoplastic slip defined as the sum of the 12 slip systems cumulative viscoplastic slip ν^{g}_{s} such as $\nu^{g}_{\Sigma} = \sum_{s=1}^{n_s} \nu^{g}_{s}$.
$max\left(\left\|\tau^{g}_{s\ 0.01\%}\right\|\right)_{s}$	Grain g maximum absolute resolved shear stress over all the slip systems s predicted after an uni-axial monotonic stress loading up to 0.01% strain (the aggregate is assumed to remain fully elastic at this strain level).

INTRODUCTION

Many different kinds of heterogeneities can be found within polycrystals such as metallurgical phases, grains morphology, inclusions, residual stresses, crystal anisotropy, etc. These heterogeneities are responsible for local stress concentrations that can lead to early crack initiations. The random character of heterogeneities makes difficult to evaluate their impact on materials fatigue life and thus requires a systematic statistical study. Performing experimentally a statistical analysis of a material fatigue life is expensive and time-consuming. For that reason, predictive tools are of significant interest.

Several numerical models exist to predict materials stress-fields which can be roughly divided into two groups: the full-field models that are accurate but computationally expensive and the mean-field models that are fast and efficient but sometimes lack of accuracy. In order to capture the full range of the stress heterogeneities within a material, all the microstructural heterogeneities must be considered, which are often disregarded by mean-field models, and a very large number of configurations of heterogeneities must be studied, which is too much time consuming with full-field models.

In order to accelerate the computation time, approximations are necessary and some heterogeneities have to be ignored. A phenomenon that is often disregarded is the grains stress variations in polycrystals due to their close environment mechanical properties, the so-called neighborhood effect. This phenomenon can generate large stress concentrations that must be predicted for a better understanding of fatigue damage. This work is an attempt to develop an analytical model with the purpose to quantify polycrystals micromechanical behavior accounting for the neighborhood effect based on simplifying assumptions for a low computational cost in order to study a large amount of heterogeneities distributions.

As a first step toward this goal, the present work is divided as follow: Chapter 1 presents the fundamental tools necessary to predict polycrystals' micromechanical behavior and the state of the art on that matter. Chapter 2 presents the rationales and objectives of the thesis. Chapter 3 displays a finite element study of the neighborhood effect within polycrystals under an elastic loading, as it was presented in a first article published in the *International Journal of Solids and Structures*. A better understanding of the grains interactions is acquired from this study, leading in Chapter 4 to the development of an analytical model, as it was presented in a second article published in the *International Journal of Solids and Structures*. The model, based on a cellular automaton and using a regular aggregate structure, accounts for the neighborhood effect in the elastic micromechanical stress fields predictions. The model predictions are compared to the finite element method ones and showed excellent performance to predict the grains resolved shear stresses and identify the specific microstructures leading to large stress concentrations. Chapter 4 presents the application of the model using an elasto-visco-plastic constitutive law. The importance of elasticity on the neighborhood effect in a visco-plastic polycrystal is pointed out. A statistical study is also presented showing the probability to get a significant stress concentration within a given volume of material capturing the volume effect often observed in polycrystals fatigue strength. Chapter 5 presents some extra studies of other stress heterogeneities sources such as the impact of a free surface and the grains morphologies. Finally, conclusions and recommendations for the future of the model are provided in the last chapter.

LITERATURE REVIEW

This literature review is divided into 3 parts: a short introduction on polycrystal fatigue, highlighting the importance of a material heterogeneities on its fatigue life performance; a presentation of the elements describing single-crystal anisotropy and related numerical models able to predict their mechanical behavior; the different kinds of numerical models commonly used to predict polycrystals micromechanical behavior. In particular, a detailed description of the cellular automaton model from which the present study started is also included.

1.1 Introduction to material fatigue

For several decades, fatigue, phenomenon responsible for mechanical parts breakage, has raised a large number of studies combining industrial and scientific expertise. According to the ASTM (Ame, 1997), material fatigue is “the process of progressive localized permanent structural change occurring in a material subjected to conditions that produce fluctuating stresses and strains at some point (or points) and that may culminate in cracks or complete fracture after a sufficient number of fluctuations”. These conditions can be of different kinds (mechanical, thermal, chemical, etc.), and mechanical loads are the sources of fluctuations studied within the framework of this thesis. Depending on the stress amplitude, these cracks can lead on the long term to the material failure without any apparent damage. The basics and generalities of metal fatigue are presented in this section. For more details on the subject, the reader is invited to consult Krupp (2007), Hertzberg, Vinci & Hertzberg (2012) and Bathias & Pineau (2013) books.

Materials fatigue life is generally studied by means of a fatigue test which consists of cyclically loading the part at a constant stress or strain amplitude until failure. From these tests are drawn the SN-curve, which represents the stress amplitude as a function of the number of cycles necessary to fail the component (Fig. 1.1). This curve can be divided in 3 domains:

- Low Cycle Fatigue (LCF) corresponds to stress amplitude close or above the material yield strength. Plasticity plays the most significant role and can be observed visibly. Cracks initiate quickly and failure occurs generally at the surface after a low number of cycles ($N < 10^5$).

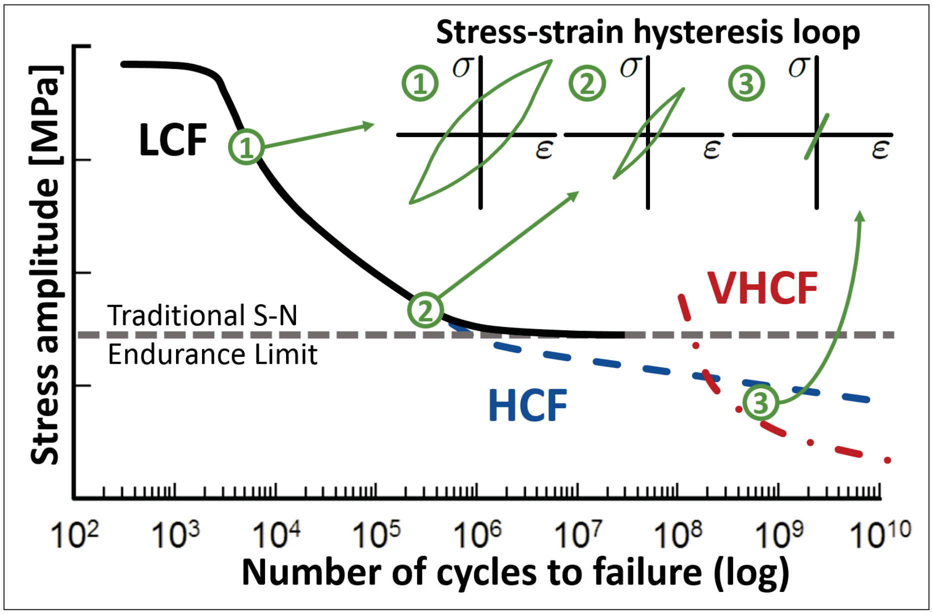

Figure 1.1 Schematic SN-curve and its corresponding hysteresis loops (adapted from Newman (2015) and Mughrabi (1999)). Black line: traditional S-N curve illustration with an endurance limit; Blue line: more realistic S-N curve without endurance limit; Red line: transition from surface-dominated fatigue damage mechanisms (blue line) to subsurface-dominated mechanisms (red line) taking over in VHCF regime.

- High Cycle Fatigue (HCF) corresponds to stress amplitude below the material yield strength. Plasticity is macroscopically low or nonexistent but still exists at the microscopic scale. Plasticity occurs locally at some microscopic regions of stress concentration where damage accumulate over the cycles. Multiple cracks generally initiate at the material surface leading to rupture after a large number of cycle ($10^5 < N < 10^7$).

- Very High Cycle Fatigue (VHCF) corresponds to very low amplitude stress and failure generally occurs internally (fisheye) after $N > 10^7$ cycles. Nowadays, car engine parts have a fatigue life of about 10^8 cycles, high-speed train of about 10^9 cycles and aerospace turbine of about 10^{10} cycles (Bj Kim, 2005).

Some material SN-curve (certain steel and titanium alloys) presents an asymptote called the fatigue or endurance limit (amplitude stress below which failure never occurs no matter the number of cycles loaded) but in reality, there is always damage made while under cyclic loading, which eventually will lead to failure after many cycles. Therefore, it is preferable to refer to fatigue strength (amplitude stress at which failure occurs after N_{fs} cycles).

Analytical models are used to predict the SN-curve through a minimal amount of tests (static traction, a limited amount of fatigue tests). The Basquin model (Basquin, 1910) is the most common in the literature as it suggests a linear relationship between the logarithm of N, C and S as follows:

$$log(N) = log(C) - m \cdot log(S) \tag{1.1}$$

where S is the amplitude stress, C and m are the model parameters. The standard technique to identify these parameters is to experimentally test the material for at least two given stresses and use a probability density function (usually a normal distribution) to describe the scatter of the data as shown in Fig. 1.2. From this data, different SN-curves are drawn depending on the probability of rupture required for a target application. Generating this data is very expensive and time-consuming, and the number of experimental data acquired is often insufficient to accurately determine the probability density function. Also, this kind of model is relevant for $N < 10^6$, but not for the HCF and VHCF regimes, which are subject to a lot more dispersions. For a given low-amplitude stress, the number of cycles to failure can easily differ of one order between different specimens from the same bulk material. These dispersions can be critical during the designing process for fatigue life predictions. Safety factors are used to account for these dispersions but are often inaccurate. It is then important to understand and predict properly this data dispersions observed in HCF and VHCF regimes, which will be the focus of this thesis.

The fatigue process can be decomposed in three steps: crack initiation, short crack propagation and long crack propagation until part failure. A description proposed by McDowell & Dunne (2010) of these steps relevant mechanisms in the LCF and HCF regimes can be found in Table 1.1. Within the purpose of predicting fatigue life in HCF and VHCF regimes, only the crack initiation step will be reviewed as it is the dominant step in these regimes.

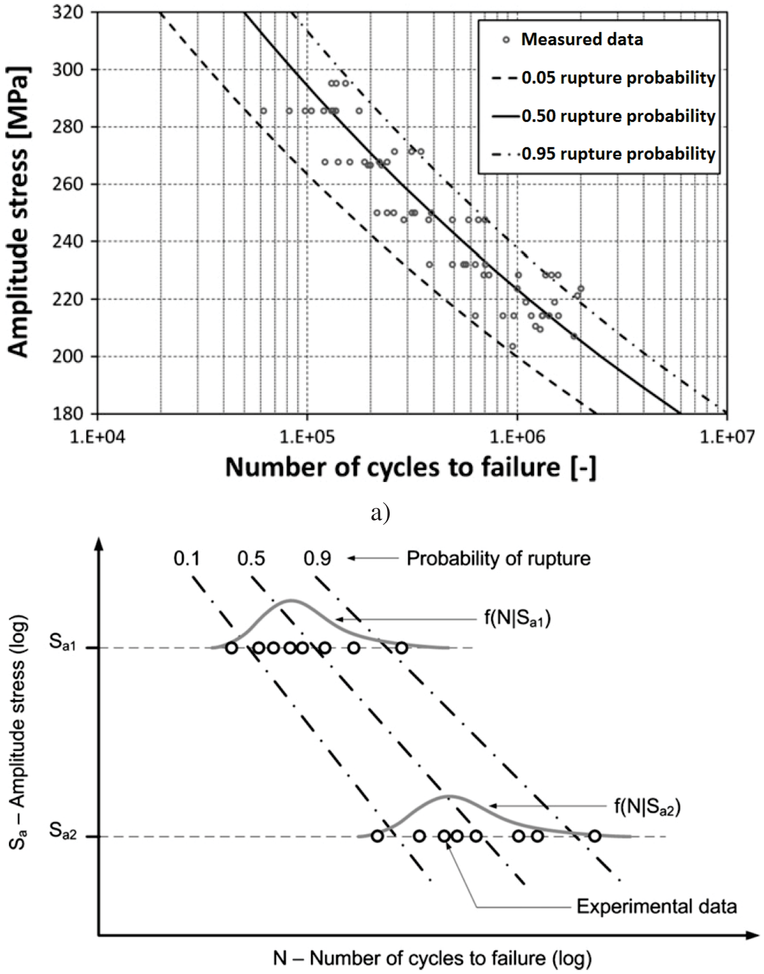

a)

b)

Figure 1.2 Scatter of the fatigue test results and their corresponding S-N curves for different failure probabilities (taken from Klemenc & Fajdiga (2012)): (a) Experimental scattered data for the S420MC steel S–N curve; (b) Typical gaussian distribution of the experimental data obtained for two stress amplitudes S_{a1} and S_{a2}.

Several factors affect crack initiation: defects, surface roughness, inclusion density, mono or poly-phase material, residual stress, macroscopic / microscopic crystallographic texture, grains size and morphology, temperature, environment, etc. They all yield to the same consequence: introducing local stress concentrations. Even if the material appears macroscopically elastic and homogeneous, some grains are locally submitted to sufficiently large stress level making them yield before the others. Crack initiation is highly impacted by these stress concentrations,

Table 1.1 Fatigue mechanisms in HCF and LCF regimes (Taken from McDowell & Dunne (2010)). LEFM: Linear Elastic Fracture Mechanics.

Mechanisms	**LCF - percolated, microplasticity**	**HCF - isolated, heterogeneous, microplasticity**
Crack formation	Propagation-dominated: largest grains or inclusions establish initial crack length in propagation analysis	**Initiation-dominated**: largest grains or inclusions control number of cycles to form a crack or to escape arrest
Microstructurally crack growth	Cracks grow in elastic-plastic field with less microstructure influence	First few microstructure barriers control fatigue limit and scatter of lifetime
Physically small and long crack growth	Elastic-plastic growth persists well into crack growth history; coalescence of multisite cracks can occur	Transition to LEFM-dominated homogeneous crack growth; single dominant crack is common

whereas, in the case of the long crack propagation, the stress field surrounding the crack tip is not affected by the material heterogeneities, and the evolution of the crack during cycling is closely related to the stress intensity factor (Bazergui, 2002). Due to the fact that these factors are difficult to control during the part manufacturing, they are considered to be random, making a statistical study of the material fatigue life systematically required.

Several numerical studies can be found in the literature on the impact of these different factors on the materials fatigue life (Guerchais, Morel & Saintier, 2017; McDowell, 2007; Przybyla, Prasannavenkatesan, Salajegheh & McDowell, 2010; Santecchia, Hamouda, Musharavati, Zalnezhad, Cabibbo, El Mehtedi & Spigarelli, 2016; Zghal, Gmati, Mareau & Morel, 2016), but there is one factor that is often neglected by authors: the neighborhood effect, which is the main interest of this thesis. The neighborhood effect is the stress-strain variations induced by a grain's close environment which, depending on its configuration, can increase or decrease the grain stress level, thus generating a stress concentration, possibly responsible for early crack initiation. The neighborhood effect has been observed experimentally through digital image correlation (DIC) combined with electron backscatter diffraction (EBSD) (Bridier, Villechaise & Mendez, 2008; Hemery, Nait-Ali, Gueguen & Villechaise, 2018; Stinville, Echlin, Texier, Bridier, Bocher & Pollock, 2016a), and also numerically (Brenner, Lebensohn & Castelnau, 2009;

Guilhem, Basseville, Curtit, Stephan & Cailletaud, 2010; Robert, Saintier, Palin-Luc & Morel, 2012a). For a given material, both methods showed that a given grain's mechanical state depends not only on its own mechanical properties but also on its close environment configuration.

1.2 Single-crystal mechanics

A mono-crystal, also called in the literature single-crystal, crystal or grain, is considered as a homogeneous anisotropic material (impurity being ignored). The crystal anisotropy is responsible for the stress heterogeneities that are observed within polycrystals. Different type of crystallographic structure exists which contrasts the crystal anisotropy. In this work, the hexagonal closest packed (HCP) and the face-centered cubic (FCC) structures were studied. A crystal mechanical response may differ depending on its orientation relatively to the loading axis due to the crystal anisotropy. The crystal anisotropy mainly comes from two different sources: its elasticity and its viscoplasticity.

1.2.1 Crystal elasticity

A crystal elastic resistance to deformation depends on the loading direction: directions for which atoms are closer to each other will be more resistant than direction where atoms are farther from each other. Fig. 1.3 shows the distribution of the crystal elastic resistance along the direction $\vec{\boldsymbol{e}}_{\mathbf{3}}$ in the standard stereo-triangle for iron (FCC) and titanium (HCP) crystals using the elastic constants presented in Table 1.2. The elastic resistance along $\vec{\boldsymbol{e}}_{\mathbf{3}}$ is the Young's modulus $E_y = \mathbb{S}^{-1}_{3333}$, where $\mathbb{S}$ the compliance tensor expressed in the global axis system which its components depend on the crystallographic orientation. Monocrystal elastic anisotropy and the ratio between the maximum and minimum Young's modulus varies depending on the material: a ratio of 2.4 is observed for the iron and nickel whereas a ratio of 1.2 and 1.4 are observed for the aluminum and titanium respectively. These significant ratios observed for the iron and nickel crystals illustrate the importance of the crystal elastic anisotropy and how stress concentrations can occur within polycrystals without even considering inclusions nor surface roughness.

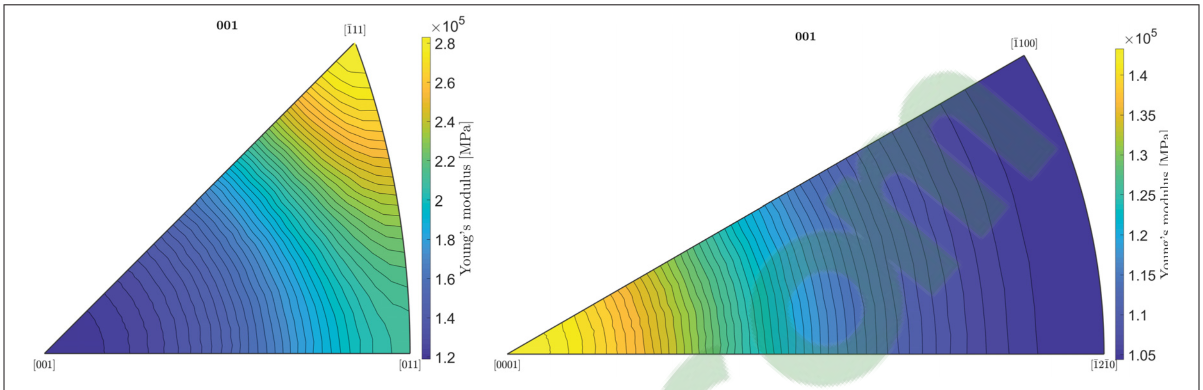

a) Iron (Cubic) b) Titanium (Hexagonal)

Figure 1.3 Young's modulus inverse pole figure in the standard stereo-triangle: (a) iron FCC structure; (b) titanium HCP stucture.

Table 1.2 Single crystal elastic constants $\mathbb{C}^{cry}$ (Simmons & Wang, 1971).

Fe	$\mathbb{C}^{cry}_{1111} = 226$	$\mathbb{C}^{cry}_{1122} = 140$	$\mathbb{C}^{cry}_{1212} = 116$	(GPa)		
Ti	$\mathbb{C}^{cry}_{1111} = 162.4$	$\mathbb{C}^{cry}_{3333} = 180.7$	$\mathbb{C}^{cry}_{1122} = 92$	$\mathbb{C}^{cry}_{1133} = 69$	$\mathbb{C}^{cry}_{1313} = 46.7$	(GPa)

1.2.2 Crystal plasticity

Plastic deformation occurs in a monocrystal through dislocations motion. Dislocations prefer to move along the most dense crystallographic plane and direction. A slip plane (defined by its normal vector $\vec{\boldsymbol{n}}_s$) and a slip direction ($\vec{\boldsymbol{l}}_s$) constitute a slip system. For FCC structures (steel, nickel), the twelve octahedral slip systems ($\{111\}$ slip planes and $< \bar{1}10 >$ directions) are the easiest to activate (Fig. 1.4c). For HCP structures, and more specifically titanium alloys, the most common slip systems to activate for a quasi-static loading at room temperature are the three prismatic ($\left\{10\bar{1}0\right\}$ slip planes and $< 11\bar{2}0 >$ directions) and the three basal ($\{0001\}$ slip planes and $< 11\bar{2}0 >$ directions) slip systems (Fig. 1.4b and 1.4b).

Dislocation motion starts when the resolved shear stress (RSS) over a slip system reaches a certain critical level. A resolved shear stress is the projection of the stress $\boldsymbol{\sigma}$ on a slip system indexed s and is calculated by means of the Schmid's tensor $\boldsymbol{m}^s$ as:

$$\tau_s = \boldsymbol{\sigma} : \boldsymbol{m}_s \tag{1.2a}$$

$$with \quad \boldsymbol{m}_s = \frac{1}{2}\left(\vec{\boldsymbol{l}}_s \otimes \vec{\boldsymbol{n}}_s + \vec{\boldsymbol{n}}_s \otimes \vec{\boldsymbol{l}}_s\right) \tag{1.2b}$$

which in the case of an uniaxial loading $F\vec{t}$ is simplified as:

$$\tau_s = M_s \cdot \frac{F}{S} \quad with \quad M_s = (\vec{t} \cdot \vec{n}_s) \times (\vec{t} \cdot \vec{l}_s) = \cos\alpha_n \cdot \cos\alpha_l \tag{1.3}$$

where M_s is the Schmid's factor, F is the force applied to the surface S, $\vec{t}$ is the loading direction as illustrated in Fig. 1.4a, α_n the angle formed by $\vec{t}$ and $\vec{n}_s$, and α_l the angle formed by $\vec{t}$ and $\vec{l}_s$. The inverse pole figures of the maximum Schmid's factor for each slip system category mentioned above are shown in Fig. 1.4 in their respective standard stereo-triangle. Crystallographic orientations showing a Schmid's factor of 0.5 along the loading direction are the most likely to start plastifying. In the case of an uniaxial stress loading such as $\vec{t} = [0; 0; 1]$ for example, the crystallographic direction [519] is the most likely to plastify for octahedral slip systems in FCC.

1.2.3 Crystal orientation and Euler angles

The orientation of a crystal has an important impact on it mechanical behavior due to its anisotropy. Along the present works, the Euler angles with Bunge convention were used to define orientations. Euler angles are a three angles set corresponding to a rotation series as illustrated in Fig. 1.5 as:

- φ_1 rotation around Z axis;
- Φ rotation around the resulting X axis from the previous rotation;
- φ_2 rotation around the resulting Z axis from the previous rotation.

Random orientation sets were generated in this work. The Euler angles are not adequate to generate random orientation sets. Due to sines and cosines involved in the rotation matrix, random generations of Euler angles do not result in a set of orientations homogeneously distributed

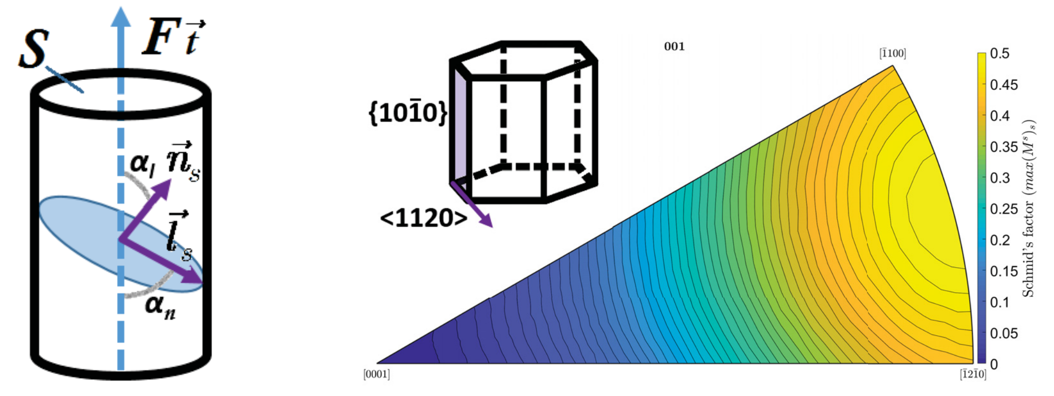

a) Schmid's factor schematic

b) Prismatic

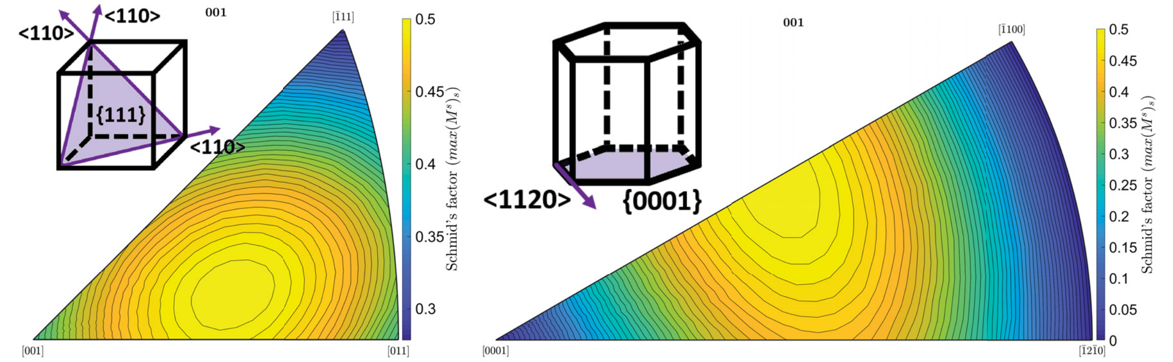

c) Octahedral

d) Basal

Figure 1.4 (a) Schmid's factor illustration and distribution of its maximum value over the inverse pole figure in the standard stereo-triangle for $\vec{t} = [0; 0; 1]$ and for each slip systems: (b) prismatic; (c) octahedral; (d) basal.

over the standard stereo-triangle (Bretin, 2016; Guilhem, 2011). The method developed by Shoemake (1992) using quaternions were used to generate uniform distributions. A quaternion is a complex number often used in robotics and industrial engineering. The details to generate a random set of orientation using the quaternion method, their relation with the Euler angles, and the definition of the rotation matrix can be found in Appendix I.

1.2.4 Mono-crystal constitutive models

This section is an introduction to mono-crystal mechanical behavior modeling. The numerical methods to integrate models equations can be found in a technical report for *Code_Aster* software (Haboussa, 2014).

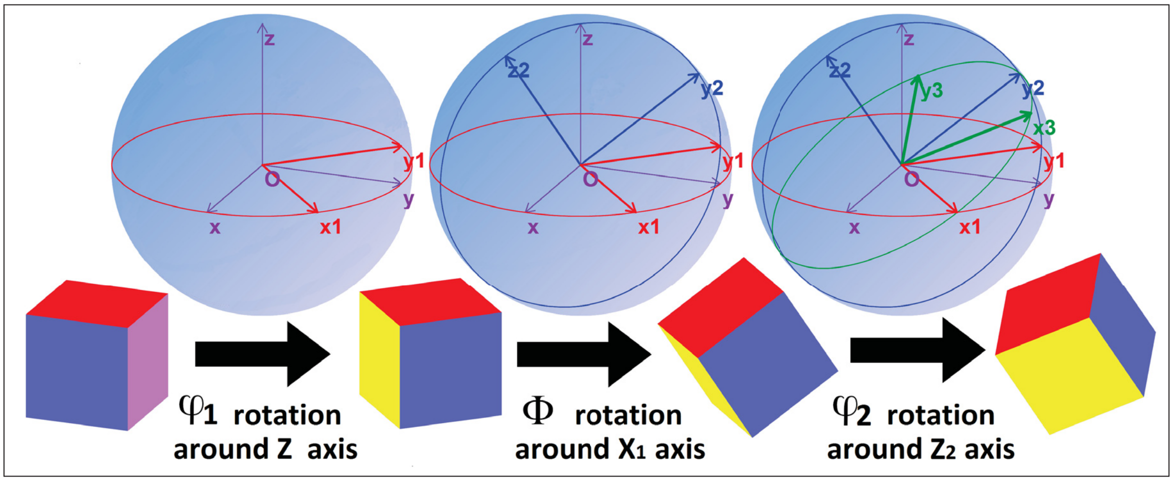

Figure 1.5 Euler angles definition representation (adapted from Tulloue (2015)).

In small deformation theory, applicable to HCF problems due to the expected low visco-plastic strain level, the material strain can be decomposed as:

$$\boldsymbol{\varepsilon} = \boldsymbol{\varepsilon_e} + \boldsymbol{\varepsilon_p} + \boldsymbol{\varepsilon_t} \tag{1.4}$$

where $\boldsymbol{\varepsilon_e}$, $\boldsymbol{\varepsilon_p}$ and $\boldsymbol{\varepsilon_t}$ are respectively the elastic, plastic and thermal strains. The thermal strain $\boldsymbol{\varepsilon_t}$ will be ignored in this work as not being part of the study framework and the Hooke's law is used to define the elastic strain as:

$$\boldsymbol{\sigma} = \mathbb{C} : \boldsymbol{\varepsilon_e} \tag{1.5}$$

where $\mathbb{C}$ is the crystal stiffness tensor that depends on the cristal elastic properties (Table 1.2) and which its components in a global axis system vary depending on the crystal orientation (Section 1.2.3 and Appendix I). The plastic strain rate can be quantified as a function of the Schmid's tensor $\boldsymbol{m}_s$ (Eq. 1.2) and the slip rate $\dot{\gamma}_s$ of each system s:

$$\dot{\boldsymbol{\varepsilon}}_{\boldsymbol{p}} = \sum_s \dot{\gamma}_s \boldsymbol{m}_s \tag{1.6a}$$

$$with \quad \boldsymbol{m}_s = \frac{1}{2}\left(\vec{\boldsymbol{l}}_s \otimes \vec{\boldsymbol{n}}_s + \vec{\boldsymbol{n}}_s \otimes \vec{\boldsymbol{l}}_s\right) \tag{1.6b}$$

The expression of the slip rate $\dot{\gamma}_s$ differs from a model to another and mono-crystal constitutive laws can be divided in two categories: physical laws, and phenomenological laws.

The so-called physical (or near-physical) models have the particularity of being based on discrete dislocation dynamic (DDD) and are generally derived from physical measurements, bringing a physical meaning to the crystal behavior. The disadvantage of this type of law is that they are poorly suited for cyclic or complex loading. They are also generally heavier in terms of CPU time. This type of models was not considered in the present works for these matters. Here is a non-exhaustive list of common physical laws that can be found in the literature:

- Tabourot, Fivel & Rauch (1997) were among the first to develop such model. Their model was developed for the elastoviscoplastic behaviour of FCC single crystals submitted to a monotonic load. The slip rate $\dot{\gamma}_s$ is expressed as:

  $$\dot{\gamma}_s = \dot{\gamma}_0 \left(\frac{\tau_s}{\tau_s^0} \right)^n \tag{1.7}$$

  where $\dot{\gamma}_0$ and n are a material parameters, τ_s is the resolved shear stress of the slip system s, and τ_s^0 is the internal stress depending on the the local disclocation densities of each slip system. Slip systems interactions are accounted by the addition of an interaction matrix. The constitutive law equations are based on a physical approach of crystal plasticity mechanism and thus all the parameters have a physical meaning.

- Déprés, Fivel & Tabourot (2008) pushed further Tabourot et al. model by adding a intragranular kinematic hardening and thus making it more suitable for the study of cyclic loading. They relied on the results from their own simulations in DDD. The model features here the concept of geometrically necessary dislocations, ensuring compatibility of grain boundary displacements, introduced by Ashby (1970). They aim at restoring the geometric incompatibilities induced by sliding near the grain boundaries of a polycrystal. Dislocation dipoles near the grain boundaries are then created. This type of dislocation may also appear in the grain core because of the heterogeneities of plastic deformation. The strength of this model is the good compatibility of the results in cyclic loading with DDD numerical simulations, while maintaining a physical approach.

- Evrard, Aubin, Degallaix & Kondo (2008a) developed a model based on observations during low-cycle fatigue tests. Some material show a cyclic softening due to a rearrangement of disclocations in hard and soft zones within the grains during cyclic straining. To answer to that problem, the model proposed to distinguish the hardening due to dislocation densities in walls and canals for each slip system. The model predicted with success the initial hardening followed by softening and the stabilized state of FCC polycrystals.

- Monnet & Vincent (2011) developed a DDD based model for body-centered cubic materials (bainitic steel) in the low thermal plastic regime with a minimum of parameters adjustable on macroscopic results. The model proved its capability to reproduce DDD simulations and experimental results.

Phenomenological laws, relaying on experimental observations from a micro and macroscopic point of view, are similar to macroscopic laws. In elastoplasticity, they are generally based on isotropic and/or kinematic hardening and rely on two material variables: the plastic strain rate and the accumulated plastic strain which is defined as the sum of plastic strain increments over the loading cycles, regardless of the loading direction (tensile/compression, axial/bi-axial). A schematic illustration of the isotropic and kinematic hardening can be found in Fig. 1.6: kinematic hardening translates the yield surface along the loading direction without deforming it whereas the isotropic hardening expand the yield surface in all direction without moving it. In the framework of monocrystal phenomenological constitutive laws, instead of considering the plastic strain as the core state variable, the slip rate $\dot{\gamma}_s$ and the accumulated dislocations density (v_s) of each slip system are used to control the crystal hardening.

A large variety of models can be found in the literature (a non-exhaustive list can be found in Haboussa (2014)) with different expressions of the slip rate $\dot{\gamma}_s$. The Méric-Cailletaud model proposed by Méric, Poubanne & Cailletaud (1991), noted the MC model in the following, is the most often used to study cubic polycrystals under many different conditions (Barbe, Decker,

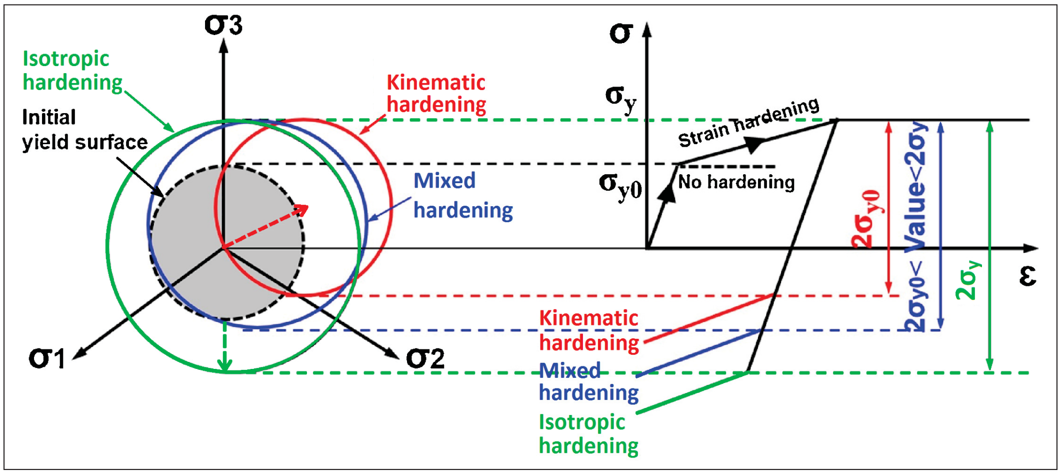

Figure 1.6 Isotropic and kinematic hardening schematic illustration (taken from Sun *et al.* (2019))

Jeulin & Cailletaud, 2001a; Eberl, 1999; Gérard, 2008; Guery, Hild, Latourte & Roux, 2016; Guilhem, Basseville, Curtit, Stephan & Cailletaud, 2013; Michel & Suquet, 2016; Musienko, Tatschl, Schmidegg, Kolednik, Pippan & Cailletaud, 2007; Zouaghi, Velay, Soveja, Pottier, Cheikh & Rézaï-Aria, 2016). The MC model plasticity flow rule is written as follow:

$$\dot{\gamma}_s = \left(\frac{\tau_s - \chi_s}{|\tau_s - \chi_s|}\right) \dot{v}_s \tag{1.8a}$$

$$\text{with} \quad \dot{v}_s = \left(\frac{(|\tau_s - \chi_s| - r_s)^+}{K}\right)^n \tag{1.8b}$$

where $(\cdot)^+$ designs the operator taking the positive part of its argument; K and n are the viscosity parameters; χ_s and r_s are respectively the kinematic and isotropic hardening. What mostly differs from a model to another is the definitions of the kinematic and isotropic hardening functions. In the case of the MC model, the hardening functions are inspired by macroscopic models: Armstrong-Frederick's kinematic hardening and Chaboche's isotropic hardening (Lemaitre, Chaboche, Benallal & Desmorat, 2009). The MC model was chosen for the elastoplastic study presented in Chapter 4 due to its simplicity and the fact that this model takes into account the 12 sliding systems of the CFC structures and the intragranular kinematic hardening, which makes it well adapted to correctly describe material fatigue behavior and capture phenomena such as the Bauschinger effect. The model equations can be found in Section 5.2.2.

The common method used to identify the parameters of phenomenological laws is to fit them to macroscopic experimental results (tension and cyclic load) by means of homogenization models such as the Berveiller-Zaoui model (see Section 1.3.3). The issue with this method is that the parameters can differ from the real crystal mechanical behavior and mislead on the physical phenomenon at stake.

1.2.5 Crack initiation criterion

Crystals can exhibit different yielding mechanisms: slip, crystal twinning, and phase transformation. At room temperature and low stress amplitude, slip is the most common mechanism, twinning is more present in titanium crystals, and phase transformation can be observed in steels (austenite to martensite). When yielding, slip forms persistent slip bands (PSB). They form intrusions and extrusions at the grain surface, as illustrated in Fig. 1.7, and, after a certain number of cycles and a certain size, they are considered as cracks.

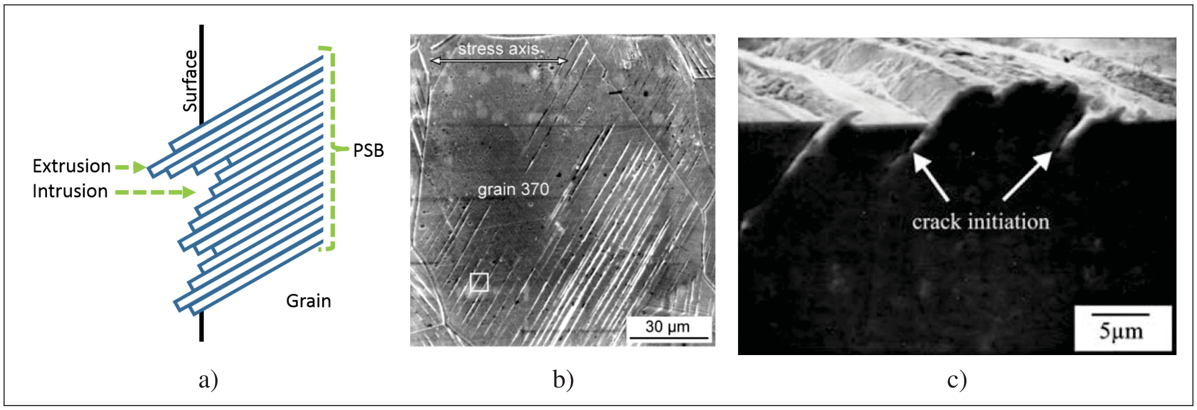

Figure 1.7 Persistent slip band mechanism: (a) schematic representation; (b) Scanning electron microscope micrograph of a 316L steel grain and its PSB (taken from Man *et al.* (2002)); (c) crack initiation observed at the surface of a copper monocrystal (taken from Bao-Tong & Laird (1989)).

Several fatigue damage criteria have been introduced in recent years, each adapted to particular conditions (type of loading, number of cycles, etc.). According to these criteria, the structure does not damage as long as the criterion does not exceed a critical threshold. Most of the criteria are adapted for a macroscopic study of the material behavior. A non-exhaustive list of these macroscopic criteria and a comparison of their efficiency can be found in Curtit, Le Pecheur & Stephan (2008).

When adapted for a mesoscopic study of the material fatigue behavior, the criteria can depend on one or several parameters, such as the stress level, the cumulative plastic strain, the dislocation density, the DDD, etc... Many different models can be found in the literature, each depending on the application conditions and/or the constitutive law chosen. Stress based approaches, such as Dang Van and Papadopoulos approaches (Dang Van, Cailletaud, Flavenot, Le Douaron & Lieurade, 2013; Papadopoulos, 1994) based on hypotheses expressed at the mesoscopic scale, are widely used in industry, whereas approaches relying on the DDD such as Déprés' approach (Déprés, Robertson & Fivel, 2006), are less frequent. Here is a short description of the most common models found in the literature:

- Dang Van criterion (Dang Van *et al.* (2013)) : a stress and time t dependent criterion has been introduced by Dang Van for determining infinite lifetime under cyclic loading with a fixed amplitude as:

  $$\sigma_{DV} = \max_{s}\left(\max_{t}\left(\tau_s^*(t) + k_{DV}P(t)\right)\right) \tag{1.9}$$

  where k_{DV} is a material parameter, $P(t)$ is the hydrostatic stress, and $\tau_s^*(t)$ is the centered resolved shear stress of the slip system s, such as:

  $$\tau_s^*(t) = \tau_s(t) - \frac{1}{2}\left(\max_{t}(\tau_s(t)) + \min_{t}(\tau_s(t))\right) \tag{1.10}$$

  As long as σ_{DV} is inferior to a predefined threshold stress during the stabilized cycles, no crack is assumed to initiate within the grain. Below a certain loading threshold, infinite lifetime is expected as all the grains are assumed to adapt to follow an elastic behavior. If the loading exceeds this threshold, some critical grains will not be able to adapt and after a certain number of cycles, this leads to the initiation of a crack. The use of $\tau_s(t)$ in the criterion is justified as fatigue cracks usually begin at the interface between slip bands, and the use of $P(t)$ is justified because it enables the crack opening.

- Park-Nelson criterion (Park & Nelson, 2000): another way to design a fatigue criterion is to relate the amount of energy dissipated during each cycle to the generation of the fatigue damage. It is assumed that under any load, the material can dissipate only a limited amount of energy. Various kinds of energies are considered: cyclic distortion elastic energy, plastic density dissipation or the hydrostatic energy density. The most popular of these models is the Park-Nelson approach that proposed a unified approach for both low and high cycles fatigue domain.

- Mounounga criterion (Mounounga, Abdul-Latif & Razafindramary, 2011): the inconvenience of all the previous model presented is that they do not considered the grain cumulative plastic slip of each slip system responsible for the PSB. Mounounga *et al.* (2011) developed a micromechanical model that introduced a damage variable for each slip system. The model was recently applied in a self-consistent model by Zghal *et al.* (2016) and reproduced correctly the experimentally observed fatigue behavior of a medium carbon steel.

- Déprés criterion (Déprés *et al.*, 2006): as an example of a fatigue criterion relying on a discrete dislocation dynamics model, Déprés developed a grain-scale model. The criterion stipulates that a crack initiates when the grain surface cumulative plastic strain, depending on the number of PSB and the cumulative plastic strain in each band, reaches a threshold value noted $\gamma_{lim}^{surf(\Delta\varepsilon_p)}$. The number of cycles to fatigue crack initiation N_i^D for a given grain is expressed as:

$$\sqrt{N_i^D} = \left(\frac{\tau_{pri}}{\tau_{cro}}\right)^{1.28} \frac{D_g}{H_g} \frac{1}{\left(1+2\frac{|\overline{\varepsilon_p^{VM}}|}{\Delta\varepsilon_p^{VM}}\right)} \frac{\gamma_{lim}^{surf(\Delta\varepsilon_p)}}{\Delta\varepsilon_p^{VM}} \tag{1.11}$$

where τ_{prim} and τ_{dev} are the resolved shear stress of the primary and cross slip systems respectively; D_g and H_g are the grain diameter and depth respectively; ε_p^{VM} is the equivalent von Mises plastic strain amplitude, $\Delta\varepsilon_p^{VM}$ the strain amplitude and $\overline{\varepsilon_p^{VM}}$ its average value (equal to 0 for a cyclic with $R = -1$). This criterion was applied by Osterstock, Robertson, Sauzay, Degallaix & Aubin (2007) on a surface grain among 180 polycrystalline aggregate computations subjected to uniaxial and equibiaxial loading. The polycrystals studied were composed of extruded hexagonal-based grains, which restricted the scope of the study to certain grain boundary configurations. The results of the application of this criterion showed that the equibiaxiality of the loading increases by 30% the number of cracked grains. This however has not been the subject of an experimental validation.

Damage criteria are often developed for a specific material and/or model. Some authors prefer to look at the grain cumulative plastic slip ν_s (Equations 1.6 and 1.8) and the following relative variables for their simplicity to assess grains damage, relatively (Roters, Eisenlohr, Bieler & Raabe, 2011):

- The sum of each slip system cumulative viscoplastic slip:

$$\nu_\Sigma = \sum_s \left(\int_0^t \dot{\nu}_s \right) \tag{1.12}$$

- The maximum cumulative viscoplastic slip among all slip system:

$$\nu_\Sigma = \max_s \left(\int_0^t \dot{\nu}_s \right) \tag{1.13}$$

- Persistent Slip Markings (PSM), characterizing the PSB height, quantified by:

$$\gamma_{surf} = \max_p (|\gamma^p_{surf}|) \times sign(\gamma^p_{surf}) \tag{1.14a}$$

$$\text{with} \quad \gamma^p_{surf} = \left(\sum_{s \in p} \gamma_s \vec{\boldsymbol{l}}_s \right) \cdot \vec{\boldsymbol{n}}_{surf} \tag{1.14b}$$

where γ_s is the slip system s dislocations density; $\vec{\boldsymbol{l}}_s$ the slip system s slip direction; $\vec{\boldsymbol{n}}_{surf}$ is the normal to the grain surface and $s \in p$ designs all the slip systems sharing the same slip plan.

1.3 Polycrystal modeling

This section is an introduction to polycrystalline mechanical behavior modeling. A larger overview on that matter can be found in Besson, Blétry, Cailletaud, Chaboche & Forest (2009) and Fritzen (2011) books, and a more summarized overview can be found in Roters, Eisenlohr, Hantcherli, Tjahjanto, Bieler & Raabe (2010) paper. A comparison between different models predictions (Self-consistent model, finite element method and Fast Fourier Transformation) can be found in Robert & Mareau (2015) work.

1.3.1 Aggregate generation

Within the framework of polycrystalline structures, Voronoi tessellation dominates the field due to its simplicity and the high representativeness of the results. The basic principles, as illustrated in Fig. 1.8, are as follow:

- Seeds are randomly or arbitrary spread in a bounded domain of space and weights are distributed randomly or arbitrary to each seeds. The weights will define the size of the grains.
- A Delaunay Triangulation with the seeds is performed (red lines): triangles are formed with the seeds such as no seed other than the three forming the triangle are inside the circumscribed circle of this triangle.
- A normal (line or plane depending on if it's in 2D or 3D) are drawn on each red lines at the seeds barycenters. These blue lines/planes delimit the cells/grains.

Several tessellation methods can be found (Poisson-Voronoi, Hardcore Voronoi, Centroidal Voronoi, Laguerre Voronoi, etc...), resulting in different microstructures (grain size distribution and morphology) depending on the ways the seeds and their weights are spread. A description of these tessellation methods can be found on NEPER's website (Quey, 2019). NEPER is an open-source software offering the tools to generate various polycrystal morphologies (Quey, 2019) with a large collection of algorithms to generate a wide variety of microstructures. NEPER was used in this work to generate and mesh our microstructures.

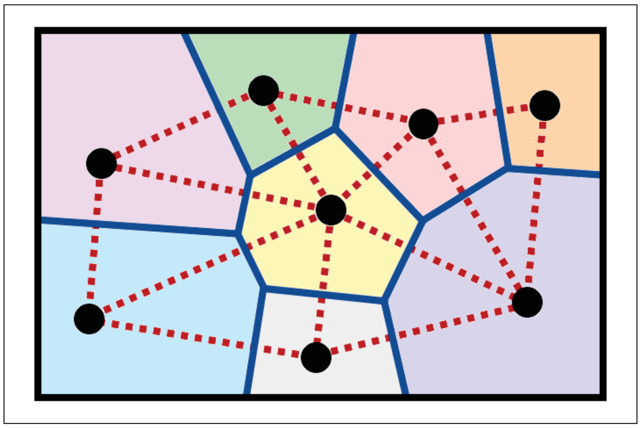

Figure 1.8 2D illustration of a Voronoi diagramm and its basic steps: Black dots: Voronoi seeds; Red lines: Delaunay triangulation; Blue lines: grains delimitation

More complex techniques can be found based on experimental destructive measurements. One of which, called the focused ion beam scanning electron microscope (FIB-SEM), consists of scanning the material in 2D, slice by slice, and reconstructing the 3D topology from the 2D scans (Groeber, Haley, Uchic, Dimiduk & Ghosh, 2006).

Numerical studies of polycrystals micromechanical behavior are carried out on aggregates volumes limited by the computational power. In order to optimize the calculations duration while maintaining the results accuracy, a representative volume element (RVE) is used. One of the first definition of a RVE proposed by Hill (1963) is “a sample that is the structurally typical of the whole microstructure for a given material, i.e. containing a sufficiently large number of heterogeneities, while being small enough to be considered homogeneous from a continuum mechanics viewpoint”. Given a polycrystalline material with “infinite” dimensions, a deterministic definition of the RVE is the smallest volume so that any subdomain from this polycrystal with that volume size has the same effective behavior than the polycrystal with infinite dimensions. In other words, a RVE is reached when the effective properties of a material sample with a given volume do not vary no matter where the sample is taken and when the sample volume increases. Using FEM, Kanit (2003) studied with a statistical approach the concept of RVE for polycrystals and observed the influence of different parameters such as crystal anisotropy, shape ratios, boundary conditions, and so on. They concluded that there is no general definition of the RVE size, and that it is preferable to do several evaluations on different samples and to average the results in order to obtain the actual material properties. In addition, the choice of boundary conditions used can influence the size of the RVE. Kanit (2003) has shown that periodic boundary conditions (PBC), in the case of an elastic polycristal, allow to reach the convergence of the effective behavior more rapidly than other boundary conditions, and thus have the effect of reducing the size of the RVE. As a matter of fact, using PBC can reduce the unwanted edges effects that may interfere with the response and therefore reduce the fraction of corrupted results in comparison to kinematic uniform boundary conditions (KUBC). To conclude, RVE depends on many parameters such as the local constitutive law, the grains morphologies, the texture, the load amplitude, the boundary conditions, the studied variables (local, mean or effective state variables). Ideally, a statistical study should be carried on systematical to define a suitable RVE for the study. More recent work on that matter be found in Yang, Dirrenberger, Monteiro & Ranc (2019).

1.3.2 Full-Field models

Full-field models, such as finite element method (FEM) and the fast Fourier transformation method (FFT), are used to compute the polycrystals local fields and are able to take into account for as many of heterogeneities as it needs to be considered in the model. They are often used as a reference tool in the study of micromechanical fields due to their unequaled accuracy. This section is a quick description of full-fields models and relative approaches.

1.3.2.1 Finite Element Method (FEM)

The finite element method (FEM), originally developed for the stress analysis of airplanes, is a robust and reliable method for the study of materials mechanical behaviors. Mika & Dawson (1998) and soon later Barbe (2000) are the pioneer in the field of micromechanical study of polycrystalline materials using the FEM. Thanks to the expansion of computational power, the

FEM fields of application have become very wide and allowed the study of complex problems. A non-exhaustive list can be found in Roters *et al.* (2010) and Benedetti & Barbe (2013).

Despite its robustness and reliability, the FEM has some drawbacks when it comes to repetitive simulations. The requirement of generating a mesh (often paired with a convergence study) and mostly the CPU time required to performed such simulations make the FEM not suitable for the statistical study of materials mechanical behaviors. For example, a single FEM simulation performed by Robert *et al.* (2012a) of a 2D aggregate mesh of 300 grains with approximately 400 triangular elements per grain with linear interpolation submitted to an elasto-visco-plastic cyclic loading (MC constitutive model) required approximately 60h for 10 cycles on an Intel Xeon X5677 processor at 3.47 GHz with 64 Gb of RAM.

Plenty of articles can be found in the literature dedicated to the study of polycrystalline materials and their local behavior in HCF regime by means of FEM (Cruzado, LLorca & Segurado, 2017; Cruzado, Lucarini, LLorca & Segurado, 2018; Martin, Ochoa, Sai, Hervé-Luanco & Cailletaud, 2014; Robert, Saintier, Palin-Luc & Morel, 2012b; Sweeney, Dunne, McHugh, Leen et al., 2015). Articles discussing about the neighborhood effect are really rare or even non-existent. An interesting one is Guilhem *et al.* (2010) work on the effect of a free surface on the local behavior. In this study he observed the impact a hard or soft neighborhood on a grain behavior and showed that such environments affect significantly the local behavior.

1.3.2.2 Fast Fourier Transformation (FFT)

The fast Fourier transformation method, initially developed for composite materials by Moulinec & Suquet (1998a) and later on adapted for polycrystals by Lebensohn (2001) and furthermore improved by Lebensohn, Kanjarla & Eisenlohr (2012) and then Lebensohn & Needleman (2016), is an accurate tool to predict the micromechanical heterogeneous behavior of polycrystalline RVE with periodic conditions. The FFT method is a highly efficient alternative to FEM because it is more computationally efficient and requires less CPU time.

The basic principles of the FFT approaches are to discretize the microstructure into voxels and solve each voxel constitutive laws in the Fourier space iteratively until convergence of stress-strain fields within a prescribed tolerance. In contrast to FEM, FFT approaches do not require meshing, making them easy to use. On the other hand, they cannot allow gradient meshing, meaning that microstructures with high aspect ratio require a high number of voxels to be accurate.

1.3.3 Mean field homogenization models

This section is a quick introduction to homogenization theories. For more details, an excellent summary on the transition rules applied to crystal plasticity was made by Cailletaud & Coudon (2016). The numerical methods to integrate models equation can be found in Haboussa (2014).

1.3.3.1 Introduction to homogenization theory

The purpose of homogenization is to define a link between the macroscopic mechanical states ($\boldsymbol{\Sigma}$ and $\boldsymbol{E}$) and the microscopic mechanical states ($\boldsymbol{\sigma}$ and $\boldsymbol{\varepsilon}$). This process can be divided in 4 steps as illustrated in Fig. 1.9:

- Representation: this step consists in defining the material. In the context of our study this is equivalent to defining the polycrystal and all the parameters required to capture its mechanical behavior (see section 1.3.1).
- Localization: this step consists in establishing a relationship between the local strain-stress and the macroscopic strain-stress applied to the polycrystal, such as:

$$\begin{aligned} \boldsymbol{\varepsilon}(\boldsymbol{x}) &= \mathbb{A}(\boldsymbol{x}) : \boldsymbol{E} \\ \boldsymbol{\sigma}(\boldsymbol{x}) &= \mathbb{B}(\boldsymbol{x}) : \boldsymbol{\Sigma} \end{aligned} \tag{1.15}$$

  where $\mathbb{A}(\boldsymbol{x})$ and $\mathbb{B}(\boldsymbol{x})$ are respectively the strain and stress localization tensors at the point $\boldsymbol{x}$.

- Constitutive law: this step establishes a relation between the local stress and the local strain. For an elastic material, Hooke's law relates these two tensors as:

$$\begin{aligned} \boldsymbol{\sigma}(\boldsymbol{x}) &= \mathbb{C}(\boldsymbol{x}) : \boldsymbol{\varepsilon} \\ \boldsymbol{\varepsilon}(\boldsymbol{x}) &= \mathbb{S}(\boldsymbol{x}) : \boldsymbol{\sigma} \end{aligned} \tag{1.16}$$

  where $\mathbb{C}(\boldsymbol{x})$ and $\mathbb{S}(\boldsymbol{x})$ are the stiffness and compliance tensors at the position $\boldsymbol{x}$ respectively.

- Homogenization: the final stage aims to average the polycrystal and determine the effective behavior.

$$\begin{aligned} \boldsymbol{\Sigma}(\boldsymbol{x}) &= \langle \boldsymbol{\sigma} \rangle_V \\ \boldsymbol{E}(\boldsymbol{x}) &= \langle \boldsymbol{\varepsilon} \rangle_V \end{aligned} \tag{1.17}$$

  where V designs the RVE and $\langle \bullet \rangle_V$ the average over V.

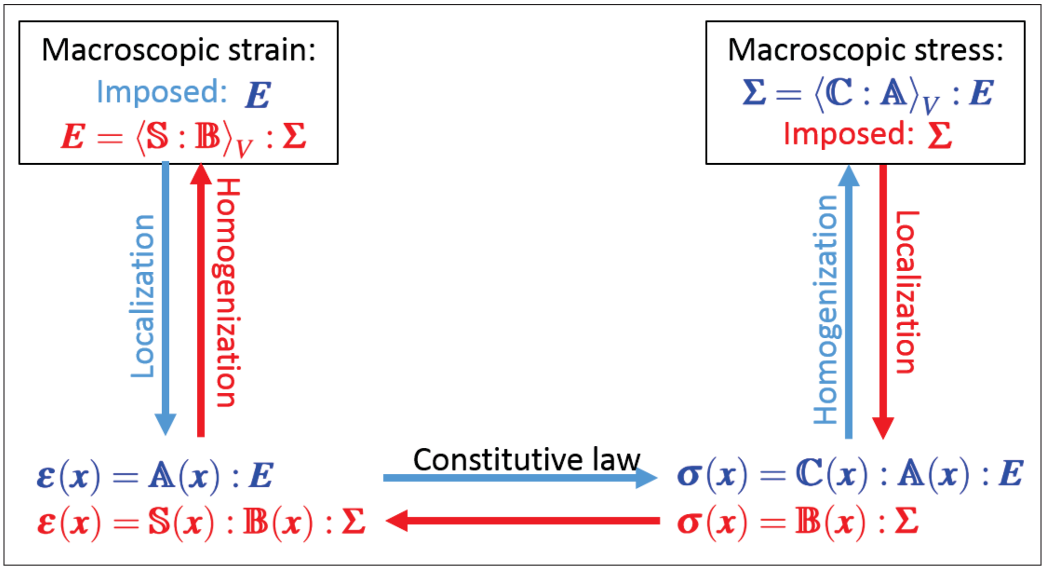

Figure 1.9 Illustration of the different steps relating the macroscopic mechanical state to the microscopic mechanical state for load control by a stress tensor (in red) and a load control by a strain tensor (in blue). (adapted from Di Paola (2010))

The following conditions on the localization tensors $\mathbb{A}$ and $\mathbb{B}$ can be deduced from equations 1.15 and 1.17:

$$\begin{aligned} \boldsymbol{E} &= \langle \boldsymbol{\varepsilon} \rangle_V = \langle \mathbb{A} : \boldsymbol{E} \rangle_V = \langle \mathbb{A} \rangle_V : \boldsymbol{E} \quad \rightarrow \quad \langle \mathbb{A} \rangle_V = \mathbb{I} \\ \boldsymbol{\Sigma} &= \langle \boldsymbol{\sigma} \rangle_V = \langle \mathbb{B} : \boldsymbol{\Sigma} \rangle_V = \langle \mathbb{B} \rangle_V : \boldsymbol{\Sigma} \quad \rightarrow \quad \langle \mathbb{B} \rangle_V = \mathbb{I} \end{aligned} \tag{1.18}$$

where $\mathbb{I}$ is the fourth order identity tensor, and the effective tensors can be deduced from equations 1.15 and 1.16 as:

$$\begin{aligned} \boldsymbol{E} = \langle \boldsymbol{\varepsilon} \rangle_V = \langle \mathbb{S} : \mathbb{B} : \boldsymbol{\Sigma} \rangle_V = \langle \mathbb{S} : \mathbb{B} \rangle_V : \boldsymbol{\Sigma} \quad &\rightarrow \quad \mathbb{S}^{eff} = \langle \mathbb{S} : \mathbb{B} \rangle_V \\ \boldsymbol{\Sigma} = \langle \boldsymbol{\sigma} \rangle_V = \langle \mathbb{C} : \mathbb{A} : \boldsymbol{E} \rangle_V = \langle \mathbb{C} : \mathbb{A} \rangle_V : \boldsymbol{E} \quad &\rightarrow \quad \mathbb{C}^{eff} = \langle \mathbb{C} : \mathbb{A} \rangle_V \end{aligned} \tag{1.19}$$

In the case where the volume V is composed of N homogeneous phases i with a volume fraction c_i and a stiffness/compliance tensor $\mathbb{C}^i/\mathbb{S}^i$, the effective stiffness and compliance tensors can be expressed as:

$$\begin{aligned} \mathbb{S}^{eff} &= \langle \mathbb{S} : \mathbb{B} \rangle_V = \sum_{i=1}^{n} c_i \ \langle \mathbb{S} : \mathbb{B} \rangle_{phase\ i} = \sum_{i=1}^{n} c_i \mathbb{S}^i : \mathbb{B}^i \\ \mathbb{C}^{eff} &= \langle \mathbb{C} : \mathbb{A} \rangle_V = \sum_{i=1}^{n} c_i \ \langle \mathbb{C} : \mathbb{A} \rangle_{phase\ i} = \sum_{i=1}^{n} c_i \mathbb{C}^i : \mathbb{A}^i \end{aligned} \tag{1.20}$$

Within the framework of the polycrystalline structure study, grains can be considered as homogeneous phases.

What mainly differentiates homogenization models from each other is the definition of localization tensors $\mathbb{A}$ and $\mathbb{B}$. For example, in the case of Reuss and Voigt models, the localization tensors are expressed as follow:

$$\begin{aligned} \boldsymbol{\sigma}^i = \boldsymbol{\Sigma} \Longleftrightarrow \mathbb{B}^i = \mathbb{I} \quad &\text{Reuss lower bound} \\ \boldsymbol{\varepsilon}^i = \boldsymbol{E} \Longleftrightarrow \mathbb{A}^i = \mathbb{I} \quad &\text{Voigt upper bound} \end{aligned} \tag{1.21}$$

Reuss and Voigt models have shown to be respectively a lower and an upper bounds of the material effective mechanical properties.

The majority of homogenization models are based on Eshelby's work on the behavior of an inclusion submerged in a homogeneous medium (Eshelby, 1957).

1.3.3.2 Eshelby's theory

Eshelby (1957) was interested in a set of problems on the stress / strain fields of ellipsoidal elastic inclusions immersed in an infinite linear-elastic body.

He was particularly interested in the behavior of an ellipsoidal inclusion (I) inserted in an infinite matrix (M) subjected to a uniform loading. The problem can be divided into two sub-problems:

- A subdomain (I) inside an infinite homogeneous matrix is submitted to a uniform stress-free strain $\boldsymbol{\varepsilon}^*$ (as a thermal deformation for example). The matrix is stress-strain free ($\boldsymbol{E} = 0$ and $\boldsymbol{\Sigma} = 0$) and the subdomain I shares the same stiffness tensor as the matrix ($\mathbb{C}^I = \mathbb{C}^M$). Due to the strain $\boldsymbol{\varepsilon}^*$ presence in I, the matrix accommodates to I distortion, as illustrated in Fig. 1.10, resulting to the following equations:

$$\begin{aligned} \boldsymbol{\sigma}(\boldsymbol{x}) &= \mathbb{C}^M : (\boldsymbol{\varepsilon}(\boldsymbol{x}) - \boldsymbol{\varepsilon}^*) \qquad \boldsymbol{x} \in I \\ \boldsymbol{\sigma}(\boldsymbol{x}) &= \mathbb{C}^M : \boldsymbol{\varepsilon}(\boldsymbol{x}) \qquad \boldsymbol{x} \in M - I \end{aligned} \tag{1.22}$$

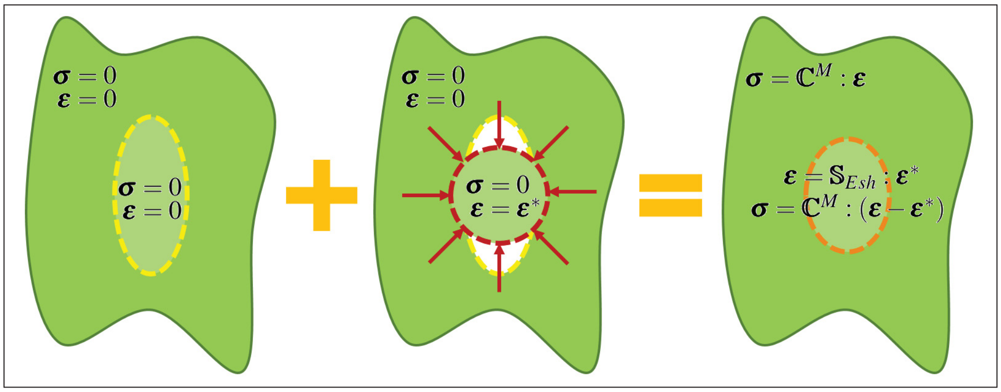

Figure 1.10 Eshelby's problem illustration: matrix subdomain submitted to a uniform stress-free strain $\boldsymbol{\varepsilon}^*$ (adapted from Bretin (2016)).

Based on Green's functions and Fourier transform, Eshelby showed that $\boldsymbol{\varepsilon}(\boldsymbol{x}) = \boldsymbol{\varepsilon}^{acc}$ is constant within the subdomain and defined a fourth order tensor, called Eshelby's tensor $\mathbb{S}_{Esh}$, linking the stress-free strain $\boldsymbol{\varepsilon}^*$ and the accommodation strain $\boldsymbol{\varepsilon}^{acc}$ as:

$$\boldsymbol{\varepsilon}(\boldsymbol{x}) = \boldsymbol{\varepsilon}^{acc} = \mathbb{S}_{Esh} : \boldsymbol{\varepsilon}^* \quad \boldsymbol{x} \in I \tag{1.23}$$

$\mathbb{S}_{Esh}$ depends only on the shape of the inclusion and the elastic properties of the matrix. In the case of a spherical inclusion immersed in an isotropic matrix, the Eshelby tensor can be expressed as follows:

$$\mathbb{S}_{Esh} = \frac{(1+\nu^M)}{3(1-\nu^M)}\mathbb{J} + \frac{2(4-5\nu^M)}{15(1-\nu^M)}\mathbb{K} \tag{1.24}$$

where ν^M is the matrix Poisson's ratio and $\mathbb{J}$ and $\mathbb{K}$ are the fourth-order spherical and deviatoric projection tensors, respectively, as:

$$\mathbb{J} = \frac{1}{3}\begin{bmatrix} 1 & 1 & 1 & 0 & 0 & 0 \\ 1 & 1 & 1 & 0 & 0 & 0 \\ 1 & 1 & 1 & 0 & 0 & 0 \\ 0 & 0 & 0 & 0 & 0 & 0 \\ 0 & 0 & 0 & 0 & 0 & 0 \\ 0 & 0 & 0 & 0 & 0 & 0 \end{bmatrix} \quad \text{et} \quad \mathbb{K} = \frac{1}{3}\begin{bmatrix} 2 & -1 & -1 & 0 & 0 & 0 \\ -1 & 2 & -1 & 0 & 0 & 0 \\ -1 & -1 & 2 & 0 & 0 & 0 \\ 0 & 0 & 0 & 3 & 0 & 0 \\ 0 & 0 & 0 & 0 & 3 & 0 \\ 0 & 0 & 0 & 0 & 0 & 3 \end{bmatrix} \tag{1.25}$$

- When the subdomain I doesn't have a free-stress strain but has properties different from the matrix ($\mathbb{C}^I \neq \mathbb{C}^M$) and the whole matrix-inclusion is submitted to a strain load $\boldsymbol{E}$ at infinity, due to the elastic incompatibility and the exterior loading, an accommodation strain ε^{acc} appears as illustrated in Fig. 1.11) such as:

$$\begin{aligned} \boldsymbol{\sigma}(\boldsymbol{x}) &= \mathbb{C}^M : (\boldsymbol{E} + \boldsymbol{\varepsilon}^{acc}(\boldsymbol{x})) \quad \boldsymbol{x} \in M - I \\ \boldsymbol{\sigma}(\boldsymbol{x}) &= \mathbb{C}^I : (\boldsymbol{E} + \boldsymbol{\varepsilon}^{acc}(\boldsymbol{x})) \qquad \boldsymbol{x} \in I \end{aligned} \tag{1.26}$$

- Coupling the two previous problems (a matrix subdomain I submitted to a stress free strain $\boldsymbol{\varepsilon}^*$ the whole submitted to an infinite load $\boldsymbol{E}$) would result to the following equations:

$$\begin{aligned} \boldsymbol{\sigma}(\boldsymbol{x}) &= \mathbb{C}^M : (\boldsymbol{E} + \boldsymbol{\varepsilon}^{acc}(\boldsymbol{x})) \qquad \boldsymbol{x} \in M - I \\ \boldsymbol{\sigma}(\boldsymbol{x}) &= \mathbb{C}^M : (\boldsymbol{E} + \boldsymbol{\varepsilon}^{acc}(\boldsymbol{x}) - \boldsymbol{\varepsilon}^*) \qquad \boldsymbol{x} \in I \\ \text{with} \quad \boldsymbol{\varepsilon}^{acc}(\boldsymbol{x}) &= \mathbb{S}_{Esh} : \boldsymbol{\varepsilon}^* \qquad \boldsymbol{x} \in I \end{aligned} \tag{1.27}$$

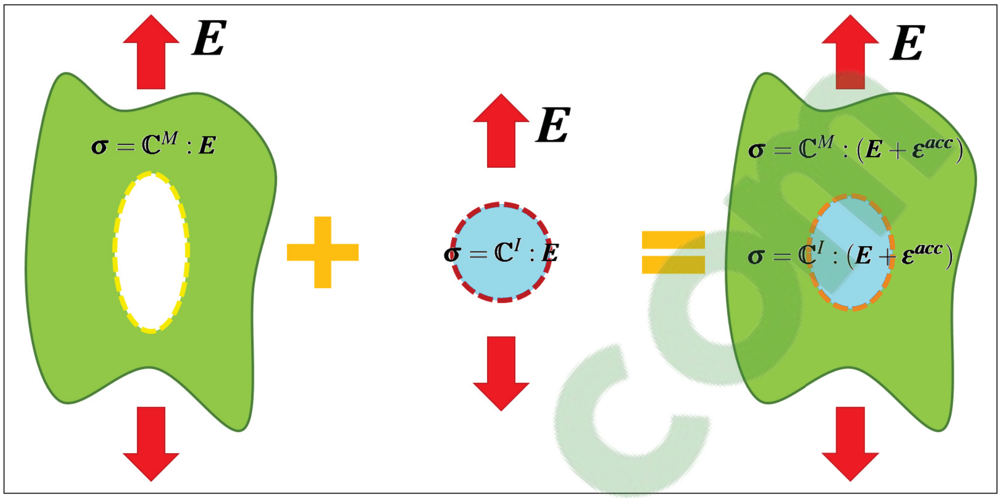

Figure 1.11 Eshelby's problem illustration: matrix-inclusion submitted to a load $\boldsymbol{E}$ at infinity (adapted from Bretin (2016)).

The condition for the equivalency of the two previous problems (the inclusion with different properties (eq. 1.26) and the inclusion submitted to a stress-free strain (eq. 1.27), both submitted to a load at infinity) is:

$$\begin{aligned} \boldsymbol{\sigma}^I = \mathbb{C}^I : (\boldsymbol{E} + \boldsymbol{\varepsilon}^{acc}) = \mathbb{C}^M : (\boldsymbol{E} + \boldsymbol{\varepsilon}^{acc} - \boldsymbol{\varepsilon}^*) \qquad & \boldsymbol{x} \in M - I \\ \Rightarrow \boldsymbol{\varepsilon}^* = [(\mathbb{C}^M - \mathbb{C}^I) : \mathbb{S}_{Esh} - \mathbb{C}^M]^{-1} : (\mathbb{C}^I - \mathbb{C}^M) : \boldsymbol{E} \qquad & \boldsymbol{x} \in I \end{aligned} \tag{1.28}$$

From this equation, the total strain within the inclusion can be deduced:

$$\boldsymbol{\varepsilon}^I = \boldsymbol{E} + \mathbb{S}_E : \boldsymbol{\varepsilon}^* = \boldsymbol{E} + \mathbb{S}_E : [(\mathbb{C}^M - \mathbb{C}^I) : \mathbb{S}_E - \mathbb{C}^M]^{-1} : (\mathbb{C}^I - \mathbb{C}^M) : \boldsymbol{E} = \mathbb{A}_E : E \tag{1.29}$$

$$\text{with (after simplification)} \qquad \mathbb{A}_E = \left(\mathbb{I} + \mathbb{S}_E : (\mathbb{C}^M)^{-1} : (\mathbb{C}^I - \mathbb{C}^M)\right)^{-1} \tag{1.30}$$

This expression of the localization tensor is called the dilute Eshelby's scheme. The term "dilute" refer to the fact that the model assumes the matrix to have inclusions far from each other. The localization $\mathbb{A}_E$ depends on the matrix and inclusion mechanical properties ($\mathbb{C}^M$ and $\mathbb{C}^I$), and the shape of the inclusion. A method for calculating the Eshelby tensor for the general case of an ellipsoidal inclusion in any matrix can be found in Gavazzi & Lagoudas (1990) work.

1.3.3.3 Linear homogenization model

Several models derived from Eshelby's theory which a non-exhaustive list of the most common models is recalled here:

- **Bounds of Hashin-Shtrikman** (HSL-HSU): Hashin & Shtrikman (1963) have established tighter bounds than the Reuss-Voigt bounds adapted to isotropic materials. Defining respectively $\mathbb{C}^{min}$ and $\mathbb{C}^{max}$ as the stiffness tensors of the phases with the lowest and highest bulk modulus, such as:

  $$\left(\boldsymbol{E} : \mathbb{C}^{min} : \boldsymbol{E}\right) \quad \leq \quad \left(\boldsymbol{E} : \mathbb{C}^{i} : \boldsymbol{E}\right) \quad \leq \quad (\boldsymbol{E} : \mathbb{C}^{max} : \boldsymbol{E}) \tag{1.31}$$

  the Hashin-Shtrikman localization tensors of a phase i is expressed as:

  $$\begin{aligned} \mathbb{A}^{i}_{HSU} &= \left(\mathbb{I} + \mathbb{S}^{max}_{Esh} : (\mathbb{C}^{max})^{-1} : (\mathbb{C}^{i} - \mathbb{C}^{max})\right)^{-1} & \text{upper bound} \\ \mathbb{A}^{i}_{HSL} &= \left(\mathbb{I} + \mathbb{S}^{min}_{Esh} : (\mathbb{C}^{min})^{-1} : (\mathbb{C}^{i} - \mathbb{C}^{min})\right)^{-1} & \text{lower bound} \end{aligned} \tag{1.32}$$

  where $\mathbb{S}^{max}_{E}$ and $\mathbb{S}^{min}_{E}$ are respectively the Eshelby's tensor calculated by using $\mathbb{C}^{min}$ and $\mathbb{C}^{max}$ as matrix properties.

- **Mori-Tanaka model** (Benveniste, 1987; Mori & Tanaka, 1973): this model takes into account the interaction between inclusions in the estimation process of the macroscopic elastic properties thus improving the dilute Eshelby's scheme. In this model, the macroscopic strain submitted to the inclusions in Eshelby's solution (Eq. 1.30) is considered equal to the matrix strain tensor $\boldsymbol{\varepsilon}^{M}$ such as:

  $$\boldsymbol{\varepsilon}^{I}_{E} = \left(\mathbb{I} + \mathbb{S}_{Esh} : (\mathbb{C}^{M})^{-1} : (\mathbb{C}^{I} - \mathbb{C}^{M})\right)^{-1} : \boldsymbol{\varepsilon}^{M} = \mathbb{T}^{I} : \boldsymbol{\varepsilon}^{M} \tag{1.33}$$

  As homogeneization law requires the macroscopic strain to be equal to the average of all the material phases (Eq. 1.17), the following equality is obtained and the matrix localization tensor can be deduced:

$$\boldsymbol{E} = \left\langle \boldsymbol{\varepsilon}^i \right\rangle_i = \sum_{i=1}^{n} c_i \mathbb{T}^i : \boldsymbol{\varepsilon}^M \quad \rightarrow \quad \boldsymbol{\varepsilon}^M = \left(\sum_{i=1}^{n} c_i \mathbb{T}^i \right)^{-1} : \boldsymbol{E} = \mathbb{A}^M : \boldsymbol{E} \tag{1.34}$$

By combining these two last equations, the inclusions localization tensor is obtained as:

$$\mathbb{A}^i = \left(\mathbb{I} + \mathbb{S}_{Esh} : (\mathbb{C}^M)^{-1} : (\mathbb{C}^i - \mathbb{C}^M) \right)^{-1} : \left(\sum_{i=1}^{n} c_i \mathbb{T}^i \right)^{-1} \tag{1.35}$$

Mori-Tanaka model is a perfect fit for composite materials with a low reinforcement volume fraction.

- **Self-Consistent model** (Hill, 1965a): in linear elasticity the SC model is very well adapted to the material having no dominant phase, which is the case of polycrystals. The principle of the SC scheme is to consider the matrix stiffness tensor from the Eshelby problem as the material effective stiffness tensor ($\mathbb{C}^{eff} = \mathbb{C}^M$), leading to a recursive expression of the localization tensor such as:

$$\circlearrowleft \begin{array}{c} \mathbb{A}^i = \left(\mathbb{I} + \mathbb{S}^i_{Esh} : (\mathbb{C}^{eff})^{-1} : (\mathbb{C}^i - \mathbb{C}^{eff}) \right)^{-1} \\ \mathbb{C}^{eff} = \sum\limits_{i=1}^{n} c_i \mathbb{C}^i : \mathbb{A}^i \end{array} \circlearrowright \tag{1.36}$$

$\mathbb{A}^i = \mathbb{I}$ can be used to initiate the recurrence.

1.3.3.4 Self-Consistent model extensions to non-linear polycrystals

Several models derived from the Self-Consistent model and are used for studying polycrystals elastoplastic behavior. These models seek to predict the average stresses and deformations per crystallographic phase. Some are also able to provide an estimate of the dispersion within a phase but can not predict the full spectrum of the local states of stress and strain as full-field models could do, which is important in the HCF regime. Here is a non-exhaustive list of simple models commonly used in the industry and more complex ones:

- **Kroner's interaction law** (Kröner, 1961): Kröner's model is one of the first SC model extensions to describe polycrystals elastoplasticity behavior. The model consists in assuming each grain as an ellipsoidal inclusion plastifying uniformly ($\boldsymbol{\varepsilon_p}^g$) and immersed in an isotropic matrix having the polycrystal effective properties and also plastifying unformly ($\boldsymbol{E_p}$). The grain plasticity is considered as a stress free strain meaning that equation 1.36 can be used with the material elastic properties. The elastic strain is also considered homogeneous ($\boldsymbol{\varepsilon_e} = \boldsymbol{E_e} = \mathbb{C}^{eff} : \boldsymbol{\Sigma}$) and the plasticity is the only source of stress heterogeneity in the material such as:

$$\begin{gathered} \boldsymbol{\sigma}^g = \boldsymbol{\Sigma} + \mathbb{L} : (\boldsymbol{E_p} - \boldsymbol{\varepsilon_p}^g) \\ \text{with} \quad \mathbb{L} = \mathbb{C}^{eff} : (\mathbb{I} - \mathbb{S}_{Esh}) \end{gathered} \tag{1.37}$$

  In the case of an spherical inclusion, equation 1.24 can be used yielding to the following simplification of equation 1.37:

$$\boldsymbol{\sigma}^g = \boldsymbol{\Sigma} + 2\mu(1-\beta)(\boldsymbol{E_p} - \boldsymbol{\varepsilon_p}^g) \tag{1.38}$$

  where μ is the effective shear modulus, $\beta = \frac{2(4-5\nu)}{15(1-\nu)}$ and ν is the effective Poisson's ratio. The main disadvantage of Kroner's interaction laws is that it predicts a polycrystal behavior too stiff.

- **Hill's model** (Hill, 1965a,6): Hill proposed an incremental model considering that each grain of a polycrystal has an ellipsoidal shape and elastoplastic behavior, and is immersed in an homogenized environment itself elastoplastic. The non-linear behavior of each grain is defined by the incremental linear relation:

$$\dot{\boldsymbol{\sigma}}^g = \mathbb{L}^g : \dot{\boldsymbol{\varepsilon}}^g \tag{1.39}$$

  Hill neglects the incremental operator disturbances in the inclusion environment, and describes the behavior of the homogenized RVE by the tensor $\mathbb{L}^{eff}$:

$$\dot{\boldsymbol{\Sigma}} = \mathbb{L}^{eff} : \dot{\boldsymbol{E}} \tag{1.40}$$

The extension of the Eshelby solution to nonlinear behavior is written in terms of velocities in the form:

$$\dot{\boldsymbol{\sigma}}^{g} = \dot{\boldsymbol{\Sigma}} + \mathbb{L}^{H} : (\dot{\boldsymbol{E}} - \dot{\boldsymbol{\varepsilon}}^{g}) \tag{1.41}$$

where $\mathbb{L}^{H} = \mathbb{L}^{eff} : (\mathbb{S}_{Esh}^{-1} - \mathbb{I})$ is the Hill tensor. The effective incremental tensor $\mathbb{L}^{eff}$ defining the homogenized behavior can be expressed as:

$$\mathbb{L}^{eff} = \left\langle \mathbb{L}^{g} : (\mathbb{L}^{g} + \mathbb{L}^{H})^{-1} : (\mathbb{L}^{eff} + \mathbb{L}^{*}) \right\rangle_{g} \tag{1.42}$$

The difficulty of this approach lies in the fact that the implicit equation 1.42 must be solved step by step on the loading path, which requires a rather heavy numerical implementation. This is why approximations have been proposed by many authors to facilitate the use of this model, one of which consists on considering the polycrystal elasticity homogeneous such as:

$$\left.\begin{aligned} \dot{\boldsymbol{\Sigma}} &= \mathbb{C}^{eff} : \dot{\boldsymbol{E}}_{\boldsymbol{e}} \\ \dot{\boldsymbol{\sigma}}^{g} &= \mathbb{C}^{eff} : \dot{\boldsymbol{\varepsilon}}_{\boldsymbol{e}}{}^{g} \end{aligned}\right\} \Rightarrow \dot{\boldsymbol{E}}_{\boldsymbol{p}} = \left\langle \dot{\boldsymbol{\varepsilon}}_{\boldsymbol{p}}{}^{g} \right\rangle_{g} \tag{1.43}$$

where $\dot{\boldsymbol{E}}_{\boldsymbol{e}}$, $\dot{\boldsymbol{\varepsilon}}_{\boldsymbol{e}}{}^{g}$, $\dot{\boldsymbol{E}}_{\boldsymbol{p}}$, $\dot{\boldsymbol{\varepsilon}}_{\boldsymbol{p}}{}^{g}$ are respectively the elastic and plastic part of the macroscopic and microscopic strain tensors such as:

$$\dot{\boldsymbol{E}} = \dot{\boldsymbol{E}}_{\boldsymbol{e}} + \dot{\boldsymbol{E}}_{\boldsymbol{p}} \tag{1.44}$$

$$\dot{\boldsymbol{\varepsilon}}^{g} = \dot{\boldsymbol{\varepsilon}}_{\boldsymbol{e}}{}^{g} + \dot{\boldsymbol{\varepsilon}}_{\boldsymbol{p}}{}^{g} \tag{1.45}$$

By doing so, the following interaction law is obtained:

$$\dot{\boldsymbol{\sigma}}^{g} = \dot{\boldsymbol{\Sigma}} + (\mathbb{I} + \mathbb{L}^{H} : \mathbb{C}^{eff\ -1})^{-1} : \mathbb{L}^{H} : (\dot{\boldsymbol{E}}_{\boldsymbol{p}} - \dot{\boldsymbol{\varepsilon}}_{\boldsymbol{p}}{}^{g}) \tag{1.46}$$

- **Berveiller-Zaoui interaction law** (Berveiller & Zaoui, 1978): The idea of Berveiller and Zaoui is to resume Kroner's work, but instead of assuming the homogenized behavior purely elastic, they assumed that it is isotropic, elastoplastic. The model conditions require the material to be isotropic, to have a homogeneous elastic behavior, and submitted to a monotonic loading. The material elasto-plastic behavior is controlled by the addition of the variable ξ depending on $\boldsymbol{E_p}$ in Kroner's equation 1.38 as:

$$\boldsymbol{\sigma}^g = \boldsymbol{\Sigma} + 2\mu(1-\beta)\xi(\boldsymbol{E_p} - \boldsymbol{\varepsilon_p}^g) \tag{1.47}$$

with $\frac{1}{\xi} = 1 + \frac{3}{2}\mu\frac{||\boldsymbol{E_p}||}{J_2(\Sigma)}$, where $J_2(\Sigma)$ is the second stress invariant and $||\boldsymbol{E_p}|| = \sqrt{\frac{2}{3}\boldsymbol{E_p} : \boldsymbol{E_p}}$. At the beginning of plastic flow, ξ is equal to 1 and the interaction law is equivalent to Kröner's law. The function ξ decreases very rapidly as the plastic flow progresses, which soften the polycrystal behavior. However, the main disadvantage of Berveiller-Zaoui's interaction law is that it is only valid for radial and monotonic loading.

Due to its application conditions, the model is not suited for complex loading paths such as cyclic loadings.

- $\boldsymbol{\beta}$ **law** (Cailletaud, 1992; Pilvin, 1994): To be able to simulate cyclic loadings, Cailletaud and Pilvin have modified Kroner's law based on the phenomenological behavior of polycrystals by introducing an intergranular accommodation variable β^g for each grain orientation. The interaction law is then rewritten for a spherical grain as:

$$\begin{aligned} \boldsymbol{\sigma}^g &= \boldsymbol{\Sigma} + 2\mu(1-\beta)(\boldsymbol{B} - \boldsymbol{\beta}^g) \\ \text{with} \quad \boldsymbol{B} &= \langle c^g \boldsymbol{\beta}^g \rangle_g \\ \text{and} \quad \dot{\boldsymbol{\beta}}^g &= \dot{\boldsymbol{\varepsilon}}_{\boldsymbol{p}}{}^g - D(\boldsymbol{\beta}^g - \delta\boldsymbol{\varepsilon_p}^g)||\dot{\boldsymbol{\varepsilon}}_{\boldsymbol{p}}{}^g|| \end{aligned} \tag{1.48}$$

where D and δ are material related parameters set to fit the material effective behavior.

This model, as well as Berveiller-Zaoui interaction law, is often found in the literature for the parameters identification of a monocrystalline plasticity model from the macroscopic experimental response of a polycrystalline material cyclically solicited or following non-proportional loading paths (Evrard, Aubin, Pilvin, Degallaix & Kondo, 2008b; Gérard, 2008; Guilhem *et al.*, 2013).

- **Affine formulations**: Rather than using a tangent or secant formulation as in the previous models, authors used an affine linearization of the elastoplastic behavior of the material. Masson, Bornert, Suquet & Zaoui (2000) was the first to use such formulation and showed an improvement in the effective properties estimation in comparison to the incremental formulation of Hill's model. More recently, affine formulation is found to be used in homogenization models based on the Self-consistent approach by Berbenni & Capolungo (2015) and Mareau & Berbenni (2015). Due to the models simplicity, they can be used into fatigue life model prediction as presented by Zghal *et al.* (2016).

- **Variational formulation and second-order moment**: The previous models consider the plastic strain uniform within a grain, which has the consequent to yield too stiff responses (Suquet, 1997). Therefore, authors have considered the use of a variational approach and the grain second order moment. The variational approach consists of introducing internal variables varying incrementally and which the potentials of the constitutive laws depend on. The second order moment is related to the standard deviation and co-variance of the local stress or strain field within the grain, whereas, the first moment (used in the models previously present) only provide the mean values.

  Castañeda (1991) start to use variational formulation into homogenization model which later on inspired Lahellec & Suquet (2007a) and Brassart, Stainier, Doghri & Delannay (2011) to push further more the development of such model. The use of the second moment in the homogeneziation models have been proven to provide a better estimation of the local stress fields Moulinec & Suquet (2003). Also, the model using the second order moment account for field fluctuations within the phases providing a statistics on the intra-grain stress field. Relatively recent models on that matter can be found in (Doghri, Brassart, Adam & Gérard, 2011; Lahellec & Suquet, 2007b). In the case of nonlinear materials, behavioral estimates and bounds are of great theoretical and practical importance when applicable. However, because of the difficulties inherent in solving local nonlinear problems, such models are generally obtained for rather restrictive assumptions on the morphology of the microstructure and on the constitutive laws used.

All the presented models have shown interesting results within certain application conditions, but they all share a common drawback: they do not account for the grain elastic anisotropy and/or the influence of the specificity of a grain neighborhood on its stress level.

1.3.3.5 Equivalent Inclusion Method

The equivalent inclusion method (EIM) started with Eshelby's work, who derived the exact solution to the problem of a single ellipsoidal inhomogeneity, embedded in an infinite matrix (Section 1.3.3.2). Then, many different inhomogeneity related problems have been studied using EIM:

- Moschovidis & Mura (1975), perfected later on by Benedikt, Lewis & Rangaswamy (2006), extended the problem to two spherical inclusions embedded inside an elastic isotropic infinite matrix. Later on the problem has been extended to anisotropic matrix (Berveiller, Fassi-Fehri & Hihi, 1987), ellipsoidal inclusions randomly oriented (Shodja, Rad & Soheilifard, 2003), non-linear inclusion/matrix (Mercier, Jacques & Molinari, 2005a). A recent version was proposed with a variational form of the EIM for multiple inclusions for applications to granular concrete (Brisard, Dormieux & Sab, 2014).
- Jasiuk, Sheng & Tsuchida (1997) changed the infinite matrix for a half-space matrix to account for a free surface effect. More recent works on that matter can be found in (Avazmohammadi, Yang & Abbasion, 2009; Lee, Zou & Ren, 2016; Zhong, Dabrowski & Jamtveit, 2018).
- The interface inclusion-matrix has been studied by several authors in the case of a weakened interface or debonding interface (Othmani, Delannay & Doghri, 2011; Qu, 1993; Tan, Huang, Liu & Geubelle, 2005).

A relatively recent review on that matter can be found in Zhou, Hoh, Wang, Keer, Pang, Song & Wang (2013).

The EIM could be useful to predict polycrystalline grains interactions, but they show some inconveniences. The more complex the problem, the more the solutions of the induced equations are heavy and require important calculations. To solve the mathematical problems, approximations are made, which are only accurate in specific cases. The most constraining condition is the distance between two inclusions: the EIM is not able to accurately predict the interaction between two inclusion very close to each other nor in contact.

1.3.4 Nonuniform Transformation Field Analysis (NTFA)

The Transformation Field Analysis (TFA) and Nonuniform Transformation Field Analysis (NTFA) approaches, unlike the mean-field models, allow a variation of the local fields around their mean value. They are much richer than conventional mean-field models due to the fact that the model provides the grain local fields unlike homogenization models that only provide the grain mean values and second moments.

The TFA was introduced initially for elastoplastic composites by Dvorak, Bahei-El-Din & Wafa (1994) who proposed to approach the local fields of internal variables by piecewise uniform distributions. A division of the RVE into subdomains where the plastic strain field is assumed to be uniform is required with the TFA. For the method to be accurate, the number of subdomains must be large. Even in this case, the TFA predicts a too stiff behavior of the microstructure. Approaching a non-uniform deformation field by piecewise uniform fields is not sufficient to reproduce the actual behavior of the material.

To compensate for this deficit, the Nonuniform Transformation Field Analysis (NTFA) has been developed by Michel & Suquet (2003). The basic principle is to decompose inelastic deformations (which are seen as free strain local fields) into a set of non-uniform empirical modes/functions defined by the user which are determined by preliminary calculations such as FEM or FFT simulations. These determinations depend on the microstruture specificity and the loading studied. To quote Michel & Suquet (2009), “A significant advantage of the NTFA is that it provides localization rules allowing for the reconstruction of local fields which are used to predict local phenomena such as the distribution of stresses or the plastic dissipation at the microscopic scale ”. The NTFA method CPU time is very efficient and it has been successfully applied to several micromechanical problems (Fritzen & Böhlke, 2010; Largenton, Michel & Suquet, 2014). The model has been further developed by Michel & Suquet (2016) for the micromechanical analysis of polycrystalline materials using single crystal elasto-visco-plastic models such as the MC model presented in Section 1.2.4. By adding a Tangent-Second-order expression of the constitutive law, the model showed an excellent accuracy in comparison to full-field models for a much lower computational cost. Nonetheless, due to its necessary pre-simulations associated to a specific microstructure, the NTFA does not allow the study of multiple different microstructure configurations.

1.3.5 Cellular Automaton (CA)

On one side, full-field models provide the micromechanical local strain-stress fields but are too heavy to repetitively produce results, on the other side, the conventional homogenization models provide fair estimates of the grains mean-fields for low computational power but have the inconvenience to ignore the neighborhood effect partly responsible of the stress heterogeneity among polycrystals. The Cellular Automaton (CA) approach has been considered to account for the neighborhood effect while remaining simple to quickly simulate several microstructures. CA approach has the particularity to considers the neighborhood effect in its solution computations while remaining simple.

The CA approach has been applied to several different fields: biology, thermodynamics, metallurgy, micromechanics, computer science, sociology, etc. In the field of material science, the CA approach was widely used to study microstructure crystallization. Meakin (1998) was the first to use a CA approach to predict the crystal nucleation under loading and the dynamic recrystallization. The model was further developed by Zhao, Billings & Coca (2009) and extended to denditric crystal nucleation. Montheillet & Gilormini (1996) proposed a micromechanical CA model for the study of two-phase polycrystals. This model, having some similarities with the self-consistent homogenization model, takes into account different microstructural parameters: the grain size, hardening and morphological softening. The LOPFA pushed further the model development. It was extended by Boutana, Bocher & Jahazi (2013) and further by Pourian, Bridier, Pilvin & Bocher (2016) for the study of two-phase titanium alloys behavior in dwell-fatigue.

The following section is an introduction of the CA approach. A detailed presentation of the CA model developed by Pourian *et al.* (2016) from where the present work started is also included.

1.3.5.1 Basic principles

A cellular automaton is a set of cells which each cell's behavior depends on that of the neighboring cells' behavior. The principle of the CA approach can be decomposed in four steps:

- The CA grid (number of cells and their spacial) is defined.
- The cells state variables are defined. These state variables may have an initial state and may change during the simulation. In our case of polycrystalline aggregate, this information would be the crystallographic orientations, the stiffness tensor, the elastic limit, hardening, the strain and stress level, etc.
- Each cell neighborhood is defined. For each cell, a set of "neighboring cells" is defined which the cell behavior depends.
- An evolution function is defined. Defining $\boldsymbol{X}_n^c$ as the list of the cell c state variables at the increment n and cn_i its neighboring cells, the evolution function f would be expressed as:

$$\boldsymbol{X}_{n+1}^c = f(\{\boldsymbol{X}_n^{cn_i}\}_{cn_i}) \tag{1.49}$$

Most of CA model use a regular grid. In 2D, cells can be triangular with 3 or 12 neighbors per cell, square with 4 (the "von Neumann neighborhood") or 8 (the "Moore neighborhood") neighbors per cell, or hexagonal with 6 neighbors per cell. In 3D, a cubic structure can be used with 6 or 26 neighbors per cell, or the Kelvin's structure formed of truncated octahedrons with 14 neighbors per cell. An illustration of an hexagonal grid and the Kelvin structure can be found in Fig. 1.12. Cells at the edge of the grid can be handled different ways: they can remain constant over the iterations, they can have fewer neighbors requiring to define new rules for these cells, or their neighbors are defined periodically, meaning that these cells are neighbors with the corresponding cells on the opposite side.

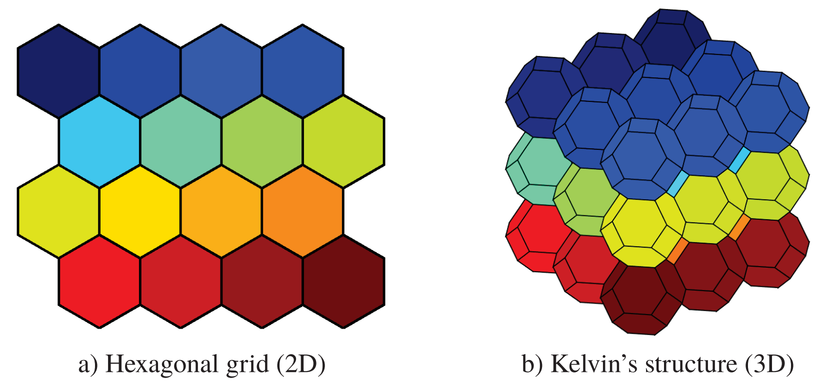

a) Hexagonal grid (2D) b) Kelvin's structure (3D)

Figure 1.12 Illustrations of a 2D and 3D CA grid: (a) hexagonal grid; (b) Kelvin's structure.

1.3.5.2 Pourian's CA model

Pourian's CA model was as a first step developed to predict the elastic micromechanical behavior of titanium alloys (Pourian, Pilvin, Bridier & Bocher, 2014) under an uniaxial loading, and further developed to predict their elastoplastic behavior (Pourian *et al.*, 2016).

For a titanium alloys submitted to an uniaxial elastic loading $\boldsymbol{E}$, the model is as follow:

- A periodic hexagonal grid of 900 cells was used with 6 neighbors per cell. A cell represent a grain from the microstructure, and a random crystallographic orientation is distributed to each one of them.
- For each grain (a cell of the CA), depending on its crystallographic orientation, the apparent Young's modulus along the loading axis is calculated ($E_y^g = 1/\mathbb{S}_{3333}^g$) as presented in Section 1.2.1 and as illustrated in Fig. 1.3. Then, each grain stiffness tensor is simplified to an isotropic tensor with its Poisson's ratio ν^g equal to the macroscopic one and its Young's modulus equal to E_y^g.
- Each grain is considered as a spherical inclusion from Eshelby's problem (Section 1.3.3.2) where the medium properties depend on the grain neighbors properties. The medium is

considered isotropic with its Poisson's ratio equal to macroscopic one and its Young's modulus equal to the average of the six neighboring grains n_i:

$$\nu^M = \nu^g = \nu \quad \text{and} \quad E_y^M = \frac{1}{6}\sum_{i=1}^{6} E_y^{n_i} \tag{1.50}$$

Each grain localization and strain tensors ($\mathbb{A}_E^g$ and $\boldsymbol{\varepsilon}^g$) are calculated using equations 1.24 and 1.30 with:

$$\mathbb{C}^I = \frac{E_y^g}{1-2\nu}\mathbb{J} + \frac{E_y^g}{1+\nu}\mathbb{K} \tag{1.51a}$$

$$\mathbb{C}^M = \frac{E_y^M}{1-2\nu}\mathbb{J} + \frac{E_y^M}{1+\nu}\mathbb{K} \tag{1.51b}$$

- In order to ensure $\langle \boldsymbol{\varepsilon}^g \rangle_g = \boldsymbol{E}$, a correction factor h_i^g proposed by Montheillet & Gilormini (1996) is applied to each grain such as:

$$h_i^g = \frac{\varepsilon_{ii}^g}{(\mathbb{A}_E^g : \boldsymbol{E}) :: \mathbb{N}_{ii}} \tag{1.52a}$$

$$\Rightarrow \varepsilon_{ii}^g = \left\langle h_i^g \right\rangle_g (\mathbb{A}_E^g : \boldsymbol{E}) :: \mathbb{N}_{ii} \tag{1.52b}$$

  where i is equal to 1,2 or 3, and $\mathbb{N}_{ii}$ is a fourth rank tensor product of the three unit vectors $\vec{\boldsymbol{e}}_{\boldsymbol{i}}$ ($\mathbb{N}_{ii} = \vec{\boldsymbol{e}}_{\boldsymbol{i}} \otimes \vec{\boldsymbol{e}}_{\boldsymbol{i}} \otimes \vec{\boldsymbol{e}}_{\boldsymbol{i}} \otimes \vec{\boldsymbol{e}}_{\boldsymbol{i}}$).

Pourian compared his model predictions to the FEM predictions. FEM simulations of 3000 aggregates composed of 512 spherical grains randomly oriented submitted to kinematic uniform boundary conditions were generated. Due to the boundary conditions applied to the aggregate generating a border effect, only the strain-stress level of the aggregate central grain was kept. The success of this model to accurately predict a grain mean stress tensor is limited. Considering the medium properties as a function of the grain neighbors had the intended effect of scattering the mechanical response of a given grain crystallographic orientation. The obtained scatter of the grains stress level as a function of their elastic properties predicted by this CA model was consistent with the scatter obtained with the FEM. But the comparison were only performed on the stress level scatter, and no comparison has been made on identical grain-neighborhood configurations.

Using the data presented in Section 4.5, Pourian's CA model predictions were compared to FEM predictions of a Kelvin structured aggregate submitted to periodic boundary conditions. The same material data as in Pourian *et al.* (2014) were used and the exact same grain-neighborhood configurations were preserved for both models in order to compare their predictions with the same simulation conditions. The only modification made in Pourian's CA model is the number of neighboring grains per grain changed from 6 to 14 to fit the 3D representation of the Kelvin structure. The grains stress scatter obtained with both models were similar, but when compared grain by grain, the models predictions were different. Several grains showed an increase in their average stress level due to neighborhood with Pourian's CA model whereas a decrease was observed with the FEM and vice-versa. This can be explained by the fact that the stress field induced by a grain on its environment differs depending on the location. The model does not differentiate the impact of a neighboring grain located on top or aside of the grain, which obviously has a different impact on a grain stress level.

The extension of the model to a dwell-fatigue load was as follows:

- All grains localization tensors $\mathbb{A}_E^g$ remain identical.
- The constitutive law, the Hooke's law in elasticity, was replaced by a 1D elastoviscoplastic law with the following plastic flaw f and isotropic hardening R as:

$$f(\sigma^g, R^g) = |\sigma| - (R^0 + R^g) \tag{1.53a}$$

$$R^g = Hp \tag{1.53b}$$

  with R^0 is the initial elastic limit, H the hardening modulus, and p the cumulative plastic strain.
- The model equations are expressed incrementally over time such as:

$$\boldsymbol{\varepsilon}^g = \mathbb{A}_E^g : \boldsymbol{E} \Rightarrow \Delta\boldsymbol{\varepsilon}^g = \mathbb{A}_E^g : \Delta\boldsymbol{E} \tag{1.54}$$

Only the slip system with the highest Schmid factor was considered without any slip system interactions.

- The interaction between a grain and its neighborhood during creep is modeled by an approach proposed by Kroner (Mura, 1987). A strain, called Kroner's strain ε_k^g, is added to each grain strain in order to integrate the effect of the neighborhood and is expressed as follow:

$$\varepsilon_k^g = (\frac{1}{6}\sum_{i=1}^{6}\varepsilon_k^{n_i}) - \varepsilon_k^g \tag{1.55}$$

When a grain neighborhood highly plastify, it has the effect to increase the stress in the grain, resulting a positive Kroner's strain. When a grain plasticity more than its neighborhood, it transfers its stress to its neighborhood, reducing its stress and resulting to a negative Kroner's strain.

The model extension has been compared to full-field model the same way it has been compared in the elastic case. Only the scatter of the data, or the macroscopic response have been compared. Several flaws that need to be improved can be mentioned:

- The one dimensional expression of the grains constitutive law.
- The consideration of only one slip system.
- Similarly as in elasticity, the model does not differentiate the impact of a neighboring grain located on top or aside of the grain.

1.4 Literature review conclusions

The different difficulties to predict polycrystals strain/stress-fields have been introduced. The heterogeneities due to the single-crystal elastic and viscoplastic mechanical properties have been explained, and the different models commonly used in the literature to predict the polycrystals micromechanical behavior have been introduced. Full-fields methods provide an accurate prediction for a high computational cost, whereas mean-fields methods trade their accuracy for computational efficiency. For the purpose of generating statistical data of a polycrystalline material strain-fields, models computationally efficient which also account for the material heterogeneity are needed.

The importance of the so-called “neighborhood effect” has been proven numerically and experimentally to have an important impact on the polycrystals strain/stress-fields due to the significant stress concentration it can be responsible for. Pourian’s CA model was a first step into accounting for these heterogeneities but the neighborhood effect wasn’t accurately predicted. A proper study of the neighborhood effect is required in order to develop a model able to account for it.

CHAPTER 2

RATIONALE AND OBJECTIVES

It has been shown, numerically and experimentally, that knowing the mechanical properties of a grain within a polycrystal is not sufficient to compute its stress level when the aggregate is mechanically loaded. In other words, the stress that a given grain undergoes depends on its neighborhood specificity as well. Each grain from an aggregate induces stress variations into its surroundings which can lead to important stress concentration. The maximum possible value of these variations is unknown, but it was found that grains with mechanical properties that supposedly should undergo a low stress level were sometimes found with an important stress level, much higher than the expected value. In HCF / VHCF regimes, the grain undergoing the highest RSS is the grain plastifying first and thus might initiate the first crack. Therefore, it is important to be able to capture these stress concentrations to predict material fatigue life with accuracy. The main objective of this thesis is to be able to capture these critical grain environments yielding to important stress concentrations responsible for early crack initiations. This main objective is divided into four steps:

- **Understanding the neighborhood effect (Chapter 3):** One of the first building blocks in such endeavor is to understand how a grain environment affects its stress level. The literature focusing on the neighborhood effect within polycrystal is almost nonexistent. Several studies pointed out the neighborhood effect importance, but none rigorously studied the mechanisms behind it. A common assumption often found in the literature is that a grain surrounded by a soft environment (grains with a low apparent Young's modulus or a low Schmid's factor) will be subjected to lower stress intensities than a grain surrounded by a hard environment. But this is just an assumption and no concrete study on the neighborhood effect has been found in the literature. It can intuitively be apprehended that a grain won't generate the same stress variation in the grain on top or aside of it, and thus each grain must be apprehended as individual and not as a whole neighborhood. In order to understand the mechanisms involved in the neighborhood effect, a quantifying definition of it was proposed and a FEM study was carried on. Simplifications were made to facilitate the study: the polycrystalline aggregate was considered elastic, composed of identical spherical grains, without a free surface (infinite material), and without non-metallic inclusions. The only source of heterogeneity within the studied aggregates was the crystal anisotropy and the grains random orientations.

- **Development of an analytical model accounting for the neighborhood effect (Chapter 4):** Due to the random character of a grain environment configuration, the stress variation induced by the environment can thus be considered as random. Most models used to predict polycrystals stress fields found in the literature either are too heavy in terms of CPU time preventing the generation of a large database (FEM, FFT), are not adapted to study large aggregates or a large number of random aggregates (NTFA), or do not account for the neighborhood effect (SC). The objective is to develop a model accounting for the neighborhood effect for a low computational cost to be able to predict grains' stress levels for a very large number of grain-neighborhood configurations in a short time. The development of a such model was based on the observations made from the first FEM study in elasticity from which simplifying assumptions regarding the neighborhood effect were drawn. To validate the model accuracy, its predictions were confronted with the FEM predictions. Taking advantage of the model efficiency, the grain environments responsible for important stress concentrations in elasticity were identified.

- **Impact of the neighborhood effect on polycrystals plastic behavior (Chapter 5):** Most polycrystalline aggregates studied in the literature only concern randomly oriented aggregates or are based on EBSD maps. Yet, as mentioned previously, the neighborhood effect can be responsible for important stress concentrations which are not necessarily present in such a small volume. The objective of this section is to study the impact of grain-neighborhood configurations responsible for high stress concentrations on the grains elastoplastic behaviors and the impact it might have on the material fatigue life. In order to study the impact of such grain-neighborhood configurations, the model developed in elasticity in the previous section was used. The constitutive equations used in the first version of the model (Hooke's law) were replaced for an elastoplastic law (the MC's model). The elastoplastic behavior of aggregates set up to have an important stress concentration was studied using both FEM and the analytical model developed. Using the later model efficiency, the probability to obtain such critical environments within a mechanical part was identified revealing a possible cause of the dispersion observed for the materials fatigue life in the HCF regime.

- **Impact of other sources of heterogeneities on the neighborhood effect and polycrystalline stress-fields (Chapter 6):** In the previous sections, the sources of heterogeneities within the studied aggregates were narrowed down to only the crystal anisotropy. To push furthermore the understanding of the neighborhood effect, its interaction with other sources of heterogeneities needs to be studied: the impact in elasticity of a free surface and of the grains morphologies on the stress-field heterogeneities has been assessed in comparison with the impact of the neighborhood effect. Similarly as for the neighborhood effect, quantifying definitions of the surface and morphology effects were proposed. Using FEM, these quantities were compared with each other for different parameters: the aggregate depth from the free surface and the grains' morphology aspect ratios.

CHAPTER 3

NEIGHBORHOOD EFFECT ON THE STRAIN DISTRIBUTION IN LINEARLY ELASTIC POLYCRYSTALS: PART 1 - FINITE ELEMENT STUDY OF THE INTERACTION BETWEEN GRAINS

Rémy Bretin[1], Martin Lévesque[2], Philippe Bocher[1]

[1] Mechanical Engineering Department, École de technologie supérieure (ÉTS),
1100 Notre-Dame Street West, Montréal, QC H3C 1K3, Canada
[2] Mechanical Engineering Department, École Polytechnique de Montréal,
2900 Boulevard Edouard-Montpetit, Montréal, QC H3T 1J4, Canada

Article accepted for publication in «International Journal of Solids and Structures» May 2019. Small modifications from the published version of the article have been brought in this chapter.

Abstract

Polycrystals are full of all kinds of heterogeneities which introduce stress concentrations. The local stress field in a grain does not depend solely on its crystallographic orientation. In fact, its neighborhood has also been shown to play a significant role. A definition and quantification method of the neighborhood effect was proposed and a finite element study was performed to evaluate the elastic strain variations of a given grain surrounded by a heterogeneous neighborhood composed of one or several grains inserted in an infinite homogeneous matrix. A regular structure was used to generate the aggregates and annihilate any grain size and shape ratio. Grains crystallographic orientations influences on a grain's strain tensor were studied with respect to their relative positions and the loading axis. A grain strain variations due to its neighborhood were found to be independent of its orientation, and a grain's influence on another grain's mean strain tensor was shown to be independent of other neighboring grains. From these observations, some simplifications were proposed to better describe the neighborhood effect in order to develop the analytic model presented in a second paper.

Keywords: Neighborhood effect, Polycrystal, Finite element analysis, Elastic anisotropy, Eshelby's inclusion

3.1 Introduction

Polycrystals exhibit different sources of heterogeneities: crystal orientation distribution, grain sizes and shapes, different material phases, property gradients induced by manufacturing processes, etc. These heterogeneities affect the polycrystal's static mechanical performance as well as its fatigue life and strength. They are typically considered as obeying a statistical distribution which implies that several samples made of the same material can exhibit different fatigue properties when submitted to a given loading condition.

Full-field techniques, such as the Finite Element Method (FEM) (Forest, Cailletaud, Jeulin, Feyel, Galliet, Mounoury & Quilici, 2002; Roters *et al.*, 2011) or algorithms relying on Fast Fourier Transforms (FFT) (Moulinec & Suquet, 1998b; Prakash & Lebensohn, 2009), have been used to simulate the micromechanical behavior of polycrystalline materials and to capture local grain behavior. However, these techniques require significant computer resources. On the other hand, mean-field homogenization schemes, such as the Self-Consistent model (SC), have provided accurate polycrystal effective elastic properties (Budiansky, 1965; Hill, 1965b), as well as fair estimates of grains mean strains/stresses (Lebensohn, Liu & Ponte Castañeda, 2004; Yaguchi & Busso, 2005) for a fraction of the FEM models computational cost.

Lebensohn *et al.* (2004) compared SC estimates results to full-field numerical simulations and showed that the more the single crystal elasticity is anisotropic, the more the polycrystal local stress field is heterogeneous, and the less accurate the SC estimates are. This is due to the fact that the SC scheme considers each grain immersed in a homogenized material, and thus neglects the heterogeneous nature of a grain environment. Brenner *et al.* (2009), by confronting local stress fields estimates resulting from the SC scheme and the FFT method, highlighted the local elastic anisotropy effects on a polycrystal yield strength. Depending on the orientation distribution, some configurations can lead to a high stress concentration in the aggregate, which results in a lower overall yield strength than expected. Predicting the exact elastic strain distribution within polycrystals is essential to accurately predict the macroscopic onset of plasticity (yield strength), as well as the very high and high cycle fatigue (VHCF and HCF) strength of a material sample.

The influence of the heterogeneities surrounding a grain on its own stress / strain / hardening state is called the *neighborhood effect* (also known as the cluster effect) and has been observed through several numerical studies (Cailletaud, Forest, Jeulin, Feyel, Galliet, Mounoury & Quilici, 2003; Guilhem *et al.*, 2010; Kocks, Tome & Wenk, 1999; Sauzay, 2007). Irrespective of the material studied or the simulation conditions, these studies all came to the same conclusion: a grain state depends not only on its crystal orientation but also on its localization within the structure and its neighboring grains. Using the FEM, Guilhem *et al.* (2010) studied the stress variations of a surface grain surrounded by hard or soft neighboring grains. Pourian *et al.* (2014) developed an analytical model to account for the neighborhood effect by considering the grain as immersed in a homogeneous medium with a stiffness equal to the average stiffness of its close neighboring grains. These studies suggest that a grain with a high stiffness along the loading axis has the effect of reducing its neighborhood strain level.

This behavior has also been experimentally observed through several in-situ tensile test analyses (Bridier *et al.*, 2008; Hemery *et al.*, 2018; Stinville, Vanderesse, Bridier, Bocher & Pollock, 2015; Stinville *et al.*, 2016a; Stinville, Lenthe, Miao & Pollock, 2016b; Zhang, Yang, Huang, Wu & Davies, 2015). All these studies illustrated the relation between the neighboring grain misorientations and crack nucleation and propagation. They evidenced the importance of the elastic anisotropy on the local stress field. Using a high resolution digital image correlation on nickel-base superalloy, Stinville *et al.* (2016b) showed that the crystal elastic anisotropy has a significant effect on the crack initiation process in fatigue due to stress concentration. The same conclusion has been drawn for titanium alloys: Hemery *et al.* (2018) observed the impact of elastic anisotropy and microtextured regions on the elastic stress field in Ti-6Al-4V and showed that a grain stress level strongly depends on its surrounding grains orientations (macrozone).

This paper studies the neighborhood effect in elastic polycrystalline aggregates for subsequent incorporation into analytical models. The neighborhood effect is defined herein as the difference between a grain mean strain tensor in a heterogeneous environment and the mean strain tensor of the same grain immersed in a homogenized environment. The influences of three parameters (the neighboring grains' stiffness in the loading direction, the grains' relative positions with respect to the loading axis, and their crystallographic orientations) on the neighborhood effect were studied.

To that end, after introducing the models and equations used in this paper (Section 3.2), a FEM study divided into three parts is presented. Firstly, the neighborhood effect observed in randomly generated polycrystalline aggregates is highlighted and documented (Section 3.3). Next, after a detailed description of the FEM models used (Section 3.4.1), the influence of one (Section 3.4.2) or several grains (Section 3.4.3) on another grain strain tensor immersed in a homogenized "infinite" matrix was studied. Approximations of the neighborhood effect are proposed from the observations made and their accuracy is evaluated in Section 3.5 on polycrystalline aggregates. Finally, Section 3.6 presents the closing remarks and conclusions.

3.2 Background and methodology

The Einstein summation convention is adopted and boldface letters denote tensors. All the simulations presented were performed using *ABAQUS 6.13-4* with input scripts generated with *MATLAB R2015a*.

3.2.1 Material properties

The mechanical properties used in this study were considered to be purely elastic. The iron crystal stiffness tensor shown in Table 3.1 (Simmons & Wang, 1971) was selected for all the simulations due to its high elastic anisotropy.

Table 3.1 Cubic iron crystal elastic constants (Simmons & Wang, 1971)

Fe	$\mathbb{C}_{1111}$ = 226 GPa	$\mathbb{C}_{1122}$ = 140 GPa	$\mathbb{C}_{1212}$ = 116 GPa

3.2.2 Generation of the polycrystalline aggregate

This work focuses on the effects of the grains' crystallographic orientations and of their relative positions within a cluster on the neighborhood effect. The Kelvin structure (Thomson, 1887)

(Fig. 3.1a) was chosen to generate a polycrystalline aggregate, instead of using the conventional Voronoi diagram method (Kumar, Kurtz & Agarwala, 1996), because it is periodically formed by truncated octahedrons and all the structure cells are identical. The Kelvin structure annihilates any effect of grain size and shape ratio on the neighboring effect. Every Kelvin structure cell was deemed to be equivalent to a grain in the polycrystal.

3.2.3 Eshelby's inclusion method

The stress/strain tensor of a grain immersed in a homogeneous environment must be known to quantify the neighborhood effect. Eshelby (1957) proposed a solution to estimate the mean stress/strain of an ellipsoidal inclusion immersed in an infinite homogeneous elastic matrix submitted to an elastic loading $\boldsymbol{E}$. This model is used to predict the mean strain tensor of a grain immersed in an infinite matrix with the aggregate homogenized mechanical properties in order to quantify the neighborhood effect. The following are the resulting equations:

$$\boldsymbol{\sigma}^{\boldsymbol{g}}_{\boldsymbol{Esh}} = \mathbb{C}^{\boldsymbol{g}} : \boldsymbol{\varepsilon}^{\boldsymbol{g}}_{\boldsymbol{Esh}} \tag{3.1a}$$

$$with \quad \boldsymbol{\varepsilon}^{\boldsymbol{g}}_{\boldsymbol{Esh}} = \mathbb{A}^{\boldsymbol{g}}_{\boldsymbol{Esh}} : \boldsymbol{E} \tag{3.1b}$$

$$and \quad \mathbb{A}^{\boldsymbol{g}}_{\boldsymbol{Esh}} = \left(\mathbb{I} + \mathbb{S}^{\boldsymbol{g}}_{\boldsymbol{Esh}} : (\mathbb{C}^{\boldsymbol{eff}})^{-1} : (\mathbb{C}^{\boldsymbol{g}} - \mathbb{C}^{\boldsymbol{eff}})\right)^{-1} \tag{3.1c}$$

where $\boldsymbol{\varepsilon}^{\boldsymbol{g}}_{\boldsymbol{Esh}}$ and $\boldsymbol{\sigma}^{\boldsymbol{g}}_{\boldsymbol{Esh}}$ are respectively the grain mean strain and stress tensors, $\mathbb{C}^{\boldsymbol{g}}$ and $\mathbb{C}^{\boldsymbol{eff}}$ are respectively the grain and the homogenized aggregate stiffness tensors, $\mathbb{A}^{\boldsymbol{g}}_{\boldsymbol{Esh}}$ is the strain-localization tensor, $\mathbb{I}$ is the fourth-rank identity tensor, and $\mathbb{S}^{\boldsymbol{g}}_{\boldsymbol{Esh}}$ is Eshelby's tensor as a function of $\mathbb{C}^{\boldsymbol{eff}}$ and the grain geometrical aspect ratios. Eshelby's tensor can be expressed as:

$$\mathbb{S}^{\boldsymbol{g}}_{\boldsymbol{Esh}} = \frac{(1+\nu^{eff})}{3(1-\nu^{eff})}\mathbb{J} + \frac{2(4-5\nu^{eff})}{15(1-\nu^{eff})}\mathbb{K} \tag{3.2}$$

for a spherical grain immersed in an isotropic aggregate and where ν^{eff} is the homogenized aggregate's Poisson's ratio, and $\mathbb{J}$ and $\mathbb{K}$ are the fourth-order spherical and deviatoric projection tensors, respectively.

Using the aggregate effective properties as the matrix properties is similar to what is done in the SC scheme, except that in our case $\mathbb{C}^{eff}$ is calculated from the numerical homogenization performed as part of this paper, while the SC scheme delivers it by iteratively solving equations 3.1.

3.2.4 Finite element method

3.2.4.1 Boundary conditions

Two types of boundary conditions were considered: kinematic uniform boundary conditions (KUBC) and periodic boundary conditions (PBC). These conditions are reminded here for the case of linear elasticity (Galvanetto & Aliabadi, 2010; Michel, Moulinec & Suquet, 1999; Sanchez-Palencia, Zaoui & Sciences, 1987; Wu, Owino, Al-Ostaz & Cai, 2014):

- KUBC: the displacement $\vec{\boldsymbol{u}}$ is imposed at any point $\vec{\boldsymbol{x}}$ on the boundary δV of the represented volume V as:

$$\vec{\boldsymbol{u}} = \boldsymbol{E} \cdot \vec{\boldsymbol{x}} \qquad \forall \vec{\boldsymbol{x}} \in \delta V \tag{3.3}$$

  with $\boldsymbol{E}$ being the second-order macroscopic strain tensor applied to the volume.

- PBC: the displacement $\vec{\boldsymbol{u}}$ for any point $\vec{\boldsymbol{x}}$ on the boundary δV of the represented volume V is set as follows:

$$\vec{\boldsymbol{u}} = \boldsymbol{E} \cdot \vec{\boldsymbol{x}} + \vec{\boldsymbol{v}} \qquad \forall \vec{\boldsymbol{x}} \in \delta V \tag{3.4}$$

  where $\vec{\boldsymbol{v}}$ is a periodic fluctuation taking the same value at two homologous points on opposite sides of V.

PBC typically require coding multi-point constraints (MPC), resulting in a longer CPU time than KUBC, but they have the advantage of not introducing a boundary effect at the surface of the mesh. Kanit, Forest, Galliet, Mounoury & Jeulin (2003) showed that PBC require a smaller representative volume element (RVE), reducing the time needed to compute effective properties.

3.2.4.2 Exploitation of FEM data

A grain's mean strain/stress tensors $\boldsymbol{\varepsilon^g}/\boldsymbol{\sigma^g}$ are computed by averaging the strain / stress tensors at the centroid position of each element constituting the grain $\boldsymbol{\varepsilon^e}/\boldsymbol{\sigma^e}$ expressed in the global axis system, weighted by the fraction of the element volume V^e and the grain volume V^g:

$$\boldsymbol{\varepsilon^g} = \frac{1}{V^g}\sum V^e \cdot \boldsymbol{\varepsilon^e} \tag{3.5a}$$

$$\boldsymbol{\sigma^g} = \frac{1}{V^g}\sum V^e \cdot \boldsymbol{\sigma^e} \tag{3.5b}$$

The aggregate's effective strain/stress tensors $\boldsymbol{E^{eff}}/\boldsymbol{\Sigma^{eff}}$ are computed by averaging the strain/stress tensors of each grain constituting the aggregate $\boldsymbol{\varepsilon^g}/\boldsymbol{\sigma^g}$ expressed in the reference axis system, weighted by the fraction of the grain volume V^g and the overall volume V^{eff}:

$$\boldsymbol{E^{eff}} = \frac{1}{V^{eff}}\sum V^g \cdot \boldsymbol{\varepsilon^g} \tag{3.6a}$$

$$\boldsymbol{\Sigma^{eff}} = \frac{1}{V^{eff}}\sum V^g \cdot \boldsymbol{\sigma^g} \tag{3.6b}$$

3.3 Highlighting the neighborhood effect in a polycrystal

To highlight the neighborhood effect among polycrystalline aggregates, Eshelby's inclusion method (EIM) and FEM estimates of grain mean strain / stress tensors submitted to an elastic loading are compared. The first model considers the grain immersed in a homogenized environment, while the second considers the grain immersed in the whole polycrystal, taking into account the heterogeneous properties of the aggregate. Therefore, a grain neighborhood influence on its strain/stress tensor can be evaluated by comparing these two models.

PBC (Section 3.2.4.1) were used to avoid the disturbances caused by edge effects, making all the grains of the aggregate exploitable, including those located at the surface of the mesh. A cubic aggregate of 686 grains (2×7^3) was chosen, as shown in Fig. 3.1b. According to Kanit

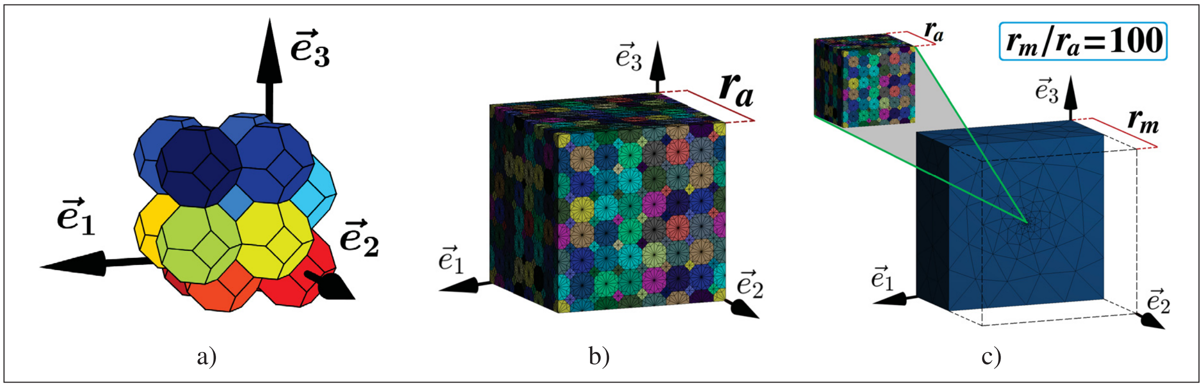

Figure 3.1 Meshes used for the numerical studies. (a) Kelvin structure sample; (b) Periodic Kelvin structure mesh of 686 cells (720 elements per grain) with a length r_a and PBC used for the simulations of a polycrystalline aggregate submitted to a mechanical loading; (c) Kelvin structure mesh of 686 cells merged at the center of a homogeneous matrix with a length r_m and KUBC used for the study of the neighborhood effect.

et al. (2003) and Yang *et al.* (2019) works, this volume size is more than sufficient to reach a RVE for a random crystallographic orientation distribution with PBC. In addition, according to Barbe *et al.* (2001a), and after a convergence study (Appendix 3.a), the aggregate was meshed with tetrahedral elements with quadratic interpolation, using 760 elements per grain. Twenty different sets of 686 random orientations were generated using the quaternion method (Altmann, 2005; Shoemake, 1992). This amounted to 13,720 different grain-neighborhood crystallographic configurations. A uniaxial strain loading $\boldsymbol{E}$ was applied to the polycrystalline aggregate, where $E_{33} = 0.1\%$ and all other components were set to 0. $\boldsymbol{\varepsilon^g_{FEM}}$ and $\boldsymbol{\sigma^g_{FEM}}$ were computed as per Equation 3.5.

The effective stress tensors $\boldsymbol{\Sigma^{eff}}$ were computed as per Equation 3.6 for each of the twenty orientation sets and their average and 95% confidence interval were obtained as:

$$\boldsymbol{\Sigma^{eff}} = \begin{bmatrix} 115.8 \pm 0.2 & 0.1 \pm 0.2 & 0.1 \pm 0.2 \\ 0.1 \pm 0.2 & 115.9 \pm 0.2 & 0.0 \pm 0.2 \\ 0.1 \pm 0.2 & 0.0 \pm 0.2 & 274.3 \pm 0.3 \end{bmatrix} \tag{3.7}$$

The very narrow confidence intervals on the main stress components confirm that the RVE was reached. The effective stiffness tensor yielding this stress state was assumed to be isotropic and defined by its Young's modulus E_Y^{eff} and Poisson's ratio ν^{eff} computed as:

$$\begin{cases} \mathbb{C}^{eff}_{1111} = \dfrac{\Sigma^{eff}_{33}}{0.1\%} \\ \mathbb{C}^{eff}_{1122} = \dfrac{\Sigma^{eff}_{11} + \Sigma^{eff}_{22}}{2 \cdot 0.1\%} \end{cases} \Rightarrow \begin{cases} E_Y^{eff} = \dfrac{\mathbb{C}^{eff\,2}_{1111} + \mathbb{C}^{eff}_{1111} \cdot \mathbb{C}^{eff}_{1122} - 2 \cdot \mathbb{C}^{eff\,2}_{1122}}{\mathbb{C}^{eff}_{1111} + \mathbb{C}^{eff}_{1122}} \approx 206\,GPa \\ \nu^{eff} = \dfrac{\mathbb{C}^{eff}_{1122}}{\mathbb{C}^{eff}_{1111} + \mathbb{C}^{eff}_{1122}} \approx 0.297 \end{cases} \tag{3.8}$$

On the other hand, using the calculated effective tensor $\boldsymbol{\mathbb{C}^{eff}}$, Equation 3.1 of EIM was used to compute the mean stress/strain tensors of the 13,720 grains generated in the FEM simulations submitted to the same strain loading $\boldsymbol{E}$. Since the shape of a Kelvin's cell closely approximates a sphere, the Eshelby's tensor formulation for a sphere was used, as introduced in Equation 3.2.

The mean strain ε^g_{33} and stress σ^g_{33} predictions in each grain obtained from FEM and EIM are plotted and compared in Fig. 3.2 as a function of their apparent Young's modulus along the $\vec{e}_3$ axis. The designation "apparent Young's modulus along $\vec{e}_3$" refers to $\mathbb{S}^{g\,-1}_{3333}$, the inverse of the grain compliance tensor component "3333" expressed in the global axis system. This parameter was arbitrarily chosen for its simplicity to differentiate the grains heterogeneous response.

A smooth curve is observed on Fig. 3.2 between grains' apparent Young's modulus and their stress/strain values obtained with EIM. This observation can be explained by Equation 3.1: $\boldsymbol{\varepsilon^g_{Esh}}$ and $\boldsymbol{\sigma^g_{Esh}}$ depend only on the grain orientation and the aggregate effective properties. On the other hand, for a given apparent Young's modulus, FEM predictions exhibit scattered results while EIM predictions seem to deliver the average of the FEM predictions (as calculated later in the second line of Table 3.2). The differences observed between the two models are due to the fact that the numerical model accounts for the explicit variations in the surrounding grain orientations.

These observations allow us to provide a clear definition of the neighborhood effect. For the purposes of this specific study, the neighborhood effect is defined as the difference between

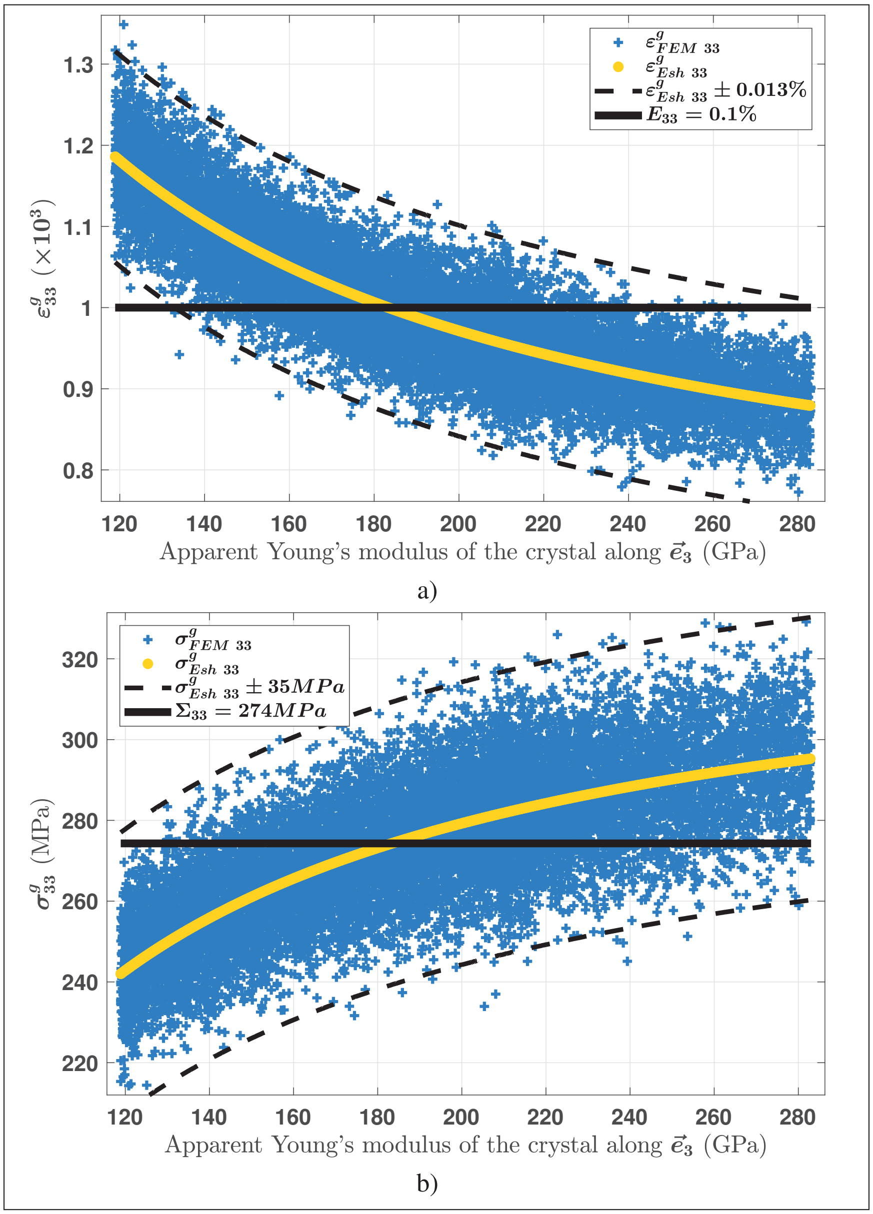

a)

b)

Figure 3.2 Assessment of the neighborhood effect by comparing FEM and EIM estimates of the mean strain $\boldsymbol{\varepsilon^g}$ (a.) and stress $\boldsymbol{\sigma^g}$ (b.) of each grain of the polycrystalline aggregates as a function of the apparent Young's modulus along the loading axis $\vec{e}_3$. The amplitude of the neighborhood effect for a given grain orientation is highlighted by the dotted lines, which represent $\varepsilon^g_{Esh\ 33}$ (or $\sigma^g_{Esh\ 33}$) plus or minus three time the standard deviation of the difference between FEM and EIM results (including 99.7% of the data).

the mean strain tensor of a grain immersed in an infinite polycrystalline aggregate ($\boldsymbol{\varepsilon}^{g}_{FEM}$) and the mean strain tensor of the same grain immersed in an infinite homogeneous matrix with the effective mechanical properties of the aggregate ($\boldsymbol{\varepsilon}^{g}_{Esh}$).

The influence of a grain orientation on its stress tensor has been shown to be as important as that of its neighborhood: overall, the amplitude of EIM predictions over all the apparent Young's modulus (from 119 to 283 GPa) reflects the grain stress variations due to its orientation, while the amplitude of the FEM predictions for a given apparent Young's modulus reflects the grain stress variations due to its neighborhood. Fig. 3.2b reveals that $\boldsymbol{\sigma}^{g}_{Esh}$ ranges from 242 to 296 MPa, which corresponds to 269±27 MPa, while, for a given grain orientation, $\boldsymbol{\sigma}^{g}_{FEM}$ varies from its average value ($\boldsymbol{\sigma}^{g}_{Esh}$) within a range of approximately ±35 MPa (dotted line in Fig. 3.2). These two amplitudes are close and the same conclusion can be drawn regarding the strain values. This implies that the impact of the neighborhood effect on a grain strain/stress tensor can be as important as the crystallographic orientation of the grain in question. It can also be observed from the FEM predictions that a grain with a low apparent Young's modulus (~120 GPa) can present a higher stress than a grain with a higher apparent Young's modulus (~280 GPa). This shows that the neighborhood effect can introduce high stress heterogeneities such that a "soft" grain (low apparent Young's modulus), that is supposed to have a low stress level, might be submitted to a higher stress level than a "hard" grain.

Table 3.2 lists the differences between the strain / stress tensors obtained with the two models, reflecting the variations due to the neighborhood effect. The density distributions of these differences show that they follow a normal distribution. On average, the differences cancel each other out, but their dispersions are significant: in the 20×686 neighborhoods tested here, the difference between the two models reached up to 18% of the applied strain. This difference can lead to early slip activity if the grain is properly oriented (with a high Schmid factor), which would result in an early crack initiation in the grain, impacting the aggregate fatigue life.

Table 3.2 Statistics of the difference between the FEM and the EIM results over the 20×686 grain-neighborhood configurations.

	$i=1$ $j=1$	$i=2$ $j=2$	$i=3$ $j=3$	$i=2$ $j=3$	$i=1$ $j=3$	$i=1$ $j=2$	Example of density distribution (case $i=3, j=3$) and its normal fitting.
E_{ij}^{eff} $(\times 10^3)$	0.00	0.00	1.00	0.00	0.00	0.00	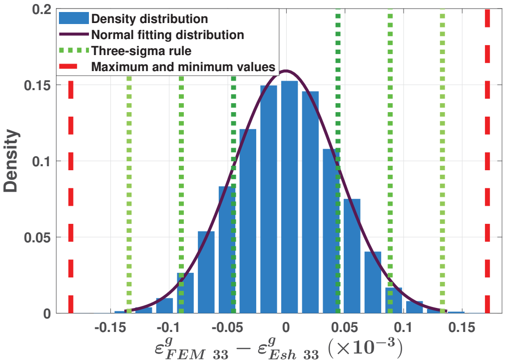
Average of $\varepsilon^g_{FEM\ ij} - \varepsilon^g_{Esh\ ij}$	0.00	0.00	0.00	0.00	0.00	0.00	
Average of $\left\lvert \varepsilon^g_{FEM\ ij} - \varepsilon^g_{Esh\ ij} \right\rvert$	0.03	0.03	0.04	0.03	0.03	0.03	
Maximum of $\left\lvert \varepsilon^g_{FEM\ ij} - \varepsilon^g_{Esh\ ij} \right\rvert$	0.16	0.16	0.18	0.14	0.16	0.15	
Σ_{ij}^{eff} (MPa)	115.8	115.9	274.3	0.0	0.1	-0.1	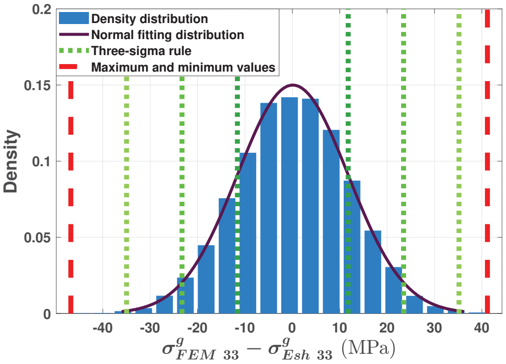
Average of $\sigma^g_{FEM\ ij} - \sigma^g_{Esh\ ij}$	-0.1	0.0	0.1	0.0	0.0	0.0	
Average of $\left\lvert \sigma^g_{FEM\ ij} - \sigma^g_{Esh\ ij} \right\rvert$	8.0	8.0	9.4	4.2	4.2	4.4	
Maximum of $\left\lvert \sigma^g_{FEM\ ij} - \sigma^g_{Esh\ ij} \right\rvert$	38.8	45.7	46.7	22.5	24.1	22.9	

3.4 Neighborhood effect investigation

3.4.1 Definition of the different FEM simulations

The strain variations of a grain surrounded by zero, one, or several grains immersed in an "infinite" homogeneous matrix were studied using the FEM to investigate the mechanisms responsible for the neighborhood effect and its impact on the local strain field of the polycrystal. Three types of grain configurations were studied: 1) only one grain is immersed in the matrix without any neighboring grain to investigate the strain variations on different subsets of its homogeneous environment, as shown in Fig. 3.3a (*S-1G*); 2) two grains are immersed, with 3 different relative positions to assess the influence of one grain on the other grain strain tensor, as shown in Fig. 3.3b-3.3d (*S-2G*); and 3) one grain and its two first layers of neighboring grains

(64 grains) are immersed to document the influence of several grains on the central grain strain tensor, as shown in Fig. 3.3e (*S-65G*).

PBC require a larger aggregate to ensure that the grains generated by the periodicity do not affect the observed grains, resulting in higher calculation time. KUBC were therefore used in this study to apply the uniaxial strain loading $\boldsymbol{E}$ (same as in Section 3.3) to reduce the calculation time. The mesh of the cubic polycrystalline aggregate used in Section 3.3 (Fig. 3.1b) with length r_a was inserted into the center of a cubic matrix with length r_m (Fig. 3.1c). To ensure that the edge disturbances due to KUBC do not affect the behavior of the observed grains in the core of the mesh, a ratio of $r_m/r_a = 100$ was arbitrarily chosen, and was confirmed to be sufficient after a convergence study (Appendix 3.a). The effective properties calculated previously (Eq. 3.8) were attributed to all the elements of the mesh, except for the specific element sets corresponding to a grain of the aggregate mesh to which the crystalline properties listed in Table 1 and a specific crystallographic orientation were attributed. The grains inserted in the homogeneous matrix had no impact on the overall behavior due to their insignificant volume faction (lower than $10^{-5}\%$).

The grain whose strain variations is observed is denoted as grain A, and its neighborhood is denoted as 0 when there is no other grain around A (only the surrounding matrix with the effective properties), B when there is one grain around A, or L^2 when there are two layers of neighboring grains around A. Following these notations, grain A's strain tensor is denoted $\boldsymbol{\varepsilon}_{\boldsymbol{0}}^{\boldsymbol{A}}$ when there is no grain around, $\boldsymbol{\varepsilon}_{\boldsymbol{B}}^{\boldsymbol{A}}$ when grain A is under grain B's influence, and $\boldsymbol{\varepsilon}_{\boldsymbol{L^2}}^{\boldsymbol{A}}$ when grain A is under the influence of its two first layers of neighbors. In some configurations, the effective properties, rather than the crystallographic properties, are assigned to grain A. To differentiate such cases from others, an "eff" index such as $\boldsymbol{\varepsilon}_{\boldsymbol{B}}^{\boldsymbol{A^{eff}}}$ is added.

The specificities of the three grain configurations mentioned above are described as follows:

- ***S-1G***: Crystallographic properties were attributed only to the central grain (Fig. 3.3a). Forty different crystallographic orientations randomly generated with the quaternion method were used for the central grain, for a total of forty different simulations. *S-1G* simulations serve two purposes: first, they provide the strain tensor $\boldsymbol{\varepsilon}_{\boldsymbol{0}}^{\boldsymbol{A}}$ of a grain immersed alone in a homogeneous

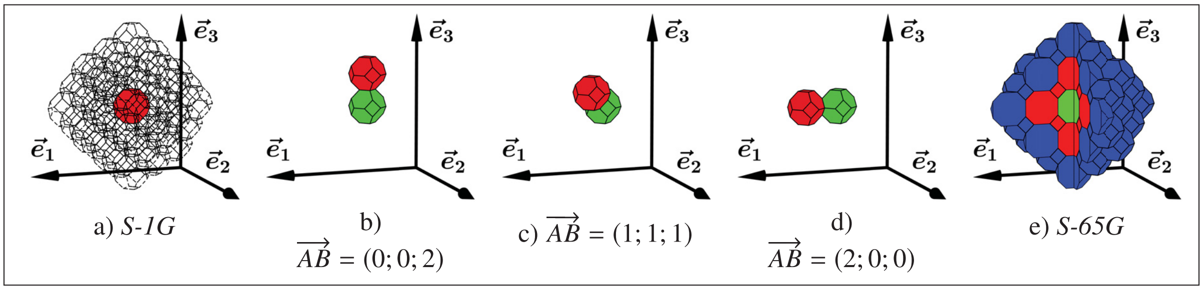

a) *S-1G* b) $\overrightarrow{AB} = (0;0;2)$ c) $\overrightarrow{AB} = (1;1;1)$ d) $\overrightarrow{AB} = (2;0;0)$ e) *S-65G*

Figure 3.3 Visual representations of the different types of FEM simulations: (a) *S-1G*: Central grain with the crystallographic properties in red, immersed in the homogeneous matrix, including the grain element sets with the effective properties shown in transparency; (b), (c), (d) *S-2G*: Grain A in green and grain B in red with the crystallographic properties, immersed in the homogeneous matrix; (e) *S-65G* (cut representation): Central grain A in green, first layer $L1$ in red, second layer $L2$ in blue with the crystallographic properties, immersed in the homogeneous matrix.

matrix (the central grain being considered as the observed grain A) for each of the forty selected orientations. These results are similar to the EIM results obtained in Section 3.3, but are more accurate because the shape of the grain (truncated octahedron Kelvin cell) is not approximated by a sphere. Second, the central grain, whose orientation changes in each simulation, can also be considered as the neighboring grain B: for each grain element set A^{eff} of the aggregate mesh with the effective properties, the mean strain tensor $\boldsymbol{\varepsilon}_{\boldsymbol{B}}^{\boldsymbol{A^{eff}}}$ is documented in order to observe the strain variations on different subsets of the aggregate mesh with the effective properties due to the presence of the central grain.

- ***S-2G***: Crystallographic properties were attributed to two grains named A and B in the case of *S-2G* simulations (Fig. 3.3c, 3.3d, 3.3b). The forty orientations generated for *S-1G* simulations were attributed independently to grains A and B, and three relative positions $\overrightarrow{AB}$ were studied: (0;0;2), (1;1;1) and (2;0;0) (1 is the grain radius), forming an angle with the loading axis $\vec{e}_3$ of 0°, ~ 55° and 90°, respectively. A total of $40 \times 40 \times 3 = 4800$ simulations were performed and the strain tensor $\boldsymbol{\varepsilon}_{\boldsymbol{B}}^{\boldsymbol{A}}$ of the central grain A was extracted for each relative position and grain orientation.

- ***S-65G***: Crystallographic properties were attributed to the central grain A, as well as the first layer $L1$ (the 14 grains verifying $\|\overrightarrow{AB}\| \leq 2$) and the second layer $L2$ (the 50 grains verifying

$2 < \|\overrightarrow{AB}\| \leq 4$) of neighboring grains (Fig. 3.3e). Three orientations (R, L, H) identified from *S-1G* simulations for grain A and each neighboring grains were attributed to each of these 65 grains and are defined as follows: "R" corresponds to a random orientation selected from the forty initial orientations; "L" and "H" respectively denote the crystallographic orientation corresponding to the lowest and highest value of $\varepsilon^{A}_{0\ 33}$ for the central grain or the lowest and highest value of $\varepsilon^{A^{eff}}_{B\ 33}$ for the neighboring grains. A fourth notation "0" is also used to define the effective properties. Therefore, one of these four properties (0, R, L, H) was attributed to the central grain A and to its two first layers of neighboring grains. For example, the notation ($A = R; L1 = 0; L2 = H$) means that the central grain A has crystallographic properties, with a random orientation; each grain of $L1$ has the same properties as the matrix (the effective properties); each grain of $L2$ has the orientation corresponding to the highest value of $\varepsilon^{A^{eff}}_{B\ 33}$ for the same relative position $\overrightarrow{AB}$ from *S-1G* simulations, and of course, the rest of the mesh has the effective properties. It should be mentioned that $L2 = H$ means that each grain B_i of $L2$ has an orientation corresponding to the highest value of $\varepsilon^{A^{eff}}_{B\ 33}$ observed in *S-1G* simulations for the corresponding relative position $\overrightarrow{AB_i}$, and thus, all the grains of $L2$ have crystallographic orientations that can differ from one location to the next. It is also important to mention that the random orientations "R" remain the same for each configuration. For example, the grains of the second layer $L2$ have the exact same orientation distribution between the configurations ($A = 0; L1 = H; L2 = R$) and ($A = R; L1 = L; L2 = R$). Therefore, a total of $4^3 - 4 = 60$ simulations were performed (simulations where the property 0 is attributed to both $L1$ and $L2$ corresponding to *S-1G* simulations) and the strain tensor $\boldsymbol{\varepsilon}^{\boldsymbol{A}}_{\boldsymbol{L^2}}$ of the central grain A was extracted for each configuration. These orientation configurations were chosen to obtain the extreme values of $\boldsymbol{\varepsilon}^{\boldsymbol{A}}_{\boldsymbol{L^2}}$ because the selected orientations have the greatest influence on the strain level individually.

Based on the definition of the neighborhood effect proposed in Section 3.3, the influence of a neighborhood (one or several grains with the crystallographic properties) on the central grain strain tensor is quantified by the difference between the mean strain tensors of this grain immersed in the matrix with its neighborhood ($\boldsymbol{\varepsilon}^{\boldsymbol{A^{eff}}}_{\boldsymbol{B}}$, $\boldsymbol{\varepsilon}^{\boldsymbol{A}}_{\boldsymbol{B}}$ or $\boldsymbol{\varepsilon}^{\boldsymbol{A}}_{\boldsymbol{L^2}}$) and without its neighborhood

($\boldsymbol{\varepsilon_0^A}$ if A has the crystallographic properties, $\boldsymbol{\varepsilon_0^{A^{eff}}} = \boldsymbol{E}$ if A has the effective properties, and thus the whole mesh is homogeneous). For brevity, the terms “the influence of a neighborhood (one or several grains) on another grain” will always refer to this definition of the neighborhood effect in the rest of this article. The effect of various parameters (mechanical properties and crystal orientations distribution, relative position between grains) on the following variables are discussed in this section:

- The influence of grain B over each grain element set A^{eff} of the aggregate mesh with the effective mechanical properties:

$$\boldsymbol{\Delta\varepsilon_B^{A^{eff}}} = \boldsymbol{\varepsilon_B^{A^{eff}}} - \boldsymbol{\varepsilon_0^{A^{eff}}} = \boldsymbol{\varepsilon_B^{A^{eff}}} - \boldsymbol{E} \tag{3.9}$$

- The influence of grain B on grain A with the crystallographic properties for each of the three relative positions $\overrightarrow{AB}$ selected:

$$\boldsymbol{\Delta\varepsilon_B^A} = \boldsymbol{\varepsilon_B^A} - \boldsymbol{\varepsilon_0^A} \tag{3.10}$$

  where grain A’s orientation from *S-1G* is identical to grain A’s orientation from *S-2G*.

- The influence of the two neighboring grain layers $L1$ and $L2$ on the central grain A:

$$\begin{cases} \boldsymbol{\Delta\varepsilon_{L^2}^{A^{eff}}} & = \quad \boldsymbol{\varepsilon_{L^2}^A} - \boldsymbol{E} \quad \text{if the effective properties are assigned to grain } A\ (A = 0) \\ \boldsymbol{\Delta\varepsilon_{L^2}^A} & = \quad \boldsymbol{\varepsilon_{L^2}^A} - \boldsymbol{\varepsilon_0^A} \quad \text{else } (A = H \text{ or } L \text{ or } R) \end{cases} \tag{3.11}$$

  where grain A’s orientation from *S-1G* is identical to grain A’s orientation from *S-65G*.

3.4.2 Influence of one grain on another grain

Tensors $\boldsymbol{\Delta\varepsilon_B^{A^{eff}}}$ and $\boldsymbol{\Delta\varepsilon_B^A}$ for the three different relative positions ((0;0;2), (1;1;1), (2;0;0)) were observed to study the influence of one grain on another. In the following sections, for simplicity, $\Delta\varepsilon_B^{A^{eff}}$ and $\Delta\varepsilon_B^A$ refer to the component “33” of the tensors $\boldsymbol{\Delta\varepsilon_B^{A^{eff}}}$ and $\boldsymbol{\Delta\varepsilon_B^A}$, respectively.

Fig. 3.4 presents $\Delta\varepsilon_B^A$ values for each orientation of grain A and B, and for their three relative positions studied. The orientations are arbitrarily classified in ascending order, depending on their apparent Young's modulus along $\vec{\boldsymbol{e}}_{\mathbf{3}}$ (orientation #1 with the lowest apparent Young's modulus and #40 with the highest) based on the common assumption that this parameter is the main consideration in describing the influence of a neighboring grain. For an applied strain loading of 10^{-3}, $\Delta\varepsilon_B^A$ varies from -4.4×10^{-5} to 3.3×10^{-5}, yielding an amplitude of 3.85×10^{-5} (Fig. 3.4a).

Each relative position shows different trends: for the relative position $\overrightarrow{AB} = (0; 0; 2)$, $\Delta\varepsilon_B^A$ increases uniformly with the value of grain B's apparent Young's modulus (Fig. 3.5a), but the trends are different for the other relative positions, which means that $\Delta\varepsilon_B^A$ depends on both the relative position $\overrightarrow{AB}$ with respect to the loading axis and the crystallographic orientations. The results from the two other relative positions are heterogeneous and no obvious correlation was observed between $\Delta\varepsilon_B^A$ and the apparent Young's modulus along $\vec{\boldsymbol{e}}_{\mathbf{3}}$ of grain B (Fig. 3.5b-3.5c). Actually, a given neighboring grain B can induce different strain fields in grain A as a function of $\overrightarrow{AB}$. For example, when grain B has the orientation #2 it can be observed that $\Delta\varepsilon_B^A$ is highly negative ($\sim -3.6 \times 10^{-5}$) for $\overrightarrow{AB} = (0; 0; 2)$, close to zero ($\sim 0.2 \times 10^{-5}$) for $\overrightarrow{AB} = (1; 1; 1)$ and slightly positive ($\sim 0.9 \times 10^{-5}$) for $\overrightarrow{AB} = (2; 0; 0)$. It is generally assumed in the literature (Guilhem *et al.*, 2010; Pourian *et al.*, 2014) that a "hard" grain increases the strain level of its environment regardless of its position, but the results here present different conclusions: a "hard" grain can either reduce or increase the strain of its neighborhood. Therefore, the grain's stiffness is not the only parameter to be considered. The crystallographic orientation, as well as the relative position of the grains between each other and with the loading axis, play a significant role on the local strain transfer.

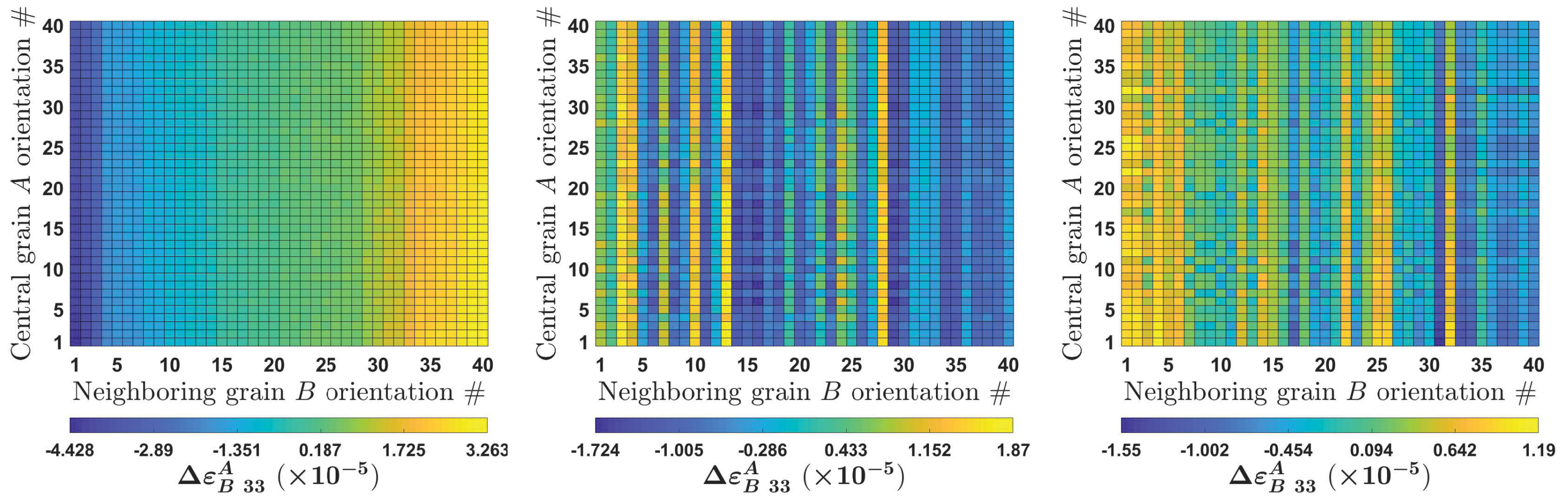

a) $\overrightarrow{AB} = (0;0;2)$

b) $\overrightarrow{AB} = (1;1;1)$

c) $\overrightarrow{AB} = (2;0;0)$

Figure 3.4 Influence of grain B on grain A: variation of $\Delta\varepsilon^A_{B\ 33}$ as a function of grain A and B orientations and their relative positions $\overrightarrow{AB}$. Orientation numbers are sorted by increasing apparent Young's modulus along $\vec{e}_3$ on the X and Y axes. Different trends are observed for each relative position, and $\Delta\varepsilon^A_{B\ 33}$ shows more variations along the X-axis than along the Y-axis.

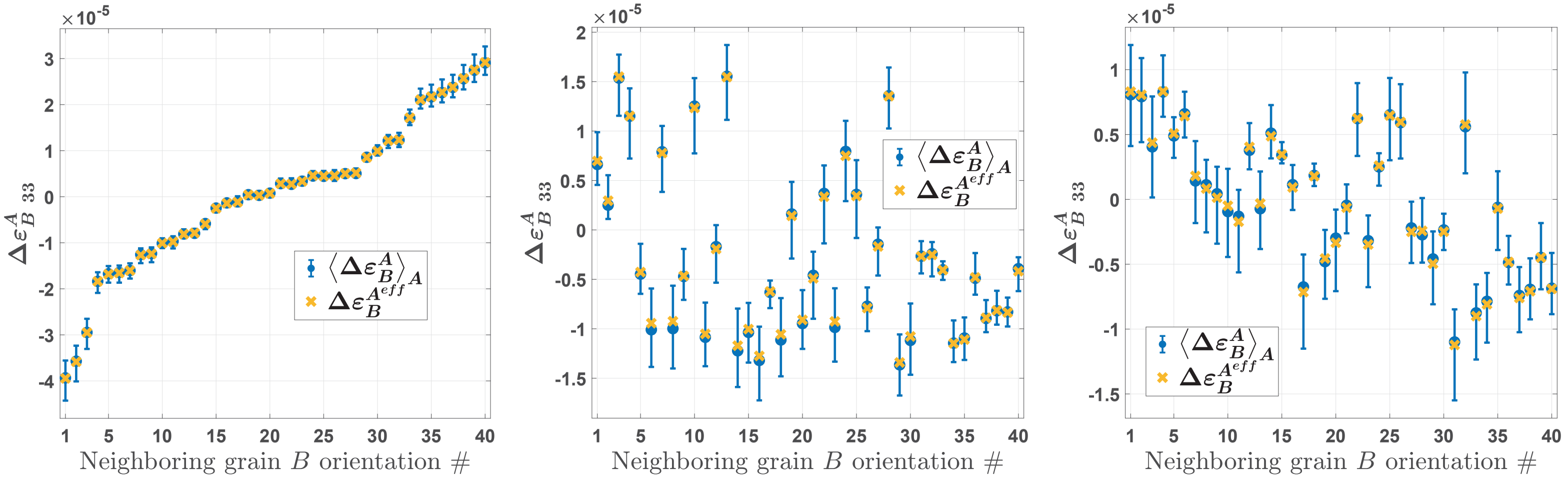

a) $\overrightarrow{AB} = (0; 0; 2)$ b) $\overrightarrow{AB} = (1; 1; 1)$ c) $\overrightarrow{AB} = (2; 0; 0)$

Figure 3.5 Influence of grain B on grain A: comparison between $\Delta\varepsilon^{A^{eff}}_{B\ 33}$ and $\Delta\varepsilon^{A}_{B\ 33}$ average value bounded by its maximum and minimum of values. Grain B's orientations number are sorted on the X axis by ascending apparent Young's modulus along $\vec{e}_3$. $\Delta\varepsilon^{A^{eff}}_{B\ 33}$ values are close to $\Delta\varepsilon^{A}_{B\ 33}$ average value for a given grain B's orientation.

Table 3.3 Statistics of the differences between $\Delta\varepsilon_B^A$ and $\Delta\varepsilon_B^{A^{eff}}$ over the 40×40 points from *S-2G* results for each relative position $\overrightarrow{AB}$.

$\overrightarrow{AB}$ $(\times 10^{-5})$	(0;0;2)	(1;1;1)	(2;0;0)	Density distribution of all the configurations
Average of $\left\|\Delta\varepsilon_B^A\right\|$	1.27	0.81	0.46	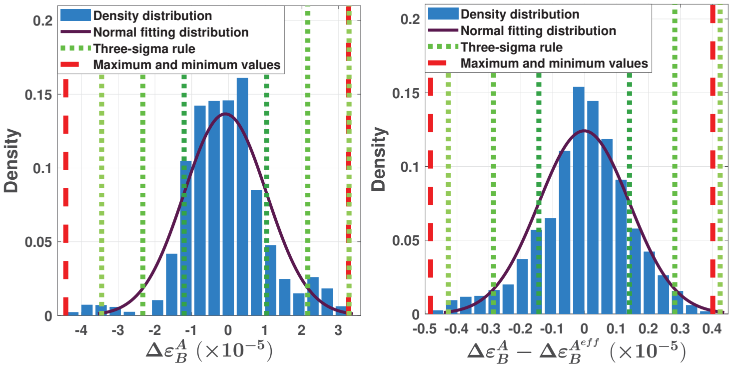
Average of $\Delta\varepsilon_B^A - \Delta\varepsilon_B^{A^{eff}}$	0.00	-0.01	0.00	
Average of $\left\|\Delta\varepsilon_B^A - \Delta\varepsilon_B^{A^{eff}}\right\|$	0.07	0.13	0.12	
Maximum of $\left\|\Delta\varepsilon_B^A - \Delta\varepsilon_B^{A^{eff}}\right\|$	0.48	0.48	0.44	

It can also be observed in Fig. 3.4 that $\Delta\varepsilon_B^A$ varies more significantly within rows than within columns, which means that grain B's orientation has a greater impact than that of grain A. $\Delta\varepsilon_B^A$ average value ($\left\langle\Delta\varepsilon_B^A\right\rangle_A$) bounded by its maximum and minimum over the different grain A's orientations for a given grain B's orientation were computed and are displayed in Fig. 3.5, together with $\Delta\varepsilon_B^{A^{eff}}$. It can be observed that $\left\langle\Delta\varepsilon_B^A\right\rangle_A$ and $\Delta\varepsilon_B^{A^{eff}}$ values are superimposed, which means that $\Delta\varepsilon_B^{A^{eff}}$ represents a good approximation of $\Delta\varepsilon_B^A$. The statistical data of the differences between $\Delta\varepsilon_B^A$ and $\Delta\varepsilon_B^{A^{eff}}$ over the 40×40 points are listed in Table 3.3. The average of the differences between $\Delta\varepsilon_B^A$ and $\Delta\varepsilon_B^{A^{eff}}$ tends toward zero, and an average accuracy of $\pm 0.134\permil$ of the applied loading in the worst case ($\overrightarrow{AB} = (1;1;1)$) was found. The values of $\Delta\varepsilon_B^A$ were found to be one order higher than $\Delta\varepsilon_B^A - \Delta\varepsilon_B^{A^{eff}}$ by comparing their density distributions. These data confirm the choice of $\Delta\varepsilon_B^{A^{eff}}$ to approximate the value of $\Delta\varepsilon_B^A$. Nonetheless, in the worst cases (maximum of $\left|\Delta\varepsilon_B^A - \Delta\varepsilon_B^{A^{eff}}\right|$), the order of the approximation error is the same as the average of $\left|\Delta\varepsilon_B^A\right|$.

These observations were made for component "33" of the tensor $\boldsymbol{\Delta\varepsilon_B^A}$ and similar conclusions were also made for its other components (Appendix 3.b). Therefore, the following approximation can be made: $\boldsymbol{\Delta\varepsilon_B^A}$, the influence of a grain B over another grain A, is independent of grain

A's orientation, and can be approximated by $\boldsymbol{\Delta\varepsilon_B^{A^{eff}}}$, the influence of the same grain B over a grain A^{eff} with the same properties of the matrix such that $\overrightarrow{AB} = \overrightarrow{A^{eff}B}$ (Fig. 3.6). This approximation reduces the number of parameters affecting $\boldsymbol{\Delta\varepsilon_B^A}$ to only grain B's orientation and the relative position $\overrightarrow{AB}$.

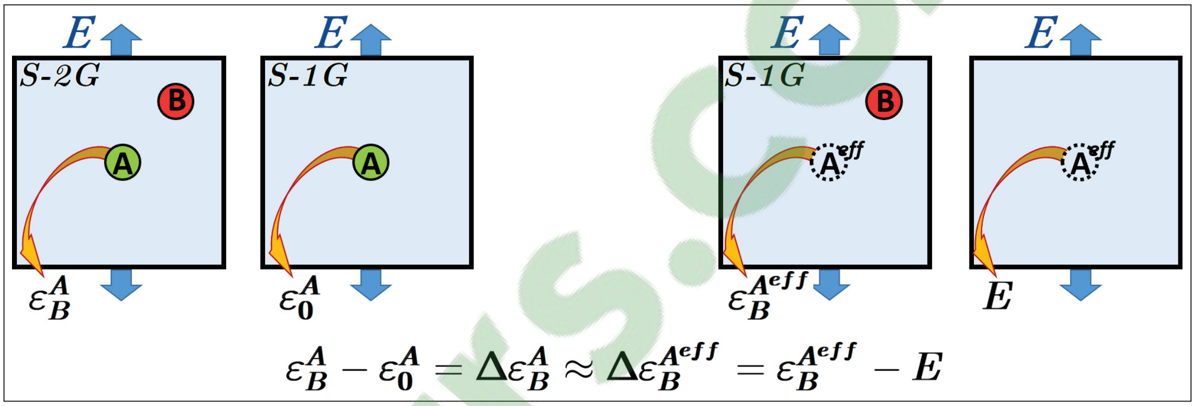

Figure 3.6 2D schematic representation of a neighboring grain B influence over a grain A approximated by the same grain B influence over a matrix element set A^{eff} such that $\overrightarrow{AB} = \overrightarrow{A^{eff}B}$.

Finally, $|\Delta\varepsilon_B^{A^{eff}}|$ average and maximum values over the 40 random orientations are compared for different neighboring positions: the impact of the angle $\theta = (\overrightarrow{AB}, \vec{\boldsymbol{e}}_3)$ can be observed in Table 3.4 and the impact of the distance between grains A^{eff} and B is seen in Table 3.5. Table 3.4 shows that the more $\overrightarrow{AB}$ is aligned with the loading axis $\vec{\boldsymbol{e}}_3$, the higher its average/maximum influence: the average/maximum value of $\Delta\varepsilon_B^{A^{eff}}$ of a neighboring grain position with an angle $\theta = 0°$ is at least 3 times higher than a grain having a position at 90° and an equal distance from the central grain. Also, it can be seen in Table 3.5 that the farther the two grains are from each other, the less their mutual influence: at an equal angle θ, the maximum of $\left|\Delta\varepsilon_B^{A^{eff}}\right|$ drops by a factor ~ 6 between the first and second layers of neighboring grains and another factor ~ 2.5 between the second and third layers. Therefore, it can be assumed that a grain farther than the third layer of a neighboring grain can have an absolute maximum influence approximately ~ 15 times smaller than a grain in the first layer.

Table 3.4 $\Delta\varepsilon_B^{A^{eff}}$ average and maximum values over the 40 random orientations: comparison between different relative positions with the same grains A and B distance but forming different angles θ with respect to the loading axis $\vec{\boldsymbol{e}}_3$.

$\overrightarrow{AB}$		(2;0;0)	(0;0;2)	(2;2;0)	(2;0;2)	(3;1;1)	(1;1;3)	(3;3;1)	(3;1;3)
$\lVert\overrightarrow{AB}\rVert$		2		2.8		3.3		4.6	
$\theta = (\overrightarrow{AB}, \vec{\boldsymbol{e}}_3)$		90°	0°	90°	45°	72°	25°	77°	47°
$\left\lvert\Delta\varepsilon_B^{A^{eff}}\right\rvert$	MEAN	0.46	1.27	0.13	0.31	0.12	0.39	0.06	0.10
$(\times 10^{-5})$	MAX	1.12	3.95	0.40	0.69	0.31	0.97	0.15	0.20

Table 3.5 $\Delta\varepsilon_B^{A^{eff}}$ average and maximum values over the 40 random orientations : comparison between different relative positions forming the same angle with respect to the loading axis $\vec{\boldsymbol{e}}_3$ but with different grains A and B distances.

$\theta = 0°$	$\left\lvert\Delta\varepsilon_B^{A^{eff}}\right\rvert$ $(\times 10^{-5})$		$\theta = 54.7°$	$\left\lvert\Delta\varepsilon_B^{A^{eff}}\right\rvert$ $(\times 10^{-5})$		$\theta = 90°$	$\left\lvert\Delta\varepsilon_B^{A^{eff}}\right\rvert$ $(\times 10^{-5})$	
$\overrightarrow{AB}$	MEAN	MAX	$\overrightarrow{AB}$	MEAN	MAX	$\overrightarrow{AB}$	MEAN	MAX
(0; 0; 2)	1.27	3.95	(1; 1; 1)	0.81	1.55	(2; 0; 0)	0.46	1.12
(0; 0; 4)	0.28	0.88	(2; 2; 2)	0.11	0.27	(4; 0; 0)	0.07	0.22
(0; 0; 6)	0.13	0.66	(3; 3; 3)	0.04	0.09	(6; 0; 0)	0.03	0.07
			(4; 4; 4)	0.02	0.04			

3.4.3 Influence of several grains on another grain

Tensors $\boldsymbol{\Delta\varepsilon_B^{A^{eff}}}$ and $\boldsymbol{\Delta\varepsilon_{L^2}^{A}}$ for the 60 different aggregate configurations of the *S-65G* simulations described in Section 3.4.1 were analyzed to study the influence of several grains on the central grain. In the following sections, for simplicity, $\Delta\varepsilon_B^{A^{eff}}$ and $\Delta\varepsilon_{L^2}^{A}$ refer to component "33" of the tensors $\boldsymbol{\Delta\varepsilon_B^{A^{eff}}}$ and $\boldsymbol{\Delta\varepsilon_{L^2}^{A}}$, respectively.

The values of $\Delta\varepsilon_{L^2}^{A}$ for each of the 60 aggregate configurations are shown in Fig. 3.7. The strain variations induced by the two grain layers range from -4.88×10^{-4} to 5.34×10^{-4} for an applied strain loading of 10^{-3}. This amplitude (5.11×10^{-4}) for the 64 grains is one order of magnitude higher than the amplitude observed for only one grain (3.85×10^{-5}) calculated in Section 3.4.2, but also 3 times higher than the amplitude observed for randomly generated polycrystalline aggregates ($\sim 1.5 \times 10^{-4}$) presented in Section 3.3, Fig. 3.2a. In the extreme

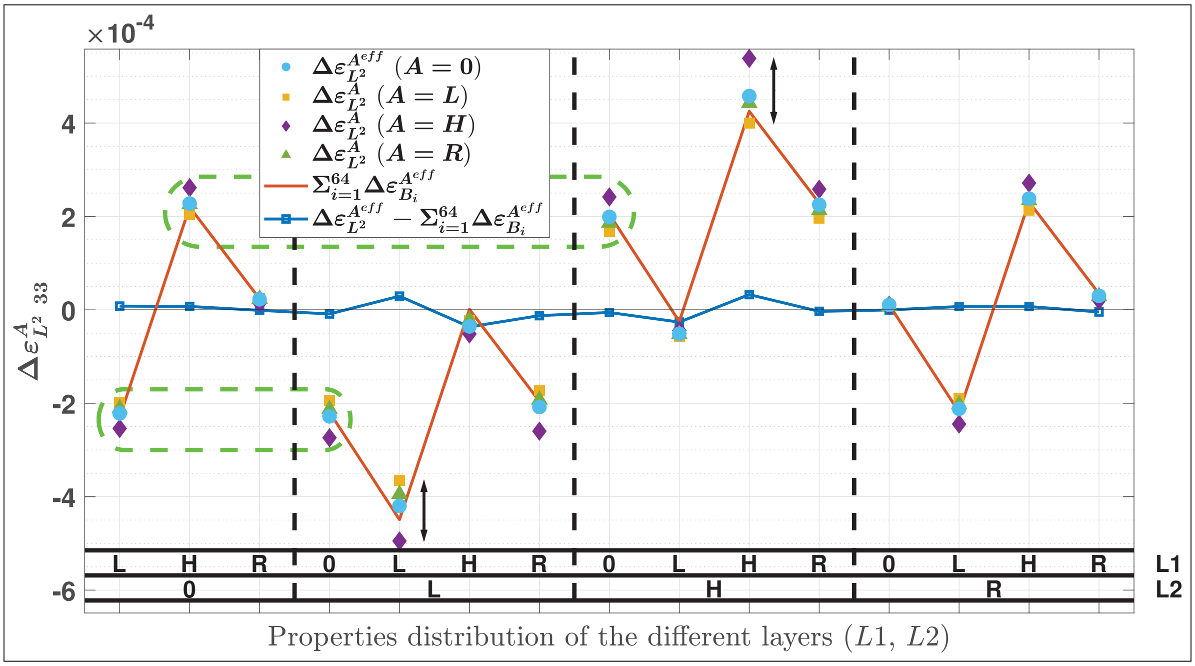

Figure 3.7 $\Delta\varepsilon^A_{L^2}$ variations as a function of grain A, $L1$, $L2$ properties configurations. Comparison with the sum of the individual influences $\varepsilon^{A^{eff}}_{B_i}$ of each grain B_i forming the two grain layers $L1$ and $L2$. Property notation "0" corresponds to the effective properties; "L", "H" correspond to the crystal properties with the orientations corresponding respectively to the lowest and highest values of ε^A_0 or $\varepsilon^{A^{eff}}_B$ from *S-1G* simulations for each grain of $L1$ and/or $L2$; "R" corresponds to random orientations. The variations of $\Delta\varepsilon^A_{L^2}$ observed due to the different neighborhood configurations are more significant than those due to the different grain A properties. $\Sigma^{64}_{i=1}\Delta\varepsilon^{A^{eff}}_{B_i}$ shows a good approximation of $\Delta\varepsilon^{A^{eff}}_{L^2}$

cases (maximum and minimum values of $\Delta\varepsilon^A_{L^2}$), the neighborhood can increase/decrease the strain in the central grain by 50% of the applied loading, which is really significant.

For a given neighborhood configuration, changing the properties of the central grain ($A = 0$, L, H or R) does not significantly change $\Delta\varepsilon^A_{L^2}$, when compared to the variations due to the different neighborhood configurations. This observation confirms those made in Section 3.4.2, extending the following approximation to a larger neighborhood:

$$\Delta\varepsilon^A_B \approx \Delta\varepsilon^{A^{eff}}_B \quad \Leftrightarrow \quad \Delta\varepsilon^A_{L^2} \approx \Delta\varepsilon^{A^{eff}}_{L^2} \tag{3.12}$$

Nonetheless, in the extreme cases (($L1 = L, L2 = L$) or ($L1 = H, L2 = H$)) highlighted by black arrows in Fig. 3.7, a difference of $\sim 10^{-4}$ (representing 10% strain level variation) can be observed between two configurations with the same neighborhood, but different grain A orientations.

The sum of the individual influences $\Delta\varepsilon_{B_i}^{A^{eff}}$ (obtained from *S-1G* simulations and presented in Fig. 3.7) of each grain B_i forming the layers $L1$ and $L2$ ($\Sigma_{i=1}^{64}\Delta\varepsilon_{B_i}^{A^{eff}}$) can be compared with $\Delta\varepsilon_{L^2}^{A^{eff}}$, showing differences from -3.64×10^{-5} to 3.27×10^{-5}, with an average of -0.05×10^{-5} for an applied strain loading of 10^{-3}. These differences are at least one order of magnitude smaller than the actual value, making $\Sigma_{i=1}^{64}\Delta\varepsilon_{B_i}^{A^{eff}}$ a good candidate to approximate $\Delta\varepsilon_{L^2}^{A^{eff}}$.

Finally, according to Equation 3.12, and assuming that the sample of 40 random orientations generated for *S-1G* simulations is sufficient to find an orientation corresponding approximately to the lowest and highest possible values of $\Delta\varepsilon_{B_i}^{A^{eff}}$ for each neighboring grain from $L1$ and $L2$, each layer influence amplitude can be assessed from the configurations ($L1 = L, L2 = 0$)/($L1 = H, L2 = 0$) for $L1$ and ($L1 = 0, L2 = L$)/($L1 = 0, L2 = H$) for $L2$. By comparing these two pairs of configurations (highlighted by the green circle in Fig. 3.7) it can be seen that layers $L1$ and $L2$ show a similar range of influence. This can be explained by the observations made in Section 3.4.2 that grains closer to the central grain may have a higher influence, but there are more grains in the second layer than in the first, which balances out the first argument.

The same observations were also made for the other components of $\boldsymbol{\Delta\varepsilon_{L^2}^{A}}$. Therefore, the following two approximations can be made:

- The influence $\boldsymbol{\Delta\varepsilon_{n}^{A}}$ of a whole neighborhood n composed of grains B_i over grain A is independent of grain A's orientation, and can be approximated by $\boldsymbol{\Delta\varepsilon_{n}^{A^{eff}}}$, which is the influence of the neighborhood n on a grain A^{eff} with the same properties as the matrix such that $\overrightarrow{AB} = \overrightarrow{A^{eff}B}$.

- The influence $\boldsymbol{\Delta\varepsilon_{n}^{A^{eff}}}$ of a whole neighborhood n over a grain A^{eff} can be approximated by summing each grain B_i's individual influence $\boldsymbol{\Delta\varepsilon_{B_i}^{A^{eff}}}$.

Therefore, by combining these two approximations, the difference between the strain tensor $\boldsymbol{\varepsilon}_{\boldsymbol{n}}^{\boldsymbol{A}}$ of a grain A under the influence of a neighborhood n constituted of grains B_i and the strain tensor $\boldsymbol{\varepsilon}_{\boldsymbol{0}}^{\boldsymbol{A}}$ of the same grain A alone in the homogeneous matrix can be approximated as follows (Fig. 3.8):

$$\Delta\boldsymbol{\varepsilon}_{\boldsymbol{n}}^{\boldsymbol{A}} \approx \sum_{B_i} \Delta\boldsymbol{\varepsilon}_{\boldsymbol{B_i}}^{\boldsymbol{A^{eff}}} \tag{3.13}$$

leading to the following grain A's mean strain and stress tensors' definition:

$$\boldsymbol{\varepsilon}_{\boldsymbol{n}}^{\boldsymbol{A}} \approx \boldsymbol{\varepsilon}_{\boldsymbol{0}}^{\boldsymbol{A}} + \sum_{B_i} \Delta\boldsymbol{\varepsilon}_{\boldsymbol{B_i}}^{\boldsymbol{A^{eff}}} \tag{3.14a}$$

$$\boldsymbol{\sigma}_{\boldsymbol{n}}^{\boldsymbol{A}} = \mathbb{C}^{\boldsymbol{A}} : \boldsymbol{\varepsilon}_{\boldsymbol{n}}^{\boldsymbol{A}} \tag{3.14b}$$

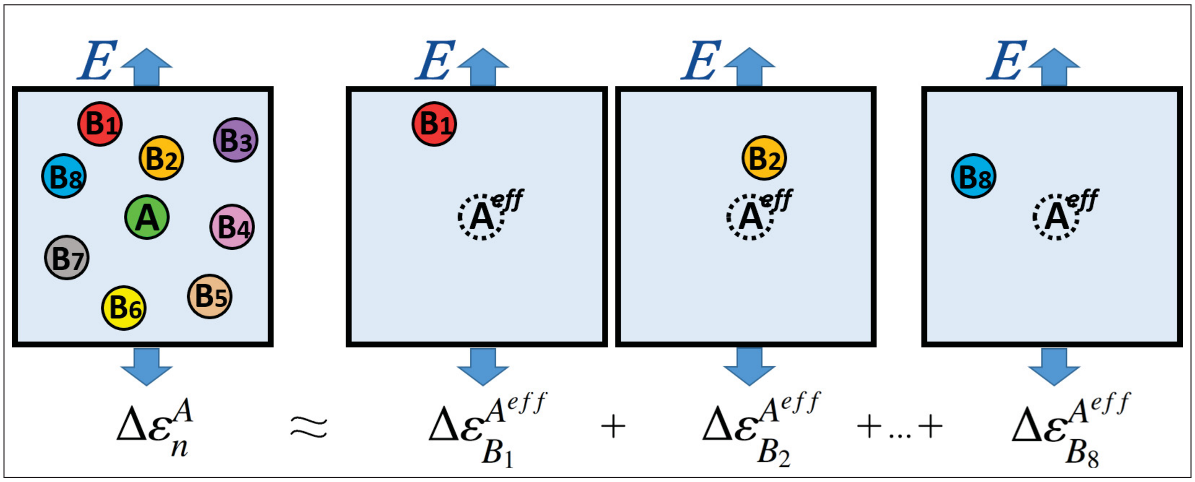

Figure 3.8 2D schematic representation of a neighborhood n (composed of grains B_i) influence over a grain A approximated by the sum of each grain B_i individual influence over a matrix element set A^{eff} such that $\overrightarrow{AB_i} = \overrightarrow{A^{eff}B_i}$.

3.5 Neighborhood effect approximation application to a polycrystalline aggregate

In order to estimate the precision of the approximation proposed in Equation 3.14, one of the twenty polycrystalline aggregate's strain field predictions with PBC described in Section 3.3 are compared to the predictions that would be obtained using Equation 3.14. To that end, a new series of S-1G simulations (Section 3.4.1) must be performed for each of the 686 orientations composing the aggregate to calculate each grain individual influence $\boldsymbol{\Delta\varepsilon_{B_i}^{A^{eff}}}$ on each surrounding grain in a radius of three layers (258 grains such as $||\overrightarrow{AB}|| \leq 6$). Periodicity must be considered when selecting the surrounding grains of a specific grain. The variable $\boldsymbol{\varepsilon_0^A}$ of Equation 3.14 is obtained using EIM results obtained in Section 3.3. Finally, respecting the periodicity, geometry, and orientation distribution of the aggregate used for the FEM simulation in Section 3.3, the stress/strain in each grain was calculated as follows:

$$\boldsymbol{\varepsilon_{Esh+NE}^{g}} = \boldsymbol{\varepsilon_{Esh}^{g}} + \sum_{i=1}^{258} \boldsymbol{\Delta\varepsilon_{B_i}^{g^{eff}}} \tag{3.15a}$$

$$\boldsymbol{\sigma_{Esh+NE}^{g}} = \mathbb{C}^{g} : \boldsymbol{\varepsilon_{Esh+NE}^{g}} \tag{3.15b}$$

Figure 3.9 shows the 686 aggregate grains mean strain and stress tensors “33” component obtained with the FEM simulation, the EIM and the EIM corrected with the neighborhood effect (Esh+NE) as a function of their apparent Young’s modulus along $\boldsymbol{\vec{e}_3}$. It can be observed that the correction due to the neighborhood effect renders the dispersion of the values obtained from the Esh+NE model very similar to those obtained from FEM simulations. Table 3.6 reports the statistics of the difference between the values obtained by FEM and those obtained with the Esh+NE scheme. The density distributions of these differences was found to follow a normal distribution. Comparing Table 3.6 with Table 3.2, we see a significant improvement in the results: on average the Esh+NE results are three to four times closer to FEM predictions than those from the EIM. The convergence is even more remarkable for the extreme difference values. These results, assuming that $\boldsymbol{\Delta\varepsilon_{B_i}^{A^{eff}}}$ can be predicted with an analytical model for any grain B orientation, justify the possible use of Equation 3.15 for the development of an analytical model capable of predicting the local strain fields in polycrystalline aggregates.

3.6 Conclusions

The main purpose of this article was to better understand and describe the neighborhood effect within polycrystalline aggregates submitted to an elastic loading. The influence of a

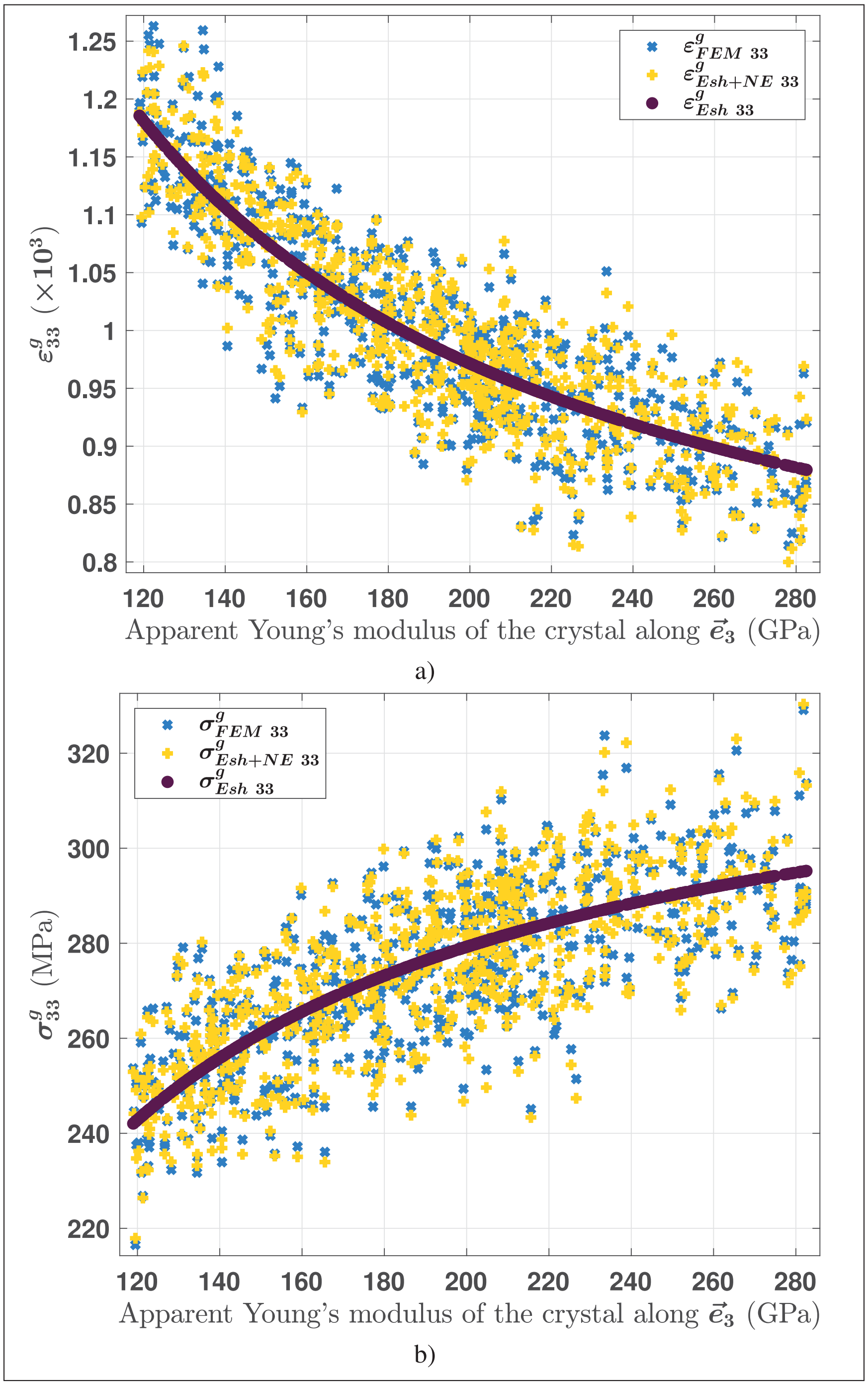

Figure 3.9 Comparison between FEM and EIM (with and without the neighborhood effect correction) models of the mean strain $\boldsymbol{\varepsilon^g}$ (a.) and stress $\boldsymbol{\sigma^g}$ (b.) of each polycrystalline aggregate grain as a function of the apparent Young's modulus along the loading axis $\vec{\boldsymbol{e}}_{\boldsymbol{3}}$.

Table 3.6 Statistics of the difference between the FEM and the Esh+NE results over the 686 grains of the aggregate.

	$i=1$ $j=1$	$i=2$ $j=2$	$i=3$ $j=3$	$i=2$ $j=3$	$i=1$ $j=3$	$i=1$ $j=2$	Example of density distribution (case $i=3, j=3$) and its normal fitting.
E^{eff}_{ij} $(\times 10^3)$	0.00	0.00	1.00	0.00	0.00	0.00	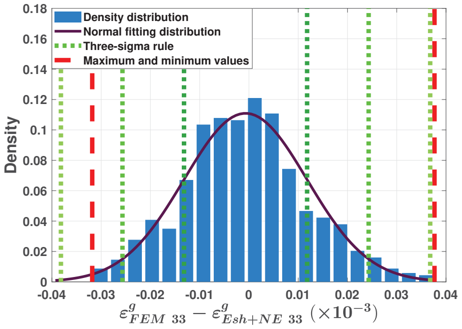
Average of $\varepsilon^g_{FEM\ ij} - \varepsilon^g_{Esh+NE\ ij}$	0.00	0.00	0.00	0.00	0.00	0.00	
Average of $\left\lvert \varepsilon^g_{FEM\ ij} - \varepsilon^g_{Esh+NE\ ij} \right\rvert$	0.01	0.01	0.01	0.01	0.01	0.01	
Maximum of $\left\lvert \varepsilon^g_{FEM\ ij} - \varepsilon^g_{Esh+NE\ ij} \right\rvert$	0.06	0.05	0.04	0.04	0.04	0.03	
Σ^{eff}_{ij} (MPa)	115.8	115.9	274.3	0.0	0.1	-0.1	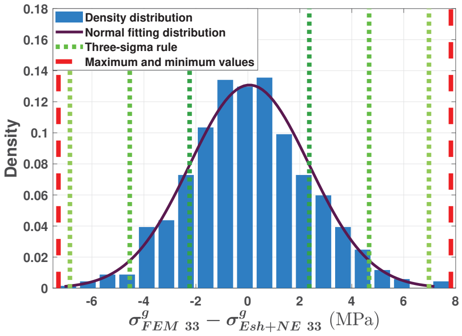
Average of $\sigma^g_{FEM\ ij} - \sigma^g_{Esh+NE\ ij}$	-0.2	0.2	0.1	0.4	0.1	0.3	
Average of $\left\lvert \sigma^g_{FEM\ ij} - \sigma^g_{Esh+NE\ ij} \right\rvert$	1.7	1.8	1.8	1.3	1.3	1.2	
Maximum of $\left\lvert \sigma^g_{FEM\ ij} - \sigma^g_{Esh+NE\ ij} \right\rvert$	6.5	8.3	7.8	5.0	5.7	6.3	

neighborhood on a grain A's strain tensor in polycrystalline aggregates has been defined as the difference between the mean strain tensor of grain A in the aggregate and the mean strain tensor of the same grain A immersed in an infinite matrix having the same mechanical properties as the homogenized aggregates and submitted to the same loading. FEM simulations on a polycrystalline aggregate generated with the Kelvin structure, for which each grain was randomly oriented, was submitted to an axial strain loading. The results show that a grain neighborhood can have a strong effect on its stress/strain level: hard grains (grains that are difficult to deform in the loading direction) can present a strain level higher than soft grains depending on their neighborhood. Some specific neighborhood configurations generated strain levels 50% higher than the average of those predicted by random sets of grains simulated by FEM. This justifies a systematic investigation of the neighborhood effect.

This specific neighborhood configuration was found thanks to a systematic study of the elastic behavior of a grain A immersed in a homogeneous isotropic elastic matrix with or without adjacent grain(s). The mean strain variations of a grain A immersed with a specific neighborhood in an infinite homogeneous matrix were studied using FEM simulations. Different neighborhood configurations were studied, and the following conclusions on the effects of the grains orientation distribution and their relative positions with respect to the loading axis on grain A's strain tensor were made:

- A grain strain variation due to a neighboring grain presence is not only related to the neighboring grain stiffness along the loading axis, but also depends on its orientation and its relative position with respect to the influenced grain $\overrightarrow{AB}$ and the loading axis.
- For a given relative position $\overrightarrow{AB}$, a grain A's mean strain variation due to a neighboring grain B is mainly dependent on grain B's orientation whereas grain A's orientation has a negligible effect. This means that a given grain B will have the same influence on a grain A regardless of grain A's crystallographic orientation. Therefore, the influence of grain B over A can be approximated by the influence of grain B, immersed alone in a homogenized matrix, over the same element set where grain A was with the homogenized properties of the matrix.
- The influence of several grains on another grain strain tensor can be approximated by the sum of the individual influence of each one of those grains.

By adding the neighborhood effect calculated with the approximations proposed above to the EIM, it has been shown that it is possible to develop an analytical model that better considers the statistical character of the neighborhood effect in polycrystalline aggregates. Nonetheless, in a context of developing a fully analytical model, a model capable of predicting the mean strain variations observed in different subsets of a homogeneous matrix due to the presence of a grain immersed in it is yet to be developed.

This can become useful for studying the fatigue behavior of polycrystalline aggregates by extending the observations made in the context of an elastic loading (linear problem) to the small deformation domain. In the high cycle regime, this is possible as the plasticity is confined to only a few grains. Non-linear behaviors, such as crystalline elasto-plasticity, could be used in the context of small deformation increments where the problem could be reduced to the linear case.

CHAPTER 4

NEIGHBORHOOD EFFECT ON THE STRAIN DISTRIBUTION IN LINEARLY ELASTIC POLYCRYSTALS: PART 2 - CELLULAR AUTOMATON

Rémy Bretin[1], Martin Lévesque[2], Philippe Bocher[1]

[1] Mechanical Engineering Department, École de technologie supérieure (ÉTS),
1100 Notre-Dame Street West, Montréal, QC H3C 1K3, Canada
[2] Mechanical Engineering Department, École Polytechnique de Montréal,
2900 Boulevard Edouard-Montpetit, Montréal, QC H3T 1J4, Canada

Article accepted for publication in «International Journal of Solids and Structures» july 2019.
Small modifications from the published version of the article have been brought in this chapter.

Abstract

This paper presents the development of a Cellular Automaton (CA) capable of describing polycrystalline structures heterogeneous behavior in the elastic domain. Based on Eshelby's inclusion problem, this model is the first step to a better consideration of heterogeneities in polycrystals by including the neighborhood effect in grain's behavior. Neighborhood effects have been defined, quantified, and approximated from observations made in the first of this two-part paper, using finite element method (FEM). Considering these approximations, and based on FEM simulations results, an analytical model of the neighborhood effect was proposed in the present paper on which the CA model was built. As a first step in the model development, a regular aggregate structure (Kelvin structure) is used where grains are considered spherical and having identical size. The stress field predictions obtained with the FEM for a polycrystalline aggregate submitted to an elastic loading were compared with the CA predictions, grain by grain, for two different crystal structures (Fe and Ti). Considering the FEM as a reference tool, CA model predictions show an excellent propensity at predicting the local stress fields in polycrystals by capturing the neighborhood effect induced by grain orientations for a low computation time cost. The CA model has also shown its facility to evaluate quickly a grain influence on another grain stress level, and therefore, the orientations generating high stress concentrations in a grain can be easily identified. Using this capacity, the neighborhood effect has been shown to be able to at least double a grain stress level without the material showing any particular texture.

Keywords: Cellular automaton, Neighborhood effect, Homogenization Model, Analytical Model, Elastic anisotropy, Eshelby's inclusion, Polycrystal

4.1 Introduction

Heterogeneities among polycrystals (crystal anisotropy, orientation distribution, grains morphology, etc...) introduce stress heterogeneities when the material is loaded. This can lead, in some cases, to local stresses higher than that nominally applied, yielding microscopic cracks initiations that trigger premature failure. Models predicting these stress heterogeneities at the grains level are of considerable interest for fatigue life prediction, especially when the objective is to identify the configuration yielding the shortest fatigue life for a given load.

The first of this two-part paper (Bretin *et al.*, 2019a) presented a Finite Element Model (FEM) that documented a grain's neighborhood influence on its mechanical response to a strain field. A definition, a quantification method, and approximations of the neighborhood effect were proposed. That work revealed that varying a given grain's neighborhood induced stress variations as important as varying the grain's orientation when the neighborhood is fixed. This result strongly suggests that a grain's neighborhood should be accounted for in multi-scale fatigue life prediction models.

Numerous methods have been developed to predict local stresses and strains in a polycrystal. Full-field simulations relying on FEMs (Forest *et al.*, 2002; Roters *et al.*, 2011) or algorithms relying on Fast Fourier Transforms (FFT) (Moulinec & Suquet, 1998b; Prakash & Lebensohn, 2009) provide local fields as accurate as required, at the expense of the computational cost. On the other hand, mean-field homogenization schemes like the Self-Consistent (SC) method (Budiansky, 1965; Hill, 1965b) are known to yield relatively accurate mean local stresses, for a comparatively small computational cost (Lebensohn *et al.*, 2004; Yaguchi & Busso, 2005). These techniques, however, have shown a lack of accuracy when the crystal anisotropy becomes important due to the neighborhood effect (Brenner *et al.*, 2009). Liu et al. (Liu, Bessa & Liu, 2016; Liu, Kafka, Yu & Liu, 2018) recently developed a data-driven self-consistent cluster analysis (SCCA). The model is divided in two parts: a data-training stage using elastic full-field simulations and k-means clustering method followed by a prediction stage using the Lippmann–Schwinger equation. Even though the model has shown an excellent quality / CPU time ratio, the data-training stage is specific to the representative volume element (RVE) studied which does not allow to easily identify the orientation distributions responsible for a local stress concentration. The Non-uniform Transformation Field Analysis (NTFA) introduced by Michel and Suquet (Michel & Suquet, 2003) and recently adapted to polycrystalline aggregates (Michel & Suquet, 2016) yielded local stress fields very close to those predicted from full-field methods, for a very low computational cost. The technique requires, however, an elaborate calibration stage to optimize the model's parameters.

The Cellular Automaton (CA) method was considered in this paper to account for the neighborhood effect in polycrystal local stress and strain field predictions, as by nature this type of model considers the neighborhood effect in its solution computations. A CA consists of a discrete mathematical model where the space is discretized into cells (Wolfram, 2002). Each cell has its own initial state (mechanical properties, strain/stress initial states, etc.) and its evolution depends on that of its neighbors through transition rules. The CA model was first used in material science in the 1990s to study polycrystals solidification and recrystallization (Hesselbarth & Göbel, 1991) and has been continuously developed in this field (Solas, Thebault, Rey & Baudin, 2010; Zhao *et al.*, 2009). It was soon after used to predict inhomogeneous two-phase materials micromechanical behavior (Montheillet & Gilormini, 1996). More recently, Boutana et al. (Boutana, Bocher, Jahazi, Piot & Montheillet, 2008a; Boutana *et al.*, 2013), and later Pourian et al. (Pourian *et al.*, 2014,1), proposed CA models to study titanium alloys behavior under elastic, creep, and dwell-fatigue loading.

The new CA model developed in this paper predicts polycrystals local stress fields under an elastic loading, with the purpose to easily identify the orientation distributions responsible for stress concentrations. Studied polycrystals are represented using a regular structure (Kelvin structure) where all grains are of identical shape and size. Section 4.2 summaries the work presented by Bretin *et al.* (2019a) and those used in this paper. Based on FEM simulations, a heuristic analytical model of the neighborhood effect is proposed in Section 4.3. The new CA model is developed by means of this model and the approximations proposed by Bretin *et al.* (2019a). The methodologies to calibrate the model parameters and its algorithm are described in Section 4.4. Using the FEM as a reference tool, FEM and CA local stress field predictions for polycrystals local stress field submitted to different elastic loadings are compared in Section 4.5 for two different crystallographic structures: iron (face-centered cubic) and titanium (hexagonal close-packed). Finally, Section 4.6 presents our CA model's capacity to straightforwardly identify the orientations responsible for significant stress concentrations, before the closing remarks and conclusions discussed in Section 4.7.

4.2 Background

4.2.1 Neighborhood effect simulated by FEM (Bretin *et al.*, 2019a)

A given neighborhood n influence on a grain A's strain tensor in a polycrystalline aggregate, $\boldsymbol{\Delta\varepsilon}_n^A$, submitted to a loading $\boldsymbol{E}$ has been defined in elasticity as the difference between the mean strain tensor of grain A immersed in the aggregate, $\boldsymbol{\varepsilon}_n^A$, and the mean strain tensor of the same grain A immersed in an infinite matrix having the homogenized aggregate properties, $\boldsymbol{\varepsilon}_0^A$, submitted to the same macroscopic strain $\boldsymbol{E}$ in each case (see an illustration in Fig. 4.1a) as:

$$\boldsymbol{\Delta\varepsilon}_n^A = \boldsymbol{\varepsilon}_n^A - \boldsymbol{\varepsilon}_0^A \tag{4.1}$$

When studying uni-axially applied loadings, our FEM investigation (Bretin *et al.*, 2019a) revealed that:

- $\boldsymbol{\Delta\varepsilon}_n^A$ can be assumed to be independent of grain A's orientation and can therefore be approximated by $\boldsymbol{\Delta\varepsilon}_n^{A^{eff}}$: the neighborhood n influence over a grain A^{eff} occupying the same location as grain A and whose elastic properties have been replaced by the aggregate's homogenized properties. This observation reads:

$$\boldsymbol{\Delta\varepsilon}_n^A \approx \boldsymbol{\Delta\varepsilon}_n^{A^{eff}} \tag{4.2a}$$

$$\text{with} \quad \boldsymbol{\Delta\varepsilon}_n^{A^{eff}} = \boldsymbol{\varepsilon}_n^{A^{eff}} - \boldsymbol{\varepsilon}_0^{A^{eff}} = \boldsymbol{\varepsilon}_n^{A^{eff}} - \boldsymbol{E} \tag{4.2b}$$

- A whole neighborhood n composed of N grains B_i influence over a grain A^{eff} strain tensor, $\boldsymbol{\Delta\varepsilon}_n^{A^{eff}}$, can be approximated by summing each grain B_i individual influence, $\boldsymbol{\Delta\varepsilon}_{B_i}^{A^{eff}}$, as:

$$\boldsymbol{\Delta\varepsilon}_n^{A^{eff}} \approx \sum_{i=1}^{N} \boldsymbol{\Delta\varepsilon}_{B_i}^{A^{eff}} \tag{4.3a}$$

$$\text{with} \quad \boldsymbol{\Delta\varepsilon}_{B_i}^{A^{eff}} = \boldsymbol{\varepsilon}_{B_i}^{A^{eff}} - \boldsymbol{\varepsilon}_0^{A^{eff}} = \boldsymbol{\varepsilon}_{B_i}^{A^{eff}} - \boldsymbol{E} \tag{4.3b}$$

  where $\boldsymbol{\varepsilon}_{B_i}^{A^{eff}}$ is grain A^{eff}'s mean strain tensor obtained by keeping grains A^{eff} and B_i specific relative spacial position and immersing them in an infinite matrix having the aggregate's homogenized properties submitted to the same loading $\boldsymbol{E}$.

Therefore, combining two approximations (see an illustration in Fig. 4.1b) to equation 4.1 yields grain A's mean strain tensor as:

$$\boldsymbol{\varepsilon}_n^A \approx \boldsymbol{\varepsilon}_0^A + \sum_{B_i} \boldsymbol{\Delta\varepsilon}_{B_i}^{A^{eff}} \tag{4.4}$$

$\boldsymbol{\varepsilon}_0^A$ can be obtained from Eshelby's inclusion method (EIM), and Section 4.3 shows a model to predict $\boldsymbol{\Delta\varepsilon}_{B_i}^{A^{eff}}$.

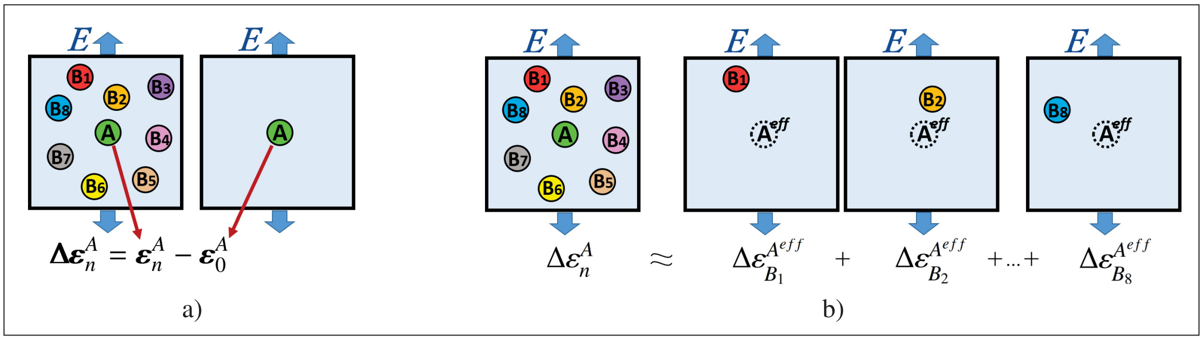

Figure 4.1 Neighborhood effect (a) Definition and (b) Approximation visual represention when submitted to a strain loading $\boldsymbol{E}$. (a) Grain A's neighborhood effect ($\Delta\boldsymbol{\varepsilon}_n^A$) is quantified by the difference between grain A's strain tensor in the polycrystalline aggregate ($\boldsymbol{\varepsilon}_n^A$) and grain A's strain tensor in an infinite matrix having the aggregate's homogenized properties ($\boldsymbol{\varepsilon}_0^A$). (b) $\Delta\boldsymbol{\varepsilon}_n^A$ is approximated by summing each grain B_i individual influence on a grain A^{eff} in wich the properties have been replaced by the homogenized aggregate properties, and $\overrightarrow{AB_i} = \overrightarrow{A^{eff}B_i}$ (Bretin *et al.*, 2019a).

4.2.2 Eshelby's diluted solution

Eshelby's solution (Eshelby, 1957) estimates, in elasticity, the mean strain tensor in an ellipsoidal inclusion immersed in an infinite homogeneous matrix submitted to a loading $\boldsymbol{E}$ as:

$$\boldsymbol{\varepsilon}_0^A = \mathbb{A}_{Esh}^A : \boldsymbol{E} \tag{4.5a}$$

$$\mathbb{A}_{Esh}^A = \left(\mathbb{I} + \mathbb{S}_{Esh}^A : (\mathbb{C}^{eff})^{-1} : (\mathbb{C}^A - \mathbb{C}^{eff})\right)^{-1} \tag{4.5b}$$

where $\mathbb{C}^A$ and $\mathbb{C}^{eff}$ are respectively grain A's (the inclusion) and the homogenized aggregate's (the matrix) stiffness tensors, $\mathbb{A}_{Esh}^A$ is the strain-localization tensor, $\mathbb{I}$ is the fourth-order identity tensor, and $\mathbb{S}_{Esh}^A$ is Eshelby's tensor that depends on the matrix properties and on the inclusion's morphology. For a spherical grain immersed in an isotropic aggregate, Eshelby's tensor is expressed as:

$$\mathbb{S}_{Esh}^A = \frac{(1+\nu^{eff})}{3(1-\nu^{eff})}\mathbb{J} + \frac{2(4-5\nu^{eff})}{15(1-\nu^{eff})}\mathbb{K} \tag{4.6}$$

where ν^{eff} is the homogenized aggregate's Poisson's ratio, and $\mathbb{J}$ and $\mathbb{K}$ are the fourth order spherical and deviatoric projection tensors, respectively.

4.2.3 Cellular Automaton

One of the CA characteristics is to define a grain's behavior as a function of its neighboring grains. A CA is generally created through 4 steps, namely:

- Defining the cellular automaton's representation: number of cells and each cell's neighborhood.
- Assigning state variables to each cell.
- Defining local interactions by transition rules: these rules define a given cell behavior that depends on its neighboring cells state variables.
- Defining a local behavior: a transition function defines each cell state variables evolution over a computation step.

For a polycrystalline aggregate submitted to a mechanical loading, a cell could be assimilated to a grain and the state variables could be the grain's stiffness and strain/stress tensors. For an elastic loading, the local behavior would be governed by Hooke's law as:

$$\boldsymbol{\sigma}^c = \mathbb{C}^c : \boldsymbol{\varepsilon}^c \tag{4.7}$$

where $\boldsymbol{\sigma}^c$, $\boldsymbol{\varepsilon}^c$ and $\mathbb{C}^c$ are respectively the cell's mean stress, mean strain and stiffness tensors. Defining the transition rules is, therefore, this paper main object as they define the grains behavior depending on their neighborhood.

Pourian *et al.* (2014) have proposed a CA model to describe an heterogenous titanium polycrystal's elastic behavior submitted to an uni-axial stress loading. In their model, a given grain's mean strain tensor was computed from EIM but where $\mathbb{C}^{eff}$ from equation 4.5b depends on the grain environment. $\mathbb{C}^{eff}$ is considered as isotropic but it relies on the homogenized material Poisson's ratio and a Young's modulus E_y^{av} equal to the average apparent Young's modulus along the loading axis of the 6 closest neighboring grains as:

$$E_y^{av} = \frac{1}{6}\sum_{n=1}^{6} E_y^n \quad \text{with} \quad E_y^n = \left(\mathbb{S}_{3333}^n\right)^{-1} \tag{4.8}$$

where $\vec{e}_3$ was the loading axis, and $\mathbb{S}^n$ the neighboring grain's compliance tensor expressed in the global coordinate system. By this definition, the higher a given grain's neighborhood stiffness in the loading axis gets (meaning the higher E_y^{av} gets), the higher its stress level along the loading axis becomes. The authors have found, that for a given grain orientation, the grain's mean stress values dispersion obtained from numerous different neighborhoods is similar to that predicted from FEM. However, significant discrepancies were observed when the predicted strain tensors obtained from the FEM and CA models were compared for the same configuration. In other words, E_y^{av} cannot be used to compute a given grain's stress tensor for a specific neighborhood. In particular, two identical grains surrounded by different neighborhoods having the same E_y^{av} value, but one with a higher standard deviation among the 6 E_y^n than the other, would present the same mean stress tensor prediction using Pourian's model, which is intuitively inaccurate and has been proved to be by Bretin *et al.* (2019a). This CA model does not account for the influence of the relative cell's positions with respect to its neighborhood and loading axis on the grain's stress tensor, which was found to be significant in detailed FE simulations (Bretin *et al.*, 2019a). These observations urge for a more accurate CA model.

4.2.4 Material properties

Two sets of single crystal elastic constants were considered (Table 4.1): the cubic iron crystal and the hexagonal titanium crystal. These crystals were selected for their high elastic anisotropy and their different crystallographic structures. Their aggregate effective properties were computed from FEM homogenization, following the method described by Bretin *et al.* (2019a).

Table 4.1 Single crystal elastic constants $\mathbb{C}^{cry}$ (Simmons & Wang, 1971) and randomly generated aggregate effective properties obtained from FEM homogenization (Bretin *et al.*, 2019a).

Fe	$\mathbb{C}^{cry}_{1111} = 226 \quad \mathbb{C}^{cry}_{1122} = 140 \quad \mathbb{C}^{cry}_{1212} = 116 \quad \text{(GPa)}$ $E_y^{eff} = 206\text{GPa} \quad \nu^{eff} = 0.297 \quad \Leftrightarrow \quad \mathbb{C}^{eff}_{1111} = 274 \quad \mathbb{C}^{eff}_{1122} = 116 \quad \text{(GPa)}$
Ti	$\mathbb{C}^{cry}_{1111} = 162.4 \quad \mathbb{C}^{cry}_{3333} = 180.7 \quad \mathbb{C}^{cry}_{1122} = 92 \quad \mathbb{C}^{cry}_{1133} = 69 \quad \mathbb{C}^{cry}_{1313} = 46.7 \quad \text{(GPa)}$ $E_y^{eff} = 115\text{GPa} \quad \nu^{eff} = 0.322 \quad \Leftrightarrow \quad \mathbb{C}^{eff}_{1111} = 165 \quad \mathbb{C}^{eff}_{1122} = 78 \quad \text{(GPa)}$

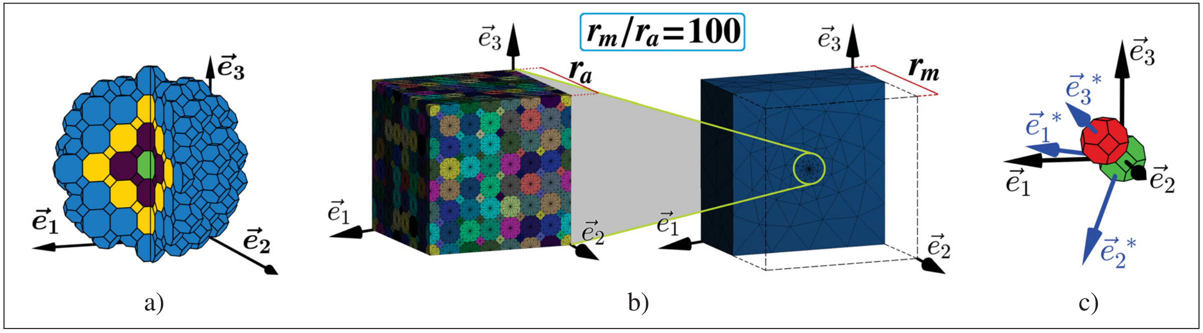

Figure 4.2 (a) Kelvin structured aggregate composed of the central grain B in green and its three neighboring grain layers: the crystallographic properties are assigned only to grain B and the effective properties are assigned to the rest; (b) Kelvin structured aggregate mesh immersed at the center of a large cube mesh; (c) $*$-axis system representation such that $\vec{\boldsymbol{e}}_3{}^*$-axis is aligned with $\overrightarrow{AB}$ (grain A in green and grain B in red) and $\vec{\boldsymbol{e}}_1{}^*$ remains in the plan ($\vec{\boldsymbol{e}}_1$;$\vec{\boldsymbol{e}}_2$).

4.3 Modelization of a grain influence on its surrounding strain field

A FEM study were performed with the purpose to express $\boldsymbol{\Delta\varepsilon}_B^{A^{eff}}$ from Equation 4.4 as a function of the applied loading $\boldsymbol{E}$ and grain B's stiffness tensor $\mathbb{C}^B$. The methodology is that presented in (Bretin *et al.*, 2019a) and is recalled here for completeness. An aggregate mesh was generated as a Kelvin structure (depicted in Fig. 4.2a) with an average of 720 quadratic interpolation tetrahedral elements per grain. The Kelvin structure was chosen to elude the grains size and morphology ratio effects on the grain's mean strain tensors by normalizing all the grains to a truncated octahedron close to a spherical shape. The aggregate mesh was then immersed in a matrix submitted to Kinematic Uniform Boundary Conditions (Fig. 4.2b). The represented volume was demonstrated to be sufficiently large to consider the matrix as infinite and to elude border effects. Crystallographic elastic properties (Iron or Titanium) and a specific orientation were assigned to the central grain B, while the effective aggregate's properties were assigned everywhere else (Table 4.1). Forty randomly generated orientations and the six elementary strain loadings $\boldsymbol{Eij}$ (i.e., $Eij_{ij} = Eij_{ji} = 1$ for a given ij and 0 for all the other components), were studied. The grains' mean strain tensors are extracted for each simulation. The strain variations due to presence of the central grain B, defined as $\boldsymbol{\Delta\varepsilon}_B^{A^{eff}}\left(\boldsymbol{Eij},\mathbb{C}^B\right)$, obtained for a specific $\boldsymbol{Eij}$ and grain's B stiffness tensor expressed in the global coordinate system, was computed from

Equation 4.3b. Using these values, and the FEM model being elastic, and therefore linear, the strain variations that would be observed under any loading E can be obtained as follow:

$$\boldsymbol{E} = \sum_{i=1}^{3}\sum_{j=i}^{3} E_{ij}\boldsymbol{Eij} \quad \Rightarrow \quad \boldsymbol{\Delta\varepsilon}_B^{A^{eff}}\left(\boldsymbol{E},\mathbb{C}^B\right) = \sum_{i=1}^{3}\sum_{j=i}^{3} E_{ij}\boldsymbol{\Delta\varepsilon}_B^{A^{eff}}\left(\boldsymbol{Eij},\mathbb{C}^B\right) \tag{4.9}$$

Figure 4.3 shows $\Delta\varepsilon^{A^{eff}}_{B\ 13}\left(\boldsymbol{E22},\mathbb{C}^B\right)$ forty values as a function of each grain B's stiffness tensor component along side with their linear regression in the case of Titanium for $\overrightarrow{AB} = (0;0;2)$. Every components show a low coefficient of determination R^2, except the component $\mathbb{C}^{B\ *}_{2213}$, which is showing an excellent coefficient. Similar linear regressions were made for each $\Delta\varepsilon^{A^{eff}}_{B\ ij}\left(\boldsymbol{Ekl},\mathbb{C}^B\right)$ components and each loading $\boldsymbol{Ekl}$, leading for $\overrightarrow{AB} = (0;0;2)$ to the following expression:

$$\Delta\varepsilon^{A^{eff}}_{B\ ij}\left(\boldsymbol{Ekl},\mathbb{C}^B\right) = \begin{cases} a^{\overrightarrow{AB}}_{ijkl} + b^{\overrightarrow{AB}}_{ijkl}\mathbb{C}^B_{3-i,3-j,k,l} + c^{\overrightarrow{AB}}_{ijkl}\mathbb{C}^B_{3,3,k,l} & \{i,j\} \in \{1,2\} \\ a^{\overrightarrow{AB}}_{ijkl} + b^{\overrightarrow{AB}}_{ijkl}\mathbb{C}^B_{i,j,k,l} & i \text{ or } j \geq 3 \end{cases} \tag{4.10}$$

For other relative positions, such as $\overrightarrow{AB} = (1;1;1)$, the relations were not as obvious. To get back to a similar case as for $\overrightarrow{AB} = (0;0;2)$, the tensors have been rotated in a new basis such that the new axis $\vec{e}^{\,*}_3$ became aligned with $\overrightarrow{AB}$. By doing so, similarly as in equation 4.10, the following relationships between $\boldsymbol{\Delta\varepsilon}^{A^{eff}}_B$ components, the applied loading $\boldsymbol{Ekl}$, and $\mathbb{C}^B$ components were found for any relative position $\overrightarrow{AB}$ and any material (Iron or Titanium):

$$\Delta\varepsilon^{A^{eff}*}_{B\ ij}\left(\boldsymbol{Lkl},\mathbb{C}^B\right) = \begin{cases} a^{\overrightarrow{AB}}_{ijkl} + b^{\overrightarrow{AB}}_{ijkl}\mathbb{C}^{B\ *}_{3-i,3-j,k,l} + c^{\overrightarrow{AB}}_{ijkl}\mathbb{C}^{B\ *}_{3,3,k,l} & \{i,j\} \in \{1,2\} \\ a^{\overrightarrow{AB}}_{ijkl} + b^{\overrightarrow{AB}}_{ijkl}\mathbb{C}^{B\ *}_{i,j,k,l} & i \text{ or } j \geq 3 \end{cases} \tag{4.11}$$

where the $*$ index refers to the tensors expressed in an orthonormal axis system whose direction 3 is collinear with $\overrightarrow{AB}$ formed by grains A and B centroids; $\boldsymbol{Lij}$ are the elementary strain loadings associated to this axis system (i.e., $Lij^*_{ij} = Lij^*_{ji} = 1$ for a given ij and 0 for all the other components); $a^{\overrightarrow{AB}}_{ijkl}$, $b^{\overrightarrow{AB}}_{ijkl}$ and $c^{\overrightarrow{AB}}_{ijkl}$ are the coefficients obtained from the linear regressions between the tensors $\boldsymbol{\Delta\varepsilon}_{B}^{A^{eff}*}\left(\boldsymbol{Lkl},\mathbb{C}^{B}\right)$ and $\mathbb{C}^{B\,*}$ components. Figure 4.4 exemplifies equation 4.11 for $\overrightarrow{AB}=(1;1;1)$ in the case of the Iron properties.

A more general expression of $\boldsymbol{\Delta\varepsilon}_{B}^{A^{eff}}\left(\boldsymbol{Ekl},\mathbb{C}^{B}\right)$ in the global axis system can be obtained from Equations 4.11 and 4.9, in order to avoid a change of basis for each relative position, which would make calculations heavier in the perspective of developing a analytical model, as follow:

$$\Delta\varepsilon_{B\ ij}^{A^{eff}}\left(\boldsymbol{Ekl},\mathbb{C}^{B}\right)=\mathbb{U}_{ijklmnop}^{\overrightarrow{AB}}\mathbb{C}_{mnop}^{B}+\mathbb{V}_{ijkl}^{\overrightarrow{AB}} \tag{4.12}$$

where $\mathbb{U}^{\overrightarrow{AB}}$ and $\mathbb{V}^{\overrightarrow{AB}}$ are respectively a eighth and fourth order tensors that depend on $\overrightarrow{AB}$ and whose components are expressed as a function of $a_{ijkl}^{\overrightarrow{AB}}$, $b_{ijkl}^{\overrightarrow{AB}}$ and $c_{ijkl}^{\overrightarrow{AB}}$ and the components of the transformation matrix between the global axis system and the $*$-axis system (see Appendix 4.a). When $\mathbb{C}^{B}=\mathbb{C}^{eff}$, the whole mesh is homogeneous, therefore:

$$\Delta\varepsilon_{B\ ij}^{A^{eff}}\left(\boldsymbol{Ekl},\mathbb{C}^{eff}\right)=0 \tag{4.13a}$$

$$\Rightarrow\quad \mathbb{V}_{ijkl}^{\overrightarrow{AB}}=-\mathbb{U}_{ijklmnop}^{\overrightarrow{AB}}\mathbb{C}_{mnop}^{eff} \tag{4.13b}$$

$$\Rightarrow\quad \Delta\varepsilon_{B\ ij}^{A^{eff}}\left(\boldsymbol{Ekl},\mathbb{C}^{B}\right)=\mathbb{U}_{ijklmnop}^{\overrightarrow{AB}}\left(\mathbb{C}_{mnop}^{B}-\mathbb{C}_{mnop}^{eff}\right) \tag{4.13c}$$

Finally, by combining equations 4.9 and 4.13c, $\boldsymbol{\Delta\varepsilon}_{B}^{A^{eff}}\left(\boldsymbol{E},\mathbb{C}^{B}\right)$ is expressed as:

$$\boldsymbol{\Delta\varepsilon}_{B}^{A^{eff}}\left(\boldsymbol{E},\mathbb{C}^{B}\right)=\mathbb{A}^{\overrightarrow{AB}}\left(\mathbb{C}^{B}\right):\boldsymbol{E} \tag{4.14a}$$

$$\text{with}\quad \mathbb{A}_{ijkl}^{\overrightarrow{AB}}\left(\mathbb{C}^{B}\right)=\begin{cases}\Delta\varepsilon_{B\ ij}^{A^{eff}}\left(\boldsymbol{Ekl},\mathbb{C}^{B}\right)=\mathbb{U}_{ijklmnop}^{\overrightarrow{AB}}\left(\mathbb{C}_{mnop}^{B}-\mathbb{C}_{mnop}^{eff}\right) & \text{if}\quad k=l\\ \dfrac{1}{2}\Delta\varepsilon_{B\ ij}^{A^{eff}}\left(\boldsymbol{Ekl},\mathbb{C}^{B}\right)=\dfrac{1}{2}\mathbb{U}_{ijklmnop}^{\overrightarrow{AB}}\left(\mathbb{C}_{mnop}^{B}-\mathbb{C}_{mnop}^{eff}\right) & \text{else}\end{cases} \tag{4.14b}$$

where $\mathbb{A}^{\overrightarrow{AB}}\left(\mathbb{C}^{B}\right)$ is a fourth order tensor that depends on $\overrightarrow{AB}$ and grain B's stiffness tensor.

Once identified for each relative position (see the Section 4.4.1 below for the specific methodology), $\mathbb{U}^{\overrightarrow{AB}}$ can be used to compute a grain A^{eff}'s strain variation due to the presence of grain B, for any grain B's crystallographic orientation, and any applied loading $\boldsymbol{E}$.

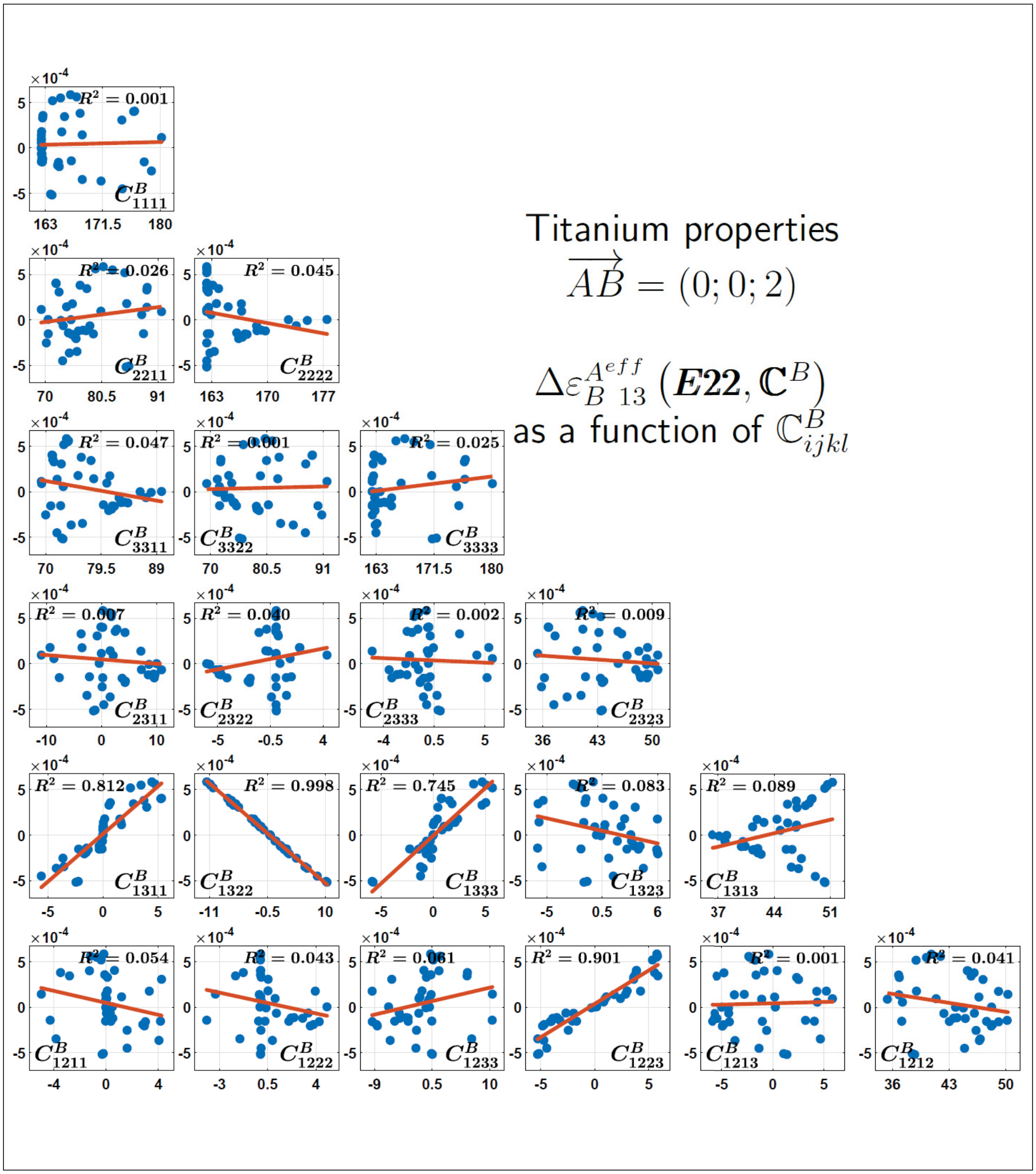

Figure 4.3 Linear regressions between $\Delta\varepsilon^{A^{eff}}_{B\ 13}\left(\boldsymbol{E22}, \mathbb{C}^B\right)$ and grain B's stiffness tensor $\mathbb{C}^B$ components (GPa) with their coefficients of determination R^2 for the relative position $\overrightarrow{AB} = (0;0;2)$ in the case of the Titanium. The component $\mathbb{C}^{B\ *}_{1322}$ shows an excellent coefficients of determination R^2 in comparison with the other components.

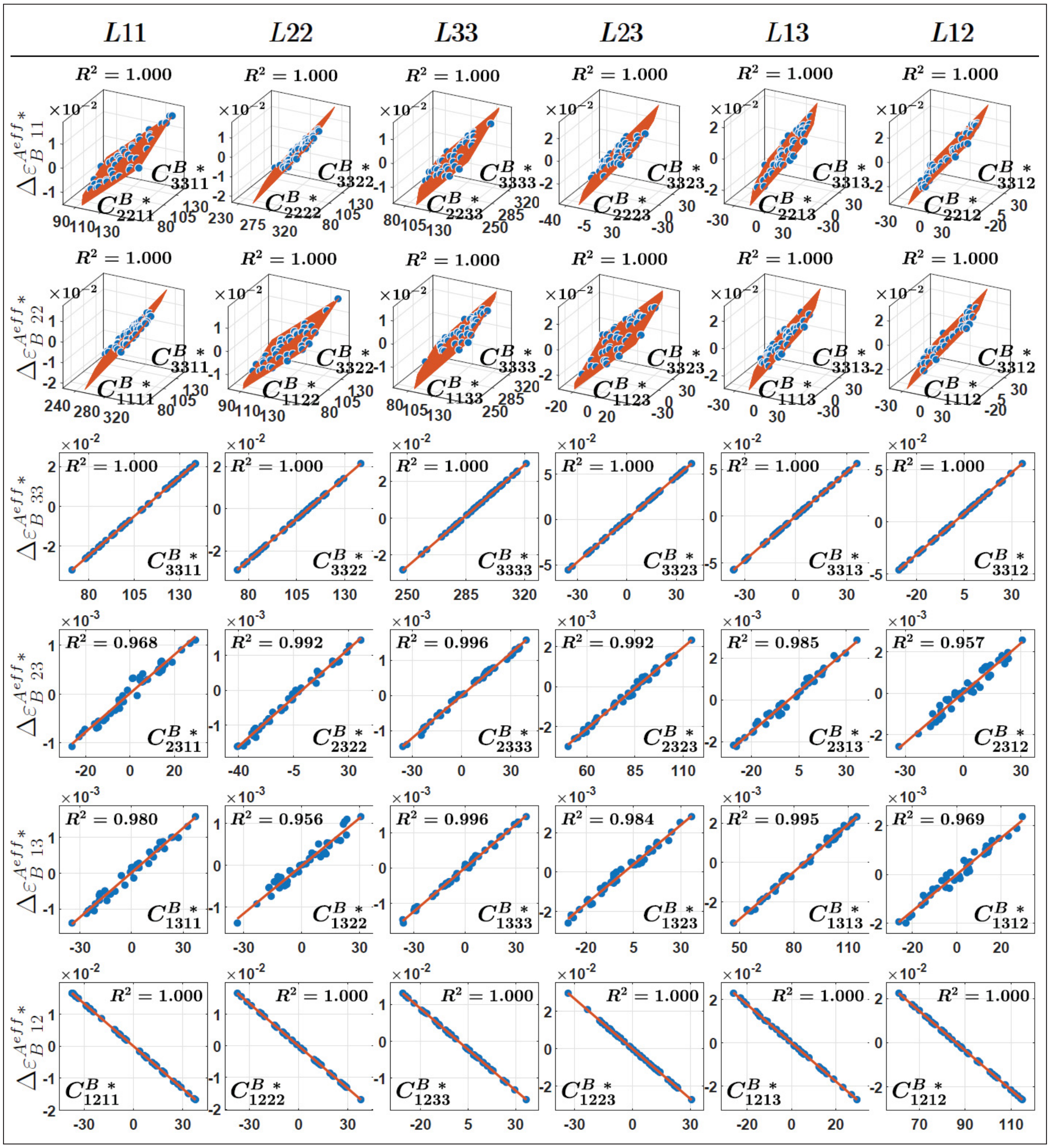

Figure 4.4 Linear regressions between $\boldsymbol{\Delta\varepsilon}_B^{A^{eff}*}$ and grain B's stiffness tensor $\mathbb{C}^{B\,*}$ components (GPa) with their coefficients of determination R^2 for each local elementary loading $\boldsymbol{Lij}$, for the relative position $\overrightarrow{AB} = (1;1;1)$ in the case of the Iron. The $*$ index refers to the tensors expressed in the $*$-coordinate system in which direction 3 is aligned with $\overrightarrow{AB}$ and direction 1 remains in the plan $(\vec{e}_1;\vec{e}_2)$.

4.4 New CA development

The idea behind the CA model is to simulate many different polycrystal crystallographic distributions, submitted to various strain loading, using a limited amount of CPU time when compared to FEM simulations, to easily identify the worst stress concentration scenario. A cellular automaton model that properly considers the polycrystal local heterogeneities was developed, based on the neighborhood effect approximations presented in Section 4.2.1, Eshelby's theory described in Section 4.2.2 and $\boldsymbol{\Delta\varepsilon}^{A^{eff}}_{B}\left(\boldsymbol{E},\mathbb{C}^{B}\right)$ modelization proposed above in Section 4.3. The model is presented in two parts: the methodology to identify the tensors $\mathbb{U}^{\overrightarrow{AB}}$ required to predict the neighborhood effect followed by the CA model algorithm.

4.4.1 Tensors $\mathbb{U}^{\overrightarrow{AB}}$ identification method

The most intuitive method to identify the tensors $\mathbb{U}^{\overrightarrow{AB}}$ would be to express this tensor, using equations 4.11 and 4.13c, as a function of the transformation matrix between the global and the $*$ coordinates, and the 84 regression coefficients ($a^{\overrightarrow{AB}}_{ijkl}$,$b^{\overrightarrow{AB}}_{ijkl}$,$c^{\overrightarrow{AB}}_{ijkl}$) obtained through FEM simulations. This method (see Appendix 4.a) requires lengthy computations and we propose an alternative algorithm.

The proposed method consists of multiple linear regressions, expressed from equation 4.13c as:

$$\begin{bmatrix} \Delta\varepsilon^{A^{eff}}_{B\,ij}\left(\boldsymbol{Ekl},\mathbb{C}^{B}(Ori_1)\right) \\ \vdots \\ \Delta\varepsilon^{A^{eff}}_{B\,ij}\left(\boldsymbol{Ekl},\mathbb{C}^{B}(Ori_n)\right) \end{bmatrix} = \dots$$

$$\dots = \begin{bmatrix} d\mathbb{C}^{B}_{m_1n_1o_1p_1}(Ori_1) & \dots & d\mathbb{C}^{B}_{m_{21}n_{21}o_{21}p_{21}}(Ori_1) \\ \vdots & & \vdots \\ d\mathbb{C}^{B}_{m_1n_1o_1p_1}(Ori_n) & \dots & d\mathbb{C}^{B}_{m_{21}n_{21}o_{21}p_{21}}(Ori_n) \end{bmatrix} \times \begin{bmatrix} \mathbb{U}^{\overrightarrow{AB}}_{ijklm_1n_1o_1p_1} \\ \vdots \\ \mathbb{U}^{\overrightarrow{AB}}_{ijklm_{21}n_{21}o_{21}p_{21}} \end{bmatrix} \qquad (4.15)$$

where $\mathbf{dC}^B(Ori_n) = \mathbb{C}^B(Ori_n) - \mathbb{C}^{eff}$ and $m_x n_x o_x p_x$ are its 21 independent components. Every $\mathbb{U}^{\overrightarrow{AB}}$ component is initially set to 0. Thanks to tensors symmetries:

$$\Delta\varepsilon^{A^{eff}}_{B\ ij}\left(\boldsymbol{Ekl},\mathbb{C}^B\right) = \Delta\varepsilon^{A^{eff}}_{B\ ji}\left(\boldsymbol{Ekl},\mathbb{C}^B\right) = \Delta\varepsilon^{A^{eff}}_{B\ ij}\left(\boldsymbol{Elk},\mathbb{C}^B\right) = \Delta\varepsilon^{A^{eff}}_{B\ ji}\left(\boldsymbol{Elk},\mathbb{C}^B\right) \tag{4.16a}$$

$$\Rightarrow \quad \mathbb{U}^{\overrightarrow{AB}}_{ijklmnop} = \mathbb{U}^{\overrightarrow{AB}}_{jiklmnop} = \mathbb{U}^{\overrightarrow{AB}}_{ijlkmnop} = \mathbb{U}^{\overrightarrow{AB}}_{jilkmnop} \tag{4.16b}$$

there is one system of 21 unknown variables to optimize for each $ijkl$ value ($6\times6 = 36$ systems), making a total of $36 \times 21 = 756$ unknowns.

Section 4.3's FEM results (40 different orientations for each elementary loading) were used in the first place to generate the 36 systems of 40 linear equations and optimize the 36×21 $\mathbb{U}^{\overrightarrow{AB}}$ unknown components. The differences between $\Delta\varepsilon^{A^{eff}}_{B\ ij}\left(\boldsymbol{Ekl},\mathbb{C}^B(Ori_i)\right)$ FEM values and their estimates using the obtained tensors $\mathbb{U}^{\overrightarrow{AB}}$ are in average 2 orders lower than $\Delta\varepsilon^{A^{eff}}_{B\ ij}\left(\boldsymbol{Ekl},\mathbb{C}^B(Ori_i)\right)$ average value, revealing the model accuracy. An example of these differences, in the case of the iron properties, for $\overrightarrow{AB} = (1;1;1)$, is presented in Appendix 4.b.

These $\mathbb{U}^{\overrightarrow{AB}}$ components were identified using 40 FEM simulations, which would take a significant amount of time to reproduce. Therefore, different orientation set out of the 40 random orientations were tested to reduce the number of required FEM simulations for $\mathbb{U}^{\overrightarrow{AB}}$ components optimization. A set of 8 orientations (see Table 4.2) was found to be the set with the lowest number of orientations showing an accuracy of the same order as when using the 40 orientations. Even though the system of linear equations 4.15 is underdetermined (21 unknown) with this limited number of orientations (8 equations), the $\Delta\varepsilon^{A^{eff}}_{B\ ij}\left(\boldsymbol{Ekl},\mathbb{C}^B(Ori_i)\right)$ estimates using the tensors $\mathbb{U}^{\overrightarrow{AB}}$ obtained with this 8-orientation set show an accuracy of the same order as when using the 40-orientation set for the identification process (see Appendix 4.b for comparison). This result could be explained by the existence of non-obvious relations between $\mathbb{U}^{\overrightarrow{AB}}$ and $\mathbb{C}^B$ components, and that all 21 $\mathbb{C}^B_{mnop}$ independent components do not necessarily play a role in $\Delta\varepsilon^{A^{eff}}_{B\ ij}\left(\boldsymbol{Ekl},\mathbb{C}^B\right)$ definition, but only a few of them, which would reduce the unknowns number. Nonetheless, the selection of an optimal orientation set (out of all the possible orientations) with fewer orientations and the same order of accuracy is still open to discussion.

Table 4.2 Orientation set used to identify the $\mathbb{U}^{\overrightarrow{AB}}$ for the case of a cubic crystallographic structure. The orientations are defined using the Euler angles according to Bunge's convention.

$\#Ori$	1	2	3	4	5	6	7	8
φ_1	-42.08	-103.90	-23.13	81.67	-17.14	57.83	84.74	51.00
ϕ	67.07	139.64	51.06	148.03	67.76	116.30	69.06	57.92
φ_2	6.24	74.92	-27.80	-59.49	-18.47	-88.42	90.31	83.55

The Kelvin structure's symmetries were also used to reduce the number of required FEM simulation to optimize $\mathbb{U}^{\overrightarrow{AB}}$. One value of $\Delta\varepsilon^{A^{eff}}_{B\;ij}\left(\boldsymbol{Ekl},\mathbb{C}^{B}\right)$ can be used in more than one linear system by performing one of the following permutations to the global axis system:

$$\begin{aligned} &\text{Permutation 1: } \vec{\boldsymbol{e}}_1 \rightarrow \vec{\boldsymbol{e}}_2^{\,*}, \quad \vec{\boldsymbol{e}}_2 \rightarrow \vec{\boldsymbol{e}}_3^{\,*}, \quad \vec{\boldsymbol{e}}_3 \rightarrow \vec{\boldsymbol{e}}_1^{\,*} \\ &\text{Permutation 2: } \vec{\boldsymbol{e}}_1 \rightarrow \vec{\boldsymbol{e}}_3^{\,*}, \quad \vec{\boldsymbol{e}}_2 \rightarrow \vec{\boldsymbol{e}}_1^{\,*}, \quad \vec{\boldsymbol{e}}_3 \rightarrow \vec{\boldsymbol{e}}_2^{\,*} \end{aligned} \tag{4.17}$$

For example, if the applied loading is $\boldsymbol{E}\mathbf{11}$ (or $\boldsymbol{E}\mathbf{12}$) and $\overrightarrow{AB} = (x, y, z)$, the following equivalences are obtained:

$$\begin{cases} \Delta\varepsilon^{A^{eff}}_{B\;ij}\left(\boldsymbol{E}\mathbf{11},\mathbb{C}^{B}\right) \Leftrightarrow \Delta\varepsilon^{A^{eff}}_{B_1\;ij}\left(\boldsymbol{E}\mathbf{22},\mathbb{C}^{B_1}\right) \Leftrightarrow \Delta\varepsilon^{A^{eff}}_{B_2\;ij}\left(\boldsymbol{E}\mathbf{33},\mathbb{C}^{B_2}\right) \\ \Delta\varepsilon^{A^{eff}}_{B\;ij}\left(\boldsymbol{E}\mathbf{12},\mathbb{C}^{B}\right) \Leftrightarrow \Delta\varepsilon^{A^{eff}}_{B_1\;ij}\left(\boldsymbol{E}\mathbf{23},\mathbb{C}^{B_1}\right) \Leftrightarrow \Delta\varepsilon^{A^{eff}}_{B_2\;ij}\left(\boldsymbol{E}\mathbf{31},\mathbb{C}^{B_2}\right) \end{cases} \tag{4.18}$$

where $\overrightarrow{AB}_1 = (y, z, x)$, $\overrightarrow{AB}_2 = (z, x, y)$, and $\mathbb{C}^{B_1}$, $\mathbb{C}^{B_2}$ denote grain B's stiffness tensors in the new coordinate system after the permutation 1 or 2. Thanks to the Kelvin structure symmetries, each relative position has its counterpart after each permutation. Therefore, by performing FEM simulations only for the applied loadings $\boldsymbol{E}\mathbf{11}$ and $\boldsymbol{E}\mathbf{12}$, a set of values $\Delta\varepsilon^{A^{eff}}_{B\;ij}\left(\boldsymbol{Ekl},\mathbb{C}^{B}(Ori_i)\right)$ can be obtained for each elementary loading $\boldsymbol{Ekl}$ and each relative positions $\overrightarrow{AB}$.

To conclude on the methodology used to optimize the tensors $\mathbb{U}^{\overrightarrow{AB}}$, 8×2 FEM simulations of a grain immersed in an infinite homogeneous matrix have to be performed (8-orientation set and the 2 loadings $\boldsymbol{E}\mathbf{11}$ and $\boldsymbol{E}\mathbf{12}$). The values $\Delta\varepsilon^{A^{eff}}_{B\;ij}\left(\boldsymbol{Ekl},\mathbb{C}^{B}(Ori_i)\right)$ are computed from each simulation for each Kelvin structured aggregate grain. Using the Kelvin structures symmetries

(Equations 4.18), these values are then used to build the linear equation systems 4.15, which, after a multiple linear regression, provides $\mathbf{U}^{\overrightarrow{AB}}$ components.

4.4.2 CA model

The CA is built as a Kelvin structure where each Kelvin cell represents an equiaxed grain of the polycrystal. An elasticity tensor (Table 4.1) and a crystal orientation is attributed to each cell. The orientations can be randomly distributed using the quaternion method Altmann (2005); Shoemake (1992) or with an EBSD map. CA's periodicity is preserved through neighborhood definitions: a cell localized at the edge will have it's neighborhood defined with the cells of the opposite side(s). For example, in the case of a squared 686 cells Kelvin structure, if cell c is located at $(0;0;0)$ (1 being equal to a grain's radius), its neighboring cell n_1 such as $\overrightarrow{cn}_1 = (0;0;-2)$ would be located at $(0;0;12)$, and its neighboring cell n_2 such as $\overrightarrow{cn}_2 = (-1;-1;-1)$ would be located at $(13;13;13)$ (see illustration in Fig. 4.5 where c is green, n_1 blue and n_2 red).

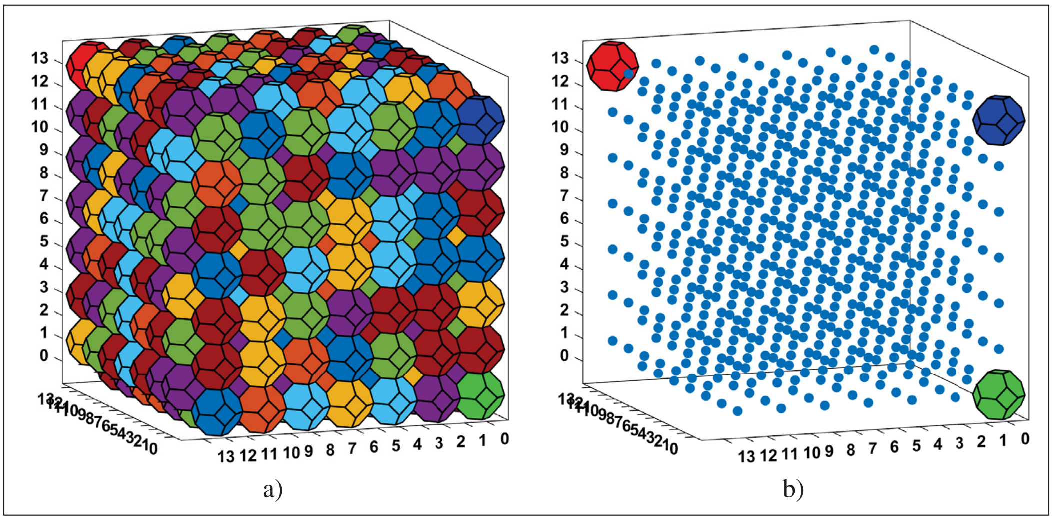

a) b)

Figure 4.5 (a) 686 cells periodic Kelvin structure; (b) Periodicity illustration: blue dots represent each cell centroid; the green, blue and red Kelvin cells are respectively the grains c, n_1 and n_2 such as, considering the periodicity, $\overrightarrow{cn}_1 = (0;0;-2)$ and $\overrightarrow{cn}_2 = (-1;-1;-1)$.

The CA's transition rule is based on the neighborhood effect approximations proposed in Bretin *et al.* (2019a) and recalled in Section 4.2.1. These approximations were justified in the first part of this work for the applied loading $\boldsymbol{E}33$, but for the development of the CA, these approximations are assumed to remain as accurate for any loading $\boldsymbol{E}$. This assumption can easily be justified: due to the model symmetries, if these approximations are true for the loading $\boldsymbol{E}33$ they are also true for the loadings $\boldsymbol{E}11$ and $\boldsymbol{E}22$. Then, for any loadings $\boldsymbol{E}$ it exists a basis in which $\boldsymbol{E}$ can be diagonalized. Thus, using the problem linearity, these approximations can be assumed to remain as accurate for any loading $\boldsymbol{E}$. Therefore, $\boldsymbol{\varepsilon}_n^c$, a cell c strain tensor under the influence of a neighborhood n constituted of cells n_i, can be obtained using Equation 4.4 (Fig. 4.1). The tensor is decomposed in two parts: the part depending on cell c's properties ($\boldsymbol{\varepsilon}_0^c$), and the part depending on neighborhood n's properties ($\sum_{n_i} \boldsymbol{\Delta\varepsilon}_{n_i}^{c^{eff}}$). $\boldsymbol{\varepsilon}_0^c$ is computed using Equations 4.5 and 4.6, assuming that a Kelvin cell is spherical, and $\boldsymbol{\Delta\varepsilon}_{n_i}^{c^{eff}}$ is computed with the model proposed in Section 4.3 and the identified $\mathbb{U}^{\overrightarrow{cn}}$ as:

$$\boldsymbol{\Delta\varepsilon}_{n_i}^{c^{eff}} = \mathbb{A}^{\overrightarrow{cn_i}} : \boldsymbol{E} \tag{4.19a}$$

$$\text{with} \quad \mathbb{A}^{\overrightarrow{cn_i}}_{ijkl} = \begin{cases} \mathbb{U}^{\overrightarrow{cn_i}}_{ijklmnop}\left(\mathbb{C}^{n_i}_{mnop} - \mathbb{C}^{eff}_{mnop}\right) & \text{if} \quad k = l \\ \frac{1}{2}\mathbb{U}^{\overrightarrow{cn_i}}_{ijklmnop}\left(\mathbb{C}^{n_i}_{mnop} - \mathbb{C}^{eff}_{mnop}\right) & \text{else} \end{cases} \tag{4.19b}$$

Therefore, a CA localization tensor $\mathbb{A}_{CA}^{A}$ is defined as:

$$\boldsymbol{\varepsilon}_n^c = \mathbb{A}_{CA}^c : \boldsymbol{E} \tag{4.20a}$$

$$\text{with} \quad \mathbb{A}_{CA}^c = \mathbb{A}_{Esh}^c + \sum_{n_i} \mathbb{A}^{\overrightarrow{cn_i}} \tag{4.20b}$$

Finally, homogenization theory requires that $\left\langle \mathbb{A}_{CA}^c \right\rangle_c = \mathbb{I}$, where the $\langle \cdot \rangle_c$ denotes an average over all the cells, which would implies $\langle \boldsymbol{\varepsilon}^c \rangle_c = \boldsymbol{E}$. Then, if $\boldsymbol{\varepsilon}^c$ is defined as:

$$\boldsymbol{\varepsilon}^c = \left\langle \mathbb{A}_{CA}^c \right\rangle_c^{-1} : \mathbb{A}_{CA}^c : \boldsymbol{E} \tag{4.21}$$

the homogenization requirement is satisfied:

$$\langle \boldsymbol{\varepsilon}^c \rangle_c = \left\langle \left\langle \mathbb{A}^c_{CA} \right\rangle_c^{-1} : \mathbb{A}^c_{CA} : \boldsymbol{E} \right\rangle_c = \left\langle \mathbb{A}^c_{CA} \right\rangle_c^{-1} : \left\langle \mathbb{A}^c_{CA} \right\rangle_c : \boldsymbol{E} = \boldsymbol{E} \tag{4.22}$$

Various neighborhood definitions were considered:

- CA_0: “Zero” neighboring grain. The grain is considered to be immersed in a homogeneous matrix with the aggregate’s effective properties (equivalent to the EIM scheme: $\boldsymbol{\varepsilon}^c_n = \boldsymbol{\varepsilon}^c_0$);
- CA_{14}: Only one neighboring grains layer is considered. These 14 grains correspond to all neighboring grains having a distance from the central grain $||\overrightarrow{AB}|| \leq 2$ (1 being equal to a grain’s radius);
- CA_{64}: The first two neighboring grains layers (64 grains): $||\overrightarrow{AB}|| \leq 4$.
- CA_{258}: The first three neighboring grains layers (258 grains): $||\overrightarrow{AB}|| \leq 6$.

The $\mathbb{U}^{\overrightarrow{AB}}$ are limited up to the third neighboring grains layer due to the aggregate’s mesh size used during the identification process (Fig. 4.2b). As shown in Bretin *et al.* (2019a) and later in the paper, the influence of a grain located at a distance greater than 3 layers can be neglected.

The full algorithm used for the cellular automaton is presented in Appendix 4.c.

4.5 FEM and CA local field predictions comparison

CA model local stress fields predictions were compared against full FEM simulations. Two types of crystallographic structures were investigated: iron’s cubic structure and titanium’s hexagonal structure (Table 4.1).

The FEM simulations were performed according to the parameters described by Bretin *et al.* (2019a): the aggregate is meshed as a 686 cells Kelvin structure with an average of 720 tetrahedral elements per grain with quadratic interpolation using periodic boundary condition (Wu *et al.*, 2014). Twenty 686 orientation sets were generated using the quaternions method (Altmann, 2005; Shoemake, 1992), making a total of 13720 grain-neighborhood configurations.

Three different strain loadings were studied:

$$\begin{aligned}
\boldsymbol{E}_{strain} = \begin{bmatrix} 0 & 0 & 0 \\ 0 & 0 & 0 \\ 0 & 0 & 1 \end{bmatrix} \times 10^{-3} \qquad \boldsymbol{E}_{shear} = \begin{bmatrix} 0 & 1 & 0 \\ 1 & 0 & 0 \\ 0 & 0 & 0 \end{bmatrix} \times 10^{-3} \\
\boldsymbol{E}_{stress\ Fe} = \begin{bmatrix} -0.396 & 0 & 0 \\ 0 & -0.396 & 0 \\ 0 & 0 & 1.334 \end{bmatrix} \times 10^{-3} \\
\boldsymbol{E}_{stress\ Ti} = \begin{bmatrix} -0.463 & 0 & 0 \\ 0 & -0.463 & 0 \\ 0 & 0 & 1.439 \end{bmatrix} \times 10^{-3}
\end{aligned} \tag{4.23}$$

$\boldsymbol{E}_{stress}$ was chosen so that the resulting effective stress tensor components ($\boldsymbol{\Sigma}^{eff}_{stress} = \mathbb{C}^{eff} : \boldsymbol{E}_{stress}$) are all equal to zero, except the "33" component which yields the same values as that of $\boldsymbol{\Sigma}^{eff}_{strain}$:

$$\Sigma^{eff}_{stress\ 33} = \Sigma^{eff}_{strain\ 33} = \begin{cases} 274.3MPa & \text{in case of the Iron} \\ 165.1MPa & \text{in case of the titanium} \end{cases} \tag{4.24}$$

For each material, $\mathbb{U}^{\overrightarrow{AB}}$ were identified using the method described in Section 4.4.1 using the crystal and effective properties presented in Table 4.1, for each material.

Two variables were chosen to compare the models: the von Mises equivalent stress σ^c_{eq} and the resolved shear stress τ^c_s (RSS) in each grain. A grain RSS on a slip system s is computed by means of the orientation tensor $\boldsymbol{m}^c_s$:

$$\tau^c_s = \boldsymbol{\sigma}^c : \boldsymbol{m}^c_s \tag{4.25a}$$

$$\text{with} \quad \boldsymbol{m}^c_s = \frac{1}{2}\left(\vec{\boldsymbol{l}}^c_s \otimes \vec{\boldsymbol{n}}^c_s + \vec{\boldsymbol{n}}^c_s \otimes \vec{\boldsymbol{l}}^c_s\right) \tag{4.25b}$$

where $\vec{\boldsymbol{n}}^c_s$ is the normal to the slip plane and $\vec{\boldsymbol{l}}^c_s$ is the slip direction. The 12 octahedral slip systems were considered for the iron face centered cubic crystal ($\{111\}$ slip planes and $< \bar{1}10 >$

directions). The 3 prismatic slip systems ($\left\{10\bar{1}0\right\}$ slip planes and $< 11\bar{2}0 >$ directions) and the 3 basal slip systems ($\{0001\}$ slip planes and $< 11\bar{2}0 >$ directions) were chosen for the titanium hexagonal crystal as they are the most activated slip systems at room temperature in Ti-alloys Sackett, Germain & Bache (2007). The RSS is an important parameter, as it reflects the susceptibility for a grain to plastify: the higher $|\tau_s^c|$ is, the higher the chance for the grain slip system s to activate. As the present paper does not deal with the actual onset of plasticity, the calculated RSSs intensity on the various slip systems will be compared on a relative base without any reference to some critical RSSs.

4.5.1 Case of the cubic iron crystal

Each grain equivalent von Mises stress σ_{eq}^c predictions obtained with FEM, EIM (equivalent to CA$_0$) and CA$_{258}$ (3 neighboring grains layers considered) models under loading $\boldsymbol{E}_{strain}$ are shown Fig. 4.6a as a function of $\mathbb{C}^c_{3333}$. The component "3333" was chosen because it better differentiates the grains heterogeneous response obtained with EIM in the case of an uniaxial loading along $\vec{\boldsymbol{e}}_3$-axis, as it can be observed in Fig. 4.6a. As noted in Bretin *et al.* (2019a), EIM values represent the average values for a given grain orientation, explaining the straight curve observed in Fig. 4.6a, while FEM values are spread around EIM values. This difference is due to the neighborhood effect: by adding it to the EIM, the CA model shows a marked improvement in its predictive capabilities. Both FEM and CA$_{258}$ models show similar stress dispersions.

Fig. 4.6b presents the differences between FEM and CA predictions for σ_{eq}^c as a function of FEM ones for each one of the four neighborhood definitions (CA$_0$, CA$_{14}$, CA$_{64}$, and CA$_{258}$). The more neighboring grains are considered in the CA model, the closer the dots are to 0, which means that the CA is reproducing more adequately the FEM results. More importantly, $\sigma^c_{eq\ FEM}$ highest predicted values are significantly improved: the five highest $\sigma^c_{eq\ FEM}$ values are under-evaluated by the CA$_0$ model by at least 25 MPa (~12% of their values) whereas these differences are reduced to less than 5 MPa (~2% of their values) with the CA$_{258}$ model. The histograms of the two models' differences along with their fitting normal density functions in the case of loading $\boldsymbol{E}_{strain}$ are shown in Fig. 4.6c. Table 4.3 lists the statistics of the difference between the two models predictions (mean, standard deviation and extreme values) for each applied strains ($\boldsymbol{E}_{strain}$, $\boldsymbol{E}_{shear}$ and $\boldsymbol{E}_{stress}$). These values can be used to define the normal distribution followed by ($\sigma^c_{eq\ FEM} - \sigma^c_{eq\ CA}$) as shown in Fig. 4.6c and also followed by ($\tau^c_{s\ FEM} - \tau^c_{s\ CA}$). These statistics confirm the observations made in Fig. 4.6b: the more neighboring grains are considered, the closer the CA predictions are to the FEM ones. Whatever the criteria observed (standard deviation or extreme differences), a significant improvement between the EIM and CA models is observed: the difference with the FEM predictions is divided by 3 from CA_0 to CA$_{258}$.

Fig. 4.6d presents the differences between FEM and CA predictions (CA$_0$ in blue and CA$_{258}$ in green) for $\tau^c_{s^c_M}$ as a function of FEM ones, where s^c_M corresponds to the grain slip system showing the highest absolute $\tau^c_{s\ FEM}$ value among the 12 slip systems considered. As for the von Mises equivalent stress, the difference between the two models gets closer to 0 when the neighborhood effect is accounted for. This improvement is even more notable for the grains with a high $|\tau^c_{s^c_M\ FEM}|$ value, which are the grains most likely to plastify first and therefore are important to predict with accuracy in the context of fatigue life prediction. The two grains with the highest $|\tau^c_{s^c_M\ FEM}|$ values (framed in red) are perfectly predicted by the CA model.

The differences statistics between τ^c_s CA and FEM predictions in each slip system, in every grain, listed in Table 4.3, show the same improvement as observed in Fig. 4.6: the difference between the two models predictions is in average divided by 3 when 258 neighboring grains are considered, for any applied loading. This ratio gets even more important if only the grains showing the 500 highest $|\tau^c_{s\ FEM}|$ values out of the $12 \times 20 \times 686$ values are considered. For example, when $\boldsymbol{E}_{strain}$ is applied, these 500 grains are such that $|\tau^c_{s\ FEM}|$ >76 MPa. The differences $|\tau^c_{s\ FEM} - \tau^c_{s\ CA_0}|$ are for these 500 grains on average 9.2 MPa (11.7% of $\tau^c_{s\ FEM}$), with a peak at 20.5 MPa (26.8% of $\tau^c_{s\ FEM}$), against 3.7 MPa when all values are considered. In contrast, the differences $|\tau^c_{s\ FEM} - \tau^c_{s\ CA_{258}}|$ are for these 500 grains on average 1.2 MPa (1.5% of $\tau^c_{s\ FEM}$), with a peak at 5.2 MPa (6.2% of $\tau^c_{s\ FEM}$), but also 1.2 MPa when all values are considered. These percentages remain the same for the two other loadings. This shows that the neighborhood effect can be captured with accuracy by the CA approach, allowing to capture with the same accuracy low and high $|\tau_s^c|$ values. This is a significant improvement that allows to identify the grain that will plastify first.

Table 4.3 Iron crystal: FEM and CA prediction differences for the equivalent von Mises stress $\sigma^c_{eq\ FEM}$ and the resolved shear stress $\tau^c_{s\ FEM}$ on each slip system over the 20×686 grains-neighborhood configurations.

Applied loading		$\boldsymbol{E}_{strain}$				$\boldsymbol{E}_{shear}$				$\boldsymbol{E}_{stress\ Fe}$			
$\sigma^c_{eq\ FEM}$ (MPa)	Mean	163.2				287.2				282.3			
	Std	21.9				41.2				37.9			
	Max	217.4				384.7				376.1			
	Min	98.6				167.3				170.5			
Number of neighboring grains		0	14	64	258	0	14	64	258	0	14	64	258
$\sigma^c_{eq\ FEM} - \sigma^c_{eq\ CA}$ (MPa)	Mean	1.4	0.1	-0.3	-0.3	2.7	0.4	-0.1	-0.2	2.3	-0.2	-0.7	-1.0
	Std	9.8	6.2	4.2	3.2	17.0	11.0	7.6	5.8	16.9	10.8	7.4	5.6
	Max	35.8	22.2	14.9	11.5	65.4	43.4	30.7	22.9	61.9	39.4	28.6	20.4
	Min	-38.0	-23.5	-16.7	-14.4	-63.0	-36.3	-25.9	-21.2	-65.7	-42.1	-31.6	-24.5
$\lvert\tau^c_{s\ FEM}\rvert$ (MPa)	Mean	30.3				52.8				52.5			
	Std	21.0				36.5				36.3			
	Max	86.8				150.6				150.2			
	Min	0.0				0.0				0.0			
Number of neighboring grains		0	14	64	258	0	14	64	258	0	14	64	258
$\tau^c_{s\ FEM} - \tau^c_{s\ CA}$ (MPa)	Mean	0.0	0.0	0.0	0.0	0.0	0.0	0.0	0.0	0.0	0.0	0.0	0.0
	Std	4.6	2.9	2.0	1.5	8.2	5.3	3.8	2.9	8.0	5.2	3.5	2.7
	Max	20.5	13.3	8.9	6.1	37.8	23.1	15.7	12.5	35.4	22.4	15.1	11.5
	Min	-19.8	-13.1	-7.9	-6.2	-36.3	-24.0	-16.2	-12.8	-34.3	-24.1	-13.9	-11.2

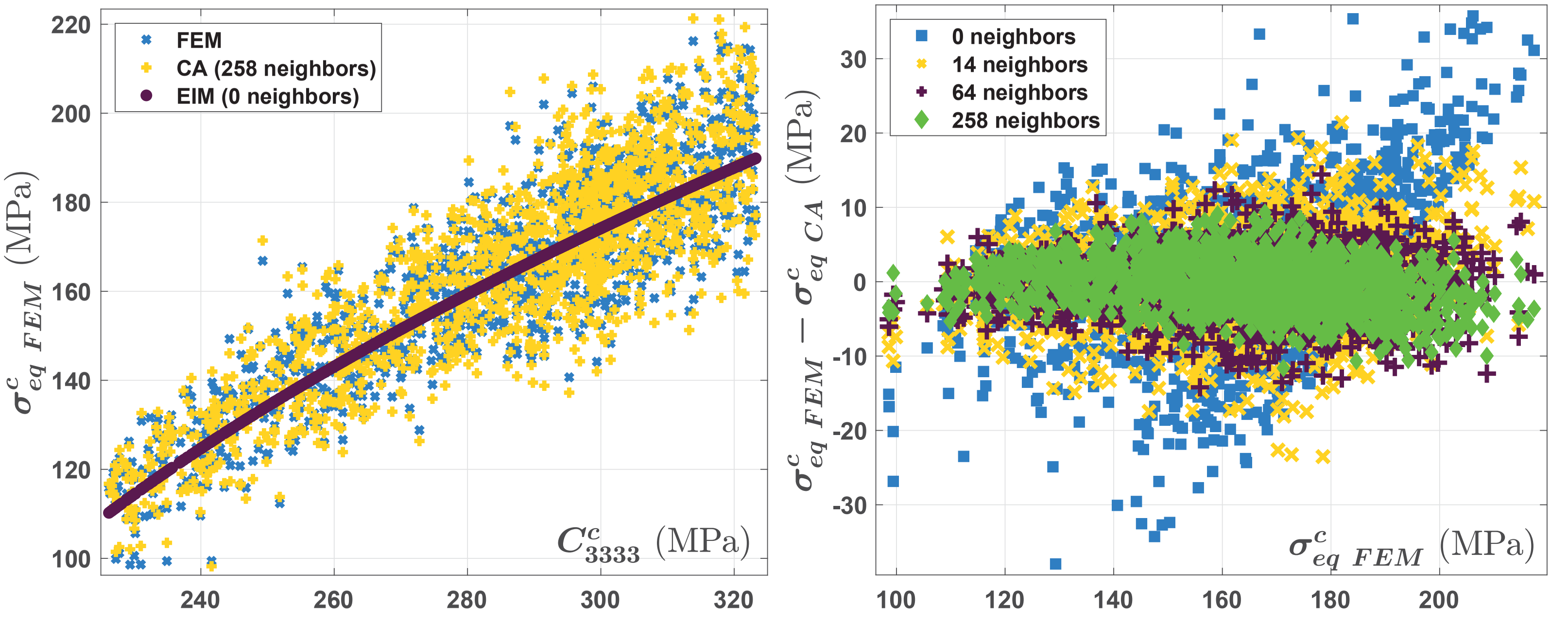

a) b)

Figure 4.6 Iron crystal: comparison between FEM and CA models predictions for different variables for each one of the 20×686 grains-neighborhood configurations under the uniaxial strain loading $\boldsymbol{E}_{strain}$ ($E_{strain\ 33} = 0.1\%$). (a) equivalent von Mises stress σ^c_{eq} obtained with FEM, CA_0 and CA_{258} models as a function of $\mathbb{C}^c_{3333}$; (b) differences between FEM and CA predictions for σ^c_{eq} as a function of FEM ones; (c) histogram and its associated normal distribution of the differences between FEM and CA predictions for σ^c_{eq}; (d) differences between FEM and CA predictions for $\tau^c_{s^c_M}$ as a function of FEM ones, where s^c_M corresponds to the grain slip system showing the highest absolute $\tau^c_{s\ FEM}$ value.

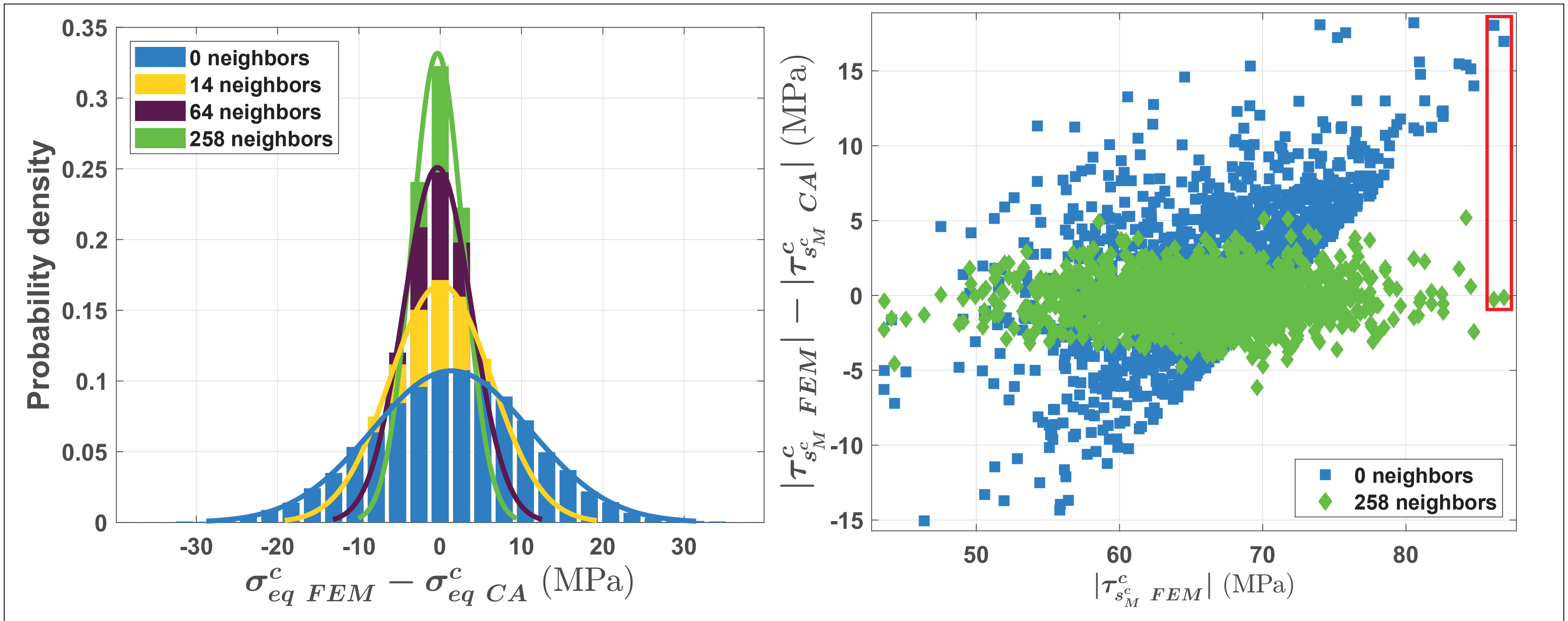

c)

d)

Figure 4.6 (continued)

Nonetheless, even if the differences between FEM and CA models reduce significantly when the number of neighboring grains considered increases, it does not seem to converge to zero. These differences are mainly due to the approximation that the strain deviation due to the neighborhood effect ($\boldsymbol{\Delta\varepsilon}_{n_i}^{c^{eff}}$) does not depend on the central grain c's orientation, but only on the neighboring grain n_i's orientation (Eq. 4.2). Even if the approximation errors can be considered negligible for each neighboring grain and they tend in average to cancel each other out, in some specific cases they could accumulate, and lead to significant divergences. Examples of these specific cases have been presented in the published previous work Bretin *et al.* (2019a).

The initial reason for developing the CA was to reduce the CPU time to generate large statistical databases for stress distributions in polycrystals. The FEM simulations needed to set up the CA parameters takes approximately 7 minutes each, leading to a total 112 min (8 orientations, 2 loadings). The strain field predictions for 686 grains polycrystal aggregate under PBC, using the same computer setup, took approximately 40 minutes by FEM and 15 seconds by CA_{258}, which is 160 times faster. Simulating the results presented in this section (twenty different orientation sets and three different loadings) required 20×3×40=2400 min by FEM, whereas it required 127 min by CA_{258} (20×3×15 seconds plus the 112 minutes to set the $\mathbb{U}^{\overrightarrow{AB}}$). In addition, the larger the number of grains per aggregate is, the larger this ratio gets because the CPU time for the FEM increases exponentially with the number of grains, while the CPU time for the CA increases linearly. Therefore, the initial cost to setup the $\mathbb{U}^{\overrightarrow{AB}}$ is profitable for large numbers of grain-neighborhood configurations, as presented in Section 4.6.

4.5.2 Case of the hexagonal titanium crystal

Even though titanium and iron crystallographic structures are significantly different, the differences between the CA and FEM predictions exhibit the same trends as those observed for iron. Table 4.4 presents FEM and CA prediction for σ_{eq}^{c} and for τ_{s}^{c} on all slip systems over the 20×686 grains-neighborhood configurations. As with iron, it is observed that regardless of the applied loading, the more neighboring grains are considered in the CA, the smaller the average difference between the two models is. This difference is reduced by a factor of approximately 3

Table 4.4 Titanium crystal: FEM and CA prediction differences for the equivalent von Mises stress $\sigma^c_{eq\ FEM}$ and the resolved shear stress $\tau^c_{s\ FEM}$ on each slip system over the 20×686 grains-neighborhood configurations.

Applied loading		$\boldsymbol{E}_{strain}$				$\boldsymbol{E}_{shear}$				$\boldsymbol{E}_{stress\ Ti}$			
$\sigma^c_{eq\ FEM}$ (MPa)	Mean	87.4				151.3				166.3			
	Std	4.8				9.5				9.7			
	Max	106.9				177.6				205.0			
	Min	76.9				123.6				145.5			
Number of neighboring grains		0	14	64	258	0	14	64	258	0	14	64	258
$\sigma^c_{eq\ FEM} - \sigma^c_{eq\ CA}$ (MPa)	Mean	0.3	0.3	0.2	0.2	0.5	0.5	0.4	0.3	0.6	0.5	0.4	0.5
	Std	2.0	1.2	0.8	0.6	3.6	2.4	1.7	1.3	3.9	2.3	1.6	1.1
	Max	9.3	6.1	3.7	2.8	14.8	10.1	6.3	5.1	17.9	11.9	7.7	5.2
	Min	-6.9	-4.5	-2.3	-1.4	-11.6	-8.2	-5.3	-4.1	-13.1	-8.4	-4.2	-2.7
$\lvert\tau^c_{s\ FEM}\rvert$ (MPa) Prismatic	Mean	16.2				28.8				30.8			
	Std	11.2				18.3				21.4			
	Max	40.8				80.4				77.5			
	Min	0.0				0.0				0.0			
Number of neighboring grains		0	14	64	258	0	14	64	258	0	14	64	258
$\tau^c_{s\ FEM} - \tau^c_{s\ CA}$ (MPa) Prismatic	Mean	0.0	0.0	0.0	0.0	0.0	0.0	0.0	0.0	0.0	0.0	0.0	0.0
	Std	1.0	0.6	0.4	0.3	1.7	1.1	0.8	0.6	1.8	1.2	0.8	0.6
	Max	3.7	2.7	1.5	1.1	7.8	4.4	2.9	2.3	6.9	5.0	2.9	2.3
	Min	-4.3	-3.0	-1.7	-1.1	-6.9	-4.8	-3.1	-2.3	-8.3	-5.7	-3.3	-2.1
$\lvert\tau^c_{s\ FEM}\rvert$ (MPa) Basal	Mean	19.3				34.3				36.7			
	Std	13.3				21.8				25.4			
	Max	48.5				96.9				92.3			
	Min	0.0				0.0				0.0			
Number of neighboring grains		0	14	64	258	0	14	64	258	0	14	64	258
$\tau^c_{s\ FEM} - \tau^c_{s\ CA}$ (MPa) Basal	Mean	0.0	0.0	0.0	0.0	0.0	0.0	0.0	0.0	0.0	0.0	0.0	0.0
	Std	1.1	0.7	0.4	0.3	1.9	1.2	0.8	0.5	2.1	1.3	0.8	0.5
	Max	4.7	2.7	1.9	1.1	8.1	5.5	3.5	2.1	9.0	5.1	3.6	2.2
	Min	-4.6	-2.8	-2.0	-1.1	-8.2	-5.1	-3.5	-2.1	-8.7	-5.3	-3.6	-2.0

between EIM and CA predictions. This ratio is even more important if only the grains showing the 500 highest $|\tau^c_{s\ FEM}|$ values out of the $12 \times 20 \times 686$ values are considered. For example, when $\boldsymbol{E}_{strain}$ is applied, these 500 grains are such that $|\tau^c_{s\ FEM}|$ >44 MPa. The differences $|\tau^c_{s\ FEM} - \tau^c_{s\ CA_0}|$ are for these 500 grains on average 1.5 MPa (3.3% of $\tau^c_{s\ FEM}$), with a peak at 4.6 MPa (9.8% of $\tau^c_{s\ FEM}$), against 0.8 MPa when all values are considered. In contrast, the differences $|\tau^c_{s\ FEM} - \tau^c_{s\ CA_{258}}|$ are for these 500 grains on average 0.2 MPa (0.6% of $\tau^c_{s\ FEM}$), with a peak at 1.1 MPa (2.3% of $\tau^c_{s\ FEM}$), but also 0.2 MPa when all values are considered. These percentages remain identical for the two other loadings. Titanium's elastic anisotropy is not as strong as the Iron's which explains why the neighborhood effect is not very important, which explains these low percentage values. Nonetheless, the improvement proportion observed is still as important as it was observed for Iron (3.3%/0.6% for the titanium versus 11.7%/1.5% for the iron). These results prove the stability of the CA robustness.

4.6 Critical neighborhood identification

According to the neighborhood effect definition proposed in Section 4.2.1 and equation 4.20, σ_{eq}^{c} or τ_s^c can be divided in two parts: the part depending on the grain's orientation and aggregate's effective properties predicted with EIM and the part due to the neighborhood effect quantified by the differences between FEM and EIM predictions. Therefore, in the case of the iron and for the applied loading $\boldsymbol{E}_{strain}$, it can be observed from Table 4.3 column "0 neighboring grain" that the neighborhood effect can be responsible for at least 20.5 MPa of a grain's RSS, and a grain's RSS can reach a maximum of 86.8 MPa. These results were observed in a microstructure generated randomly without any texture, but this ratio can get even more important in some specific configurations.

One of CA's key potential is its ability to determine the neighboring environment that will generate the most stress concentration. We exemplify in this section grain A's orientation and its three layers orientation set (258 grains such that $||\overrightarrow{AB}|| \leq 6$) that maximize its RSS τ_s^A on one of its slip systems, when $\boldsymbol{E}_{strain}$ is applied and iron properties are used. Coupling equations 4.20 and 4.25 yields:

$$\begin{cases} \tau_s^A = \tau_{s\,0}^A + \sum\limits_{B_i} \Delta\tau_{s\,B_i}^A & \text{(4.26a)} \\ \text{with} \quad \tau_{s\,0}^A = \mathbb{C}^A : \mathbb{A}_{Esh}^A : \boldsymbol{E}_{strain} : \boldsymbol{m}_s^A & \text{(4.26b)} \\ \text{and} \quad \Delta\tau_{s\,B_i}^A = \mathbb{C}^A : \mathbb{A}^{\overrightarrow{AB_i}} : \boldsymbol{E}_{strain} : \boldsymbol{m}_s^A & \text{(4.26c)} \end{cases}$$

where $\boldsymbol{C}^A$, $\boldsymbol{A}_{Esh}^A$ and $\boldsymbol{m}_s^A$ depend on grain A's orientation, and $\mathbb{A}^{\overrightarrow{AB_i}}$ depends on grain B_i's orientation. τ_s^A is therefore divided into two parts: $\tau_{s\,0}^A$ represents the part due to grain A's properties (which is the average value that a given grain orientation would exhibit in a polycrystalline aggregate, as it was shown in Bretin *et al.* (2019a)), and $\sum_{B_i} \Delta\tau_{s\,B_i}^A$ represents the part due to its close environment.

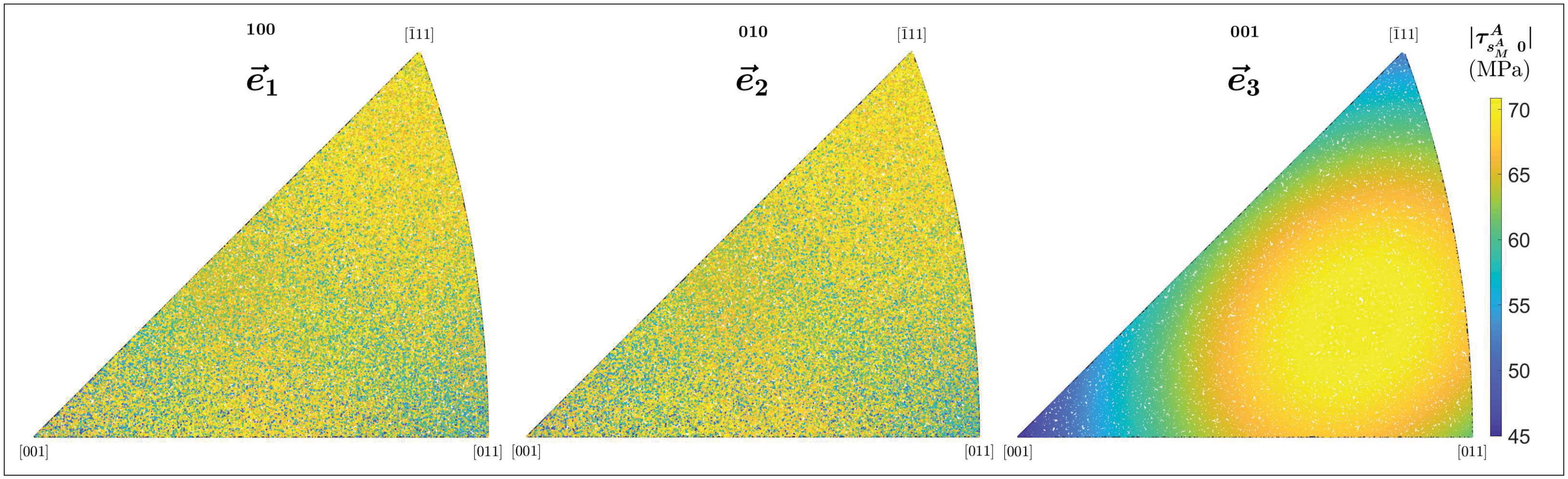

Figure 4.7 Inverse pole figure in the global axis direction of grain A's orientation in the cubic standard stereo-triangle, color coded as a function of the maximum absolute resolved shear stress $|\tau_{s_M^A\ 0}^A|$ over 100,000 random orientations.

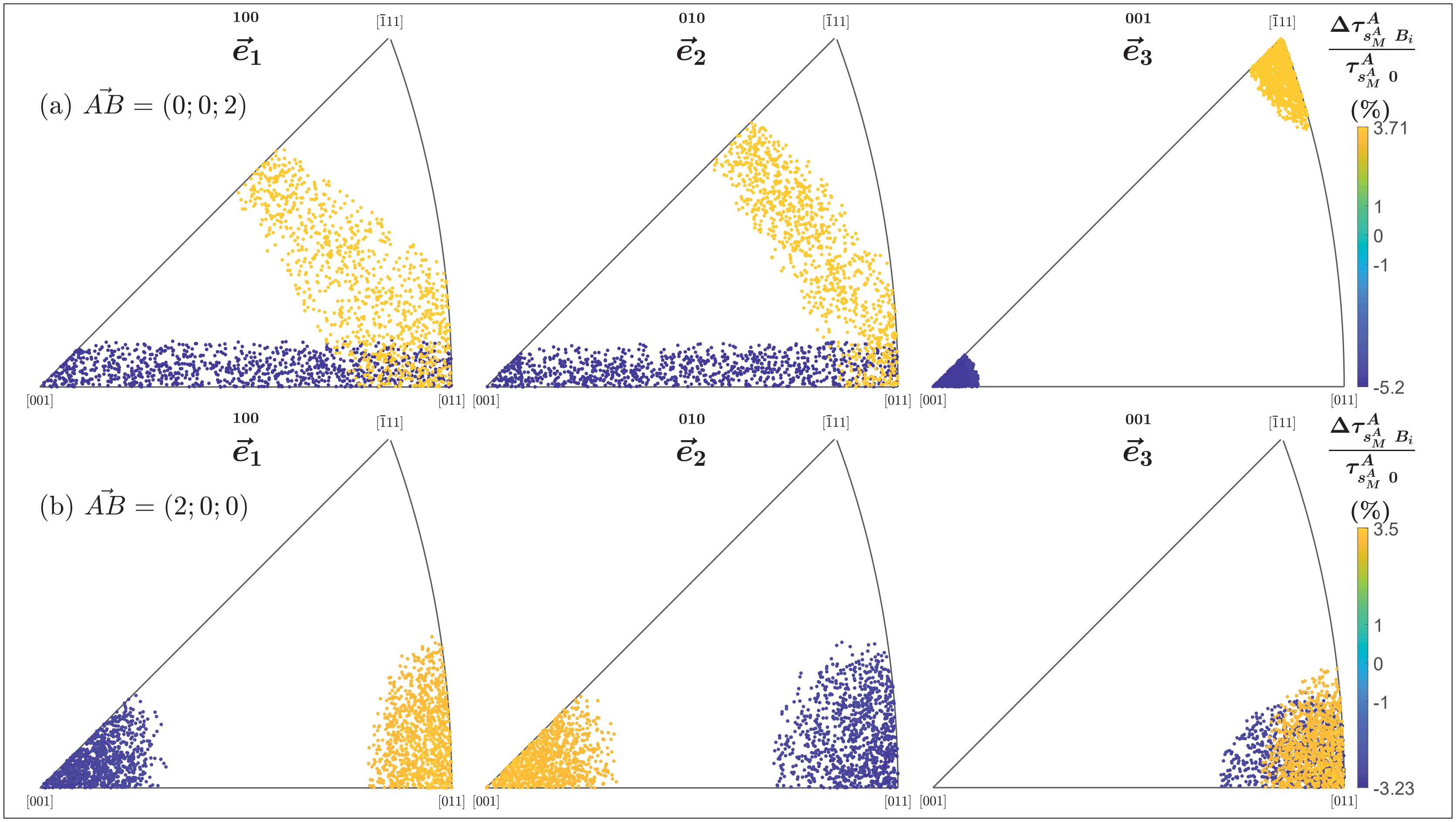

Figure 4.8 Inverse pole figure in the global axis direction of grain B_i's orientation in the cubic standard stereo-triangle, color coded as a function of the resolved shear stress percentage variations ($\Delta\tau^A_{s^A_M\ B_i}/\tau^A_{s^A_M\ 0}$) over 100,000 random orientations (only the 1,000 lowest (shades of blue) and the 1,000 highest (shades of yellow) values are plotted) in the case where grain A's Euler angles are $(0, 144.8, 161.5)$ such that $\tau^A_{s^A_M\ 0} = 70.9$ MPa, for four different relative positions.

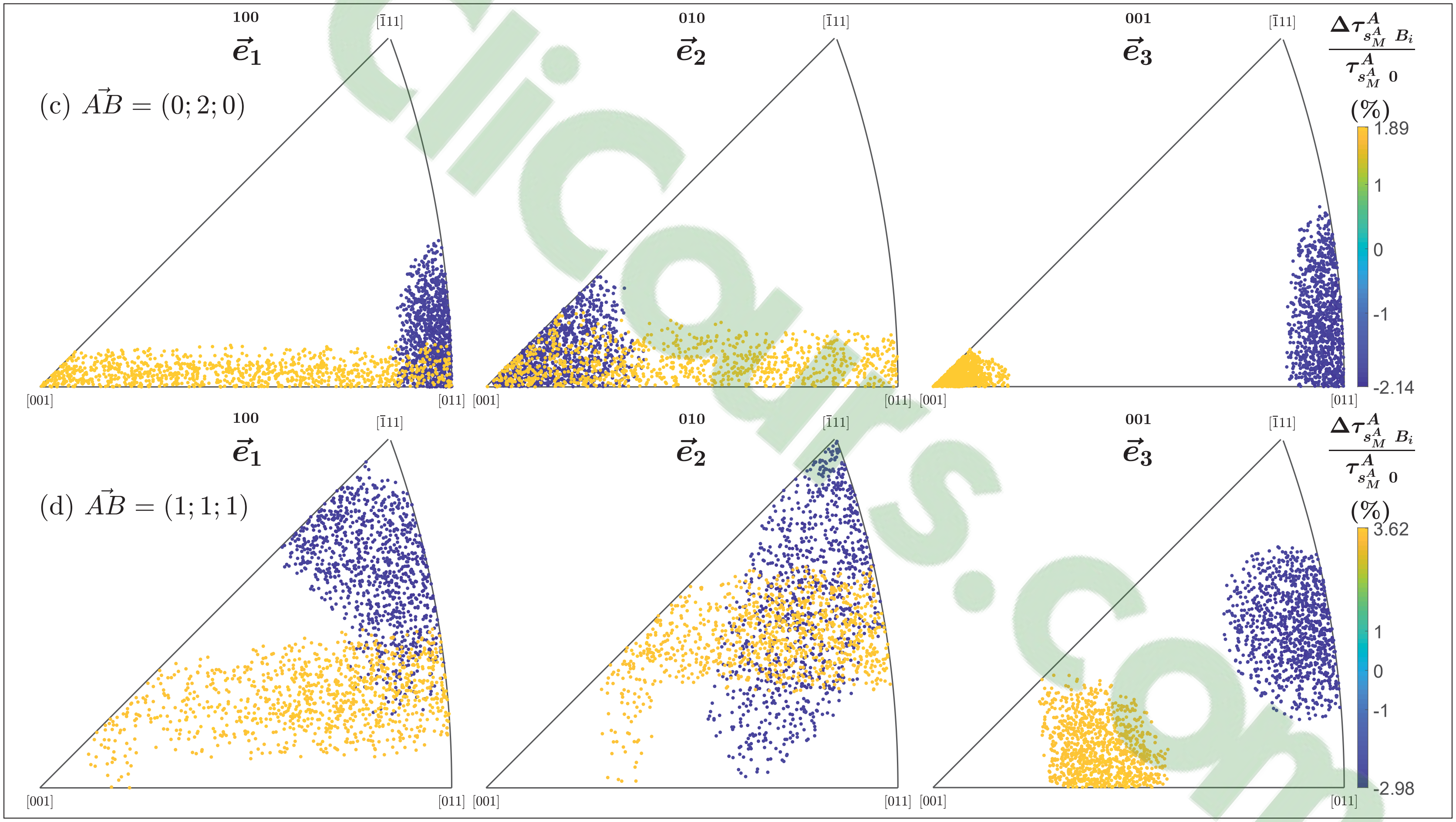

Figure 4.8 (continued)

Using Euler angles to define a grain orientation, $\tau^A_{s\,0}$ can be written as a function of grain A's angles $(\varphi^A_1, \phi^A, \varphi^A_2)$ and $\Delta\tau^A_{s\,B_i}$ as a function of grains A and B_i angles $(\varphi^{B_i}_1, \phi^{B_i}, \varphi^{B_i}_2)$. Fig. 4.7 shows $|\tau^A_{s^A_M\,0}|$ values over 100,000 orientations randomly generated with the quaternion method on grain A's inverse pole figure (IPF) in a standard stereo-triangle, where s^A_M corresponds to the slip system showing the highest absolute $\tau^A_{s\,0}$ for a given orientation. The values observed range from 44.9 MPa to 70.9 MPa, which concurs with the values observed in Fig. 4.6d. No texture is observed along $\vec{\boldsymbol{e}}_1$ and $\vec{\boldsymbol{e}}_2$ axes, but a clear texture is observed along $\vec{\boldsymbol{e}}_3$ axis. The highest $\tau^A_{s\,0}$ are observed in the triangle's center, which corresponds approximately to the crystallographic direction [2 6 9].

The stress variations $\Delta\tau^A_{s^A_M\,B_i}$ induced by a neighboring grain B_i on grain A's slip system s^A_M are computed over the same 100,000 random orientations, for each relative position $\overrightarrow{AB}$. Grain A's orientation is arbitrarily set to the Euler angles $(0, 144.8, 161.5)$, which corresponds to one of the orientations showing the maximum $\tau^A_{s^A_M\,0} = 70.9$ MPa on its slip system s^A_M, such as $\vec{\boldsymbol{l}}^A_{s^A_M} = (-1;0;1)/\sqrt{2}$ and $\vec{\boldsymbol{n}}^A_{s^A_M} = (1;1;1)/\sqrt{3}$ in the crystal axis system. Fig. 4.8 shows the 1,000 lowest (shades of blue) and 1,000 highest (shades of yellow) $\Delta\tau^A_{s^A_M\,B_i}$ out of the 100,000 computed values (only these values are plotted for more readability) for four different relative positions $\overrightarrow{AB}$ on grain B_i's IPF in standard stereo-triangle. The orientations increasing the most grain A's RSS can easily be identified but they are completely different for each relative position and correspond to:

- Fig. 4.8a. ($\overrightarrow{AB} = (0;0;2)$): the orientations with their crystallographic direction [111] aligned with $\vec{\boldsymbol{e}}_3$ (correspond to the orientations with the highest $\mathbb{C}_{3333}$);
- Fig. 4.8b. ($\overrightarrow{AB} = (2;0;0)$): the orientations with their crystallographic direction [001] aligned with $\vec{\boldsymbol{e}}_2$ and their directions [011] aligned with $\vec{\boldsymbol{e}}_1$ and $\vec{\boldsymbol{e}}_3$;
- Fig. 4.8c. ($\overrightarrow{AB} = (0;2;0)$): the orientations with their crystallographic direction [001] aligned with $\vec{\boldsymbol{e}}_3$;
- Fig. 4.8d. ($\overrightarrow{AB} = (1;1;1)$): the orientations with their crystallographic direction [10 1 30] approximately aligned with $\vec{\boldsymbol{e}}_3$.

The orientations showing the highest $\Delta\tau^{A}_{s^{A}_{M}\ B_i}$ increase are not necessarily the orientations generating the highest increase of stress along the loading direction ($\Delta\sigma^{A}_{B_i\ 33}$). These observations results from a compromise between $\boldsymbol{\Delta\sigma}^{A}_{B_i}$ components in order to apply the highest RSS on the slip system s^{A}_{M}. These IPF not only depends on grain B_i's orientation but also on grain A's orientation due to the variables $\boldsymbol{m}^{A}_{s}$ and $\mathbb{C}^{A}$ in $\Delta\tau^{A}_{s}$ definition (Eq. 4.26). An example of the different textures obtained when changing grain A's orientation to the Euler angle (0;0;0), such that $\tau^{A}_{s^{A}_{M}\ 0} = 44.9$ MPa, is given in Appendix 4.d. It can be seen that the maximum contributions are less significant and that some combination can be overturn and grain B's orientations that increase the grain A's RSS in some situation can lower it in other (blue and yellow zones on figures 4.8d. and 4.d-0d. along $\vec{\boldsymbol{e}}_{\boldsymbol{3}}$ axis are flipped).

When grain A's Euler angles are $(0, 144.8, 161.5)$, the crystallographic orientation giving the maximum $\Delta\tau^{A}_{s^{A}_{M}\ B_i}$ were identified for every 258 neighboring grains using a maximization function, yielding:

$$\tau^{A}_{s\ 0} = 70.9 \text{ MPa} \tag{4.27a}$$

$$\sum_{B_i} \Delta\tau^{A}_{s\ B_i} = \begin{array}{l} 27.1 \text{ MPa from the first layer (14 grains)} \\ 30.3 \text{ MPa from the second layer (50 grains)} \\ 34.1 \text{ MPa from the third layer (194 grains)} \end{array} \tag{4.27b}$$

$$\Rightarrow \tau^{A}_{s} = \tau^{A}_{s\ 0} + \sum_{B_i} \Delta\tau^{A}_{s\ B_i} = 70.9 + 91.5 = 162.4 \text{ MPa} \tag{4.27c}$$

It can be observed from these results that the part due to the central grain properties (70.9 MPa) is less important than the part due the neighborhood effect (91.5 MPa). A ratio of 2.3 is observed between the average RSS expected for grain A (70.9 MPa) and the RSS obtained when the neighborhood is critically oriented (162.4 MPa). Also, the stress obtained is 1.9 times more important than the maximum observed in Table 4.3 (86.8 ⇒ 162.4 MPa) and the part due to the neighborhood effect is 4.5 times more important than the greatest observed in Table 4.3 (20.5 ⇒ 91.5 MPa).

Aggregate simulations under $\boldsymbol{E}_{strain}$ were performed with the CA_{258} model following the same method as in Section 4.5 to observe how this orientation set would impact the stress fields in a polycrystalline aggregate. These simulations were also carried out with the FEM model to validate whether the CA_{258} model is still accurate in case of high stress concentration. Four simulations were performed with both models: first the 686 grains are randomly generated, except for the central grain A whose orientation is in Euler angles $(0, 144.8, 161.5)$. Then, layer by layer (up to the third layer), grain A's neighbors are reoriented to generate a stress concentration in grain A. Fig. 4.9a compares $|\tau^c_{s^c_M}|$ predictions obtained with the CA_{258} and FEM models in each of the 686 grains, and Fig. 4.9b shows how much the grain's RSS was amplified by the neighborhood effect $(|\tau^c_{s^c_M}|_{CA}/|\tau^c_{s^c_M\,0}|)$ as a function of $|\tau^c_{s^c_M}|_{CA}$, where s^c_M is the slip system presenting the grain highest $|\tau^c_s|$ with the CA_{258} model.

As expected, the central grain A's RSS (pointed out by arrows) increases with the number of neighboring grains reoriented. Grain A's neighboring environment was initially neutral $(|\tau^c_{s^c_M}|_{CA} \approx |\tau^c_{s^c_M\,0}|)$, and when the 258 neighboring grain orientations were changed to those maximizing $\Delta\tau^A_{s\,B_i}$, they generated a stress concentration that more than doubled the initial RSS $(|\tau^c_{s^c_M}|_{CA}/|\tau^c_{s^c_M\,0}| = 2.3)$. When the three layers are reoriented (in green), few grains show a stress increase higher than the average (framed in red in Fig. 4.9b). These grains are part of grain A's first layer. This can be explained by the fact that the second and third layers grain orientations increasing the stress in the central grain also increase the stress in the first layer. For example, calling B_1, B_2 and B_3 grain's A neighboring grains such that $\overrightarrow{AB}_1 = (0; 0; 2)$, $\overrightarrow{AB}_2 = (0; 0; 4)$ and $\overrightarrow{AB}_3 = (0; 0; 6)$, the texture observed in Fig. 4.8a for the relative position $\overrightarrow{AB}_1$ is very similar for $\overrightarrow{AB}_2$ and $\overrightarrow{AB}_3$. Consequently, grains B_2 and B_3, set up to increase grain A's stress, also have the effect of increasing grain B_1's stress, and therefore, the stress concentration observed in the grain A also extends to the neighboring grain first layer.

This effect is very well captured by the CA model, as seen in Figure 4.9a. All the dots are close to the $x = y$-axis, revealing CA_{258} model accuracy, when compared to the FEM. Even when the stress is significant in the central grain, the CA model remains accurate. A value of 162.4 MPa is predicted by the CA_{258} model, and 156.7 MPa by the FEM model, which corresponds to a difference of 3.6% between the CA and FEM models. Nonetheless, a little offset (dots slightly under the $x = y$-axis) is observed when the three layers were reoriented (in green). This is due to the fact that the aggregate's effective properties differ from those obtained in a fully random aggregate, but these offset remains negligible ($\langle \tau^{c}_{s^{c}_{M}\ CA} - \tau^{c}_{s^{c}_{M}\ FEM} \rangle_{c} / \langle \tau^{c}_{s^{c}_{M}\ FEM} \rangle_{c} = 3\%$).

The IPF (Fig. 4.10) for the 686-orientation set when the three neighboring grain layers were reoriented (red points are the 259 orientations chosen to generate a stress concentration in grain A, and blue points are the remaining grains randomly oriented) shows that, even if the central grain presents a stress at least double the average stress observed, the aggregate does not present any relevant sign of texture. These results reveal the importance of considering the neighborhood effect in the prediction of polycrystalline aggregate stress field even though the material is not textured. Our model shows that a grain can exhibit a RSS more than twice that present in other grains of the aggregate. This grain will reach its yield strength and possibly lead to early crack initiation while the rest of the aggregate remains totally elastic and shows no macroscopic sign of plasticity.

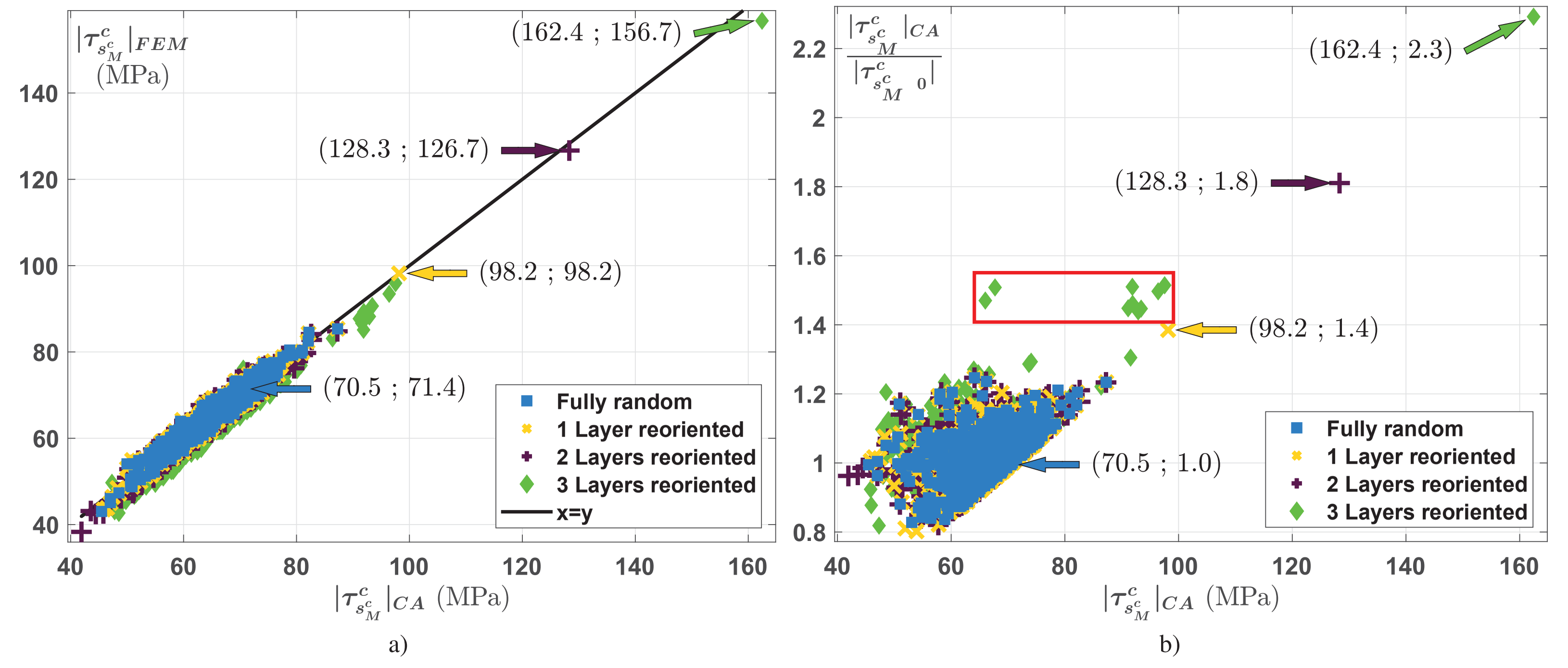

a)

b)

Figure 4.9 Resolved shear stress predictions over the aggregate's 686 grains in which the orientations were randomly distributed except for the central grain neighbors favorably oriented to generate stress concentration: (a) FEM predictions for $|\tau^c_{s^c_M}|$ as a function of the CA_{258} predictions; (b) resolved shear stress "amplification factor" due to the neighborhood effect ($|\tau^c_{s^c_M}|_{CA}/|\tau^c_{s^c_M\ 0}|$) as a function of $|\tau^c_{s^c_M}|_{CA}$, where s^c_M is the slip system presenting the highest $|\tau^c_s|$ with the CA_{258} model. The central grain A's values, in which the stress concentration is localised, are pointed out by arrows.

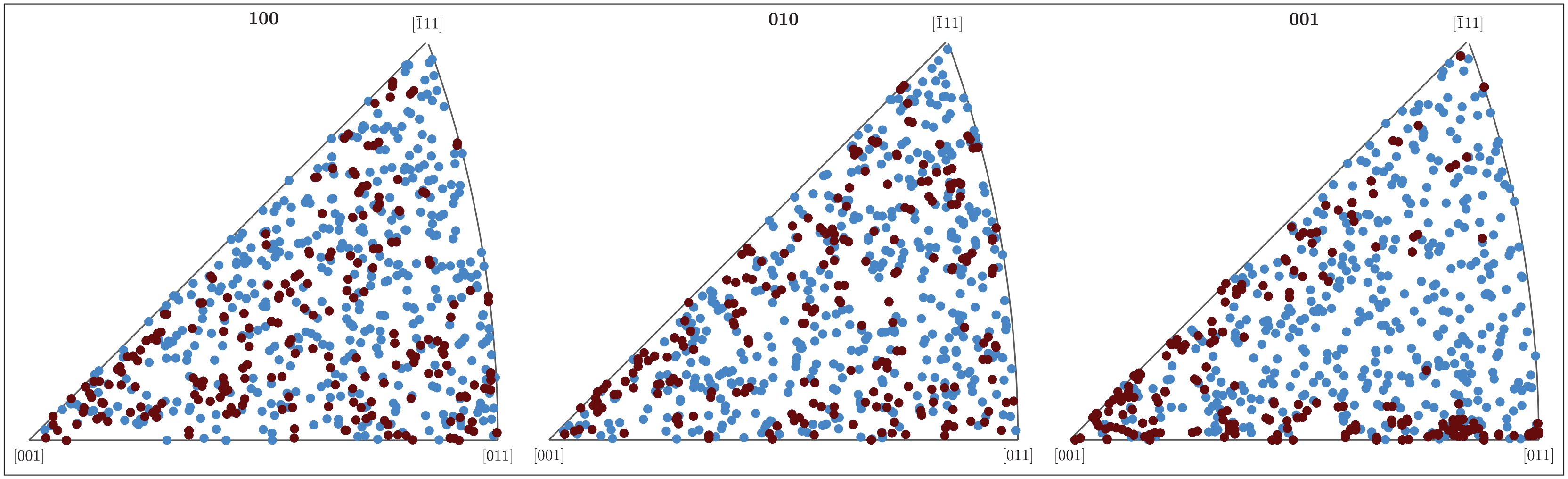

Figure 4.10 Inverse pole figure in the global axis direction (001 being the loading axis $\vec{e}_3$) of the 686 grain orientations used for the polycrystalline aggregate simulation under the strain loading $\boldsymbol{E}_{strain}$ (Eq. 4.23), where the 256 close neighboring grains of the central grain (red dots) were oriented to generate a stress concentration in the later, and the other orientations (blue dots) were random.

By reproducing the methodology used to obtain equations 4.27 (in this case, grain A's orientation is in Euler angle $(0, 135, 150)$, and s_M^A corresponds to the basal slip system such as $\vec{\boldsymbol{l}}^A_{s_M^A} = (-1; \sqrt{3}; 0)/2$ and $\vec{\boldsymbol{n}}^A_{s_M^A} = (0; 0; 1)$ in the crystal axis system), the highest RSS obtained using the titanium crystal properties (Table 4.1) is:

$$\tau^A_{s\,0} = 45.1 \text{ MPa} \tag{4.28a}$$

$$\sum_{B_i} \Delta\tau^A_{s\,B_i} = \begin{array}{l} 7.7 \text{ MPa from the first layer (14 grains)} \\ 7.2 \text{ MPa from the second layer (50 grains)} \\ 8.0 \text{ MPa from the third layer (194 grains)} \end{array} \tag{4.28b}$$

$$\Rightarrow \tau^A_s = \tau^A_{s\,0} + \sum_{B_i} \Delta\tau^A_{s\,B_i} = 45.1 + 22.9 = 68.0 \text{ MPa} \tag{4.28c}$$

By opposition to iron, the part due to the central grain properties (45.1 MPa) is still more important than the part due the neighborhood effect (22.9 MPa). A ratio of 1.5 is observed between the average RSS expected for grain A (45.1 MPa) and the RSS obtained when the neighborhood is critically oriented (68.0 MPa), while the iron was showing a ratio of 2.3. The stress obtained is 1.4 times more important than the maximum one observed in Table 4.4 (48.5 ⇒ 68.0 MPa), while it was 1.9 in the iron case. Nonetheless, even if the titanium crystal does not present an anisotropy as important as the iron, the part due to the neighborhood effect is 4.8 times more important than the largest observed in Table 4.4 (4.7 ⇒ 22.9 MPa), i.e., an increase as much important as it was observed in the iron case (Eq. 4.27).

Finally, once the $\mathbb{U}^{\overrightarrow{AB}}$ identified, computing $\Delta\tau^A_{s_M^A\,B_i}$ over 100,000 different orientations, to generate for example one of the sub-figure from Fig. 4.8, takes less than 10 seconds, which would take indefinitely with FEM. CA's computation speed makes the identification of critical orientation sets possible.

4.7 Conclusions

A Cellular Automaton has been developed to predict the neighborhood effect in polycrystals which the representation is simplified to a regular aggregate (Kelvin structure). The model relies on Eshelby's inclusion theory to which the neighborhood effect is added. Neighborhood effect approximations and patterns with the material parameters were proposed from different FEM studies, yielding to a data-driven model. A methodology to identify the model parameters from FEM simulations, using a low CPU time cost, was defined. These parameters are related to the material effective properties but are independent of the orientation distribution. A grain's stress tensor from the polycrystal, surrounded by any neighborhood, submitted to any elastic loading, can be obtained in a fraction of a second using the CA model.

Our CA predictions were compared against FEM simulations of a polycrystalline aggregate randomly oriented generated as a Kelvin structure for different submitted elastic loading. The more neighboring grains are considered in the CA model, the closer it gets to the FEM results. The CA model predicted the highest RSS values with an accuracy of about 1.5%, when compared to the FEM in the case of the iron crystal, and of about 0.3%, in the case of the titanium crystal. The CPU time required for this type of simulations is about two orders of magnitude shorter than the FEM, for the same accuracy.

CA model can easily identify the sets of orientations that generates the most stress concentration in a grain in a really short calculation time and with high accuracy. The results showed that a stress at least twice as high as those observed in the random case can be obtained, where no remarkable texture was observed.

CA model has only been applied to small aggregates. Its applications to larger aggregates, with local heterogeneities in grain orientation distribution (macrozones), could be performed in future works.

Adding features to account for the grains morphology and the effect of a free surface have also been considered. Preliminary works have already been made on this matter which might lead to a future article.

The next step into CA model's development is to expend the model applications to the early stage of plasticity to simulate high cycle fatigue conditions where only few grains plastify, but the overall material remains elastic. An elastoplastic behavior to the model local law will be built and applied to different aggregates to extend the model to fatigue problems.

CHAPTER 5

CELLULAR AUTOMATON DEVELOPMENT FOR THE STUDY OF THE NEIGHBORHOOD EFFECT WITHIN POLYCRYSTALS STRESS-FIELDS

Rémy Bretin[1], Martin Lévesque[2], Philippe Pilvin[3], Philippe Bocher[1]

[1] Mechanical Engineering Department, École de technologie supérieure (ÉTS),
1100 Notre-Dame Street West, Montréal, QC H3C 1K3, Canada
[2] Mechanical Engineering Department, École Polytechnique de Montréal,
2900 Boulevard Edouard-Montpetit, Montréal, QC H3T 1J4, Canada
[3] IRDL, UMR CNRS 6027, Université de Bretagne-Sud,
Rue de Saint-Maudé, F-56321 Lorient Cedex, France

Article submitted for publication in «International Journal of Fatigue» september 2019. Small modifications from the submitted version of the article have been brought in this chapter.

Abstract

Polycrystals heterogeneities generate stress concentration which can be responsible for premature failure of mechanical parts and thereby need to be considered in mechanical models. A grain's close neighborhood has shown to significantly impact its mechanical behavior. The more the crystal is anisotropic, the more this impact can be, which in some specific configuration can double a grain's stress level than it would normally have in an "average" random environment. The impact of such stress concentration on the elastoplastic behavior of polycrystalline material has been studied by means of a cellular automaton (CA) and finite element (FE) models. The studied aggregates were single-phase with grains of identical size and spherical shape. The grains' anisotropy and crystallographic orientations were the only sources of heterogeneities studied. The CA model, originally developed for the study of elastic loadings, was adapted for the study of elastoplastic loadings in high cycle fatigue regime and compared to the FE model. Using the CA model, a statistical study was carried out to determine the true elastic limit probability distribution due to the random character of the neighborhood effect. The obtained probability distribution could be linked to the fatigue test scatter observed experimentally.

Keywords: Micromechanics, Cellular automaton, Neighborhood effect, Model reduction, Crystal plasticity, Polycrystal

5.1 Introduction

Fatigue damage is a multiscale phenomenon, ranging from the atomic scale where the dislocations motion starts, to the grain scale where cracks initiate, to the macroscopic scale where cracks propagate until part failure. In the low cycle fatigue (LCF) regime, fatigue life is mainly governed by the crack growth rate and thus can be studied at the macroscopic scale. In the high cycle fatigue and very high cycle fatigue (HCF and VHCF respectively), however, the fatigue life is mainly governed by the crack nucleation phase, which highly depends on the microscopic material stress fields (McDowell, 2004).

Heterogeneities within materials (e.g. inclusions, defects, microstructure texture and morphology, crystal anisotropy, etc.), induce variations in the local stress field. For some specific configurations of heterogeneities, these fluctuations can induce important stress concentrations leading to an early crack initiation and premature failure. The probability for these specific configurations to occur is tied to the random character of these heterogeneities, which are controlled by manufacturing processes within defined boundaries. Specimens from the same bulk material can therefore show a variation in their number of fatigue cycles to failure, which is especially significant in HCF and VHCF regimes where the submitted stress is close, or lower to, the material yield strength, and thus predominantly elastic (Klemenc & Fajdiga, 2012). Many expensive testing campaigns are therefore required to obtain statistically significant and robust database for the experimentally based fatigue life prediction models (Weibull, 1952; Wirsching, 1983).

Numerical tools have been developed in the last decades to better understand the mechanisms of fatigue damage and to predict material fatigue lives. On the one hand, the full-field methods, such as finite element (FE) or fast-Fourier transform (FFT) based methods, were developed to study the effect of several microstructure parameters and loading conditions on the fatigue life

(Guerchais *et al.*, 2017; Guilhem *et al.*, 2013; Robert *et al.*, 2012a). These methods provide detailed information on the local stress fields, crack initiation conditions and localization. However, they require large amounts of computational resources, which hinders the execution of probabilistic analyses. On the other hand, the mean-field / analytical models (McDowell, 2007; Przybyla *et al.*, 2010; Santecchia *et al.*, 2016; Zghal *et al.*, 2016) provide a simplified approach of the material mechanical behavior for a lower computational cost. However, due to their simplifying assumptions, these models do not account for the full microstructure description and therefore do not capture the full range of possible stress levels that can occur locally within the polycrystal. Therefore, more accurate numerical fatigue life prediction tools must be developed to estimate metals' fatigue life probability through a multi-scale approach, from crack nucleation to crack propagation. One of the first building blocks in such an endeavor is to accurately predict stress field heterogeneities at the microscopic level and be able to predict and locate the highest stress-levels possible within the material.

Capturing accurately the polycrystal elasto-plastic stress-field in HCF for a low computational cost is a key issue into the prediction of the full local stress-level range. Several (semi-)analytical models were developed for that matter. Among well-known schemes one may cite the self-consistent approximations which started with Hill's approach (Hill, 1965b) and later on led to Berveiller-Zaoui's model (Berveiller & Zaoui, 1978). Even though this model is often used to fit the crystal constitutive equations parameters, its tangent and secant formulations of the local stress-strain relation is well-known to yield overstiff local responses (Suquet, 1997). The use of the second-order method (Lahellec & Suquet, 2007b), and/or variational formulations (Lahellec & Suquet, 2007a), leads to more accurate models (Badulescu, Lahellec & Suquet, 2015; Lahellec & Suquet, 2013; Mareau & Berbenni, 2015) that predict the first and second-order statistics of the local stress field in the different phases. Recent methods, requiring pre-simulations to fit the model parameters (data-driven), were proposed (Liu *et al.*, 2016; Michel & Suquet, 2016) and showed promising predictions of the local stress field in comparison to the full-fields models for lower computational cost. Nonetheless, most of these models share a common issue (Robert & Mareau, 2015): they do not account for the crystal elastic anisotropy and/or the effect of the grains close environment. This was evidenced by several authors, using high-resolution digital image correlation (Bridier *et al.*, 2008; Hemery *et al.*, 2018; Stinville *et al.*, 2015,1) or numerical models (Brenner *et al.*, 2009; Bretin *et al.*, 2019a; Guilhem *et al.*, 2010; Robert *et al.*, 2012a), to be responsible of significant stress variations when the aggregate is submitted to macroscopic stress levels typically yielding HCF and VHCF. The models that account for it are inconveniently too complex, making the simulation of different microstructure configurations to generate a large amount of data for a statistical analysis an heavy process.

Bretin *et al.* (2019a) carried out a FE analysis to understand how a grain's neighborhood affects its stress level when a macroscopically homegeneous stress field is applied to a polycrystal representative volume element. The authors referred to such local stress variations as the neighborhood effect. This study showed that a neighborhood's crystallographic orientation configuration has, in average, as much impact on a grain's stress level (equivalent von Mises stress and resolved shear stress) as its own crystallographic orientation, revealing the importance of the neighborhood effect for the polycrystal microscopic stress field. That study led to a cellular automaton (CA) model (Bretin, Levesque & Bocher, 2019b) that predicted the neighborhood effect in the linearly elastic regime. CA models have found many application, ranging from biology (Wolfram, 2002) to metal solidification studies (Hesselbarth & Göbel, 1991) and micro-mechanical materials studies (Montheillet & Gilormini, 1996; Pourian *et al.*, 2016). The CA model proposed by Bretin et al. predicts grains' mean stress fields within polycrystals in the elastic domain based on Eshelby's inclusion problem (Eshelby, 1957) to which a correction factor was applied depending on the grain's neighborhood's orientation configuration. The model was shown to predict, in elasticity, the highest resolved shear stress (RSS) values within 1.5% in an iron aggregate and within 0.6% in a titanium aggregate, when compared to converged FE predictions. Owing to the fact that the model is semi-analytical, its capability to easily identify a grain's critical environments responsible for high-stress concentration was also demonstrated. In the case of the iron crystal, some specific neighborhood configurations were shown to yield a two-fold increase in the grain maximum resolved shear stress, when compared to the average value of the grains with identical crystallographic orientation, but random environments.

The CA model applications presented by Bretin *et al.* (2019b), originally developed for linearly-elastic load using Hooke's law as constitutive law, is extended in the present work to elastoviscoplastic analyses of polycrystalline materials. Simplifying assumptions were made in order to conserve the model quickness at the expense of the plastic-fields prediction accuracy to allow a statistical study of polycrystals plasticity distributions while accounting for the neighborhood effect. Several constitutive laws can be found in the literature to describe a single crystal elasto-visco-plastic behavior (Besson *et al.*, 2009). A widely used model in the framework of crystal plasticity theory is the Meric-Cailletaud's model (Méric *et al.*, 1991). This model contains kinematic and isotropic hardening functions deriving from Armstrong-Frederick and Chaboche's macroscopic models (Lemaitre *et al.*, 2009). This model has been proven over the years to be adequately adapted to the study of cubic polycrystal fatigue behavior. Therefore, Meric-Cailletaud's model is the constitutive law chosen in this paper to replace the Hooke's law formerly used and to illustrate the CA model applications to polycrystals submitted to macroscopic stress levels typically yielding HCF and VHCF. The 316L steel model's parameters identified by Guilhem *et al.* (2013) from monotonic and dynamic experimental data were used.

The main focus of this article is to extend the study of the neighborhood effect to the case of an elastoviscoplastic load in HCF regime. As presented by Bretin *et al.* (2019a,1), the studied aggregates were single-phase shaped as a periodic Kelvin structure where all the grains are of identical spherical shape. By eluding the morphology and border effect, the crystal anisotropy and the crystallographic orientation distribution were the only sources of heterogeneities remaining. Using the CA model capability to easily identify in elasticity the specific crystallographic configurations responsible for important stress concentrations as presented by Bretin *et al.* (2019b), two types of orientations' distributions were studied: one fully randomly distributed and the second specifically distributed to generate high-stress concentration on a grain's slip system, both using the same orientations' pool. The impact differences of such distributions on the polycrystal HCF behavior were studied using FE analyses and the CA model.

The paper is organized as follows. The CA model equations as well as the Meric-Cailletaud's model equations and the CA model adaptation to the case of an elastoviscoplastic load, are recalled in Section 5.2. Section 5.3 presents the FE model used for the study of the neighborhood effect and all the simulation conditions such as the aggregate structure used, the studied loads, and the methodology to generate the two different types of crystallographic orientation distributions studied. Section 5.4 discusses the results obtained from the different simulations in two parts: monotonic loading in Section 5.4.1 and cyclic loading in Section 5.4.2. The predicted state values (equivalent von Mises stress and resolved shear stress, plastic strain and cumulative viscoplastic slip) obtained for each studied crystallographic distribution type are discussed in Section 5.4.1.1 highlighting the importance of the neighborhood effect on polycrystals HCF behavior. CA model predictions are also confronted with the FE analyses used as a reference. The CA model's capability to identify with accuracy the critical orientations' configurations and to approximately reproduce the full-field simulations at a much lower cost than FE method is shown. A statistical study has been carried out in Section 5.5 to show the importance of the neighborhood effect on the true elastic limit scatter (macroscopic stress at which the first grain of the material starts to plastify) which can be related to the fatigue strength scatter. Closing remarks and conclusions are discussed in Section 5.6.

5.2 Cellular automaton model

5.2.1 Model's definition in elasticity

The CA model, developed by Bretin *et al.* (2019b) for polycrystalline aggregates submitted to an elastic load $\boldsymbol{E}$, is a mean-field data-driven analytical model. It defines a grain g's mean strain tensor surrounded by a neighborhood N composed of grains n_i as:

$$\boldsymbol{\varepsilon}_N^g = \boldsymbol{\varepsilon}_0^g + \boldsymbol{\Delta\varepsilon}_N^g \tag{5.1}$$

where $\boldsymbol{\varepsilon}_0^g$ corresponds to the grain g's mean strain tensor when immersed in a homogeneous infinite matrix having the polycrystal effective elastic properties ($\mathbb{C}^{eff}$), and $\boldsymbol{\Delta\varepsilon}_N^g$ is the grain g's strain deviation due to its neighborhood N as illustrated in Fig. 5.1a.

$\boldsymbol{\varepsilon}^g_0$ is obtained from Eshelby's inclusion theory Eshelby (1957) as:

$$\boldsymbol{\varepsilon}^g_0 = \mathbb{A}^g_{Esh} : \boldsymbol{E} \tag{5.2a}$$

$$\mathbb{A}^g_{Esh} = \left(\mathbb{I} + \mathbb{S}^g_{Esh} : (\mathbb{C}^{eff})^{-1} : (\mathbb{C}^g - \mathbb{C}^{eff})\right)^{-1} \tag{5.2b}$$

where $\mathbb{C}^g$ and $\mathbb{C}^{eff}$ are respectively the grain's and the homogenized aggregate's stiffness tensors, $\mathbb{A}^g_{Esh}$ is the strain-localization tensor, $\mathbb{I}$ is the fourth-order identity tensor ($\mathbb{I}_{ijkl} = (\delta_{ik}\delta_{jl}+\delta_{il}\delta_{jk})/2$, where δ_{ij} is the Kronecker delta equal to 1 if $i = j$ and 0 if $i \neq j$), and $\mathbb{S}^A_{Esh}$ is Eshelby's tensor that depends on $\mathbb{C}^{eff}$ and on the inclusion's morphology. For a spherical grain immersed in an isotropic aggregate, Eshelby's tensor reads as follows:

$$\mathbb{S}^g_{Esh} = \frac{(1+\nu^{eff})}{3(1-\nu^{eff})}\mathbb{J} + \frac{2(4-5\nu^{eff})}{15(1-\nu^{eff})}\mathbb{K} \tag{5.3}$$

where ν^{eff} is the aggregate's Poisson's ratio, and $\mathbb{J}$ and $\mathbb{K}$ are the fourth order spherical and deviatoric projection tensors, respectively ($\mathbb{J}_{ijkl} = \frac{1}{3}(\delta_{ij}\delta_{kl})/2$ and $\mathbb{K}$=$\mathbb{I} - \mathbb{K}$).

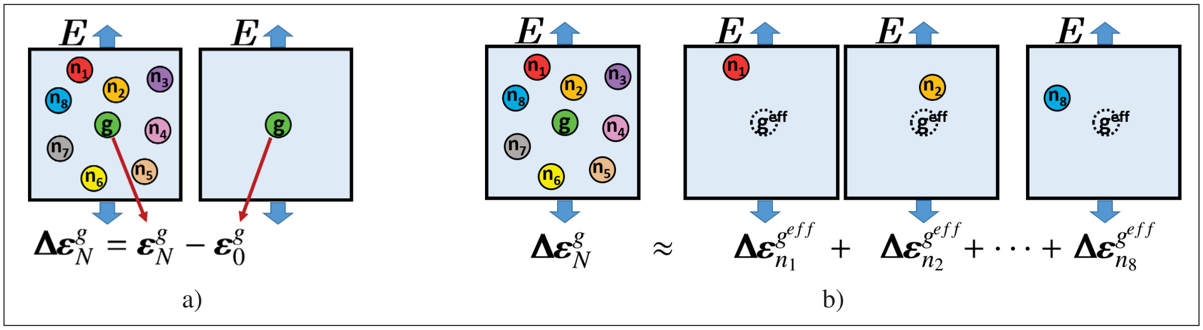

a) b)

Figure 5.1 Neighborhood effect (a) definition and (b) approximation visual representations when the material is submitted to an overall uniform strain loading $\boldsymbol{E}$. (a) Grain g's strain deviation due to the neighborhood N ($\boldsymbol{\Delta\varepsilon}^g_N$) is quantified by the difference between grain g's strain tensor in the polycrystalline aggregate ($\boldsymbol{\varepsilon}^g_N$) and grain g's strain tensor in an infinite matrix having the aggregate's homogenized properties ($\boldsymbol{\varepsilon}^g_0$). (b) $\boldsymbol{\Delta\varepsilon}^g_N$ is approximated by summing each neighboring grain n_i's individual influence on a grain g^{eff} in which the properties have been replaced by the homogenized aggregate's properties. Both grains relative positions remains identical as in the aggregate ($\overrightarrow{gn_i} = \overrightarrow{g^{eff}n_i}$) (Bretin *et al.*, 2019a).

$\boldsymbol{\Delta\varepsilon}^{g}_{N}$, as illustrated in Fig. 5.1b, is approximated by Bretin *et al.* (2019a):

$$\boldsymbol{\Delta\varepsilon}^{g}_{N} \approx \sum_{i=1}^{N} \boldsymbol{\Delta\varepsilon}^{g^{eff}}_{n_i} \tag{5.4a}$$

$$\text{with} \quad \boldsymbol{\Delta\varepsilon}^{g^{eff}}_{n_i} = \boldsymbol{\varepsilon}^{g^{eff}}_{n_i} - \boldsymbol{\varepsilon}^{g^{eff}}_{0} = \boldsymbol{\varepsilon}^{g^{eff}}_{n_i} - \boldsymbol{E} \tag{5.4b}$$

where the index “eff” means that the grain’s mechanical properties are replaced by the aggregate’s homogenized properties, and $\boldsymbol{\Delta\varepsilon}^{g^{eff}}_{n_i}$ is the strain deviation observed in the grain g^{eff} immersed with the grain n_i in an infinite homogeneous matrix having the aggregate’s homogenized properties and both grains’ relative position $\overrightarrow{gn_i}$ is identical as in the aggregate. Approximation 5.4 was tested in Bretin *et al.* (2019a) on single-phase materials with high elastic anisotropy and has shown excellent accuracy. It was also shown that the more grain g elastic properties differ from the effective properties, the less accurate this approximation is. This observation might affect the approximation accuracy in the case of a two-phase material which hasn’t been tested.

A data-driven empirical fitting model was proposed in Bretin *et al.* (2019b) to predict $\boldsymbol{\Delta\varepsilon}^{g^{eff}}_{n_i}$ values as:

$$\boldsymbol{\Delta\varepsilon}^{g^{eff}}_{n_i} = \mathbb{A}^{\overrightarrow{gn_i}}(\mathbb{C}^{n_i}) : \boldsymbol{E} \tag{5.5a}$$

$$\text{with} \quad \mathbb{A}^{\overrightarrow{gn_i}}_{ijkl}(\mathbb{C}^{n_i}) = \begin{cases} \mathbb{U}^{\overrightarrow{gn_i}}_{ijklmnop}\left(\mathbb{C}^{n_i}_{mnop} - \mathbb{C}^{eff}_{mnop}\right) & \text{if} \quad k \geq l \\ 0 & \text{else} \end{cases} \tag{5.5b}$$

where $\mathbb{U}^{\overrightarrow{gn_i}}$ is an eighth-order tensor identified from a specific set of $\boldsymbol{\Delta\varepsilon}^{g^{eff}}_{n_i}$ values pre-predicted by a FE model for a given $\mathbb{C}^{eff}$. The tensor $\mathbb{U}^{\overrightarrow{gn_i}}$ is identified for each neighboring grain relative position $\overrightarrow{gn_i}$ that we wish to account for into the neighborhood effect (see Bretin *et al.* (2019b) for more details on $\mathbb{U}^{\overrightarrow{gn_i}}$ identification methodology). Eq. 5.5 is base on the fact that the problem is elastic-linear and thus the strain variation observed for a loading $\boldsymbol{E}$ can be decomposed as follow:

$$\boldsymbol{E} = \sum_{i=1}^{3}\sum_{j=i}^{3} E_{ij}\boldsymbol{Eij} \quad \Rightarrow \quad \boldsymbol{\Delta\varepsilon}^{g^{eff}}_{n_i}(\boldsymbol{E}) = \sum_{i=1}^{3}\sum_{j=i}^{3} E_{ij}\boldsymbol{\Delta\varepsilon}^{g^{eff}}_{n_i}(\boldsymbol{Eij}) \tag{5.6}$$

This expression is true in elasticity but is inexact for a nonlinear behavior.

Combining Eq. 5.1 to 5.5 yields to the following formulation of a grain's mean strain tensor:

$$\boldsymbol{\varepsilon}_N^g = \boldsymbol{\varepsilon}_0^g + \sum_{i=1}^{N} \boldsymbol{\Delta\varepsilon}_{n_i}^{g^{eff}} = \mathbb{A}_N^g : \boldsymbol{E} \tag{5.7a}$$

$$\text{with} \quad \mathbb{A}_N^g = \mathbb{A}_{Esh}^g + \sum_{i=1}^{N} \mathbb{A}^{\overrightarrow{gn_i}}(\mathbb{C}^{n_i}) \tag{5.7b}$$

Finally, the homogenization theory requires that the localization tensors spatial average is equal to $\mathbb{I}$, implying that $\langle \boldsymbol{\varepsilon}_{CA}^g \rangle_g = \boldsymbol{E}$, where the $\langle \cdot \rangle_g$ denotes the spatial average value over all grains. Therefore, a CA grain's mean strain tensor is defined as:

$$\boldsymbol{\varepsilon}_{CA}^g = \mathbb{A}_{CA}^g : \boldsymbol{E} \tag{5.8a}$$

$$\text{with} \quad \mathbb{A}_{CA}^g = \left\langle \mathbb{A}_N^g \right\rangle_g^{-1} : \mathbb{A}_N^g \tag{5.8b}$$

The Kelvin structure, which is a periodic structure where grains are represented by truncated octahedron (Fig. 5.2a), is used in the CA model to represent polycrystalline aggregates. That way, all grains have the same size and shape and are considered as spheres. A Kelvin cells radius is considered in the following as the reference unit distance. In the present work, only the neighboring grains within a radius of 3 grain's diameters are considered in the neighborhood effect calculations (Eq. 5.4a). They correspond to the first 258 closest grains such that $||\overrightarrow{gn_i}|| \leq 6$, where $\overrightarrow{gn_i}$ is the vector formed by grains g and n_i centroids as illustrated in Fig. 5.2b. With the aim of comparing CA model with FE model predictions, CA boundary conditions can be defined periodically through the way grains' neighborhoods are defined: grains located at the aggregate's edges have their neighborhood composed with the grains located on the opposite sides as illustrated in Fig. 5.2c.

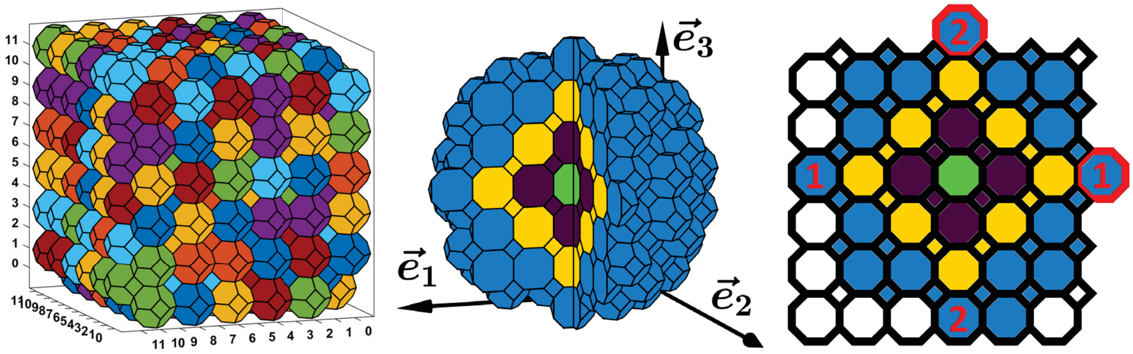

a) b) c)

Figure 5.2 (a) Kelvin structured aggregate (432 grains); (b) Representation of a grain and its 3 neighboring grains' layers (258 grains); (c) 2D illustration of a grain's neighborhood definition taking into account the aggregate's periodicity: some grains (highlighted in red) can be accounted twice due to periodicity.

5.2.2 Constitutive equations for single crystals: Meric-Cailletaud's model

Under the small strain assumption, a grain's viscoplastic strain tensor resulting from slips on different slip systems can be expressed as:

$$\boldsymbol{\varepsilon}^g = \boldsymbol{\varepsilon_e}^g + \boldsymbol{\varepsilon_v}^g \tag{5.9a}$$

$$\boldsymbol{\varepsilon_e}^g = \mathbb{C}^{g\ -1} : \boldsymbol{\sigma}^g \tag{5.9b}$$

$$\boldsymbol{\varepsilon_v}^g = \sum_{s=1}^{12} \gamma_s^g \boldsymbol{m}_s^g \tag{5.9c}$$

where $\boldsymbol{\varepsilon_e}^g$ and $\boldsymbol{\varepsilon_v}^g$ correspond respectively to the grain's elastic and viscoplastic strain tensors, γ_s^g is the slip density of the grain's slip system s, and $\boldsymbol{m}_s^g$ is the Schmid tensor of the grain g's slip system s defined as:

$$\boldsymbol{m}_s^g = \frac{1}{2}\left(\vec{\boldsymbol{l}}_s^g \otimes \vec{\boldsymbol{n}}_s^g + \vec{\boldsymbol{n}}_s^g \otimes \vec{\boldsymbol{l}}_s^g\right) \tag{5.10}$$

where $\vec{\boldsymbol{n}}_s^g$ is the normal to the slip plane and $\vec{\boldsymbol{l}}_s^g$ is the slip direction. The 12 octahedral slip systems shown in Table 5.a-2 were considered. A grain's resolved shear stress τ_s^g (RSS) is computed by means of $\boldsymbol{m}_s^g$ as:

$$\tau_s^g = \boldsymbol{\sigma}^g : \boldsymbol{m}_s^g \tag{5.11}$$

Meric-Cailletaud's model (Méric *et al.*, 1991), inspired by Amstrong and Frederick phenomenological model (Frederick & Armstrong, 2007) describing metals macroscopic behavior with kinematic and isotropic hardening, modified this model to extend its application to the study of metallic cubic crystal behavior. A grain's slip system viscoplastic slip rate $\dot{\gamma}_s^g$ is defined as:

$$\dot{\gamma}_s^g = \left(\frac{\tau_s^g - \chi_s^g}{|\tau_s^g - \chi_s^g|}\right)\dot{v}_s^g \tag{5.12a}$$

$$\text{with} \quad \dot{v}_s^g = \left(\frac{\left(|\tau_s^g - \chi_s^g| - r_s^g\right)^+}{K}\right)^n \tag{5.12b}$$

where $(\cdot)^+$ denotes the operator taking the positive part of its argument; K and n are the viscosity parameters; χ_s^g and r_s^g are respectively the kinematic and isotropic hardening.

The kinematic and isotropic hardening are respectively defined as follow:

$$\chi_s^g = c_\chi \alpha_s^g \tag{5.13a}$$

$$\text{with} \quad \dot{\alpha}_s^g = \dot{\gamma}_s^g - d\alpha_s^g|\dot{\gamma}_s^g| \tag{5.13b}$$

$$r_s^g = r_0 + Qb\sum_{u=1}^{12} h_{su}\rho_u^g \tag{5.13c}$$

$$\text{with} \quad \dot{\rho}_s^g = (1 - b\rho_s^g)|\dot{\gamma}_s^g| \tag{5.13d}$$

where α_s^g and ρ_s^g are internal state variables; c_χ and d are material parameters characterizing the kinematic hardening; Q and b are material parameters characterizing the isotropic hardening. The hardening matrix $\boldsymbol{h}$ reflects the self-hardening and the latent hardening between slip systems.

316L austenitic stainless steel (face centered cubic structure) parameters taken from Guilhem *et al.* (2013) work were chosen as an example to demonstrate the CA model benefits. All the simulations presented in this article were performed using the material parameters listed in Appendix 5.a.

5.2.3 Adaptation to non-linear constitutive equations

Bretin *et al.* (2019b) CA model was developed for the study of linear elastic loading using Hooke's law as constitutive law which has been replaced by the Méric-Cailletaud's model in the present work. In the context of VHCF and HCF, materials are submitted to cyclic loads where they can be assumed to remain macroscopically in the elastic regime, meaning that the matrix from the Eshelby's theory is assumed elastic. Also, the assumption that the neighborhood effect can still be linearly decomposed as presented in Eq. 5.5 and 5.6, and the resulting errors from this decomposition are negligible, are made. Finally, the assumption that grains' plasticity has a negligible impact on the neighborhood effect is made for the sake of simplicity. Therefore, the CA localization tensor remains identical as in the elastic problem (Section 5.2.1, Eq. 5.8) and thus is considered constant over time:

$$\boldsymbol{\varepsilon}^{g}_{CA}(t) = \mathbb{A}^{g}_{CA} : \boldsymbol{E}(t) \tag{5.14}$$

Using $\boldsymbol{\varepsilon}^{g}_{CA}(t)$ as input, the other state variables are calculated through Meric-Cailletaud's model (Section 5.2.2). The solutions are evaluated at several time points using the Newton-Raphson implicit method as described in Haboussa (2014). In the present work, all state variables ($\boldsymbol{\sigma}^{g}$, $\boldsymbol{\varepsilon_{e}}^{g}$, $\boldsymbol{\varepsilon_{v}}^{g}$, γ^{g}_{s}, ν^{g}_{s}, α^{g}_{s}, ρ^{g}_{s}) were all considered null at the start of each simulation, but non-zero values can be attributed to them in order to account for residual stress, mechanical hardening and/or micro-hardness.

With this formulation (Eq.5.14), each grain's behavior can be predicted separately from others, enabling the prediction of only the grains of interest behavior. Also, as it was the case in Bretin *et al.* (2019b) for an elastic load, complex loading paths can be studied as long as the material remains elastic macroscopically.

5.3 Simulations description and methodology

5.3.1 Finite element models

Finite element method was used as a reference tool to compare with the CA model's results. FE simulations were performed using ABAQUS software to which Meric-Cailletaud's model was implemented using the UMAT function borrowed from SiDoLo software (Pilvin, 2010).

The polycrystalline aggregate's mesh was generated as a Kelvin structure of 432 grains (Fig. 5.2a), which should be sufficient to reach a RVE according to Barbe *et al.* (2001a) and Yang *et al.* (2019). The RVE convergence of the effective responses is also confirmed in Section 5.4.1.1. After a mesh convergence study of the mean state variables (Appendix 5.b), a mesh with an average of 1567 tetrahedral elements with quadratic interpolation per grain was selected.

Periodic boundary conditions (PBC) were applied to the mesh: the displacement of all nodes belonging to the mesh boundary ($\vec{\boldsymbol{u}}_-$) was linked to the displacement of its homologous point on the opposite side ($\vec{\boldsymbol{u}}_+$) such that:

$$\vec{\boldsymbol{u}}_-(t) = \boldsymbol{E}(t) \cdot \vec{\boldsymbol{x}} + \vec{\boldsymbol{u}}_+(t), \qquad \forall \vec{\boldsymbol{x}} \in \delta V \tag{5.15}$$

where $\vec{\boldsymbol{x}}$ is a the vector separating the two nodes, and $\boldsymbol{E}$ is the applied strain load.

The stress, strain, viscoplastic strain and cumulative viscoplastic slip (respectively noted $\boldsymbol{\sigma}^{el}$, $\boldsymbol{\varepsilon}^{el}$, $\boldsymbol{\varepsilon}_p^{el}$, $\boldsymbol{v}_s^{el}$) are extracted from each element at each time increment. Grains' mean values are obtained by averaging the values of the elements composing the grain weighted by the element volume ($\bullet^g = \left\langle \bullet^{el} \right\rangle_{el}$). Effective values are obtained by averaging the 432 grains' mean values (all grains having the same volume).

5.3.2 Studied variables

The distribution within the polycrystal and the evolution during the loading of the following grain variables, which are related to the grain's susceptibility to plastify and initiate a crack, were studied throughout the present work:

- The von Mises equivalent stress σ^g_{eq} :

$$\sigma^g_{eq} = \sqrt{\frac{3}{2}\boldsymbol{s}^g : \boldsymbol{s}^g} \tag{5.16}$$

  where $\boldsymbol{s}^g$ is the deviatoric stress.

- The von Mises equivalent viscoplastic strain:

$$\varepsilon^g_{v\ eq} = \sqrt{\frac{2}{3}\boldsymbol{\varepsilon_v}^g : \boldsymbol{\varepsilon_v}^g} \tag{5.17}$$

- The total cumulative viscoplastic slip v^g_Σ defined as the sum of the 12 slip systems cumulative viscoplastic slip v^g_s which is a variable often used in the crack nucleation criterions:

$$v^g_\Sigma = \sum_{s=1}^{12} v^g_s \tag{5.18}$$

5.3.3 Studied loadings

Both FE and CA models were submitted to a strain loading input. Using the effective compliance tensor obtained after the homogenization of FE simulations (see 23), the applied strain tensor is taken as follows:

$$\begin{cases} E_{33} = X, \\ E_{11} = E_{22} = -\nu^{eff} E_{33}, \\ E_{12} = E_{23} = E_{13} = 0, \end{cases} \tag{5.19}$$

where X is the desired strain amplitude. This strain loading yields to an uni-axial stress loading along $\vec{e}_3$ (all components $\Sigma_{ij} = 0$, except Σ_{33}) until the material reaches its macroscopic elastic limit which is observed later on (Section 5.4.1 Fig. 5.4a) at $E_{33} \approx 0.08\%$ and $\Sigma_{33}^{eff} \approx 134$ MPa. Above this point, the resulting stress is no longer uni-axial and lateral stresses appear.

Four loadings verifying Eq. 5.19 were studied, namely:

- A monotonic tensile load up to $E_{33} = 0.3\%$.
- Three tension-compression cyclic loads with a load ratio $R = -1$ and strain amplitudes ΔE of 0.06%, 0.08% and 0.1%.

Only 8 fatigue cycles were simulated with the FE due to the CPU time necessary to run these simulations, but more cycles could have easily been simulated using the CA model (see section 5.4.3 regarding the CPU times). Each simulation was performed at a constant strain rate of $\dot{E}_{33} = 10^{-3} s^{-1}$.

5.3.4 Crystallographic orientations' distribution

A total of 6 different polycrystalline aggregates were studied. Three sets of 432 orientations (S_1, S_2, S_3) were randomly generated using the quaternion method (Altmann, 2005; Shoemake, 1992) and distributed over the aggregate (Fig. 5.2a) with two different methods:

- $S_i.R$: Orientations are distributed randomly over the aggregate.
- $S_i.C$: Orientations are distributed using CA's equations such that a high RSS concentration is generated on a given grain's slip system.

CA's ability to identify orientations' sets generating high RSS concentrations has been proven by Bretin *et al.* (2019b). The value $\tau^g_{s\ 0.01\%}$, which represents a grain's slip system RSS at the end of a monotonic load at $E_{33} = 0.01\%$ noted $\boldsymbol{E_{0.01\%}}$ (the aggregate is assumed to remain fully elastic at this strain level), defined as:

$$\begin{cases} \tau^g_{s\ 0.01\%} = \tau^g_{s\ 0} + \sum\limits_{n_i} \Delta\tau^g_{s\ n_i} & (5.20\text{a}) \\ \text{with} \quad \tau^g_{s\ 0} = \mathbb{C}^g : \mathbb{A}^g_{Esh} : \boldsymbol{E}_{\mathbf{0.01\%}} : \boldsymbol{m}^g_s & (5.20\text{b}) \\ \text{and} \quad \Delta\tau^g_{s\ n_i} = \mathbb{C}^g : \mathbb{A}^{\overrightarrow{gn_i}} : \boldsymbol{E}_{\mathbf{0.01\%}} : \boldsymbol{m}^g_s & (5.20\text{c}) \end{cases}$$

was used to evaluate a grain's susceptibility to plastify. $\tau^g_{s\ 0.01\%}$ is similar to the Schmid's Factor with the difference that the neighborhood effect is accounted for in the variable. The methodology to generate $S_i.C$ orientations' distributions was as follows: first, $\tau^g_{s\ 0}$ is calculated for each orientation of the set (432) and each slip system (12). The orientation and the corresponding slip system s_M showing $\tau^g_{s\ 0}$ highest value among the 432-orientations set is assigned to the aggregate's central grain, which will be called grain c in the sequel. Then, for each of its 258 neighboring grains n_i (from the closest to the farthest), $\Delta\tau^c_{s_M\ n_i}$ is calculated for each remaining orientation of the set and the orientation showing the highest value is attributed to that neighboring grain. Once the 258 neighboring grains accounted for in the neighborhood effect of grain c have their orientation attributed, the remaining orientations of the set are randomly distributed to the 176 remaining aggregate's grains ($= 432 - 1 - (258 - 3)$ (3 orientations are counted twice in the neighborhood effect as illustrated in Fig. 5.2c)).

For each distribution $S_i.R$ and $S_i.C$ generated, Fig. 5.3 displays the absolute value of $\tau^g_{s\ 0.01\%}$ as a function of their part due to the grain's orientation ($|\tau^g_{s\ 0}|$). All the grains from the $S_i.R$ distributions have a RSS value close to their $\tau^g_{s\ 0}$ value within plus or minus 2.7 MPa. A maximum stress deviation due to the neighborhood effect of 2.7 MPa is observed for the $S_i.R$ distributions. In the case of $S_i.C$ distributions, all values are also within this range ($\left|\sum_{n_i} \Delta\tau^g_{s\ n_i}\right| \leqslant 2.7$ MPa) except for some grains whose the neighborhood effect is much more pronounced. These grains correspond to grain c and its close neighbors. The maximum RSS observed in $S_i.R$ distributions is 9.6 MPa whereas it is 21.3 MPa for $S_i.C$ distributions. The aggregate can be considered fully elastic and so linear before any grain reaches its critical RSS of 40 MPa. Therefore, the first signs of plasticity would occur in the grain with the maximum RSS which for $S_i.C$

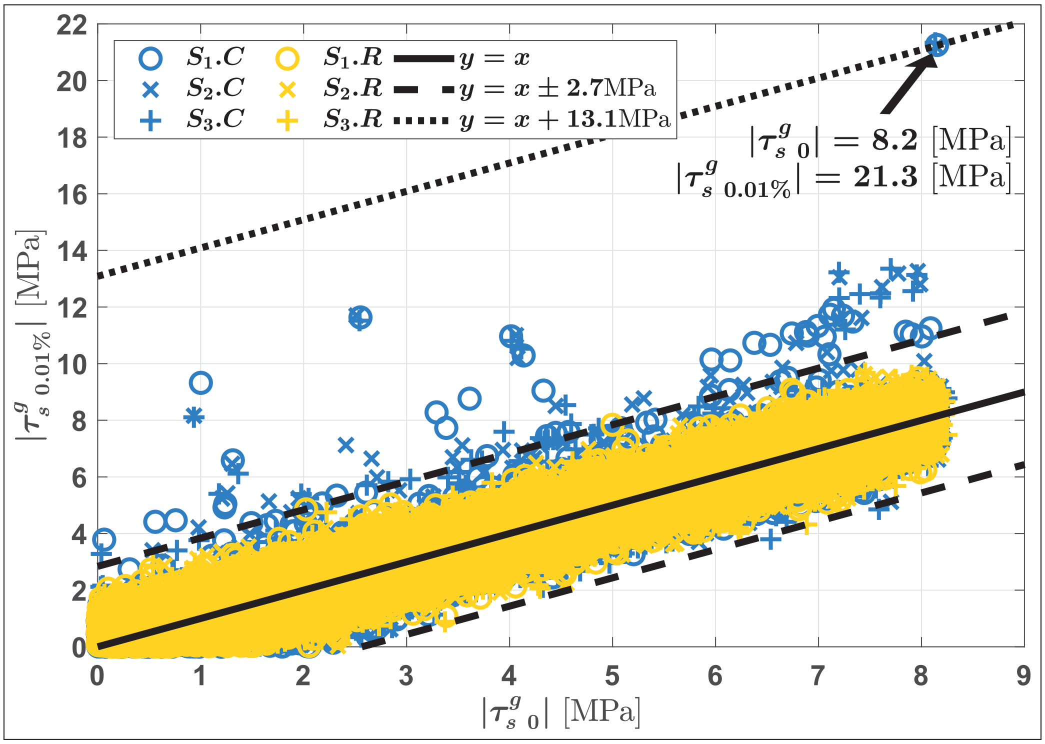

Figure 5.3 Grains' RSS predicted with the CA model after a monotonic load at $E_{33} = 0.01\%$ ($|\tau^g_{s\ 0.01\%}|$) as a function of its part due to the grain's orientation ($|\tau^g_{s\ 0}|$) for each orientations' distribution generated. $|\tau^g_{s\ 0.01\%}|$ is related to the susceptibility of a grain's slip system to plastify. Orientations are randomly distributed in $S_i.R$ distributions (with a maximum stress variation $\sum_{n_i} \Delta\tau^g_{s\ n_i}$ due to the neighborhood observed at 2.7 MPa), whereas they are specifically distributed in $S_i.C$ distributions to generate a high RSS on a given grain's slip system, hence the maximum RSS value observed at 21.3 MPa (+13.1 MPa due to the neighborhood effect).

distributions would be at $E^{eff}_{33} = 40/21.3 \times 0.01\% = 0.019\%$ and for $S_i.R$ distributions at $E^{eff}_{33} = 40/9.6 \times 0.01\% = 0.042\%$. The macroscopic Young's modulus being of 196 MPa, these values correspond to a true elastic limit of $\Sigma^{eff}_{33} = 37$ MPa and $\Sigma^{eff}_{33} = 82$ MPa, respectively. These values are way below the macroscopic elastic limit predicted at $\sigma_y = 134$ MPa in Figure 5.4a. $S_i.C$ distributions true elastic limit is more than twice that of $S_i.R$ and are even lower than the Mailander theoretical fatigue limit (Lalanne, 2002) $\sigma_f = 0.65\sigma_y = 87$ MPa, showing the importance of the neighborhood effect on a grain's behavior.

5.4 Results and discussion

5.4.1 Monotonic load

The mechanical behavior of the polycrystalline aggregates submitted to the tension load up to $E_{33} = 0.3\%$, leading to plastic deformation, was studied using FE and CA models for each orientations' distributions generated ($S_i.R$ and $S_i.C$). Fig. 5.4 presents the results of these simulations at the macroscopic elastic limit ($t = 0.8s.$, $E_{33}^{eff} = 0.08\%$, $\Sigma_{33}^{eff} \approx 134$ MPa) and at the load's end ($t = 3s.$, $E_{33} = 0.3\%$, $\Sigma_{33}^{eff} \approx 312$ MPa):

- Fig. 5.4a presents the effective strain-stress curves.
- Fig. 5.4b compares $max\left(\left|\tau_{s\ 0.01\%}^{g}\right|\right)_{s}$ predictions (grain's maximum absolute RSS predictions at $E_{33}^{eff} = 0.01\%$) obtained with FE and CA models, where $max(\bullet_{s}^{g})_{s}$ designs the maximum value among the 12 slip systems for a given grain g.
- Fig. 5.4c and 5.4d show the total cumulative viscoplastictic slip (v_{Σ}^{g}) predicted with the FE method as a function of $max\left(\left|\tau_{s\ 0.01\%}^{g}\right|\right)_{s}$ from FE model. v_{Σ}^{g} statistics are also shown in the figure for each distribution method alongside with a linear regression for all the data.
- Fig. 5.4e and 5.4f compare v_{Σ}^{g} FE and CA predictions. The statistics of the models predictions differences are also shown in the figure alongside with a linear regression for all the data.
- Fig. 5.4g and 5.4h show v_{Σ}^{g} predicted with the FE method as a function of $\sigma_{eq\ FE}^{g}$ from FE model. $\sigma_{eq\ FE}^{g}$ statistics are also shown in the figure for each distribution method alongside with a linear regression of all the data.

5.4.1.1 $S_i.R$ and $S_i.C$ orientations' distributions comparison

In figure 5.4a, each orientations' distribution shows an identical effective strain-stress curve, meaning that 432 grains is enough to reach a RVE, and also that $S_i.R$ and $S_i.C$ distribution methods have no impact on the aggregate's macroscopic behavior. Also, still from a macroscopic point of view, v_{Σ}^{g} mean values displayed in Fig. 5.4c and 5.4d, which relate to the total plasticity accumulated over the aggregates, show only a maximum difference of 5% between the two

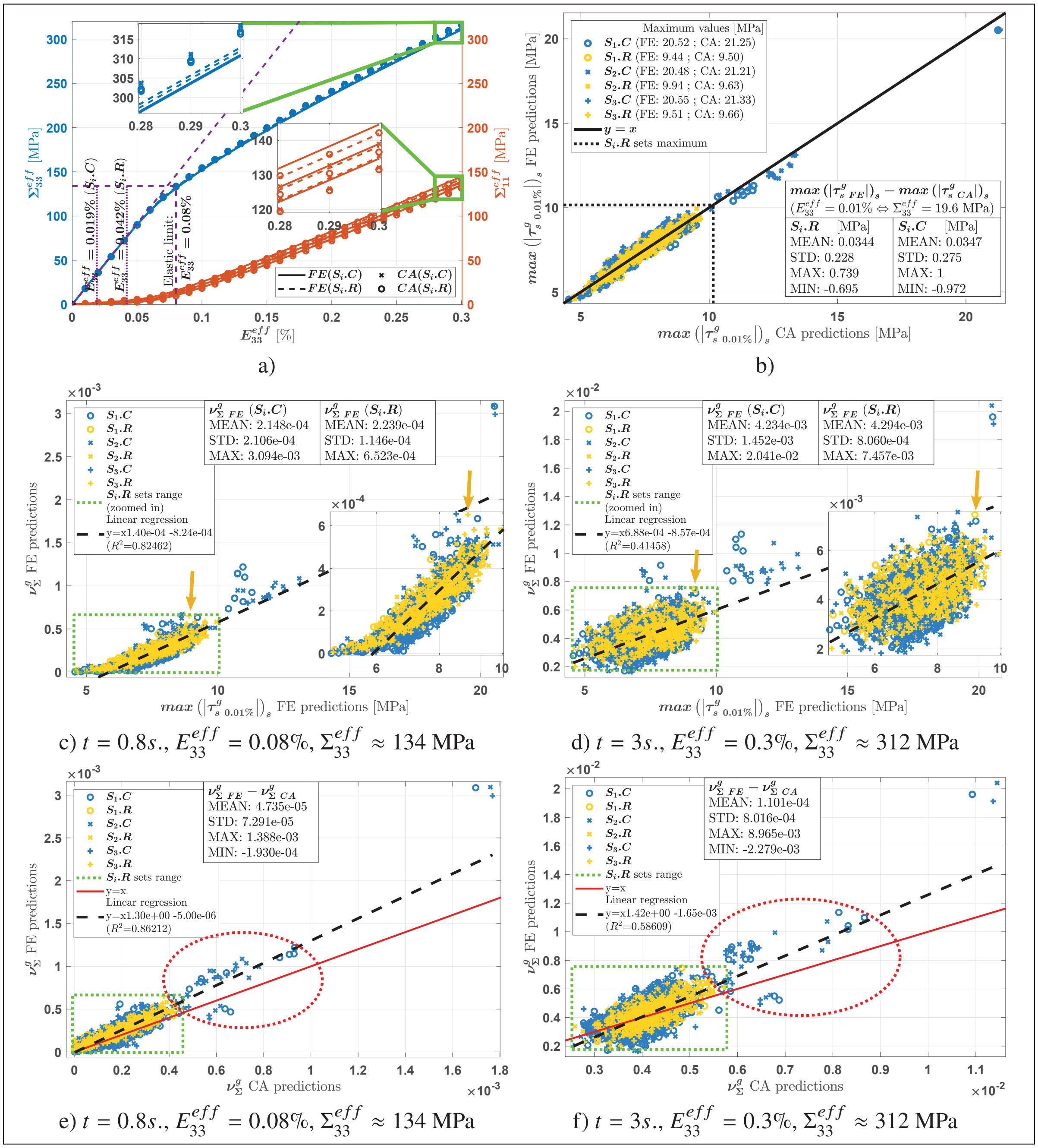

a)

b)

c) $t = 0.8s.$, $E_{33}^{eff} = 0.08\%$, $\Sigma_{33}^{eff} \approx 134$ MPa

d) $t = 3s.$, $E_{33}^{eff} = 0.3\%$, $\Sigma_{33}^{eff} \approx 312$ MPa

e) $t = 0.8s.$, $E_{33}^{eff} = 0.08\%$, $\Sigma_{33}^{eff} \approx 134$ MPa

f) $t = 3s.$, $E_{33}^{eff} = 0.3\%$, $\Sigma_{33}^{eff} \approx 312$ MPa

Figure 5.4 FE and CA simulations of a tensile test on polycrystalline's aggregate for each orientations' distributions ($S_i.R$:orientation randomly distributed; $S_i.C$:orientation distributed to generate RSS concentration): (a) effective strain-stress curves along $\vec{e}_3$ and $\vec{e}_1$ axes; (b) comparison between FE and CA $max\left(\left|\tau_{s\ 0.01\%}^{g}\right|\right)_s$ predictions; (c-d) ν_{Σ}^{g} predicted with the FE method at t=0.8s and t=3s, respectively, as a function of $max\left(\left|\tau_{s\ 0.01\%}^{g}\right|\right)_s$ FE predictions alongside with ν_{Σ}^{g} statistics and a linear regression of all the data; (e-f) comparison between ν_{Σ}^{g} FE and CA prediction alongside with predictions differences statistics between both models and a linear regression of all the data.

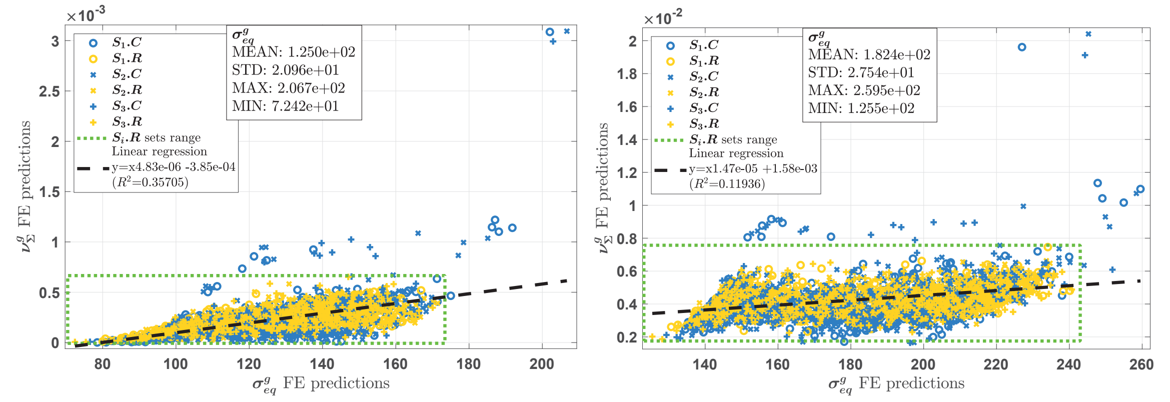

g) $t = 0.8s.$, $E^{eff}_{33} = 0.08\%$, $\Sigma^{eff}_{33} \approx 134$ MPa h) $t = 3s.$, $E^{eff}_{33} = 0.3\%$, $\Sigma^{eff}_{33} \approx 312$ MPa

Figure 5.4 (continued): (g-h) ν^g_Σ from FE results as a function of σ^g_{eq} alongside with σ^g_{eq} statistics and a linear regression of all the data.

models, meaning that the total amounts of plasticity generated in both distributions are really close.

Even though $S_i.R$ and $S_i.C$ show the same macroscopic behavior, they are both really different microscopically. The maximum ν^g_Σ value observed for $S_i.C$ is three times higher than that observed for $S_i.R$ and its standard deviation twice higher (Fig. 5.4c-5.4d). For each orientations' distribution, similarly as for the $max\left(\left|\tau^g_{s\ 0.01\%}\right|\right)_s$ values, the 10 grains showing the highest ν^g_Σ values are located differently, depending on the distribution method: they are sporadically located within the aggregate for $S_i.R$ while they are all located in grain c and its neighboring grains' first layer for $S_i.C$. All the plasticity is located in a concentric location for $S_i.C$, due to the fact that the grain c and its neighbors are undergoing high stress concentration resulting in a concentration of the plastic strain, whereas plasticity is spread over the aggregate for $S_i.R$ due to a more homogeneous distribution of stress within the aggregate.

These differences highlights the importance of the neighborhood effect and of the aggreagate's elastic behavior on its plastic behavior. $S_i.C$ orientations' distributions, generated based on grains' elastic behavior, would have significantly more chance to crack than $S_i.R$ distributions even though their macroscopic behavior are identical.

5.4.1.2 Plasticity localization

The highest v_Σ^g value observed is located in grain c from $S_i.C$ orientations' distributions, in which the orientations were distributed to maximize $|\tau^c_{s\ 0.01\%}|$ on one of its slip systems. This value (~ 0.003 at $E_{33}^{eff} = 0.08\%$, ~ 0.020 at $E_{33}^{eff} = 0.3\%$) is at least twice that observed for any other grain (> 0.0012 at $E_{33}^{eff} = 0.08\%$, > 0.0116 at $E_{33}^{eff} = 0.3\%$).

Different parameters have been tested to find a correlation with v_Σ^g in order to be able to predetermine grains' v_Σ^g relative values. From figures 5.4c-5.4d it can be observed that the grains showing the highest v_Σ^g values are those with the highest $max\left(\left|\tau^g_{s\ 0.01\%}\right|\right)_s$ values. A correlation was found between those two variables from the linear regression at $E_{33} = 0.08\%$ with a regression coefficient of determination $R^2 = 0.82$. However, this correlation does not yield as high R^2 values for $E_{33} = 0.3\%$ ($R^2 = 0.41$). This can be explained by the fact that only one slip system is activated within grains at $E_{33} = 0.08\%$, whereas several slip systems are activated at $E_{33} = 0.3\%$. Therefore, the average absolute RSS over the 12 slip systems ($\left\langle\left|\tau^g_{s\ 0.01\%}\right|\right\rangle_s$) has also been considered, and the regression coefficients of determination can be found in Table 5.1. By considering $\left\langle\left|\tau^g_{s\ 0.01\%}\right|\right\rangle_s$, an improvement in these coefficients of determination is found for high strains, but it is still not enough to use these parameters to predetermine the grains relative plasticity distribution with certainty above the macroscopic limit.

Table 5.1 Correlation between v_Σ^g and $\tau^g_{s\ 0.01\%}$: regression over the $6 \times 432 = 2592$ grains (only grains with $v_\Sigma^g > 10^{-5}$ are considered in the regression).

v_Σ^g regression equations	Regression coefficients of determination R^2					
	E_{33}^{eff} =	0.06%	0.08%	0.1%	0.2%	0.3%
$y = a + b \times max\left(\left|\tau^g_{s\ 0.01\%}\right|\right)_s$		0.83	0.82	0.78	0.51	0.41
$y = a + b \times \left\langle\left|\tau^g_{s\ 0.01\%}\right|\right\rangle_s$		0.71	0.70	0.71	0.71	0.67
$y = a + b \times max\left(\left|\tau^g_{s\ 0.01\%}\right|\right)_s + c \times \left\langle\left|\tau^g_{s\ 0.01\%}\right|\right\rangle_s$		0.87	0.88	0.85	0.72	0.68

Using these parameters to localize plasticity concentration has some limits: the highest ν_{Σ}^{g} values from $S_i.R$ distributions are not necessarily those corresponding to the highest $\tau_{\Sigma\ 0.01\%}^{g}$ values (see dot pointed by yellow arrow in Fig. 5.4c-5.4d), and a ratio of 2 can be found between grains with the same $max\left(\left|\tau_{s\ 0.01\%}^{g}\right|\right)_s$ value. In fact, $max\left(\left|\tau_{s\ 0.01\%}^{g}\right|\right)_s$ and $\left\langle\left|\tau_{s\ 0.01\%}^{g}\right|\right\rangle_s$ are insufficient to localize plasticity concentration because $\tau_{s\ 0.01\%}^{g}$ depends on the neighborhood elastic strain and does not consider the neighborhood plastic strain, which can also have the effect to increase or decrease neighboring grains' RSS. At $E_{33}^{eff} < 0.1\%$, grains' plastic strains are low and therefore have a low impact on their neighborhood explaining the good regression coefficients of determination. At higher loads, grains' plastic strains increase, lowering the regression accuracy.

Nonetheless, within the frame of macroscopic stress levels typically yielding HCF and VHCF, $max\left(\left|\tau_{s\ 0.01\%}^{g}\right|\right)_s$ remains a good parameter to locate plasticity concentration within polycrystalline aggregates at low plastic strain without actually predicting the actual plasticity fields intensity.

The von Mises stress σ_{eq}^{g} is sometimes used as an indicator to a grain's susceptibility to plastification. It can be observed from the FE results exposed in Fig. 5.4g-5.4h that this variable is not a good indicator of grain's damage. Several grains with a high ν_{Σ}^{g} value show a von Mises stress below the average, as revealed by the low regression coefficients of determination.

5.4.1.3 CA and FE predictions comparison

From a macroscopic point of view, CA and FE models show the same results. Only a difference of ~ 5.6 MPa (~ 1.8% of the stress) is observed between the two models in Fig. 5.4a at the end of the load along the loading axis $\vec{e}_3$ at 0.3% deformation.

$\tau_{s\ 0.01\%}^{g}$ CA predictions reported in Fig. 5.4b are in good agreement with the FE predictions as it has already been shown by Bretin *et al.* (2019b). The differences between those two models cancel each other out on average and show a very low standard deviation. The maximum gap (~ 1.0 MPa), observed at the maximum values (~ 21.3 MPa), shows the efficiency of the CA model to predict with accuracy the grains total RSS $\tau^{g}_{s\ 0.01\%}$ and locate the plasticity within the aggregate as shown in the previous section 5.4.1.2.

Conversely, the ν^{g}_{Σ} values predicted by the CA model are not as in good agreement with the FE predictions as it is for $\tau^{g}_{s\ 0.01\%}$. The statistics in Fig. 5.4e-5.4f of the differences between the FE and CA predictions show that, in average, the CA model underestimate the level of plasticity within the grains. This situation worsens for higher loading levels: the linear regression slope increases between $E_{33} = 0.08\%$ and $E_{33} = 0.3\%$. The maximum gap is observed in grain c from $S_i.C$ orientations' distributions for which the maximum ν^{g}_{Σ} is underestimated almost by half by the CA model, when compared to the FE model.

These differences between the CA and FE model predictions can be explained by the fact that the CA model only considers the neighborhood elastic properties but not their plastic state. Bretin *et al.* (2019a) showed, in simple words, that grains with a higher strain along the loading axis have the tendency to decrease the strain level of the neighboring grains aligned with the loading axis ($(\overrightarrow{gn_i}, \vec{\boldsymbol{e}}_{\boldsymbol{3}}) \approx 0°$) and increase the strain level of the neighboring grains perpendicular with the loading axis ($(\overrightarrow{gn_i}, \vec{\boldsymbol{e}}_{\boldsymbol{3}}) \approx 90°$). Grain c from $S_i.C$, having a high ν^{g}_{Σ} value, would then generate strain variations within its neighborhood, but the CA model, considering only the elastic strain from the neighboring grains, would under/overestimate grain c influence on its neighbors strain level. This can be confirmed by observing the dots circled in red in Fig. 5.4e-5.4f. These dots correspond to grain c first layer of neighboring grains. The underestimated grains correspond to those having their strain increased by grain c (the 12 relative positions n_i such that $\overrightarrow{cn_i} = [\pm 1; \pm 1; \pm 1]$, $[\pm 2; 0; 0]$ and $[0; \pm 2; 0]$), and the overestimated grains correspond to those having their strain decreased by grain c (the 2 relative positions $[0; 0; \pm 2]$).

Nonetheless, the classification orders of the grains' ν^{g}_{Σ} values are similar for both models. The linear regression coefficient of determination $R^2 = 0.86$ at $E_{33} = 0.08\%$ suggests that the classification order is, overall, conserved. The grains showing the most important plastic levels are systematically the same for both models, even for the $S_i.R$ sets. When the plasticity level becomes higher, at $E_{33} = 0.3\%$, this coefficient decreases to 0.59, revealing that the CA model applications are limited to low strain levels.

5.4.2 Cyclic load

The orientations' distribution $S_1.C$ was selected to study the impact of a cyclic load on an aggregate with a high stress concentration. The amplitude strain 0.06%, 0.08% and 0.1% were chosen due to the fact that the aggregate starts plastifying macroscopically around 0.08%.

Fig. 5.5 presents the results of these simulations:

- Fig. 5.5a presents the effective strain-stress curve at the 8th cycle for $\Delta E = 0.10\%$.
- Fig. 5.5b compares v_{Σ}^{g} obtained at the end of the first tensile load ($t_{cyc}/4$, where t_{cyc} is a cycle duration) and at the end of the 8th cycle ($8t_{cyc}$).
- Fig. 5.5c-5.5d-5.5e compares FE and CA v_{Σ}^{g} predictions at the end of the 8th cycle for each loading amplitude alongside with the FE predictions statistics and the differences between FE and CA predictions statistics.
- Fig. 5.5f shows the grains' average total viscoplastic slip accumulated during each cycle $\left(v_{\Sigma}^{g}(n_c t_{cyc}) - v_{\Sigma}^{g}((n_c - 1)t_{cyc})\right)$ normalized by $v_{\Sigma}^{g}(t_{cyc}/4)$ predicted by FE and CA models for $\Delta E = 0.10\%$. The monocrystal behavior, such that $\boldsymbol{\varepsilon}^{g}(t) = \boldsymbol{E}(t)$, is also plotted to assess the single crystal cyclic behavior. The cyclic evolution predicted by FE and CA models in grain c and a grain n_i chosen far from grain c influence, such that $\overrightarrow{cn_i} = [6; 6; 2]$, are also shown.
- Fig. 5.5g and 5.5h show the equivalent stress, strain and plastic strain over time predicted by FE and CA models for $\Delta E = 0.10\%$ during the 8th cycle observed in grains c and n_i respectively, such that $\overrightarrow{cn_i} = [6; 6; 2]$.

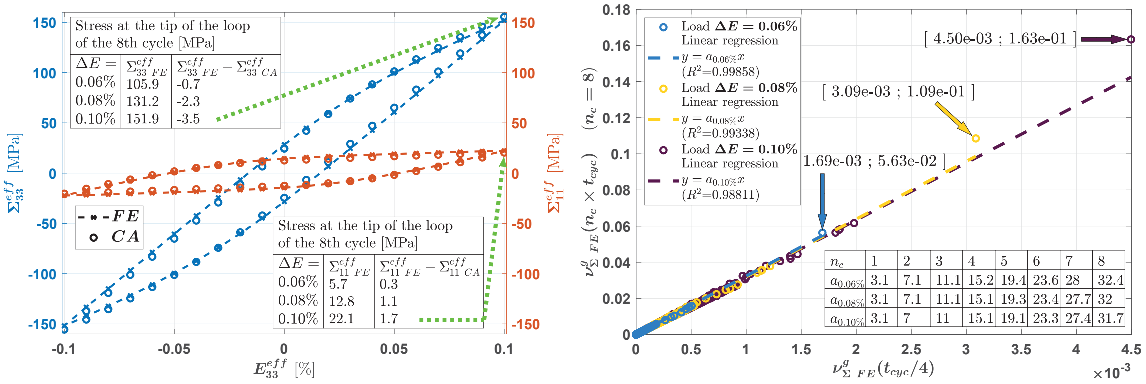

Stress at the tip of the loop of the 8th cycle [MPa]

$\Delta E =$	$\Sigma_{33\ FE}^{eff}$	$\Sigma_{33\ FE}^{eff} - \Sigma_{33\ CA}^{eff}$
0.06%	105.9	-0.7
0.08%	131.2	-2.3
0.10%	151.9	-3.5

Stress at the tip of the loop of the 8th cycle [MPa]

$\Delta E =$	$\Sigma_{11\ FE}^{eff}$	$\Sigma_{11\ FE}^{eff} - \Sigma_{11\ CA}^{eff}$
0.06%	5.7	0.3
0.08%	12.8	1.1
0.10%	22.1	1.7

n_c	1	2	3	4	5	6	7	8
$a_{0.06\%}$	3.1	7.1	11.1	15.2	19.4	23.6	28	32.4
$a_{0.08\%}$	3.1	7.1	11.1	15.1	19.3	23.4	27.7	32
$a_{0.10\%}$	3.1	7	11	15.1	19.1	23.3	27.4	31.7

a) Load $\Delta E = 0.10\%$, 8th cycle

b)

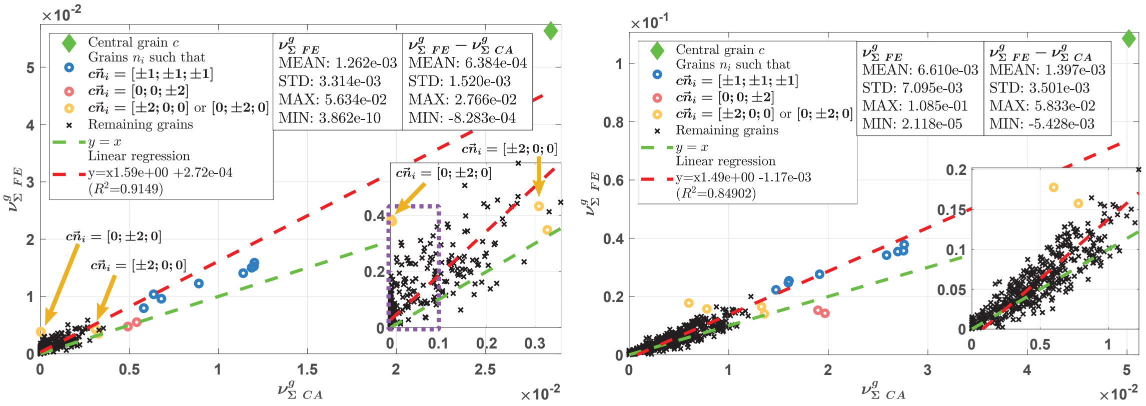

$\nu^g_{\Sigma\ FE}$	$\nu^g_{\Sigma\ FE} - \nu^g_{\Sigma\ CA}$
MEAN: 1.262e-03	MEAN: 6.384e-04
STD: 3.314e-03	STD: 1.520e-03
MAX: 5.634e-02	MAX: 2.766e-02
MIN: 3.862e-10	MIN: -8.283e-04

$\nu^g_{\Sigma\ FE}$	$\nu^g_{\Sigma\ FE} - \nu^g_{\Sigma\ CA}$
MEAN: 6.610e-03	MEAN: 1.397e-03
STD: 7.095e-03	STD: 3.501e-03
MAX: 1.085e-01	MAX: 5.833e-02
MIN: 2.118e-05	MIN: -5.428e-03

c) Load $\Delta E = 0.06\%$, $t = 8t_{cyc}$

d) Load $\Delta E = 0.08\%$, $t = 8t_{cyc}$

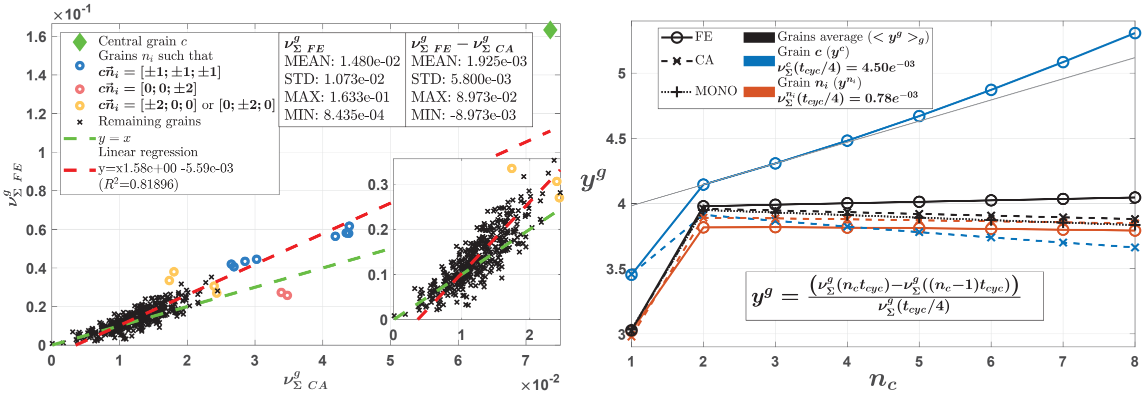

$\nu^g_{\Sigma\ FE}$	$\nu^g_{\Sigma\ FE} - \nu^g_{\Sigma\ CA}$
MEAN: 1.480e-02	MEAN: 1.925e-03
STD: 1.073e-02	STD: 5.800e-03
MAX: 1.633e-01	MAX: 8.973e-02
MIN: 8.435e-04	MIN: -8.973e-03

e) Load $\Delta E = 0.10\%$, $t = 8t_{cyc}$

f) Load $\Delta E = 0.10\%$

Figure 5.5 FE and CA simulations of a cyclic load on a polycrystalline aggregate with the orientations' distribution $S_1.C$ in which a RSS concentration was intentionally generated in grain c: (a) effective strain-stress curves along $\vec{e}_3$ and $\vec{e}_1$ axes predicted by FE and CA models for $\Delta E = 0.10\%$; (b) comparison between ν^g_Σ predicted by FE model at the end of the first tensile load ($t_{cyc}/4$, where t_{cyc} is a cycle duration) and at the end of the 8th cycle ($8t_{cyc}$); (c-e) comparison between FE and CA ν^g_Σ predictions at the end of the 8th cycle alongside with the models differences statistics for each studied load; (f) Grains' average viscoplastic increment predicted by FE and CA models for $\Delta E = 0.10\%$ alongside with the monocrystal behavior and with grains c and n_i cyclic evolution, n_i being chosen far from grain c influence such that $\vec{cn_i} = [6; 6; 2]$.

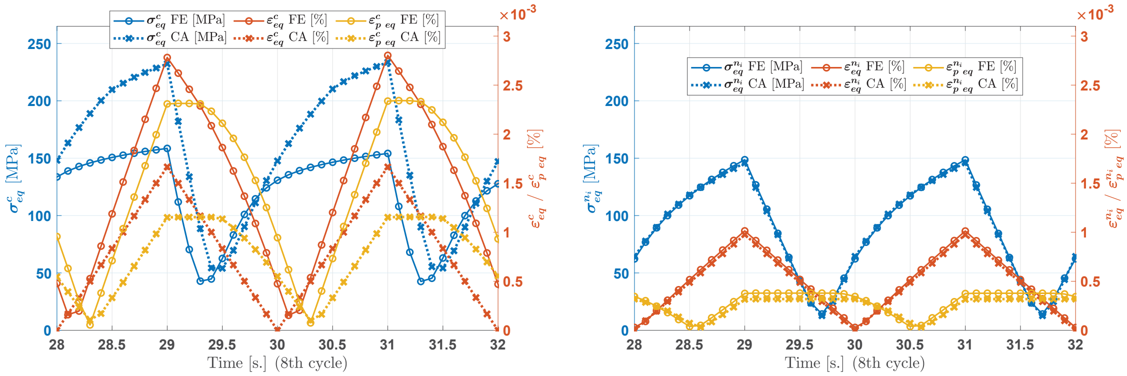

g) Load $\Delta E = 0.10\%$, 8th cycle, $\nu^c_{\Sigma\ FE}(8t_{cyc}) = 0.163$

h) Load $\Delta E = 0.10\%$, 8th cycle, $\nu^{n_i}_{\Sigma\ FE}(8t_{cyc}) = 0.023$

Figure 5.5 (continued): (g-h) equivalent stress, strain and plastic strain over time predicted by FE and CA models for $\Delta E = 0.10\%$ during the 8th cycle observed in grains c and n_i respectively.

5.4.2.1 Plasticity localization

Similarly to the monotonic tensile load, the grain c, where $max\left(\left|\tau^g_{s\ 0.01\%}\right|\right)_s$ was maximized, followed by its close neighbors, is still the grain showing the highest ν^g_Σ values after several cyclic loads, as shown in Fig. 5.5c-5.5e. The linear regressions between the ν^g_Σ values obtained from the FE model at the end of the first tensile load ($t_{cyc}/4$) with the values at the end of the 8th cycle ($8t_{cyc}$) (Fig. 5.5b) show coefficients of determination R^2 superior to 0.98, indicating an excellent fit. This means that the grains' classification from the most to the less plastified is preserved after several cycles. Therefore, all the discussion about plasticity localization in Section 5.4.1.2 can also be applied to cyclic loads, and $max\left(\left|\tau^g_{s\ 0.01\%}\right|\right)_s$ is still a reliable indicator to localize plasticity within pollycrystalline aggregates in the HCF regime.

Nevertheless, grain c values diverge from the linear regressions in Fig. 5.5b and this is even more significant for the highest load amplitude ($\Delta E = 0.1\%$). This observation can be explained by looking at ν^g_Σ increment per cycle in Fig. 5.5f: irrespectively of the grain's orientation, the single crystal behavior starts with a softening during the 2 first cycles followed by a continuous slow hardening. However, this behavior differs when the grains are within a polycrystalline aggregate: several grains show a slow softening even after the second cycle with the FE model. This softening (explained in Section 5.4.2.2) is even more important in grain c where v_{Σ}^{g} increment increases exponentially per cycle, causing grain c deviation from the linear regression in Fig. 5.5b.

5.4.2.2 CA and FE predictions comparison

From a macroscopic point of view, as for the monotonic loads presented in section 5.4.1.3, CA and FE models are in good agreement: a maximum gap of 3.5 MPa along the loading axis ($\sim 2.3\%$ of the stress) is observed for $\Delta E = 0.1\%$ after 8 cycles (Fig. 5.5a).

As for the monotonic loads results, the CA model underestimates v_{Σ}^{g}, when compared to the FE predictions. Again, grain c equivalent stress σ_{eq}^{c} is overestimated, and the equivalent plastic strain $\varepsilon_{p\ eq}^{c}$ is underestimated, as shown in Fig. 5.5g. In this grain, plasticity is twice that of other grains., leading to an important gap between the two models predictions. But if one looks at another grain, far from grain c influence, its v_{Σ}^{g} value is well predicted by the CA model, as shown in Fig. 5.5h.

In the CA model, a grain's strain rate is constant over time, as observed in Fig. 5.5g-5.5h, due to the fact that the tensors $\mathbb{A}_{CA}^{g}$ only depend on neighboring grains' elastic properties and thus are constant over time (Eq. 5.14). Consequently, grains are not affected by their neighborhood plastic behavior. However, it can be observed from the FE predictions that a grain's plastic behavior can highly affect its neighborhood behavior. This phenomenon can be observed by looking at the close neighboring grains of grain c pointed by yellow arrows in Fig. 5.5c: both grains n_i such that $\overrightarrow{cn_i} = [\pm 2; 0; 0]$ have a $max\left(\left|\tau_{s\ 0.01\%}^{g}\right|\right)_{s}$ of 8.6 and 8.7 MPa, and both grains n_i such that $\overrightarrow{cn_i} = [0; \pm 2; 0]$ have a $max\left(\left|\tau_{s\ 0.01\%}^{g}\right|\right)_{s}$ of 7.5 and 7.6 MPa. These values are barely sufficient for $\overrightarrow{cn_i} = [0; \pm 2; 0]$ to reach the critical RSS for $\Delta E = 0.06\%$ ($7.6 \times 0.06\%/0.01\% = 45.6$ MPa is barely superior to $r_0 = 40$ MPa) explaining why these grains' v_{Σ}^{g} values predicted by the CA model are close to zero after 8 cycles, while higher plasticity is predicted by the CA model in the two other grains $\overrightarrow{cn_i} = [\pm 2; 0; 0]$ having higher values of $max\left(\left|\tau_{s\ 0.01\%}^{g}\right|\right)_{s}$. On the other hand, the FE predictions show approximately the same v_{Σ}^{g} value for these four grains because of grain

c high plastic strain dragging its two close neighboring grains and thus increasing their plastic levels, which is not captured by the CA model. As explained in section 5.4.1.3, grain c high plasticity has the effect to increase the strain in the grains with an angle $(\overrightarrow{cn_i}, \vec{\boldsymbol{e}}_{\mathbf{3}})$ close to 90° (for example $\overrightarrow{cn_i} = [\pm 2; 0; 0]$ or $\overrightarrow{cn_i} = [0; \pm 2; 0]$ or $\overrightarrow{cn_i} = [\pm 1; \pm 1; \pm 1]$) and to decrease the strain in the grains with an angle close to 0° (for example $\overrightarrow{cn_i} = [0; 0; \pm 2]$).

The use of the grain's mean values in the CA model (mean strain tensor, mean RSS, etc.) is another reason why so many grains show a v_Σ^g prediction null for $\Delta E = 0.06\%$ with the CA model but plastify in the FE model. The RSS value τ_s^g used in CA model is an average of the local RSS values within the grain which are not homogeneous. At certain spots within the grain, this value can get higher up to the critical RSS leading to the grain's plastification whereas the grain's average RSS does not reach its critical value. Then, as explained previously, this local plasticity would then generate more strain in its surrounding and so more plasticity within the grain. This is a well-known phenomenon observed by authors (Nemat-Nasser & Hori, 1999): using average values and elastic properties leads to stiffer estimates.

Nonetheless, assuming that differences observed between the two models predictions for the grains showing a v_Σ^g close to zero with the CA model are only due to the plastic neighborhood effect, the plasticity generated in these grains remains negligible in comparison to grain c plasticity. For example, considering all the grains with a v_Σ^g predicted by the CA model inferior to 10^{-3} (framed in purple in Fig. 5.5c), the highest value predicted among these grains by the FE model is $4 \cdot 10^{-3}$ for the grain n_i such that $\overrightarrow{cn_i} = [0; \pm 2; 0]$, which are highly influenced by grain c plastic strain. This value of $4 \cdot 10^{-3}$ is approximately 10% of that observed for grain c $(5.6 \cdot 10^{-2})$, and four times lower than the second highest v_Σ^g value.

Another consequence of the strain-stress variations induced by the neighboring grains' plasticity is the grains' cyclic behavior observed with the FE model. In Fig. 5.5f, the single crystal's model shows that at a constant amplitude strain, no matter the crystal orientation, a softening is observed between the two first cycles followed by a continuous slow hardening. This behavior is directly linked to the constitutive law parameters. The same behavior is observed in the CA model due to the fact that the grain's strain amplitudes are also constant over time (Eq. 5.14). But the cyclic behavior observed with the FE model differs: the softening continues after the second cycle at a slower pace. Due to the fact that a grain's plastic strain generates strain variations in its neighboring grains, it also gets a strain variation from its neighboring grains. This means that a plastifying grain generates plasticity in its neighboring grains which, in return, also generates a strain variation in that grain increasing its plasticity. This consequently generates continuous variations of the cyclic strain amplitude to which these grains are submitted to. This phenomenon can be observed through grain *c* and its neighboring grains cyclic behaviors, which their strain amplitudes slightly increase each cycle, following the same trend as v_{Σ}^{c} cycle increment in Fig. 5.5f, explaining their continuous softening predicted by the FE model.

Another source of error might come from the periodicity and the short size of the RVE. Fig. 5.6 shows the grain *c* and its first layer of neighbors in which almost all the plasticity is localized. Due to the PBC, this zone of plasticity is also close to other zones of plasticity, which are its "periodic clones". In the case of the CA model, these zones are too far (further than 3 grains layer) to be accounted for in the neighborhood effect, but in the case of the FE model, due to the short size of the RVE, these clones (6 in total by counting the closest ones) might not be far enough to neglect their influence on each other's behavior due to their high plasticity level.

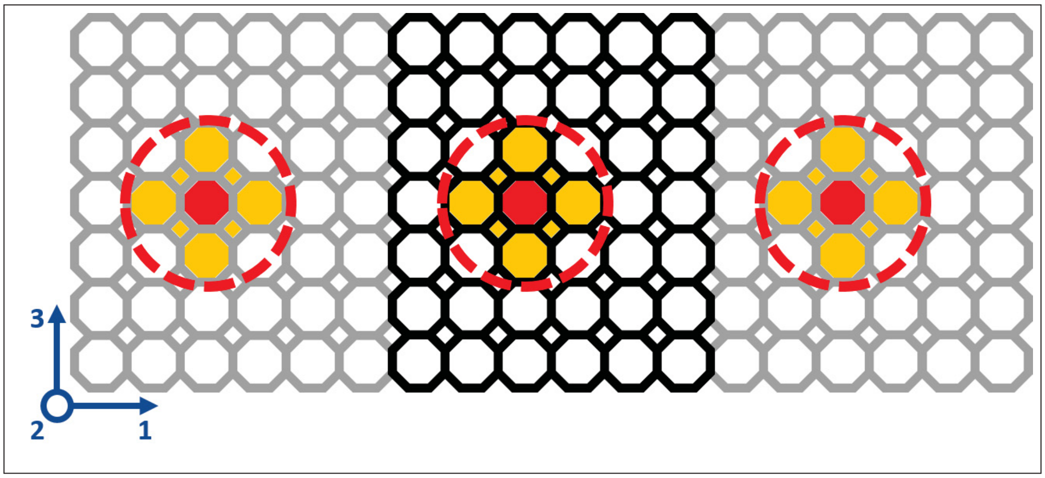

Figure 5.6 2D illustration of the grain *c* and its first layer of neighbors, in which almost all the plasticity is localized, and their periodic "clones" due to the PBC.

Nonetheless, even though the CA model underestimates ν_Σ^g values within grains, the classification orders of the grains' plasticity level are similar for both models. The linear regression coefficient of determination $R^2 > 0.8$ displayed in Fig. 5.5c-5.5e shows that the classification order is overall conserved. The grains showing the most important plastic level are the same for both models. The grains showing the largest prediction differences are those close to the grain showing a high ν_Σ^g value, which are easy to identify thanks to the $max\left(\left|\tau^g_{s\ 0.01\%}\right|\right)_s$ parameter. This proportionality relationship between CA and FE models ν_Σ^g predictions can be explained by the fact that ν_Σ^g is proportional to $max\left(\left|\tau^g_{s\ 0.01\%}\right|\right)_s$ for both models, which they both provide close predictions (Fig. 5.4b).

5.4.3 CPU times

The CPU times for the FE and CA models are compared in Table 5.2. FE simulations were performed on a calculation server using a 16-cores processor with 31.7 GB per core, while the CA model simulations were performed on a laptop equipped with an Intel Core i7-360QM @ 2.4 GHz. The acceleration provided by the CA model is about 1-3×10^4. In other words, what takes hours to simulation with the FE model, takes seconds with the CA model. The 2 hours of FE simulations necessary to calibrated CA's model parameters $\mathbb{U}^{\overrightarrow{gn_i}}$ is negligible in comparison, and they can be reused to study different orientations' distributions and classify their susceptibility to generate early plasticity, as shown in Section 5.5. Also, as grains are linked to each other only by their elastic properties and as these are constant over time in the current model, a grain's state over time can be obtained without processing all the other grains, but only the relevant ones. This allows to only process the critical grains (those with a high $max\left(\left|\tau^g_{s\ 0.01\%}\right|\right)_s$ value) and to focus only on the important grain-neighborhood configurations.

Table 5.2 CPU times comparison between FE and CA models

	Monotonic load	Cyclic load (8 cycles)			CPU time to setup
	$\boldsymbol{E}_{0.3\%}$	$\boldsymbol{E}_{0.06\%}$	$\boldsymbol{E}_{0.08\%}$	$\boldsymbol{E}_{0.10\%}$	CA model's parameters $\mathbb{U}^{\overrightarrow{gn_i}}$
FE	~32h.	~142h.	~248h.	~357h.	-
CA	~9s.	~19s.	~31s.	~43s.	+ ~2h.
Ratio	~12800	~26900	~28800	~29900	-

5.5 Neighborhood effect statistics

The analysis of the FE simulations showed how much the neighborhood effect can increase plasticity within a grain and potentially accelerate crack initiation. The parameter $\tau^g_{s\ 0.01\%}$, the grain's RSS on slip system s predicted by the CA model for a monotonic loading at $E_{33} = 0.01\%$ / $\Sigma^{eff}_{33} = 19.6$ MPa, was shown to be a good indicator of the grains' relative plasticity levels. The three random distributions $S_i.R$ of 432 grains generated for the FE analysis showed a maximum $max\left(\left|\tau^g_{s\ 0.01\%}\right|\right)_s$ of 9.66 MPa (Fig. 5.4b). However, by generating a specific neighborhood ($S_i.C$ distributions), this value was increased to 21.33 MPa, leading to a high plasticity level as observed in Sections 5.4.1 and 5.4.2. The purpose of this section is to determine the probability and the maximum possible value of $\tau^g_{s\ 0.01\%}$ to estimate the true elastic limit (the lowest stress Σ^{eff}_{33} at which plasticity would start in one of the aggregate grains) probability distribution for different aggregate's size using the CA model. For a given load, the lowest the part true elastic limit is, the more plasification will occur in the plastifying grain, accelerating the crack nucleation within it, which means that the true elastic limit is tied to the material fatigue strength.

5.5.1 $\tau^g_{s\ 0.01\%}$ highest value

The following procedure has been followed to determine the highest $|\tau^g_{s\ 0.01\%}|$ value mathematically possible given the present material parameters:

- For each slip system, $\tau^g_{s\ 0}$ has been computed (Eq. 5.20b) for 10^5 grain g's random orientations generated with the quaternion method. The distribution of each grain's maximum absolute RSS ($max(|\tau^g_{s\ 0}|)_s$) is displayed in Fig. 5.7a.
- From these results, 100 grain g's orientations were selected (alongside the slip system number corresponding to the orientation giving the maximum absolute RSS) such that their $max(|\tau^g_{s\ 0}|)_s$ values are linearly spaced within the range of value obtained.
- For a given grain g's orientation and a given relative position $\overrightarrow{gn_i}$, the grain n_i's orientation increasing the most $|\tau^g_{s\ 0} + \Delta\tau^g_{s\ n_i}|$ were found using a maximizing function based on Eq.

5.20c. By repeating this process for each one of 258 neighboring grains, the 258-grains neighborhood increasing the most grain g's RSS ($\sum_{n_i}^{258} max(\Delta\tau^g_{s\ n_i})$) was identified. Fig. 5.7b shows the maximum absolute RSS values obtained with these neighborhood for each one of the 100 grain g's orientation selected as a function of $max(|\tau^g_{s\ 0}|)_s$ alongside with the deviation due the neighborhood ($\sum_{n_i}^{258} max(\Delta\tau^g_{s\ n_i})$). The maximum RSS increase observed due to the neighborhood effect is approximately constant at 14.3 ± 0.3 MPa no matter grain g's orientation, and the highest value of $\tau^g_{s\ 0.01\%}$ possible found with our set of material parameters is 23.0 MPa, 2.4 times higher than the maximum value obtained in the random $S_i.R$ distributions. Higher values could eventually be found if more grains would be considered in the neighborhood effect (more than three grain's layers as presented in Fig. 5.2b).

5.5.2 $\tau^g_{s\ 0.01\%}$ probability density function

The probability to draw a specific neighborhood that would generate a value of $\tau^g_{s\ 0.01\%}$ similar as $S_i.C$ distributions in a periodic aggregate of 432 grains randomly oriented is extremely low, but mechanical parts are made of millions of millions of grains in which this unlikely neighborhood could occur. A Monte-Carlo method was built to evaluate grains' $max(|\tau^g_{s\ 0.01\%}|)_s$ probability, as follows:

- 10^8 aggregates of 259 grains randomly orientated as presented in Fig. 5.2b (grain g and its 258 neighboring grains n_i) were generated.

- For each aggregate, $\tau^g_{s\ 0.01\%}$ was computed (eq. 5.20) for each slip system, and only the maximum absolute value among these slip systems ($max(|\tau^g_{s\ 0.01\%}|)_s$) was kept.

- Fig. 5.7c displays the distribution of these 10^8 values. The highest value obtained among these 10^8 draws is 12.1 MPa which is much lower than the maximum theoretical value of 23.0 MPa. A Burr probability distribution function (Burr, 1942) was used to fit the distribution as it is a flexible distribution family that can express a wide range of distribution shapes. Its probability density function (pdf) and cumulative distribution function (cdf) are expressed

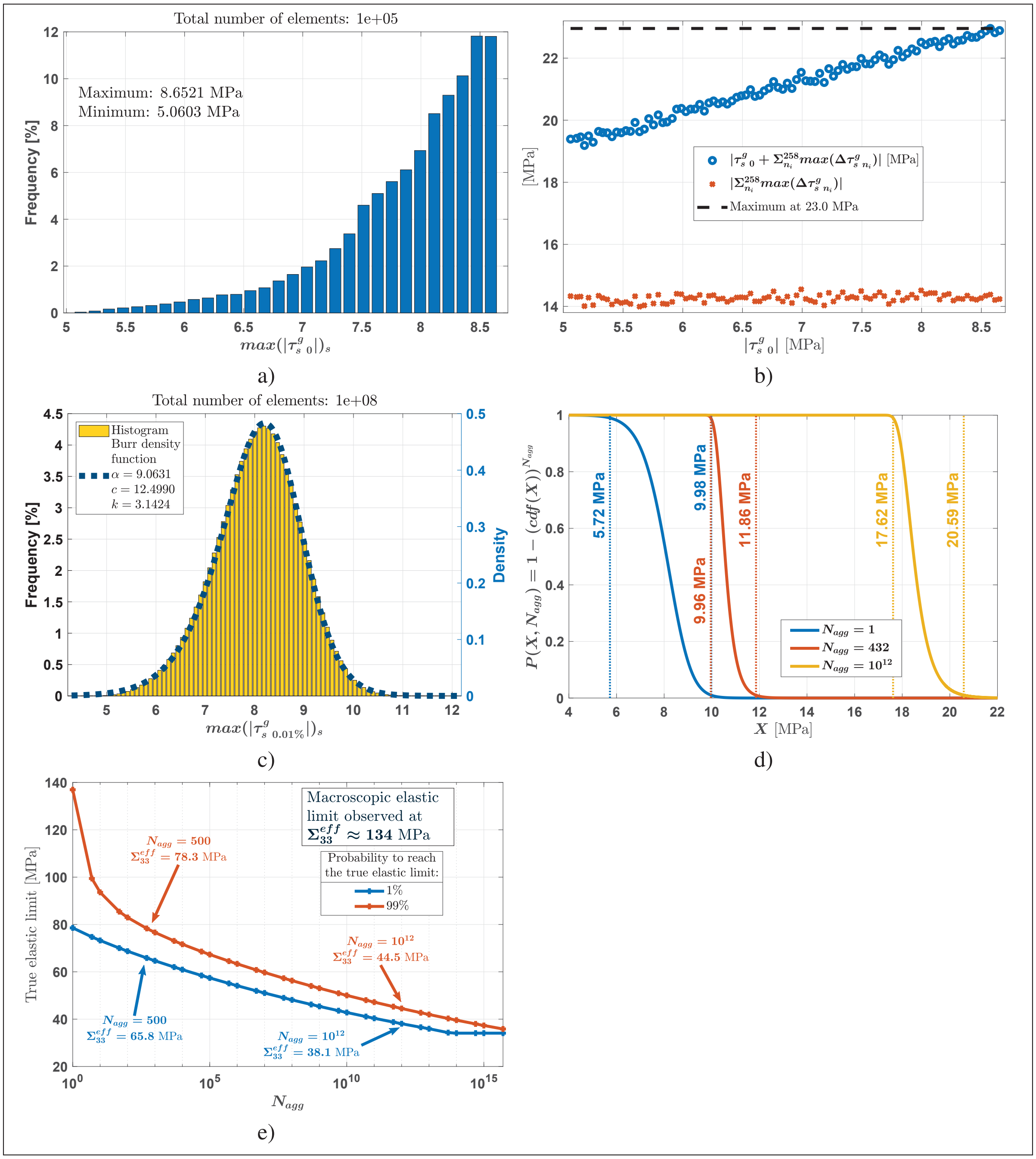

Figure 5.7 $\tau^g_{s\ 0.01\%}$ probability: (a) $max(|\tau^g_{s\ 0}|)_s$ distribution over 10^5 random orientations; (b) Maximum possible value of $\tau^g_{s\ 0.01\%}$ for a given grain g's orientation as a function of $|\tau^g_{s\ 0}|$; (c) $max(|\tau^g_{s\ 0.01\%}|)_s$ distribution over 10^8 random 259-grains aggregate randomly oriented and its probability function; (d) Probability to draw a grain-neighborhood's configuration with $max(|\tau^g_{s\ 0.01\%}|)_s$ superior to X after N_{agg} draws (values at 1% and 99% probability are displayed); (e) True elastic limit (lowest stress at which dislocations move with 1% and 99% chance) predicted by CA model as a function of the aggregate's size N_{agg}.

as follow:

$$pdf(X) = \frac{\frac{kc}{\alpha}\left(\frac{X}{\alpha}\right)^{c-1}}{\left(1+\left(\frac{X}{\alpha}\right)^{c}\right)^{k+1}} \quad X > 0, \alpha > 0, c > 0, k > 0 \tag{5.21a}$$

$$cdf(X) = 1 - \frac{1}{\left(1+\left(\frac{X}{\alpha}\right)^{c}\right)^{k}} \quad X > 0, \alpha > 0, c > 0, k > 0 \tag{5.21b}$$

- The probability P to have among N_{agg} grain-neighborhood's configurations one grain with $max(|\tau^{g}_{s\ 0.01\%}|)_{s}$ superior to X can then be calculated as:

$$P(X, N_{agg}) = 1 - (cdf(X))^{N_{agg}} \tag{5.22}$$

Four values of N_{agg} were used to illustrate the method: 1, 432 and 10^{12} grain-neighborhood's configurations. The obtained curves are displayed in Fig. 5.7d together with the values at a probability of 1% and 99%. By looking at the case $N_{agg} = 432$, the fitting Burr density function might overestimate the probability: the three $S_i.R$ distributions of 432 grains showed a $max(|\tau^{g}_{s\ 0.01\%}|)_{s,g}$ of 9.50, 9.63 and 9.66 MPa, while the probability function gives 99% chance to get a $max(|\tau^{g}_{s\ 0.01\%}|)_{s,g}$ superior to 9.96 MPa within 432 grain-neighborhood's configuration. Nonetheless, putting aside the fact that the probability function might be overestimated, in the case $N_{agg} = 10^{12}$, a probability of 1% to have a configuration with $max(|\tau^{g}_{s\ 0.01\%}|)_{s,g} > 20.59$ MPa (similar to $S_i.C$ distributions) is found. The critical RSS being of 40 MPa, this means that in a volume of 10^{12} grains, there is 1% chance that plasticity would occur within the volume if the applied load is such that $E^{eff}_{33} = 40/20.59 \times 0.01\% = 0.0194\%$ which is equivalent to $\Sigma^{eff}_{33} = 38.1$ MPa.

- By repeating this previous calculation to different aggregate's size, the true elastic limit (the lowest stress at which dislocations would start moving within the aggregate with 1% and 99% chance) have been calculated for different aggregate's size and displayed in Fig. 5.7e. The bigger the aggregate is, the higher the chance to obtain a critical grain-neighborhood's configuration is, lowering the true elastic limit. The lowest theoretical true elastic limit of 34.1 MPa, in the case where only the 258 closest neighboring grains influences are considered, is reached for aggregates bigger than 10^{14} grains. The difference between an aggregate of $\sim 10^5$ grains (size of a fatigue test specimen) and an aggregate of $\sim 10^{12}$ grains (size of a 1 m^3 mechanical part composed of ~ 50 μm diameter grains) could explain the differences commonly observed between the fatigue life of a functioning mechanical part and the fatigue life measured on a specimen (Beretta, Clerici & Matteazzi, 1995; Lin, Binoniemi, Fett, Woodard, Punch, Tyne, Taylor & Matlock, 2006). Also, among other factors, the gap between the red and blue curves could explained the experimental fatigue tests distributions commonly observed.

This data is to be taken with caution: a more detailed statistical study has to be performed to accurately capture the probability distribution function and the extremes values probability, but these results reveal the CA potential to study these specific issues. Also, in our case, only the 258 closest neighboring grains influences are considered, each grain has an identical shape, and each grain's orientation is drawn independently from each other. Expanding the number of neighboring grains taken into account in the model, or adding a free surface, a random grain morphology, a texture or even macrozones (large areas of grains with an identical orientation Germain, Gey, Humbert, Bocher & Jahazi (2005)) would add even more heterogeneities to the aggregate which would have the effect to widen Fig. 5.7c distribution and thus to increase the probability to get a $max(|\tau^{g}_{s\ 0.01\%}|)_s$ high value.

To conclude this section and accentuate on the efficient and quickness of the CA model, the time calculation necessary to generate the 10^8 values presented in Fig. 5.7c was approximately 21 hours.

5.6 Conclusions

A study of the neighborhood effect on the elastoviscoplastic behavior of a polycrystalline material has been performed. The 316L steel, modeled with the Méric-Cailletaud model, was chosen for the study to highlight the importance of the neighborhood effect due to its significant elastic and plastic anisotropy. The Kelvin structure was used to represent the aggregate with periodic boundary conditions, eluding the morphology and border effects and leaving the crystal anisotropy and the crystallographic orientation distribution as the only sources of heterogeneities.

The study was performed using the FE method as a reference and the CA model. The latter, initially developed in Bretin *et al.* (2019b) for the study of elastic loadings, was adapted to the study of elastoviscoplastic loadings in HCF and VHCF regime. The simplifying assumptions that the material remains macroscopically elastic and that the grains plastic behavior does not affect the neighborhood effect were made in order to preserve the model quickness for the purpose of statistical studies.

Two different methods of crystallographic orientation distributions were studied: one fully random (orientation set and orientation distribution), and the second, using the same orientation set, has its orientations distributed such that an important stress concentration is generated in a given grain's slip system. For the latter method, the CA model was used to identify each neighboring grain orientation from the set that would increase the most the given grain RSS. While both distribution methods showed identical macroscopic behaviors, they also showed significant microscopic differences. The distributions specifically set up showed a plasticity level in the grain undergoing important stress concentration a plasticity level twice higher than the maximum one observed in a random distribution. These differences reveal the importance of the neighborhood effect within polycrystals and show that even with a set of random orientations, significant plasticity concentrations can occur in some specific configurations.

In the context of HCF and VHCF, and for the material studied, a correlation was found between the grain plastic levels and their elastic behavior. Grains with the highest RSS values during the elastic part of the load were found with plasticity levels proportionally as high. Therefore, the strain variations due to the neighborhood effect were shown to be mainly guided by the grains' elastic properties. Grains surrounding a significant plasticity concentration were shown to be affected by it, but the plasticity level variations observed were negligible in comparison to the variations due to the grains' elastic properties.

Taking advantage of the CA model quickness, a statistical study was performed to determine the probability of a grain's resolved shear stress level when the material would be submitted to a certain load in the elastic domain. From the probability function of a grain RSS, the true elastic limit probability of a part made of a given number of grains, which is linked to the part fatigue strength, has been determined. This probability study could explain the statistical spread of the material fatigue life experimentally observed and the ratio between the elastic limit and the fatigue strength.

Using the FE model as a reference, the CA model showed excellent accuracy from a macroscopic point of view, but lack of accuracy at predicting the local fields. As already demonstrated in Bretin *et al.* (2019b) in the case of an elastic load, the CA model predicted the local stress-fields with accuracy in the elastic domain until plasticity occurs within the aggregate generating predictions gaps between the two models. Grains' plasticity levels were underestimated by the CA model, proportionally to the grain's plasticity level. Despite the model underestimations, the CA capability to identify the critical orientations' configurations has been verified: the grains showing the highest plasticity level are the same for both models. The CA model can be used to identify the critical orientations' distribution and a more accurate model could then be used to study these aggregate behaviors. The computational time necessary to perform the presented simulations with the FE model is reduced by at least four orders of magnitude with the CA model.

Recommendations

Even though the results presented in this article demonstrate the CA model potential to identify accurately the microstructure configurations yielding to important stress concentrations, the CA model is still very simplistic in its current state. Several problems have been pointed out along the article (Sections 5.4.1.3 and 5.4.2.2). Here are four solutions suggestions to cop for these issues that should be looked at in priority:

- The Eshelby's inclusion problem (Eq. 5.2) should be updated. In the presented case, the model still considers the inclusion elastic-linear in a homogeneous elastic-linear matrix (Mercier, Jacques & Molinari, 2005b). In the case of HCF regime, the matrix can still be considered elastic-linear, but the inclusion should be considered nonlinear.

- In order to account for the neighboring grain plastic strain, the use of an incremental secant or tangent modulus instead of the elastic stiffness tensor would be more appropriate in the calculation of $\boldsymbol{\Delta\varepsilon}_{n_i}^{g^{eff}}$ (Eq. 5.5).

- As mentioned in Section 5.2.1, the more grain g properties differ from the effective properties, the more the approximation $\boldsymbol{\Delta\varepsilon}_{n_i}^{g} \approx \boldsymbol{\Delta\varepsilon}_{n_i}^{g^{eff}}$ (Eq. 5.4) becomes inaccurate. Therefore, the more grain g plastifies, the more this approximation becomes inaccurate. A new model accounting for grain g properties to predict $\boldsymbol{\Delta\varepsilon}_{n_i}^{g}$ might improve the model predictions in HCF regime.

- Dividing grains into several Kelvin cells would help to predict plastic strain heterogeneity within a grain, but this would require to broaden the number of neighboring grains accounted for the neighborhood effect making the calculations heavier. One might also look at the second-order moment or variational formulations of the localization tensors (Lahellec & Suquet (2007a), Lahellec & Suquet (2007b)).

CHAPTER 6

EXTRA STUDIES ON THE EFFECT OF A FREE SURFACE AND GRAINS MORPHOLOGIES ON THE NEIGHBORHOOD EFFECT IN ELASTICITY

6.1 Surface effect

The impact in elasticity of a free surface on the neighborhood effect has also been studied using FEM. FE simulations presented in Section 3.4 ($S-1G$ and $S-65G$) were reproduced with some modifications. The matrix mesh surrounding the aggregate's mesh was modified to leave an aggregate face free as presented in Fig. 6.1. The KUBC applied to the mesh were modified as follow:

- u_3=0 in $z=0$ and $u_3 = 0.1\text{‰} \times r_m$ in $z = r_m$;
- u_1=0 in $x=0$ and no boundary condition in $x = r_m^*$ (with $r_m^* = r_m/2 + r_a/2$);
- u_2=0 in $y=0$ and $u_2 = -0.297\text{‰} \times r_m$ in $y = r_m$ in order to adjust to the free surface displacement and obtained an uniaxial stress loading such that Σ_{33}^{eff} = 205.6 MPa and all the other components are equal to zero.

Due to the free surface, the size of the neighborhood studied is cut in half, reducing the number of neighboring grains considered from 64 grains to 38 grains (9 from the first layer and 29 from the second) and the orientations' configurations assigned to the neighboring grains are identical as those assigned earlier (see Section 3.4.3 Fig. 3.7). Eight different aggregate depths were simulated, starting from position 0 to position 7, 1 being a grain radius. As defined in Section 3.4.1, the tensors $\boldsymbol{\sigma}_n^A(d)$, $\boldsymbol{\sigma}_0^A(d)$, $\boldsymbol{\sigma}_{B_i}^{A^{eff}}(d)$ and $\boldsymbol{\Delta\sigma}_n^A(d) = \boldsymbol{\sigma}_n^A(d) - \boldsymbol{\sigma}_0^A(d)$ are extracted from these simulations, where the variable "d" denotes the aggregate depth.

Before getting into the analysis of these results, it is important to mention that these simulations were performed out of curiosity. The same aggregate mesh used in Section 3.4 Fig. 3.1b was reused but a new mesh convergence study should have been performed to confirm if the aggregate mesh still converges even with the addition of the free surface. Therefore, the quantitative results

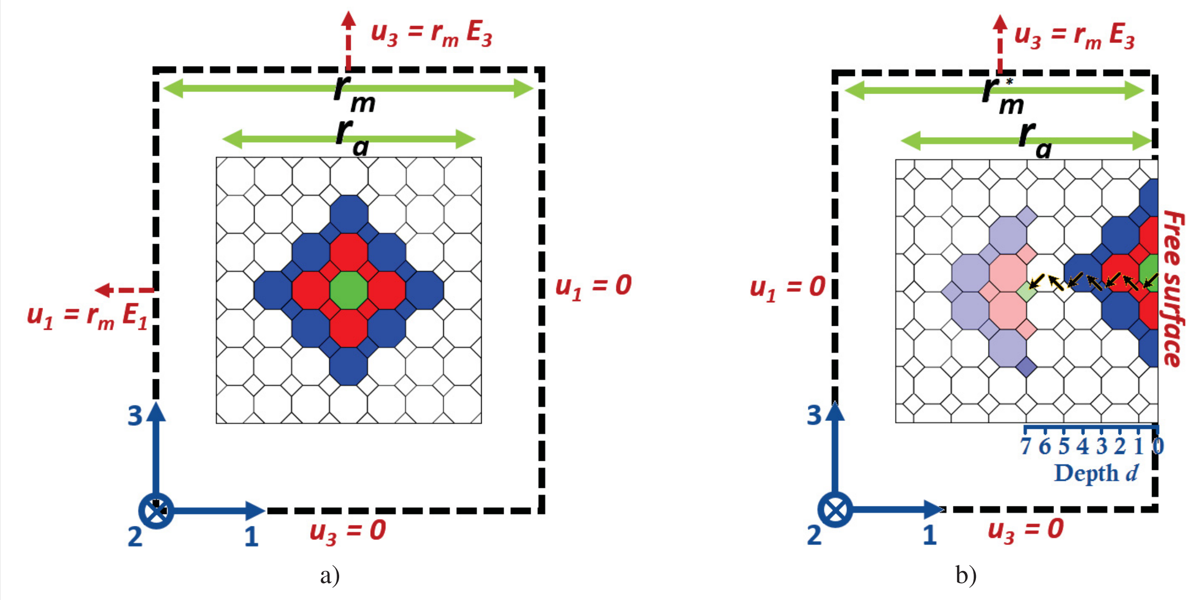

Figure 6.1 2D illustrations of the studied meshes and the KUBC applied to their edges: (a) KUBC used in Section 3.4; (b) KUBC used for the surface effect study.

presented in this section must be taken with caution but the observed trends and the conclusions drawn from these results are viable and deserved to be mentioned.

Similarly as in Fig. 3.7, Fig. 6.2 shows the stress deviation due to the neighborhood along $\vec{e}_3$-axis, for different aggregate depths (0,1,2 and 7). The observations drawn from Fig. 6.2 are similar to those drawn from Fig. 3.7:

- For a given depth, $\boldsymbol{\Delta\sigma}^{A}_{L^2}$ remains invariant to the change of grain A properties in comparison with the variations due to the different neighborhood configurations. Therefore, the approximation illustrated in Fig. 3.6 remains relevant even with a free surface:

$$\boldsymbol{\Delta\sigma}^{A}_{n}(d) \approx \boldsymbol{\Delta\sigma}^{A^{eff}}_{n}(d) \tag{6.1}$$

- The gap observed between $\boldsymbol{\Delta\sigma}^{A^{eff}}_{L^2}(d)$ and $\sum_{i=1}^{38} \boldsymbol{\Delta\sigma}^{A^{eff}}_{B_i}(d)$ remains low in comparison to $\boldsymbol{\Delta\sigma}^{A^{eff}}_{L^2}(d)$ values. Therefore, the approximation illustrated in Fig. 3.8 remains relevant even

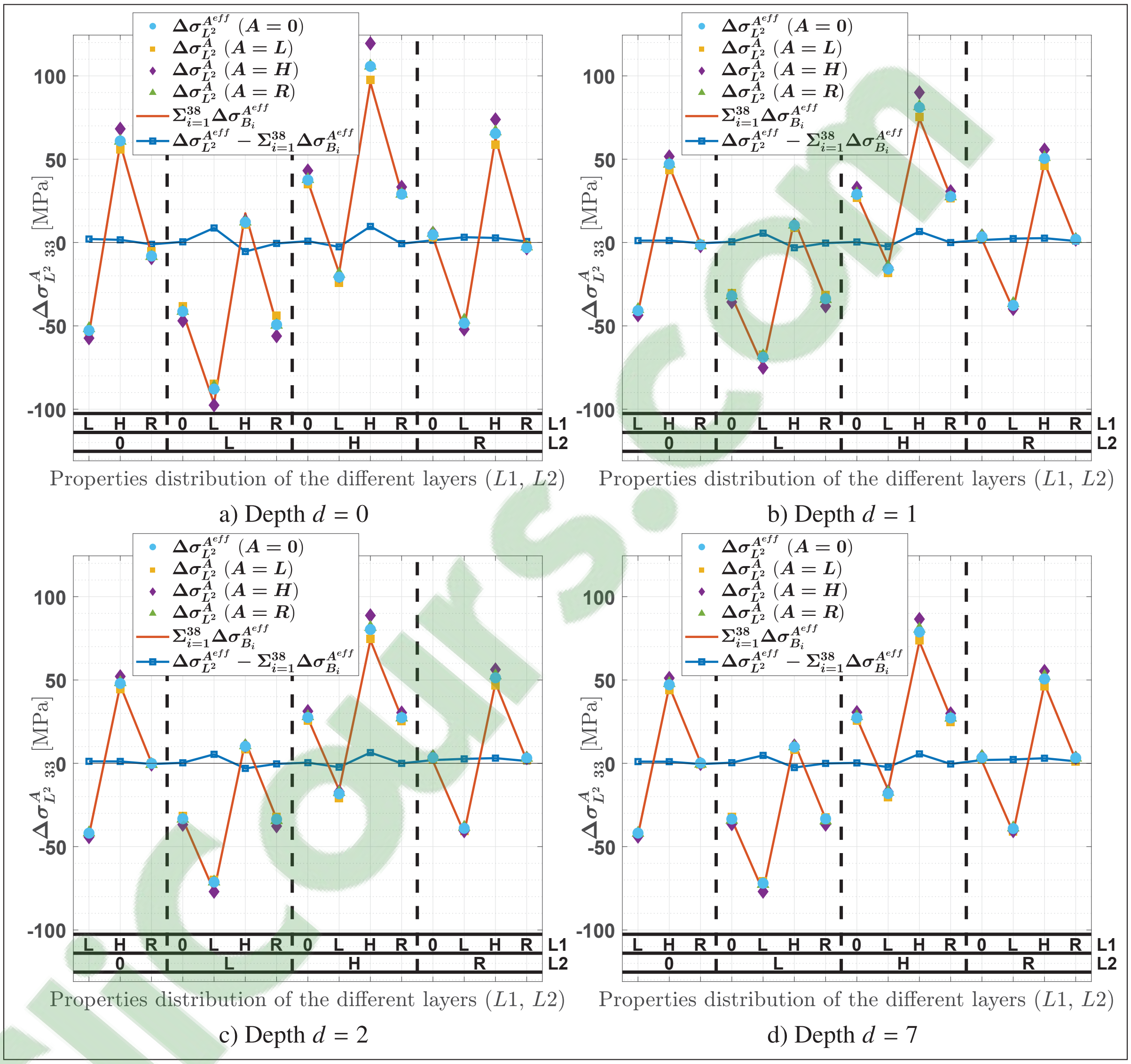

a) Depth $d = 0$

b) Depth $d = 1$

c) Depth $d = 2$

d) Depth $d = 7$

Figure 6.2 $\Delta\sigma_{L^2}^{A}$ variations as a function of grain A, $L1$, $L2$ properties configurations for different aggregate depth. Comparison with the sum of the individual influences $\sigma_{B_i}^{A^{eff}}$ of each grain B_i forming the two grain layers $L1$ and $L2$. Property notation "0" corresponds to the effective properties; "L", "H" correspond to the crystal properties with the orientations corresponding respectively to the lowest and highest values of ε_0^A or $\varepsilon_B^{A^{eff}}$ from *S-1G* simulations for each grain of $L1$ and/or $L2$; "R" corresponds to random orientations. The variations of $\Delta\sigma_{L^2}^{A}$ observed due to the different neighborhood configurations are more significant than those due to the different grain A properties whatever the depth. $\Sigma_{i=1}^{64}\Delta\sigma_{B_i}^{A^{eff}}(d)$ shows a good approximation of $\Delta\sigma_{L^2}^{A^{eff}}(d)$.

with a free surface:

$$\boldsymbol{\Delta\sigma}_n^{A^{eff}}(d) \approx \sum_{B_i} \boldsymbol{\Delta\sigma}_{B_i}^{A^{eff}}(d) \tag{6.2}$$

To conclude, the approximation presented in Section 3.4 Eq. 3.14 remains accurate with a free surface but this expression becomes depth dependent as $\boldsymbol{\sigma}_0^A(d)$ and $\boldsymbol{\Delta\sigma}_{B_i}^{A^{eff}}(d)$ are depth dependent:

$$\boldsymbol{\Delta\sigma}_n^{A}(d) \approx \sum_{B_i} \boldsymbol{\Delta\sigma}_{B_i}^{A^{eff}}(d) \quad \Rightarrow \quad \boldsymbol{\sigma}_n^{A}(d) \approx \boldsymbol{\sigma}_0^{A}(d) + \sum_{B_i} \boldsymbol{\Delta\sigma}_{B_i}^{A^{eff}}(d) \tag{6.3}$$

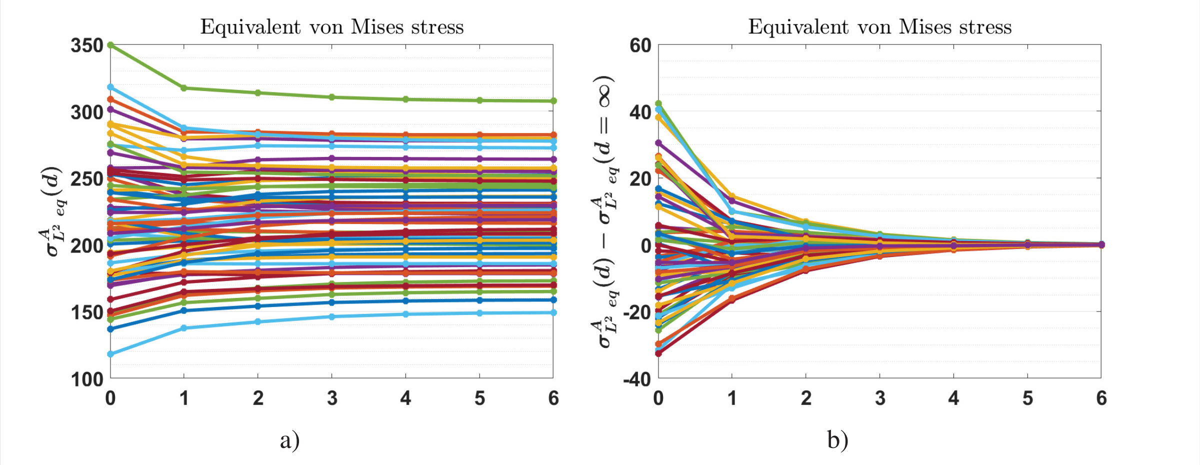

a) b)

Figure 6.3 Grain A's equivalent von Mises stress ($\sigma^A_{L^2\ eq}(d)$) as a function of grain A's depth d obtained for the 60 different orientations' configurations. Each curves is a different set of orientations (4×15 sets).

In order to apprehend the surface effect on a grain stress level, the variation of grain A equivalent von Mises stress ($\sigma^A_{L^2\ eq}(d)$) has been observed depending on the depth of the aggregate composed of the grain A and its 38 neighbors. Fig. 6.3 shows $\sigma^A_{L^2\ eq}(d)$ as a function of grain A's depth. The free surface has the effect to widen the stress distribution: near the surface, the values seem to divergence from the macroscopic stress (205.6 MPa). Therefore, grains with high-stress have their stress levels increased by the free surface, which might also increase the grain's slip system RSS when favorably oriented.

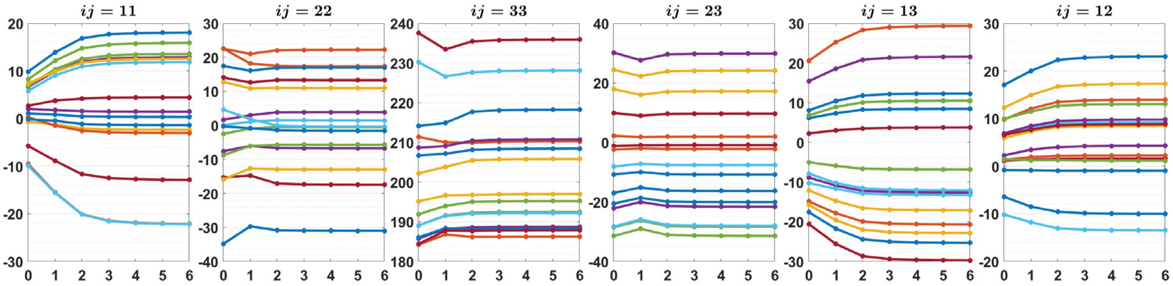

a) Abscissa: depth d; Ordinate: $\sigma_{0\ ij}^{A}(d)$ MPa

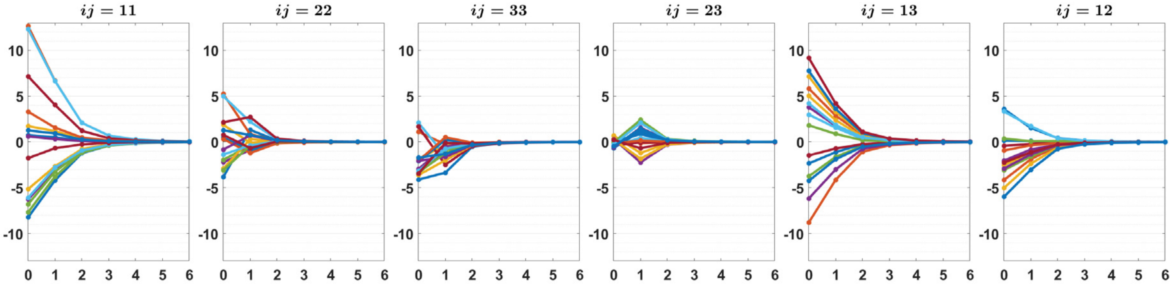

b) Abscissa: depth d; Ordinate: $\sigma_{0\ ij}^{A}(d) - \sigma_{0\ ij}^{A}(d = \infty)$ MPa

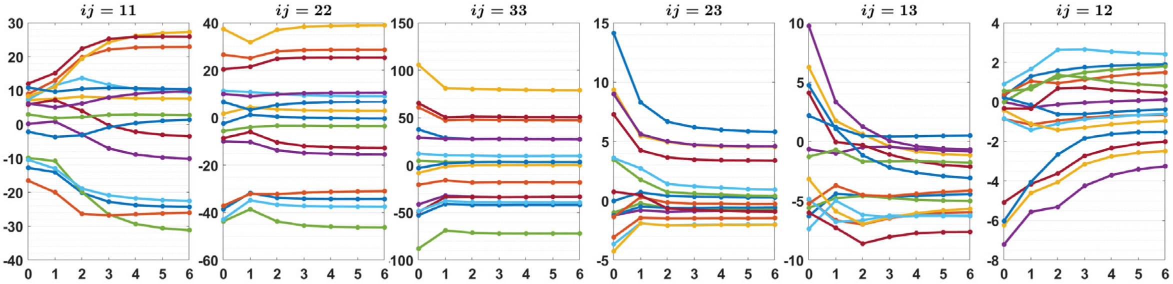

c) Abscissa: depth d; Ordinate: $\Delta\sigma_{L^2\ ij}^{A^{eff}}(d)$ MPa

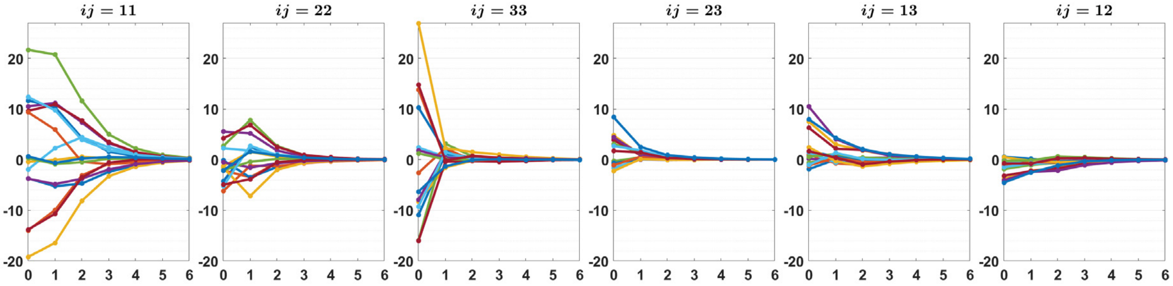

d) Abscissa: depth d; Ordinate: $\Delta\sigma_{L^2\ ij}^{A^{eff}}(d) - \Delta\sigma_{L^2\ ij}^{A^{eff}}(d = \infty)$ MPa

Figure 6.4 $\sigma_0^A(d)$ and $\Delta\sigma_{L^2}^{A^{eff}}(d)$ as a function of the aggregate depth for 15 different orientations' configurations. $\sigma_0^A(d)$ is the part of grain A's stress tensor depending on grain A's properties, and $\Delta\sigma_{L^2}^{A}(d)$ is the part of grain A's stress tensor depending on the neighborhood's properties. Each curves is a different set of orientations (15 sets).

In order to apprehend the surface effect on each part of grain A stress tensor components, Fig. 6.4 shows $\sigma_0^A(d)$ and $\Delta\sigma_{L^2}^{A^{eff}}(d)$ components as a function of grain A's depth d for 15 different orientations' configurations. As a reminder, $\sigma_0^A(d)$ is the part of grain A's stress tensor depending on grain A's properties, and $\Delta\sigma_{L^2}^A(d)$ is the part of grain A's stress tensor depending on the neighborhood's properties. Also, as the mesh hasn't been adapted to the study of a free surface, it is important to consider with precaution the data resulting from the FE simulations: variations observed on the two first grain layers are probably an artifact due to a coarse mesh. Three trends can be drawn from Fig. 6.4 observations:

- $\sigma_0^A(d)$ components 11, 13 and 12 seem to be more affected by the free surface than its other components. They seems to converge towards 0 near the surface. The higher the value in the core is, the faster the convergence toward 0 is.
- $\Delta\sigma_{L^2}^{A^{eff}}(d)$ components 11 (normal to the free surface) and 33 (loading direction) seem to be more affected by the free surface than its other components. The component 11 seems to converge toward 0 while the component 33 diverges from 0 near the surface. The variations observed for the component 33 concern only the depth 0 and 1 whereas the variations observed for the component 11 remains deeper. Again, component 33 variations might be an artifact due to a coarse mesh.
- The ranges of values observed in Fig. 6.4b are wider than the ranges of values observed in 6.4d, meaning that the free surface affects more $\Delta\sigma_{L^2}^{A^{eff}}(d)$ than $\sigma_0^A(d)$.

An idea to account for the surface effect in the CA model would be to predict $\sigma_0^A(d)$ using the solution of the Eshelby's problem in an half space (Lee *et al.*, 2016), and to predict $\Delta\sigma_{B_i}^A(d)$ with tensors $\mathbb{U}^{\overrightarrow{AB}}(d)$ identified at different depths (from 0 to 6, which corresponds to three grain layers, and ∞), which would increase the number of preliminary FE simulations necessary to identify these tensors to $(7 + 1) \times 2 \times 8$.

Within the purpose to estimate the maximum stress concentration possible and its probability, it would be interesting to reproduce the probabilistic analysis presented in Section 4.6 for different depth and look at the evolution of the true elastic limit and its probability function for different depth. Hypothetically, the highest possible value could happen in the core but the probability function could be wider at the surface, meaning that there is more chance to get a higher value at the surface.

6.2 Morphology effect

A quick overview in elasticity of the grains morphology effect on the stress field has been performed and compared to the neighborhood effect. Using the same methodology as for the FE simulations performed in Section 3.3 (polycrystalline aggregate randomly oriented submitted to an uni-axial strain loading along $\vec{e}_3$ with PBC), new aggregate morphologies of 432 grains were studied to assess the stress-strain variations induced by grains' morphology different from the Kelvin cell. As a reminder, PBC were used for these simulations and the aggregates were submitted to an uniaxial loading along $\vec{e}_3$ axis resulting in the following effective stress:

$$\boldsymbol{\Sigma}^{eff} = \begin{bmatrix} 115.8 \pm 0.2 & 0.1 \pm 0.2 & 0.1 \pm 0.2 \\ 0.1 \pm 0.2 & 115.9 \pm 0.2 & 0.0 \pm 0.2 \\ 0.1 \pm 0.2 & 0.0 \pm 0.2 & 274.3 \pm 0.3 \end{bmatrix} \tag{6.4}$$

The meshes were generated with the Voronoi method. A Kelvin structure can be regarded as a regular Voronoi diagram where seeds occupy all the positions $(x; y; z)$, such that x, y, z is a set of three odd or three even integers, with identical growth speeds. Two different methods were used to generate aggregate morphologies slightly different from the Kelvin structure:

- Regular distorted aggregates with different grain's shapes from the Kelvin cell were obtained as follow: Kelvin structure's seeds were linearly spread along a direction ($\vec{e}_1$ or $\vec{e}_3$) creating different type of grain morphology as presented in Fig. 6.5a. Instead of having all grains with a spherical shape, they all have an identical ellipsoidal shape.
- A random morphology can be obtained by relocating the Kelvin structure's seeds from the initial place by a vector $\vec{\boldsymbol{\delta}}^g$ randomly generated for each seed such as $||\vec{\boldsymbol{\delta}}^g|| < \delta_{max}$. Two values of δ_{max} were tested (0.5 and 1) and four random aggregate morphologies of 432

grains were randomly generated for each δ_{max} value. An example of the mesh obtained with $\delta_{max} = 0.5$ is presented Fig. 6.5b.

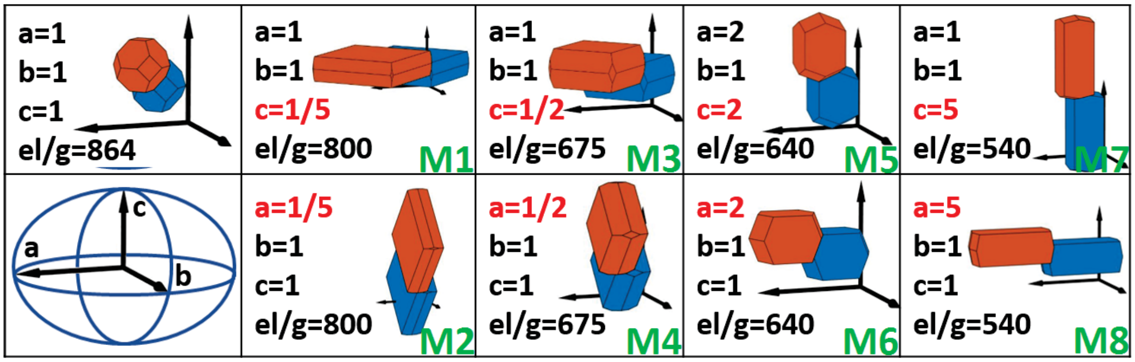

a) Regular Voronoi aggregate: different grain morphologies studied

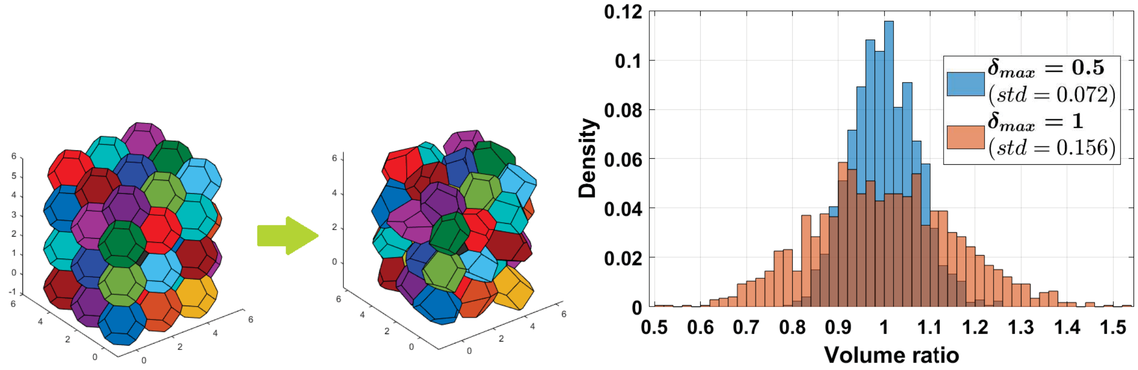

b) Random Voronoi aggregate: example of the obtained morphologies for $\delta_{max} = 0.5$

c) Random Voronoi aggregate: grains volume distribution

Figure 6.5 Graphic representations of the different aggregate morphologies studied: (a) Different regular structures and grain morphologies studied; (b) Random Voronoi aggregate example obtained with $\delta_{max} = 0.5$; (c) Grain volume ratio distributions obtained from the random Voronoi aggregates using a Kelvin cell volume as reference.

The 432 crystallographic orientations are randomly generated and identically distributed over each aggregate morphology. A regular grid mesh of eight-node brick elements were used to generate the aggregate meshes. No mesh convergence study was performed. Therefore, the results obtained are to be considered inaccurate, but the trends observed shouldn't be affected by this due to the fact that the number of element per grain remains relatively close to that of the mesh used in Section 3.3. The number of elements per grains in the regular meshes (el/g value in Fig. 6.5a) can vary depending on the morphology but is identical for the 432 grains within the regular aggregate. On the other hand, in the random Voronoi aggregates, the grains volumes vary from the volume of a Kelvin cell: the distributions of the volume ratio between a grain volume and a Kelvin cell volume can be found in Fig. 6.5c. Due to the fact that the seeds positions vary more from their initial position when $\delta_{max} = 1$, a wider distribution of the volume ratio is observed when $\delta_{max} = 1$ than when $\delta_{max} = 0.5$.

The morphology effect, similarly as for the neighborhood effect, is quantified by the difference between the resulting stress $\boldsymbol{\sigma}^g_{VOR}$ in a random or distorted Voronoi aggregate (aggregate on the right side of Fig. 6.5b) and the resulting stress $\boldsymbol{\sigma}^g_{KS}$ in a regular aggregate (when $a = 1$, $b = 1$, $c = 1$ and $\delta_{max} = 0$), equivalent to the Kelvin structure (aggregate on the left side of Fig. 6.5b).

Fig. 6.6 displays some examples of $\sigma^g_{33\ VOR} - \sigma^g_{33\ KS}$ distributions over the 432 grains aggregate. It can be observed that these distributions follow a normal distribution centered in 0. The same observation was made for each morphology studied and each tensor component. Therefore, the standard deviations of these distributions will be used to compare them and assess the importance of the morphology effect depending on the aggregate morphology. These values are displayed in Table 6.1. In addition, the standard deviation of the stress variations due to the neighborhood effect observed in Section 3.3 Table 3.2 are also displayed in Table 6.1 to assess the importance of the morphology effect in comparison to the neighborhood effect.

Different trends can be drawn from Table 6.1 concerning the morphology effect:

- The stress variations due to the morphology effect are doubled between the random Voronoi aggregates with $\delta_{max} = 0.5$ and the one with $\delta_{max} = 1$. The same ratio was observed in Fig. 6.5c between the standard deviations of the grain volume distributions (0.156/0.072=2.17). This means that the more the grains morphologies differ from the regular one, the more stress variations due to the morphology effect, and this proportionally to the aspect ratio. Nonetheless, the stress variations due to the morphology effect observed for the random Voronoi aggregates remains below the stress variations due to the neighborhood effect. For component 33, the stress variations due to the neighborhood effect showed a standard

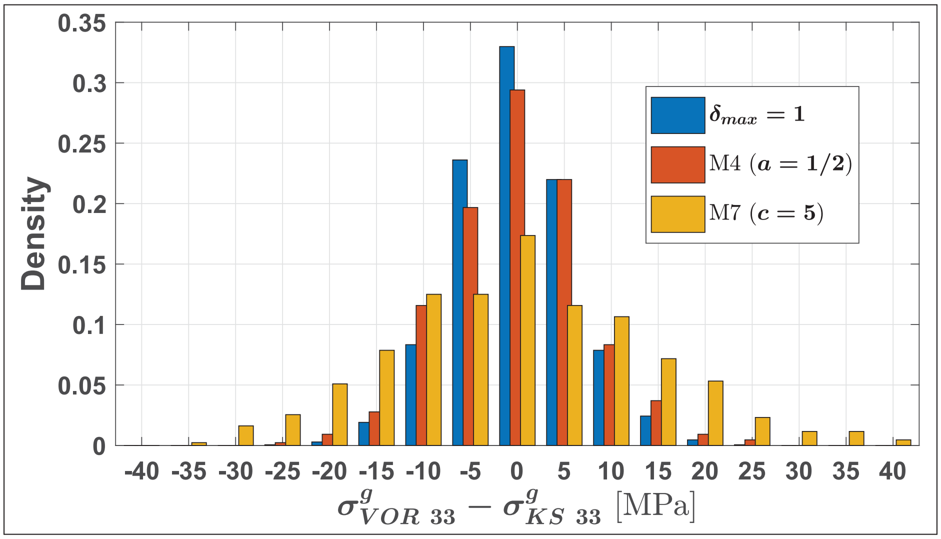

Figure 6.6 Examples of the stress variation distributions due to the morphology effect ($\sigma^g_{33\ VOR} - \sigma^g_{33\ KS}$) obtained for different aggregate morphologies.

deviation of 11.69 MPa and the stress variations due to the morphology effect for $\delta_{max} = 1$ showed a standard deviation of 6.24 MPa.

- The regular distorted aggregates with a higher aspect ratio M1, M2, M7 and M8 show wider distributions than M3, M4, M5 and M6. Roughly, a ratio of $\sim 1.5 \pm 0.1$ is observed for each component between the standard deviation of morphology with an aspect ratio of 5 and its homologous with an aspect ratio of 2. Therefore, as expected, the more the aspect ratio, the more stress variations due to the morphology effect.

- The morphology aspect direction relatively to the loading direction has an impact on how the grains stress levels are impacted by the morphology effect. Morphologies with an aspect ratio along the loading axis $\vec{e}_3$ (M1, M3, M5, M7) show wider distributions than their homologous morphologies with an aspect ratio along the axis $\vec{e}_1$ (M2, M4, M6, M8). This difference is even more significant for the component 33 where a ratio of $\sim 1.3 \pm 0.1$ is observed between their standard deviations. Also, morphologies with an aspect ratio along the axis $\vec{e}_1$ (M2, M4, M6, M8) show wider distributions for the component 11 than for the component 22 whereas no difference is observed between these components for the other morphologies.

Table 6.1 Standard deviations of the morphology effect distribution ($\boldsymbol{\sigma}^g_{VOR} - \boldsymbol{\sigma}^g_{KS}$) obtained with the different aggregate's meshes studied. The neighborhood effect standard deviations ($\boldsymbol{\sigma}^g_{FEM} - \boldsymbol{\sigma}^g_{Esh}$) obtained from the data presented in Section 3.3 Table 3.2 are also displayed to assess the importance of the morphology effect in comparison to the neighborhood effect. Each distribution follows a Normal distribution centered in 0.

	Standard deviation [MPa]					
Morphology effect $\sigma^g_{ij\ VOR} - \sigma^g_{ij\ KS}$	$i = 1$ $j = 1$	$i = 2$ $j = 2$	$i = 3$ $j = 3$	$i = 2$ $j = 3$	$i = 1$ $j = 3$	$i = 1$ $j = 2$
M1 ($c = 1/5$)	11.19	11.06	13.27	7.45	7.61	4.88
M2 ($a = 1/5$)	10.28	9.28	11.16	6.54	7.18	6.08
M3 ($c = 1/2$)	6.90	6.58	9.15	4.97	5.06	3.39
M4 ($a = 1/2$)	7.24	5.77	7.42	4.35	4.74	4.03
M5 ($c = 2$)	6.90	6.74	10.81	4.34	4.24	4.28
M6 ($a = 2$)	8.55	6.29	7.33	4.69	4.05	3.69
M7 ($c = 5$)	8.92	8.24	13.84	6.06	5.95	5.48
M8 ($a = 5$)	11.72	8.40	9.63	6.10	5.67	5.17
$\delta_{max} = 0.5$	2.51	2.51	2.94	1.34	1.38	1.37
$\delta_{max} = 1$	5.56	5.39	6.24	2.84	2.90	2.94
Neighborhood effect $\sigma^g_{ij\ FEM} - \sigma^g_{ij\ Esh}$	9.99	9.96	11.69	5.34	5.36	5.55

- Among all the morphologies studied, some morphologies showed stress variation distributions due to the morphology effect as wide as the one due to the neighborhood effect. This means that the morphology effect can be as important as the neighborhood effect and thus needs to be considered when grains show significant aspect ratio.

Two recommendations can be considered to account for the morphology effect:

- The first idea would be to divide grains into several Kelvin cells. This would require to increase the number of neighboring cells considered in the CA model to a wider range than just the current three cell layers (and thereby, this would require a larger mesh than the one display in Fig. 3.1c), but this would also have the benefits to provide stress field within grains without actually increasing too much the CPU time.

- A second idea, quite similar to the first one, would be to identify the tensors $\mathbb{U}^{\overrightarrow{AB}}$ for different location instead of predefined volume. In the current model, $\boldsymbol{\Delta\varepsilon}^A_{B_i}$ is the average mean strain deviation observed in a predefined volume, a.k.a. a Kelvin cell (Fig. 6.7a). Instead of doing so, the strain deviation could be measured in each voxel (the use of a grid mesh would more be appropriated, and thereby the use of the FFT method also) and the tensors $\mathbb{U}^{\overrightarrow{AB}}$ would be identified for each voxel (Fig. 6.7b). Then, depending on the grains morphology, a grain strain deviation due to another grain would be the average of the voxel composing that grain, such as:

$$\boldsymbol{\varepsilon}_B^{A^{eff}} = \frac{1}{N_X} \sum_{i=1}^{N_X} \boldsymbol{\varepsilon}_B^{X_i^{eff}} \qquad \forall X \in A \tag{6.5a}$$

$$\Rightarrow \mathbb{U}^{\overrightarrow{AB}} = \frac{1}{N_X} \sum_{i=1}^{N_X} \mathbb{U}^{\overrightarrow{X_i B}} \tag{6.5b}$$

The tensors $\mathbb{U}^{\overrightarrow{XB}}$ could also be evaluated for different grain B morphologies (increasing inconveniently the number of preliminary FE simulations necessary to their identifications) and linear interpolation could be used for in-between shapes.

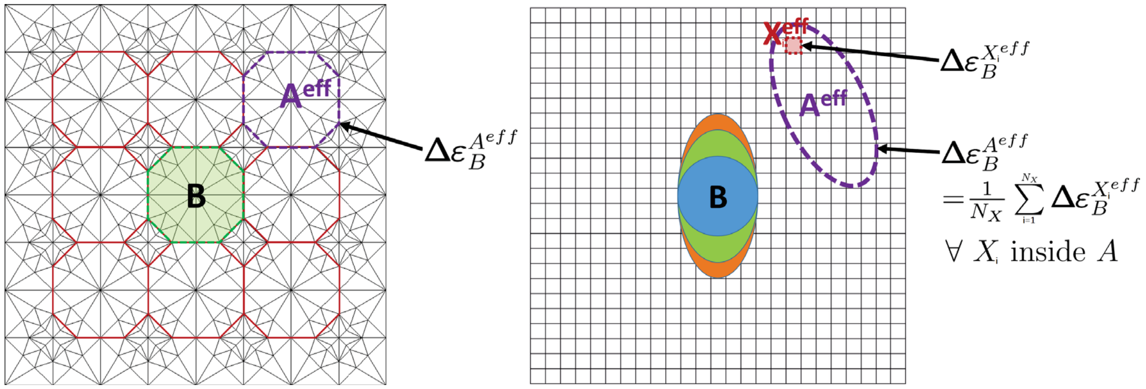

a) b)

Figure 6.7 Illustrations of possible methods to account for the morphology effect in the CA model.

CONCLUSIONS AND RECOMMENDATIONS

A micromechanical model, based on the Eshelby's inclusion problem and the cellular-automaton approach, has been developed with the purpose to predict the stress-strain fields within polycrystals, to identify the microstructure configurations responsible for high stress and plasticity concentrations, and to determine their probability to occur. This study has contributed to a better understanding of the neighborhood effect highlighting the parameters governing this phenomenon. By taking advantage of the model efficiency, millions of grain-neighborhood configurations can be studied in a few hours, allowing to identify the critical ones and also to establish a probability function of a grain stress level.

The finite element study on the neighborhood effect highlighted several points concerning this one. In order to quantify the neighborhood effect, a clear definition has been proposed: the neighborhood effect is the variation between the stress value of a grain immersed in a homogenous matrix having the material effective properties and the stress value of the same grain in its actual environment. In the case of a polycrystal of iron or titanium randomly oriented submitted to an elastic loading, the stress variations observed in a given grain for different neighborhoods are on average as significant as the stress variations observed in a grain by changing its crystallographic orientation and keeping its exact same neighborhood. Even if a grain is not favorably oriented, this grain can still be subjected to an above-average stress because of the neighborhood effect. Some specific neighborhood configurations have shown to lead to a stress level increase of 2.3 for the iron and 1.5 for the titanium of the average stress the grain is supposedly be subject to. Two approximations of the neighborhood have been proposed from the FEM analysis:

- The stress variation induced in a grain by its neighborhood is independent on its crystallographic orientation.
- The stress variation induced by a grain on another grain is independent of the other surrounding grains crystallographic orientation.

Based on the results of the FEM analysis and the approximations proposed, a data-driven analytical model has been developed based on the Eshelby's inclusion problem and the cellular-automaton approach. The model applies to regular structures where all grains are of identical size and spherical. The model concept is as follow: first, the grains stress is approximated with the Eshelby's diluted scheme, then each neighboring grain induced stress variation are added. The stress variation induced by a grain depends on its orientation, its position relatively to the induced grain and the material effective properties. A data-driven model was proposed to predict this value expressing the stress variation as a multilinear function of the grain stiffness tensor. The methodology to identify the model parameters is made through a few numbers of FEM simulations for given material effective properties. Once these parameters are identified, the CA model can be used to predict the stress level in any grain-neighborhood configuration. In the case of an elastic loading, the model predictions of a polycrystal micromechanical fields have shown an excellent accuracy in comparison to the FEM predictions. The grains showing the high RSS values were predicted with an average/minimum accuracy of 1.5%/6.2% for the Iron crystal and 0.6%/2.3% for the titanium crystal.

In the case of an elastoplastic loading, the model predictions were not as promising. The grains plasticity levels were under-evaluated by the CA model in comparison to the FEM predictions. Nonetheless, the study highlighted that the plastic field is mostly governed by the grains elastic field: the grains showing the most plasticity were the grains with the highest RSS during the elastic part of the load.

The major asset of the CA model is its efficiency. When it would take several days or weeks with the FEM to predict the stress level of millions of grain-neighborhood configurations, it only takes a few hours with the CA model. This asset has been brought to the fore by the statistical study of a material true elastic limit. By generating millions of data in a short time, a probability function of a grain RSS for a given elastic loading was obtained. The higher the material volume, the higher the chances are to get the specific crystallographic configurations grain-neighborhood leading to a very high stress concentration with the consequent to reduce the material true elastic limit. This phenomenon might explain the differences observed between the fatigue life of a material sample (small volume means less chance to get a critical configuration, so a higher true elastic limit) and the full size mechanical part (big volume means more chance, so lower true elastic limit). Also, for a given volume, the probability of the true elastic limit, which depends on the probability to get the specific crystallographic configuration grain-neighborhood leading to a very high stress concentration, differs significantly between its 1% and 99% probabilities which could be an explanation to the experimental dispersion of a material fatigue life in HCF.

The neighborhood effect has shown to have a significant effect on the polycrystals micromechanical fields but this is not the only phenomenon able to generate stress concentration. Other phenomena such as the effect of a free surface or grains morphologies have also been studied. These studies reveal that this phenomenon can generate stress variations as significant as the stress variations induced by the neighborhood effect.

Recommendations

Many recommendations were proposed all along this thesis and are recalled here:

- The predictions of the plastic fields need to be improved. A recommendations section for that matter can be found at the end of Chapter 5. Different suggestions are proposed to improve the model predictions of a polycrystal elastoplastic behavior.

- The addition of a fatigue damage variable to the constitutive law as proposed by Zghal *et al.* (2016) would push the model developed further into the prediction of crack initiation.

- Crack initiation is usually a very localized phenomenon inside a grain. The CA model only provides the mean state of a grain but doesn't provide its heterogeneous behavior. One solution to cop for this could be to divide a grain into several Kelvin cells. This would require to increase the number of neighboring grains accounted for in the neighborhood effect which would increase considerably the CPU time. Another possible solution would be the use of the second order moment.

- In Chapter 6 different suggestions were proposed to account for the surface and morphology effect in the CA model which were shown to have a significant impact on the micromechanical stress fields.

- The application of the CA model to textured materials with macrozones could be considered to assess the impact of macrozones on the material stress fields. Expand the neighborhood effect to more than 3 grain layers would be necessary.

- It is possible to control materials textures within a certain range through manufacturing processes. Using the CA model, and considering the margin of error of the manufacturing processes, the textures that would lead to a lower probability of stress concentration can be identified. These textures might lead to more sustainable material fatigue strength.

- The use of EIM, as introduced in Section 1.3.3.5, could be a good source of reflection to replace the preliminary FE simulations necessary to identify the CA model parameters $\mathbb{U}^{\overrightarrow{AB}}$. Meng, Heltsley & Pollard (2012) shared the MATLAB code of an analytical model that evaluates the elastic fields inside and especially outside of an ellipsoidal inclusion immersed in an infinite homogeneous isotropic matrix. Inconveniently, the inclusion is also considered isotropic in the shared code, but that would be a good start toward the replacement of the preliminary FE simulations. Such model could be used to predict the value of $\boldsymbol{\Delta\varepsilon}^{A}_{B_i}$ necessary to identify the parameters $\mathbb{U}^{\overrightarrow{AB}}$ instead of predicting these values with the FEM, which would make the CA model faster and fully autonomous. Also, using such model would help to account for a larger radius of neighboring grains and account for the morphology effect (see recommendations in Section 6.2).

APPENDIX I

ORIENTATION SET DEFINITION AND GENERATION

1. Change of basis

The change of basis from an orthonormal axis system A to an orthonormal axis system B is done by means of the transformation matrix $\boldsymbol{P}$ as follow:

- $\boldsymbol{M}_A$ is a 2nd tensor expressed in the axis system A, and $\boldsymbol{M}_B$ denotes that same tensor expressed in the axis system B. Therefore, the following relation can be written:

$$\begin{cases} \boldsymbol{M}_A = \boldsymbol{P} \times \boldsymbol{M_B} \times \boldsymbol{P}^{-1} \\ \boldsymbol{M}_B = \boldsymbol{P}^{-1} \times \boldsymbol{M_A} \times \boldsymbol{P} \end{cases} \tag{A I-1}$$

- $\mathbb{T}_A$ is a 4th tensor expressed in the axis system A, and $\mathbb{T}_B$ denotes that same tensor expressed in the axis system B. Therefore, the following relation can be written for each $(m, n, o, p) \in [1; 3]$:

$$\begin{cases} \mathbb{T}_{Bmnop} = \sum_{i=1}^{3} \sum_{j=1}^{3} \sum_{k=1}^{3} \sum_{l=1}^{3} P_{im} P_{jn} P_{ko} P_{lp} \mathbb{T}_{Aijkl} \\ \mathbb{T}_{Amnop} = \sum_{i=1}^{3} \sum_{j=1}^{3} \sum_{k=1}^{3} \sum_{l=1}^{3} (P^{-1})_{im} (P^{-1})_{jn} (P^{-1})_{ko} (P^{-1})_{lp} \mathbb{T}_{Bijkl} \end{cases} \tag{A I-2}$$

In the case of the euler angle, the transformation matrix is a sequence of three rotation matrix. The transformation matrix from the crystal axis system C having the Euler angles $(\varphi_1; \Phi; \varphi_2)$ to the global axis system G is expressed after simplification as:

$$\boldsymbol{P} = \begin{bmatrix} c_1 c_2 - s_1 c_0 s_2 & s_1 c_2 + c_1 c_0 s_2 & s_0 s_2 \\ -c_1 s_2 - s_1 c_0 c_2 & -s_1 s_2 + c_1 c_0 c_2 & s_0 c_2 \\ s_1 s_0 & -c_1 s_0 & c_0 \end{bmatrix} \tag{A I-3}$$

$$\text{with}\begin{cases} c_1 = \cos\varphi_1 & s_1 = \sin\varphi_1 \\ c_0 = \cos\phi & s_0 = \sin\phi \\ c_2 = \cos\varphi_2 & s_1 = \sin\varphi_2 \end{cases}$$

2. Quaternion method

The method used to generate uniformly random orientation sets by means of quaternion numbers is as follows:

- R_1, R_2, R_3 are three numbers randomly generated between 0 and 1 for each orientation that we want to generate (using the Matlab function *rand(3,N)* for example).
- γ_1 and γ_2 are two angles calculated as:

$$\begin{cases} \gamma_1 = 2\pi R_1 \\ \gamma_2 = 2\pi R_2 \end{cases} \tag{A I-4}$$

- The four quaternion's components are calculated as:

$$\begin{cases} q_0 = \sqrt{R_3} cos(\gamma_2) \\ q_1 = \sqrt{1 - R_3} sin(\gamma_1) \\ q_2 = \sqrt{1 - R_3} cos(\gamma_1) \\ q_3 = \sqrt{R_3} sin(\gamma_2) \end{cases} \tag{A I-5}$$

3. Quaternion - Euler angles conversion

Once the orientations set is generated by quaternions, it is possible to convert them in Euler angles as follow:

$$\begin{cases} \varphi_1 = a + b \\ \Phi = 2arccos\sqrt{q_0^2 + q_3^2} \\ \varphi_2 = b - a \end{cases} \tag{A I-6}$$

where:

$$\begin{cases} a = \dfrac{\pi}{4} \quad if \quad |q_1| < 10^{-5} \quad and \quad |q_2| < 10^{-5} \\ a = arctan\left(\dfrac{q_2}{q_1}\right) \quad else \end{cases} \tag{A I-7}$$

and

$$\begin{cases} b = \dfrac{\pi}{4} \quad if \quad |q_0| < 10^{-5} \quad and \quad |q_3| < 10^{-5} \\ b = arctan\left(\dfrac{q_3}{q_0}\right) \quad else \end{cases} \tag{A I-8}$$

APPENDIX 3.a

CONVERGENCE STUDIES OF FEM MESHES

A convergence study was performed for each of the meshes used in this paper (Fig. 3.1). The same conditions as in the paper, namely, PBC or KUBC, were applied, depending on the mesh studied. The strain loading $\boldsymbol{E}$ is such that all its components are equal to zero, except for $E_{33} = 0.1‰$.

1. Convergence of the Kelvin structure mesh

Different meshes of the Kelvin structure schematized in Fig. 3.1a were generated with different numbers n_e of elements per Kelvin cell. Two sets of 686 random orientations generated with the quaternion method were tested for each mesh size. The convergence of the variable $\delta^c_{n_e}$ for each cell defined as:

$$\delta^c_{n_e} = \left| \frac{\varepsilon^c_{n_e\,33} - \varepsilon^c_{2800\,33}}{\varepsilon^c_{2800\,33}} \right| \tag{A 3.a-1}$$

was calculated for different numbers of elements. $\varepsilon^c_{n_e\,33}$ is the value of the component "33" of the mean strain tensor of the cell obtained with an average of elements per cell n_e. The maximum value of n_e was 2800, which provided the most accurate mesh. The convergence of the average and maximum values of $\delta^c_{n_e}$ over the 2×686 grains for each mesh size is presented in Fig. 3.a-1a, and shows that for a value of n_e greater than 760 elements, the maximum of $\delta^c_{n_e}$ drops below 1‰. Therefore the mesh with an average of 760 elements per grain was chosen for the FEM study.

2. Convergence of the Kelvin structure mesh

The second convergence study was carried out using the aggregate mesh selected in the previous convergence study and merging it into a cube with a different size ratio $r = r_m/r_a$ (with r_a being the length of the aggregate mesh and r_m the length of the cubic matrix). The crystallographic properties with 259 random orientations were attributed only to the grains in the center of the aggregate (all the grains at a distance lower than or equal to 6 from the center of the mesh) and

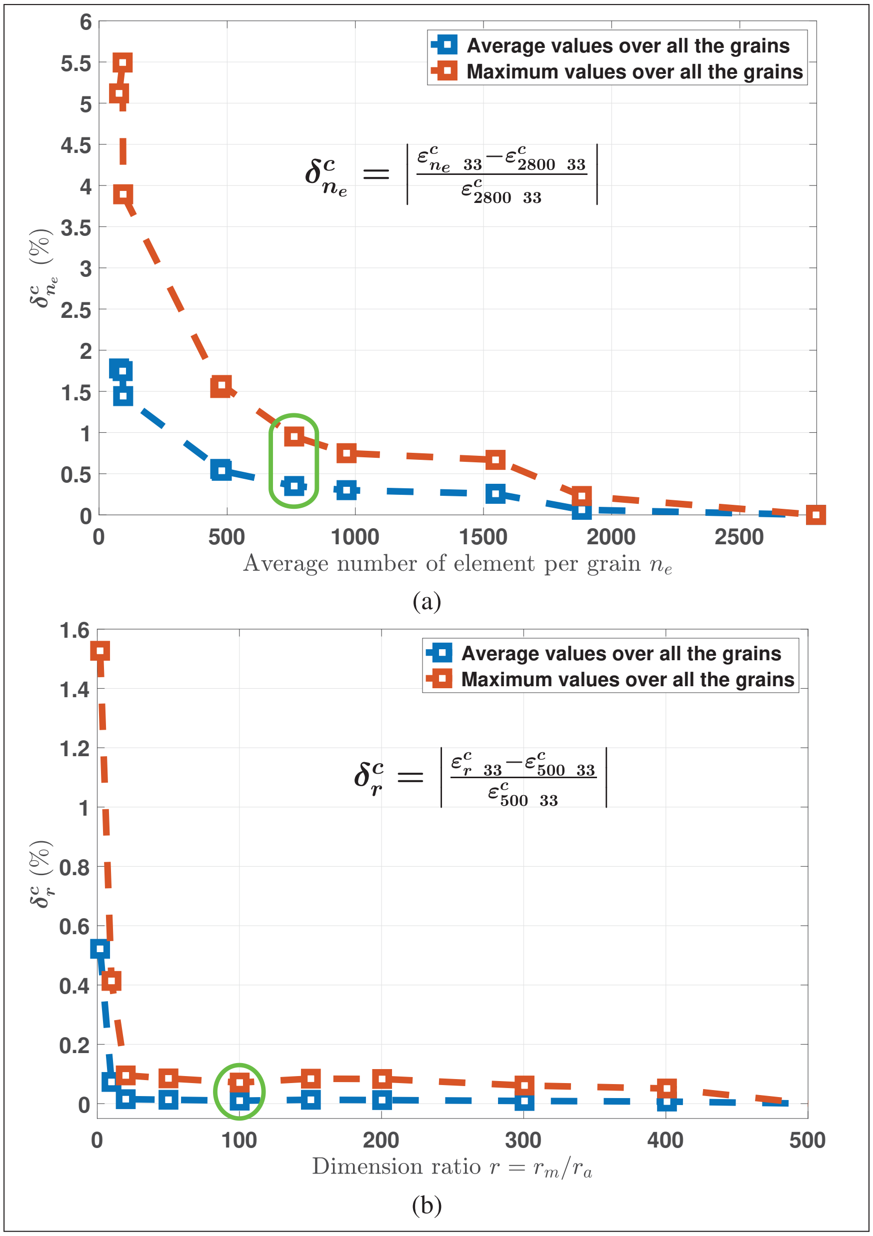

(a)

(b)

Figure-A 3.a-1 Convergence studies of cells mean strain ε^c_{33} submitted to a uniaxial strain loading along $\vec{e}_3$ axis for the PBC and KUBC meshes used in this paper (Fig. 3.1). (a) Influence of the number of elements per grain n_e on its mean stress value over a 686-grain aggregate with PBC; (b) Influence of the size ratio between the matrix cube with KUBC and the merged aggregate cube ($r = r_m/r_a$) on the mean stress value of a grain at the center of the mesh.

the rest of the mesh (the remaining grains and the matrix) had the effective elastic properties. The mean strain variation of these grains were calculated as a function of the value of r. The rest of the mesh had the effective elastic properties. Four sets of orientations were tested for each size ratio. Much like in the previous convergence study, the convergence of the variable δ_r^c of each cells defined as:

$$\delta_r^c = \left| \frac{\varepsilon^c_{r\ 33} - \varepsilon^c_{500\ 33}}{\varepsilon^c_{500\ 33}} \right| \tag{A 3.a-2}$$

was studied, where $\varepsilon^c_{r\ 33}$ is the value of the component "33" of the mean strain tensor of the cell obtained with a size ratio r, with 500 being the maximum ratio r and therefore the most accurate mesh. The convergence of the average and maximum values of δ_r^c over the 4×259 grains for each size ratio is presented in Fig. 3.a-1b. For a value of r greater than $r = 20$, the maximum of δ_r^c over the 4×259 grains converged to its minimum value. An arbitrary size ratio of $r = 100$ was chosen for the FEM study.

APPENDIX 3.b

STATISTICAL DATA REVEALING THE ACCURACY OF THE APPROXIMATION OF $\Delta\varepsilon_B^A$ BY $\Delta\varepsilon_B^{A^{EFF}}$ (EXTENSION OF TABLE 2.3 TO ALL TENSORS COMPONENTS)

Table-A 3.b-1 Statistical data of the difference between the tensors $\boldsymbol{\Delta\varepsilon_B^A}$ and $\boldsymbol{\Delta\varepsilon_B^{A^{eff}}}$ over the 40×40 points from *S-2G* results for each relative position $\overrightarrow{AB}$.

ij	$\times 10^{-5}$	$\overrightarrow{AB} = (0;0;2)$	$\overrightarrow{AB} = (1;1;1)$	$\overrightarrow{AB} = (2;0;0)$
11	Average of $\left\|\Delta\varepsilon^A_{B\ ij}\right\|$	0.4383	0.6127	1.0532
	Average of $\Delta\varepsilon^A_{B\ ij} - \Delta\varepsilon^{A^{eff}}_{B\ ij}$	0.0008	0.0045	-0.0009
	Average of $\left\|\Delta\varepsilon^A_{B\ ij} - \Delta\varepsilon^{A^{eff}}_{B\ ij}\right\|$	0.0830	0.1240	0.0970
	Maximum of $\left\|\Delta\varepsilon^A_{B\ ij} - \Delta\varepsilon^{A^{eff}}_{B\ ij}\right\|$	0.5632	0.5452	0.5328
22	Average of $\left\|\Delta\varepsilon^A_{B\ ij}\right\|$	0.4016	0.5180	0.4918
	Average of $\Delta\varepsilon^A_{B\ ij} - \Delta\varepsilon^{A^{eff}}_{B\ ij}$	0.0000	0.0026	-0.0024
	Average of $\left\|\Delta\varepsilon^A_{B\ ij} - \Delta\varepsilon^{A^{eff}}_{B\ ij}\right\|$	0.0879	0.1311	0.1221
	Maximum of $\left\|\Delta\varepsilon^A_{B\ ij} - \Delta\varepsilon^{A^{eff}}_{B\ ij}\right\|$	0.5717	0.5334	0.5006
33	Average of $\left\|\Delta\varepsilon^A_{B\ ij}\right\|$	1.2721	0.8050	0.4552
	Average of $\Delta\varepsilon^A_{B\ ij} - \Delta\varepsilon^{A^{eff}}_{B\ ij}$	0.0009	-0.0089	0.0039
	Average of $\left\|\Delta\varepsilon^A_{B\ ij} - \Delta\varepsilon^{A^{eff}}_{B\ ij}\right\|$	0.0665	0.1344	0.1233
	Maximum of $\left\|\Delta\varepsilon^A_{B\ ij} - \Delta\varepsilon^{A^{eff}}_{B\ ij}\right\|$	0.4828	0.4783	0.4363
23	Average of $\left\|\Delta\varepsilon^A_{B\ ij}\right\|$	0.0945	0.6663	0.5671
	Average of $\Delta\varepsilon^A_{B\ ij} - \Delta\varepsilon^{A^{eff}}_{B\ ij}$	0.0002	0.0049	-0.0018
	Average of $\left\|\Delta\varepsilon^A_{B\ ij} - \Delta\varepsilon^{A^{eff}}_{B\ ij}\right\|$	0.0820	0.1020	0.0684
	Maximum of $\left\|\Delta\varepsilon^A_{B\ ij} - \Delta\varepsilon^{A^{eff}}_{B\ ij}\right\|$	0.4461	0.3610	0.2916
13	Average of $\left\|\Delta\varepsilon^A_{B\ ij}\right\|$	0.0889	0.5511	0.0841
	Average of $\Delta\varepsilon^A_{B\ ij} - \Delta\varepsilon^{A^{eff}}_{B\ ij}$	-0.0005	0.0017	-0.0025
	Average of $\left\|\Delta\varepsilon^A_{B\ ij} - \Delta\varepsilon^{A^{eff}}_{B\ ij}\right\|$	0.0803	0.1046	0.0739
	Maximum of $\left\|\Delta\varepsilon^A_{B\ ij} - \Delta\varepsilon^{A^{eff}}_{B\ ij}\right\|$	0.4484	0.4301	0.3504
12	Average of $\left\|\Delta\varepsilon^A_{B\ ij}\right\|$	0.2764	0.8873	0.0729
	Average of $\Delta\varepsilon^A_{B\ ij} - \Delta\varepsilon^{A^{eff}}_{B\ ij}$	0.0002	0.0042	-0.0039
	Average of $\left\|\Delta\varepsilon^A_{B\ ij} - \Delta\varepsilon^{A^{eff}}_{B\ ij}\right\|$	0.0614	0.1236	0.0701
	Maximum of $\left\|\Delta\varepsilon^A_{B\ ij} - \Delta\varepsilon^{A^{eff}}_{B\ ij}\right\|$	0.3345	0.4611	0.3049

APPENDIX 4.a

ALTERNATIVE $\mathbb{U}^{\overrightarrow{AB}}$ IDENTIFICATION METHOD

This alternative method to identify the $\mathbb{U}^{\overrightarrow{AB}}$ is based on equations 4.11 and 4.13. An expression this tensor can be obtained as a function of the regression coefficients $a^{\overrightarrow{AB}}_{ijkl}$, $b^{\overrightarrow{AB}}_{ijkl}$ and $c^{\overrightarrow{AB}}_{ijkl}$, and the transformation matrix $\boldsymbol{P}^{\overrightarrow{AB}}$ components between the global and the $*$-axis systems through the following equations:

- Tensors $\mathbb{U}^{\overrightarrow{AB}}$ definition :

$$\Delta\varepsilon^{A^{eff}}_{B\;ij}\left(\boldsymbol{Ekl},\mathbb{C}^{B}\right) = \mathbb{U}^{\overrightarrow{AB}}_{ijklmnop}\left(\mathbb{C}^{B}_{mnop} - \mathbb{C}^{eff}_{mnop}\right) \tag{A 4.a-1}$$

- $\boldsymbol{\Delta\varepsilon}^{A^{eff}}_{B}\left(\boldsymbol{Ekl},\mathbb{C}^{B}\right)$ expressed as a function of $\boldsymbol{\Delta\varepsilon}^{A^{eff}}_{B}\left(\boldsymbol{Lkl},\mathbb{C}^{B}\right)$ and $\boldsymbol{P}^{\overrightarrow{AB}}$ components:

$$\left\{\begin{array}{ll}
Ekl^{*}_{ij} = P^{\overrightarrow{AB}}_{mi}P^{\overrightarrow{AB}}_{nj}Ekl_{mn} = \begin{cases} P^{\overrightarrow{AB}}_{ki}P^{\overrightarrow{AB}}_{lj} & \text{if} \quad k = l \\ (P^{\overrightarrow{AB}}_{ki}P^{\overrightarrow{AB}}_{lj} + P^{\overrightarrow{AB}}_{li}P^{\overrightarrow{AB}}_{kj}) & \text{if} \quad k \neq l \end{cases} & \text{(A 4.a-2a)} \\
\boldsymbol{Ekl} = \displaystyle\sum_{i=1}^{3}\sum_{j=i}^{3} Ekl^{*}_{ij}\boldsymbol{Lij} & \text{(A 4.a-2b)} \\
\Rightarrow \boldsymbol{\Delta\varepsilon}^{A^{eff}}_{B}\left(\boldsymbol{Ekl},\mathbb{C}^{B}\right) = \displaystyle\sum_{i=1}^{3}\sum_{j=i}^{3} Ekl^{*}_{ij}\boldsymbol{\Delta\varepsilon}^{A^{eff}}_{B}\left(\boldsymbol{Lij},\mathbb{C}^{B}\right) & \text{(A 4.a-2c)}
\end{array}\right.$$

- $\boldsymbol{\Delta\varepsilon}_{B}^{A^{eff}}\left(\boldsymbol{Lkl},\mathbb{C}^{B}\right)$ expressed as a function of the regression coefficients $a_{ijkl}^{\overrightarrow{AB}}$, $b_{ijkl}^{\overrightarrow{AB}}$ and $c_{ijkl}^{\overrightarrow{AB}}$, and $\mathbb{C}^{B}$ and $\boldsymbol{P}^{\overrightarrow{AB}}$ components:

$$\begin{cases} \mathbb{C}_{ijkl}^{B\ *} = P_{mi}^{\overrightarrow{AB}} P_{nj}^{\overrightarrow{AB}} P_{ok}^{\overrightarrow{AB}} P_{pl}^{\overrightarrow{AB}} \mathbb{C}_{mnop}^{B} & \text{(A 4.a-3a)} \\ \Delta\varepsilon_{B\ ij}^{A^{eff}\ *}\left(\boldsymbol{Lkl},\mathbb{C}^{B}\right) = \dots & \\ \dots = \begin{cases} a_{ijkl}^{\overrightarrow{AB}} + b_{ijkl}^{\overrightarrow{AB}} \cdot \mathbb{C}_{3-i,3-j,k,l}^{B\ *} + c_{ijkl}^{\overrightarrow{AB}} \cdot \mathbb{C}_{3,3,k,l}^{B\ *} & \{i,j\} \in \{1,2\} \\ a_{ijkl}^{\overrightarrow{AB}} + b_{ijkl}^{\overrightarrow{AB}} \cdot \mathbb{C}_{i,j,k,l}^{B\ *} & i \geq 3 \end{cases} & \text{(A 4.a-3b)} \\ \Delta\varepsilon_{B\ ij}^{A^{eff}}\left(\boldsymbol{Lkl},\mathbb{C}^{B}\right) = P_{mi}^{\overrightarrow{AB}} P_{nj}^{\overrightarrow{AB}} \Delta\varepsilon_{B\ mn}^{A^{eff}\ *}\left(\boldsymbol{Lkl},\mathbb{C}^{B}\right) & \text{(A 4.a-3c)} \end{cases}$$

For each relative position $\overrightarrow{AB}$, the tensor $\boldsymbol{P}^{\overrightarrow{AB}}$ is expressed as follow:

$$\overrightarrow{AB} = (x;y;z) \Rightarrow \begin{cases} \theta_z = \begin{cases} arccos\left(\dfrac{x}{\sqrt{x^2+y^2}}\right) - \dfrac{\pi}{2} & \text{if} \quad y \geq 0 \\ 2\pi - arccos\left(\dfrac{x}{\sqrt{x^2+y^2}}\right) - \dfrac{\pi}{2} & \text{if} \quad y < 0 \\ 0 & \text{if} \quad x = y = 0 \end{cases} \\ \theta_x = -arccos\left(\dfrac{z}{\sqrt{x^2+y^2+z^2}}\right) \end{cases} \qquad \text{(A 4.a-4a)}$$

$$\Rightarrow P = \begin{bmatrix} cos(\theta_z) & -sin(\theta_z) & 0 \\ sin(\theta_z) & cos(\theta_z) & 0 \\ 0 & 0 & 1 \end{bmatrix} \times \begin{bmatrix} 1 & 0 & 0 \\ 0 & cos(\theta_x) & -sin(\theta_x) \\ 0 & sin(\theta_x) & cos(\theta_x) \end{bmatrix} \qquad \text{(A 4.a-4b)}$$

The first step is to identify the regression coefficients $a_{ijkl}^{\overrightarrow{AB}}$, $b_{ijkl}^{\overrightarrow{AB}}$ and $c_{ijkl}^{\overrightarrow{AB}}$. Taking into account the tensor symmetries, there are 6×6 $a_{ijkl}^{\overrightarrow{AB}}$, 6×6 $b_{ijkl}^{\overrightarrow{AB}}$ and 6×2 $c_{ijkl}^{\overrightarrow{AB}}$ coefficients, which makes a total of 84 coefficients to identify. A system of linear equations "$M \times X = N$" can be obtained from equations A 4.a-1-A 4.a-3, where X would be a vector formed by these 84 coefficients; N would be a n-dimension vector built with $\Delta\varepsilon_{B\ ij}^{A^{eff}}\left(\boldsymbol{Ekl},\mathbb{C}^{B}\right)$ values obtained from FEM simulations for different grain B's orientations and different loadings $\boldsymbol{Ekl}$; and M a $n \times 84$ array expressed as a function of $\mathbb{C}^{B}$, $\boldsymbol{Ekl}$ and $\boldsymbol{P}^{\overrightarrow{AB}}$ components. Then, the vector X can be identified by applying a multiple linear regression function to the system. Finally, $\mathbb{U}^{\overrightarrow{AB}}$ components can be identified after expressing them as a function of $a_{ijkl}^{\overrightarrow{AB}}$, $b_{ijkl}^{\overrightarrow{AB}}$ and $c_{ijkl}^{\overrightarrow{AB}}$ from equations A 4.a-1-A 4.a-3.

APPENDIX 4.b

ACCURACY OF THE OPTIMIZED TENSORS $\mathbb{U}^{\overrightarrow{AB}}$ COMPARED TO THE FEM RESULTS

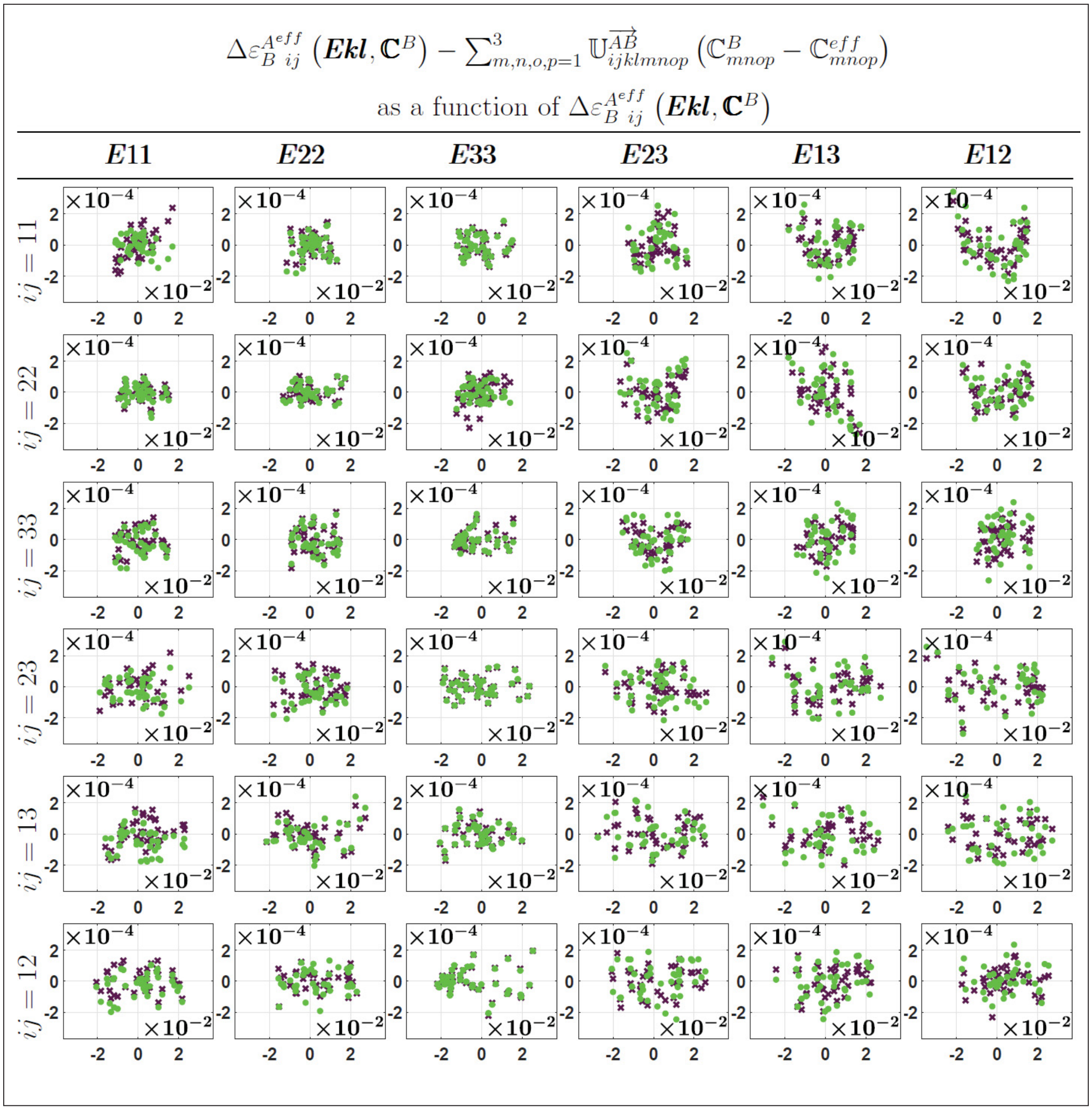

$\Delta\varepsilon^{A^{eff}}_{B\ ij}\left(\boldsymbol{Ekl},\mathbb{C}^{B}\right) - \sum_{m,n,o,p=1}^{3} \mathbb{U}^{\overrightarrow{AB}}_{ijklmnop}\left(\mathbb{C}^{B}_{mnop} - \mathbb{C}^{eff}_{mnop}\right)$

as a function of $\Delta\varepsilon^{A^{eff}}_{B\ ij}\left(\boldsymbol{Ekl},\mathbb{C}^{B}\right)$

Figure-A 4.b-1 Difference between $\boldsymbol{\Delta\varepsilon}_{B}^{A^{eff}}\left(\boldsymbol{Ekl},\mathbb{C}^{B}\right)$ FEM values and their estimates $\mathbb{U}^{\overrightarrow{AB}} : \left(\mathbb{C}^{B} - \mathbb{C}^{eff}\right)$, as a function of $\boldsymbol{\Delta\varepsilon}_{B}^{A^{eff}}\left(\boldsymbol{Ekl},\mathbb{C}^{B}\right)$ FEM values, for $\overrightarrow{AB} = (1;1;1)$ in the case of the Iron properties. The purple crosses refer to the tensor $\mathbb{U}^{\overrightarrow{AB}}$ optimized by using the 40 random orientation set and the green dots refer to the tensor $\mathbb{U}^{\overrightarrow{AB}}$ optimized by using the 8 orientation set. Each figure shows approximetely 2 orders of difference between the x and y axis revealing the accuracy of the estimates.

APPENDIX 4.c

CA ALGORITHM

Algorithm-A 4.c-1 CA algorithm

```
Input: Macroscopic applied loading $\boldsymbol{E}$, macroscopic mechanical properties (stiffness tensor $\mathbb{C}^{eff}$, Poisson ratio $\nu^{eff}$), stiffness tensor of the crystal structure $\mathbb{C}^{cry}$, position $(x^c; y^c; z^c)$ and orientation $[\varphi_1^c, \phi^c, \varphi_2^c]$ of each cell center, tensor $\mathbb{U}^{\overrightarrow{AB}}$ for each relative position $\overrightarrow{AB}$ identified from the FEM simulations, the radius of the neighborhood influence $R$.
Output: Mean stress/strain fields for each cells ($\boldsymbol{\sigma}^c$ and $\boldsymbol{\varepsilon}^c$), macroscopic stress $\boldsymbol{\Sigma}$.
Start:
$\mathbb{S}_E \leftarrow \frac{(1+\nu^{eff})}{3(1-\nu^{eff})}\mathbb{J} + \frac{2(4-5\nu^{eff})}{15(1-\nu^{eff})}\mathbb{K}$
for each cells $c$ do
    Change of basis (Local to Global) : $\mathbb{C}^c \xleftarrow{[\varphi_1^C;\phi^C;\varphi_2^C]} \mathbb{C}^{cry}$
    $\mathbb{A}_E^c \leftarrow \left(\mathbb{I} + \mathbb{S}_E : \mathbb{C}^{eff\,-1} : (\mathbb{C}^c - \mathbb{C}^{eff})\right)^{-1}$
end
for each cells $c$ do
    $\mathbb{A}_{CA}^c \leftarrow \mathbb{A}_E^c$
    for each neighboring cells $n$ do
        $\overrightarrow{cn} \leftarrow (x^n - x^c; y^n - y^c; z^n - z^c)$   ▹ (periodicity have to be considered to calculate the distance between the two grains)
        if $\|\overrightarrow{cn}\| \leq R$ then
            $\mathbb{A}_{ijkl}^{\overrightarrow{cn}} \leftarrow \begin{cases} \mathbb{U}_{ijkl}^{\overrightarrow{cn}}(\mathbb{C}_{mnop}^n - \mathbb{C}_{mnop}^{eff}) & \text{if} \quad k = l \\ \frac{1}{2}\mathbb{U}_{ijkl}^{\overrightarrow{cn}}(\mathbb{C}_{mnop}^n - \mathbb{C}_{mnop}^{eff}) & \text{else} \end{cases}$
            $\mathbb{A}_{CA}^c \leftarrow \mathbb{A}_{CA}^c + \mathbb{A}^{\overrightarrow{cn}}$
        end
    end
end
for each cells $c$ do
    $\boldsymbol{\varepsilon}^c \leftarrow \langle \mathbb{A}_{CA}^c \rangle_c^{-1} : \mathbb{A}_{CA}^c : \boldsymbol{E}$   ▹ (To ensure $\langle \boldsymbol{\varepsilon}^c \rangle_c = \boldsymbol{E}$)
    $\boldsymbol{\sigma}^c \leftarrow \mathbb{C}^c : \boldsymbol{\varepsilon}^c$
end
$\boldsymbol{\Sigma} \leftarrow \langle \boldsymbol{\sigma}^c \rangle_c$
```

APPENDIX 4.d

IPF OF $\Delta\tau^{A}_{S^{A}_{M}\ B_{I}}$ IN THE CASE $(\varphi^{A}_{1}, \phi^{A}, \varphi^{A}_{2}) = (0,0,0)$

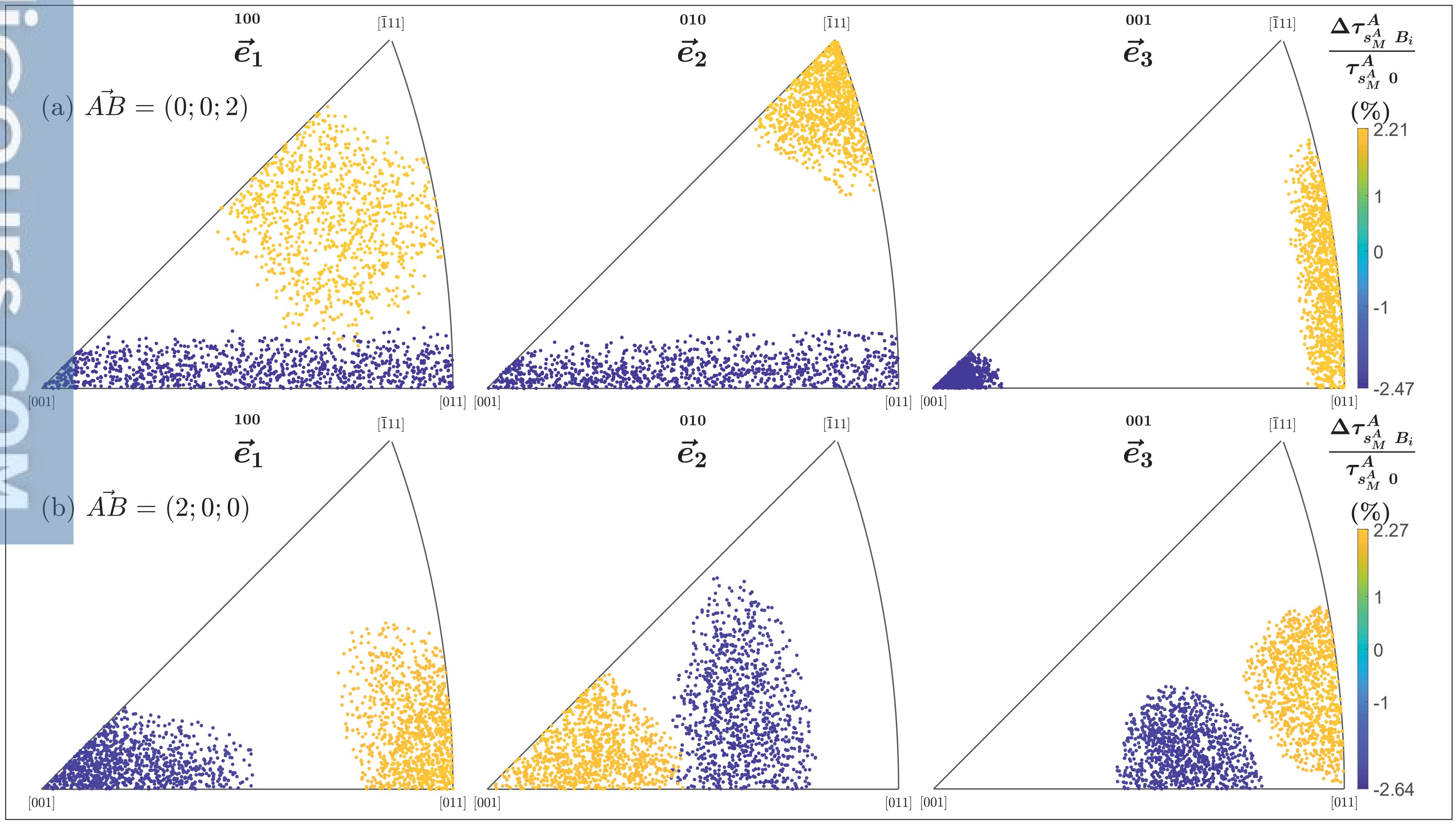

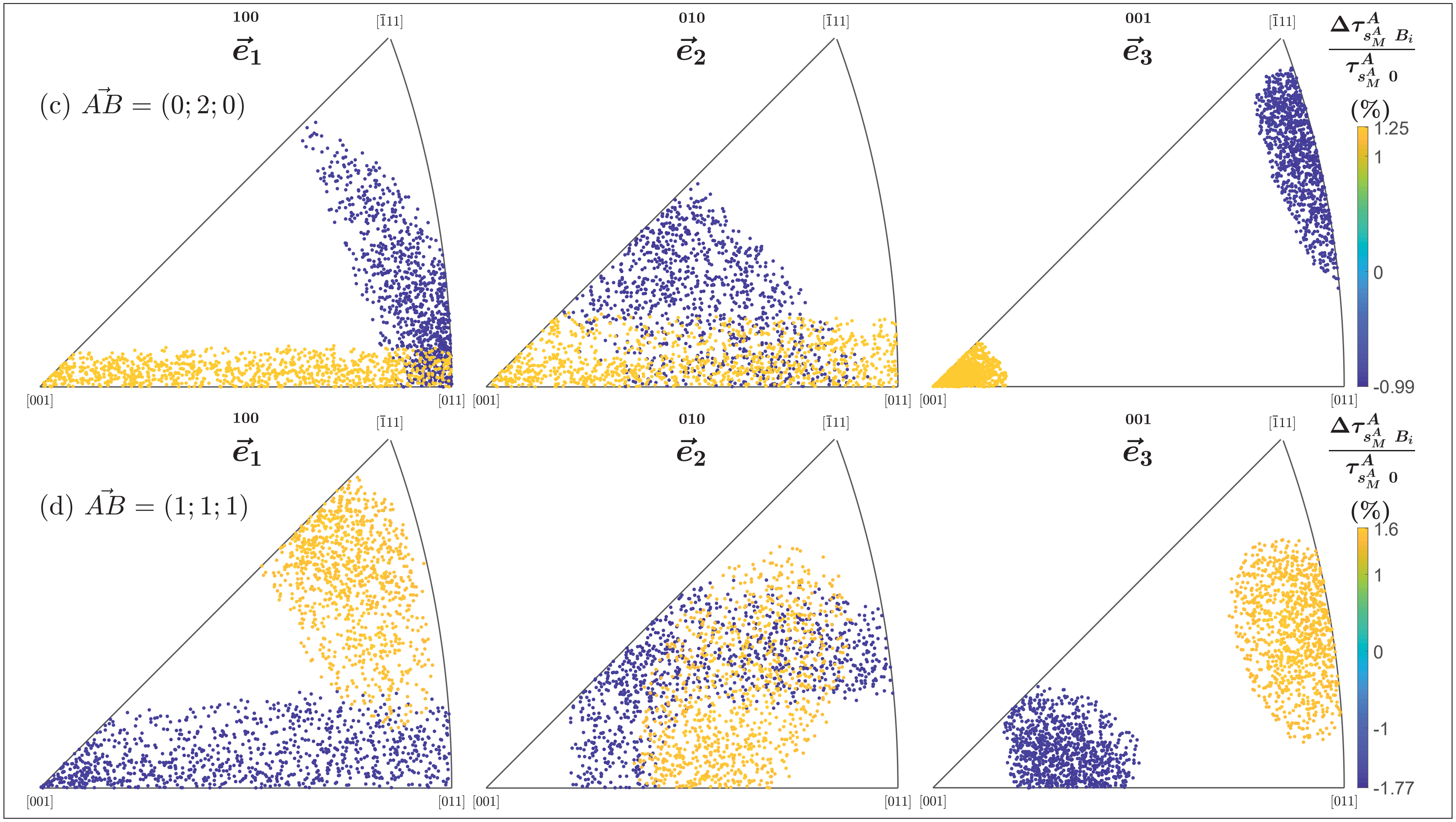

Figure-A 4.d-0 Inverse pole figure in the global axis direction of grain B_i's orientation in the cubic standard stereo-triangle, color coded as a function of the resolved shear stress percentage variations ($\Delta\tau^{A}_{s^A_M\ B_i}/\tau^{A}_{s^A_M\ 0}$) over 100,000 random orientations (only the 1,000 lowest and the 1,000 highest values are plotted), in the case where grain A's Euler angles are $(0,0,0)$ such that $\tau^{A}_{s^A_M\ 0} = 44.9$ MPa for the loading $\boldsymbol{E}_{strain}$, for three different relative positions: (a) $\overrightarrow{AB} = (0;0;2)$, (b) $\overrightarrow{AB} = (2;0;0)$, (c) $\overrightarrow{AB} = (1;1;1)$.

APPENDIX 5.a

MATERIAL DATA FOR 316L STEEL

316L steel is a face centered cubic material with twelve octahedral slip systems. The material cubic stiffness tensor are provided by Huntington (1958) and the material plastic model parameters are provided by Guilhem *et al.* (2013) identified from solving the inverse problem by means of a mean field model. The material parameters are presented in Table 5.a-1, and the list of the slip systems in Table 5.a-2.

The effective elastic properties of the material were assumed to be isotropic with a Young's modulus E_y^{eff} of 196 GPa and a Poisson's ratio ν^{eff} of 0.280. These values were obtained through the homogenization of FE simulations of a polycrystalline aggregate RVE submitted to an elastic loading by following the method described by Bretin *et al.* (2019a).

As a reminder, the crystal cubic tensor and the isotropic effective tensor can be defined by means of the projector tensors as:

$$\mathbb{C}^{eff} = \frac{E_y^{eff}}{1-2\nu^{eff}}\mathbb{J} + \frac{E_y^{eff}}{1+\nu^{eff}}\mathbb{K} \qquad \text{(A 5.a-1a)}$$

$$\mathbb{C}^{cry} = \frac{E_y^{cry}}{1-2\nu^{cry}}\mathbb{J} + \frac{E_y^{cry}}{1+\nu^{cry}}\mathbb{K}_a + 2G^{cry}\mathbb{K}_b \qquad \text{(A 5.a-1b)}$$

where E_y, ν and G are respectively the Young's modulus, Poisson's ratio and shear modulus of the crystal ($\bullet^{cry}$) or the effective material ($\bullet^{eff}$); $\mathbb{J}$, $\mathbb{K}$, $\mathbb{K}_a$ and $\mathbb{K}_b$ are the projector tensors such that $\mathbb{J}_{ijkl} = \frac{1}{3}(\delta_{ij}\delta_{kl})/2$, $\mathbb{K}$=$\mathbb{I} - \mathbb{K}$, $\mathbb{K}_a = \mathbb{Z} - \mathbb{J}$ and $\mathbb{K}_b = \mathbb{I} - \mathbb{Z}$ with $\mathbb{Z}_{ijkl} = \delta_{ij}\delta_{ik}\delta_{il}$.

In order to account for the crystal orientation relatively to the global axis, a change of basis has to be performed on $\mathbb{C}^{cry}$ to obtained $\mathbb{C}^g$ by means of the rotation tensor $\boldsymbol{P}$ which depends on the crystal orientation as follow:

$$\mathbb{C}^g{}_{mnop} = \sum_{i=1}^{3}\sum_{j=1}^{3}\sum_{k=1}^{3}\sum_{l=1}^{3} P_{im}P_{jn}P_{ko}P_{lp}\mathbb{C}^{cry}{}_{ijkl} \qquad \text{(A 5.a-2)}$$

Table-A 5.a-1 Material parameters of the 316L steel (Guilhem *et al.*, 2013; Huntington, 1958).

E_y^{eff} (GPa)	ν^{eff}		$\mathbb{C}_{1111}^{eff}$ (GPa)	$\mathbb{C}_{1122}^{eff}$ (GPa)		
196	0.280		251	97.9		
E_y^{cry} (GPa)	ν^{cry}	G^{cry} (GPa)	$\mathbb{C}_{1111}^{cry}$ (GPa)	$\mathbb{C}_{1122}^{cry}$ (GPa)	$\mathbb{C}_{1212}^{cry}$ (GPa)	
100	0.3882	122	197	125	122	
K ($MPa.s^{-n}$)	n	r_0 (MPa)	Q (MPa)	b	c_χ (MPa)	d
12	11	40	10	3	40	1500
$h1$	$h2$	$h3$	$h4$	$h5$	$h6$	
1	1	0.6	12.3	1.6	1.8	

Table-A 5.a-2 Slip system list and their hardening matrix.

Plane	Direction	System #	A2	A3	A6	B2	B4	B5	C1	C3	C5	D1	D4	D6
$(\bar{1}11)$	$[0\bar{1}1]$	A2	h_1	h_2	h_2	h_4	h_5	h_5	h_3	h_5	h_6	h_3	h_6	h_5
$(\bar{1}11)$	$[101]$	A3	h_2	h_1	h_2	h_5	h_3	h_6	h_5	h_4	h_5	h_6	h_3	h_5
$(\bar{1}11)$	$[110]$	A6	h_2	h_2	h_1	h_5	h_6	h_3	h_6	h_5	h_3	h_5	h_5	h_4
(111)	$[0\bar{1}1]$	B2	h_4	h_5	h_5	h_1	h_2	h_2	h_3	h_6	h_5	h_3	h_5	h_6
(111)	$[\bar{1}01]$	B4	h_5	h_3	h_6	h_2	h_1	h_2	h_6	h_3	h_5	h_5	h_4	h_5
(111)	$[1\bar{1}0]$	B5	h_5	h_6	h_3	h_2	h_2	h_1	h_5	h_5	h_4	h_6	h_5	h_3
$(11\bar{1})$	$[011]$	C1	h_3	h_5	h_6	h_3	h_6	h_5	h_1	h_2	h_2	h_4	h_5	h_5
$(11\bar{1})$	$[101]$	C3	h_5	h_4	h_5	h_6	h_3	h_5	h_2	h_1	h_2	h_5	h_3	h_6
$(11\bar{1})$	$[1\bar{1}0]$	C5	h_6	h_5	h_3	h_5	h_5	h_4	h_2	h_2	h_1	h_5	h_6	h_3
$(1\bar{1}1)$	$[011]$	D1	h_3	h_6	h_5	h_3	h_5	h_6	h_4	h_5	h_5	h_1	h_2	h_2
$(1\bar{1}1)$	$[\bar{1}01]$	D4	h_6	h_3	h_5	h_5	h_4	h_5	h_5	h_3	h_6	h_2	h_1	h_2
$(1\bar{1}1)$	$[110]$	D6	h_5	h_5	h_4	h_6	h_5	h_3	h_5	h_6	h_3	h_2	h_2	h_1

APPENDIX 5.b

MESH CONVERGENCE STUDIES

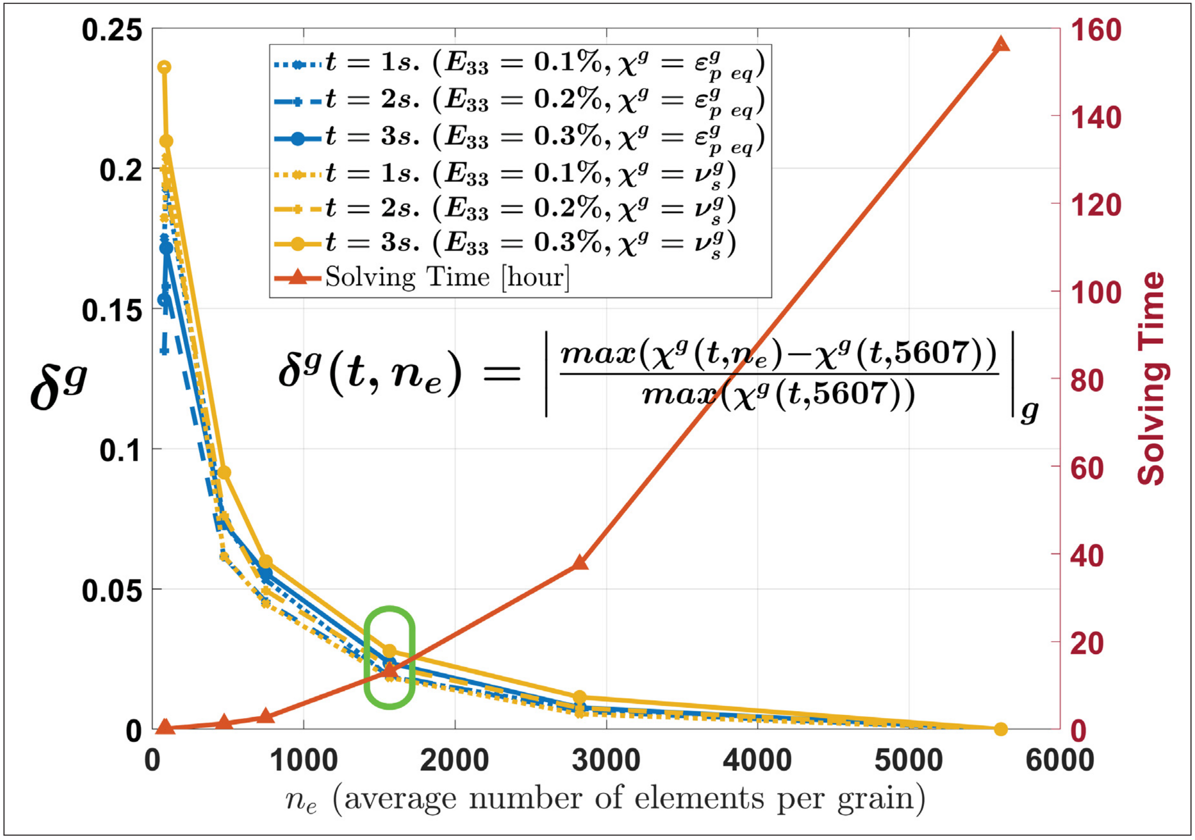

Figure-A 5.b-1 Mesh convergence study of finite element analysis with different mesh sizes with respect to $\varepsilon^g_{p\ eq}$ and ν^g_s over all grains. The selected mesh is framed in green

A mesh convergence study was performed. Kelvin structures of 250 grains were meshed with tetrahedral elements with quadratic interpolation with different mesh density. Three randomly orientated aggregates were used for the mesh convergence study making a total of 3×250 grain's mean values to compare. The monotonic load described in Eq. 5.19 was submitted to the aggregate up to $E_{33} = 0.3\%$ as presented in section 5.4.1. For each mesh size and each orientations' set, the values $\varepsilon^g_{p\ eq}$ and ν^g_s as defined in section 5.3.1 are computed and compared grain by grain (and slip system by slip system for ν^g_s) to the values obtained with the finest mesh (~ 5607 elements per grain). Fig. 5.b-1 exhibits the maximum difference observed with each mesh for both variables over all grains normalized by the maximum values observed with the finest mesh (δ) as a function of the average number of the element per grain (n_e). Alongside those values are exhibited the solving time for each mesh size. The mesh with an average of 1567 element per grain (framed in green) was selected due to a compromise between accuracy and solving time.

REFERENCES

Altmann, S. (2005). *Rotations, Quaternions, and Double Groups*. Dover Publications.

American Society for Testing and Materials. (1997). *Standard Terminology Relating to Fatigue and Fracture Testing*. ASTM International E1823-97. West Conshohoken: American Society for Testing and Materials.

Ashby, M. (1970). The deformation of plastically non-homogeneous materials. *The Philosophical Magazine: A Journal of Theoretical Experimental and Applied Physics*, 21(170), 399–424.

Avazmohammadi, R., Yang, F. & Abbasion, S. (2009). Effect of interface stresses on the elastic deformation of an elastic half-plane containing an elastic inclusion. *International Journal of Solids and Structures*, 46(14), 2897 - 2906. doi: https://doi.org/10.1016/j.ijsolstr.2009.03.012.

Badulescu, C., Lahellec, N. & Suquet, P. (2015). Field statistics in linear viscoelastic composites and polycrystals. *European Journal of Mechanics - A/Solids*, 49, 329 - 344. doi: https://doi.org/10.1016/j.euromechsol.2014.07.012.

Bao-Tong, M. & Laird, C. (1989). Overview of fatigue behavior in copper single crystals—I. Surface morphology and stage I crack initiation sites for tests at constant strain amplitude. *Acta Metallurgica*, 37(2), 325 - 336. doi: https://doi.org/10.1016/0001-6160(89)90217-4.

Barbe, F. (2000). *Etude numérique de la plasticité d'agrégats polycristallins*. (Thesis, Écolde des Mines de Paris).

Barbe, F., Decker, L., Jeulin, D. & Cailletaud, G. (2001a). Intergranular and intragranular behavior of polycrystalline aggregates. Part 1: F.E. model. *International Journal of Plasticity*, 17(4), 513 - 536. doi: https://doi.org/10.1016/S0749-6419(00)00061-9.

Barbe, F., Forest, S. & Cailletaud, G. (2001b). Intergranular and intragranular behavior of polycrystalline aggregates.Part 2: Results. *International Journal of Plasticity*, 17(4), 537 - 563. doi: https://doi.org/10.1016/S0749-6419(00)00062-0.

Basquin, O. (1910). The Exponential Law of Endurance Tests. *American Society for Testing and Materials Proceedings*, 10, 625 - 630.

Bathias, C. & Pineau, A. (2013). *Fatigue of Materials and Structures: Fundamentals*. Wiley.

Bazergui, A. (2002). *Résistance des matériaux*. Presses internationales Polytechnique.

Benedetti, I. & Barbe, F. (2013). Modelling Polycrystalline Materials: An Overview of Three-Dimensional Grain-Scale Mechanical Models. *Journal of Multiscale Modelling*, 05(01), 1350002. doi: 10.1142/S1756973713500029.

Benedikt, B., Lewis, M. & Rangaswamy, P. (2006). On elastic interactions between spherical inclusions by the equivalent inclusion method. *Computational Materials Science*, 37(3), 380-392. doi: https://doi.org/10.1016/j.commatsci.2005.10.002.

Benveniste, Y. (1987). A new approach to the application of Mori-Tanaka's theory in composite materials. *Mechanics of Materials*, 6(2), 147-157. doi: http://dx.doi.org/10.1016/0167-6636(87)90005-6.

Berbenni, S. & Capolungo, L. (2015). A Mori–Tanaka homogenization scheme for non-linear elasto-viscoplastic heterogeneous materials based on translated fields: An affine extension. *Comptes Rendus Mécanique*, 343(2), 95 - 106. doi: https://doi.org/10.1016/j.crme.2014.12.003. Mechanics of granular and polycrystalline solids.

Beretta, S., Clerici, P. & Matteazzi, S. (1995). The effect of sample size on the confidence of endurance fatigue tests. *Fatigue & Fracture of Engineering Materials & Structures*, 18(1), 129-139. doi: 10.1111/j.1460-2695.1995.tb00147.x.

Berveiller, M. & Zaoui, A. (1978). An extension of the self-consistent scheme to plastically-flowing polycrystals. *Journal of the Mechanics and Physics of Solids*, 26(5–6), 325-344. doi: http://dx.doi.org/10.1016/0022-5096(78)90003-0. SC.

Berveiller, M., Fassi-Fehri, O. & Hihi, A. (1987). The problem of two plastic and heterogeneous inclusions in an anisotropic medium. *International Journal of Engineering Science*, 25(6), 691-709. doi: https://doi.org/10.1016/0020-7225(87)90058-9.

Besson, J., Blétry, M., Cailletaud, G., Chaboche, J. & Forest, S. (2009). *Non-Linear Mechanics of Materials*. Springer Netherlands. Consulted at https://books.google.ca/books?id=AIP0wmnXQ8YC.

Bj Kim, D. K. (2005). *Fatigue Endurance Diagram for Materials with Defects Fatigue and Fracture Mechanics, 34th Volume*. West Conshohocken, PA: ASTM International. doi: 10.1520/STP11502S.

Boutana, N., Bocher, P., Jahazi, M., Piot, D. & Montheillet, F. (2008a). Microstructural modeling of cold creep/fatigue in near alpha titanium alloys using cellular automata method. *Transactions of the Canadian Society for Mechanical Engineering*, 32(2), 195-213. Consulted at https://www.scopus.com/inward/record.uri?eid=2-s2.0-58149488893&partnerID=40&md5=ea44922e9c0db73bc91b692cced4593d. cited By 7.

Boutana, N., Bocher, P., Jahazi, M., Piot, D. & Montheillet, F. (2008b). The microstructural modelling of room temperature creep in titanium alloys using a cellular automata model. *International Journal of Microstructure and Materials Properties*, 3(4-5), 642-653. doi: 10.1504/IJMMP.2008.022041. cited By 2.

Boutana, N., Bocher, P. & Jahazi, M. (2013). Discrepancy between fatigue and dwell-fatigue behavior of near alpha titanium alloys simulated by cellular automata. *International Journal of Fatigue*, 51, 49-56. doi: 10.1016/j.ijfatigue.2012.09.012. cited By 5.

Brassart, L., Stainier, L., Doghri, I. & Delannay, L. (2011). A variational formulation for the incremental homogenization of elasto-plastic composites. *Journal of the Mechanics and Physics of Solids*, 59(12), 2455 - 2475. doi: https://doi.org/10.1016/j.jmps.2011.09.004.

Brenner, R., Lebensohn, R. A. & Castelnau, O. (2009). Elastic anisotropy and yield surface estimates of polycrystals. *International Journal of Solids and Structures*, 46(16), 3018-3026. doi: http://dx.doi.org/10.1016/j.ijsolstr.2009.04.001.

Bretin, R., Levesque, M. & Bocher, P. (2019a). Neighborhood effect on the strain distribution in linearly elastic polycrystals: Part 1 – Finite element study of the interaction between grains. *International Journal of Solids and Structures*, 176-177, 36 - 48. doi: https://doi.org/10.1016/j.ijsolstr.2019.05.015.

Bretin, R., Levesque, M. & Bocher, P. (2019b). Neighborhood effect on the strain distribution in linearly elastic polycrystals: Part 2 – Cellular Automaton. *International Journal of Solids and Structures*, 176-177, 49 - 67. doi: https://doi.org/10.1016/j.ijsolstr.2019.07.005.

Bretin, R. (2016). *Développement d'un modèle analytique pour l'analyse en élasticité linéaire de champs de déformation et contrainte au sein d'un polycristal. comparaison avec la méthode des éléments finis.* (Master's thesis, École de technologie supérieure, Montréal). Consulted at http://espace.etsmtl.ca/1654/.

Bridier, F., Villechaise, P. & Mendez, J. (2008). Slip and fatigue crack formation processes in an α/β titanium alloy in relation to crystallographic texture on different scales. *Acta Materialia*, 56(15), 3951-3962. doi: https://doi.org/10.1016/j.actamat.2008.04.036.

Brisard, S., Dormieux, L. & Sab, K. (2014). A variational form of the equivalent inclusion method for numerical homogenization. *International Journal of Solids and Structures*, 51(3), 716-728. doi: https://doi.org/10.1016/j.ijsolstr.2013.10.037.

Budiansky, B. (1965). On the elastic moduli of some heterogeneous materials. *Journal of the Mechanics and Physics of Solids*, 13(4), 223-227. doi: http://dx.doi.org/10.1016/0022-5096(65)90011-6.

Burr, I. W. (1942). Cumulative Frequency Functions. *Ann. Math. Statist.*, 13(2), 215–232. doi: 10.1214/aoms/1177731607.

Cailletaud, G. (1992). A micromechanical approach to inelastic behaviour of metals. *International Journal of Plasticity*, 8(1), 55 - 73. doi: https://doi.org/10.1016/0749-6419(92)90038-E.

Cailletaud, G., Forest, S., Jeulin, D., Feyel, F., Galliet, I., Mounoury, V. & Quilici, S. (2003). Some elements of microstructural mechanics. *Computational Materials Science*, 27(3), 351-374. doi: http://dx.doi.org/10.1016/S0927-0256(03)00041-7.

Cailletaud, G. & Coudon, F. (2016). Scale Transition Rules Applied to Crystal Plasticity. In Trovalusci, P. (Ed.), *Materials with Internal Structure: Multiscale and Multifield Modeling and Simulation* (pp. 1–15). Cham: Springer International Publishing. doi: 10.1007/978-3-319-21494-8_1.

Castañeda, P. & Willis, J. (1995). The effect of spatial distribution on the effective behavior of composite materials and cracked media. *Journal of the Mechanics and Physics of Solids*, 43(12), 1919 - 1951. doi: https://doi.org/10.1016/0022-5096(95)00058-Q.

Castañeda, P. P. (1991). The effective mechanical properties of nonlinear isotropic composites. *Journal of the Mechanics and Physics of Solids*, 39(1), 45–71.

Castaneda, P. P. & Suquet, P. (1997). Nonlinear composites. In *Advances in applied mechanics* (vol. 34, pp. 171–302). Elsevier.

Cruzado, A., LLorca, J. & Segurado, J. (2017). Modeling cyclic deformation of inconel 718 superalloy by means of crystal plasticity and computational homogenization. *International Journal of Solids and Structures*, 122, 148–161.

Cruzado, A., Lucarini, S., LLorca, J. & Segurado, J. (2018). Microstructure-based fatigue life model of metallic alloys with bilinear Coffin-Manson behavior. *International Journal of Fatigue*, 107, 40–48.

Curtit, F., Le Pecheur, A. & Stephan, J. (2008). Comparison of Fatigue Damage Criteria Applied to Multiaxial Fatigue. *ASME 2008 Pressure Vessels and Piping Conference*, pp. 403–410.

Dang Van, K., Cailletaud, G., Flavenot, J. F., Le Douaron, A. & Lieurade, H. P. (2013). Criterion for High-Cycle Fatigue Failure under Multiaxial Loading.

Di Paola, F. (2010). *Modélisation multi-échelles du comportement thermo-mécanique de composites à renforts sphériques*. (Thesis, École Centrale Paris).

Dilmi, H., Chouaib, A., Safi, B., Boudjema, B., Saidi, M. & Lounas, O. (2015). The fatigue flexural behavior of fiber reinforced concrete: Effect of the parameters of coarse aggregates. *Scientific Research and Essays*, Vol.10,, 31-40. doi: 10.5897/SRE2014.6137.

Doghri, I., Brassart, L., Adam, L. & Gérard, J.-S. (2011). A second-moment incremental formulation for the mean-field homogenization of elasto-plastic composites. *International Journal of Plasticity*, 27(3), 352 - 371. doi: https://doi.org/10.1016/j.ijplas.2010.06.004.

Déprés, C., Robertson, C. & Fivel, M. (2006). Low-strain fatigue in 316L steel surface grains: A three dimension discrete dislocation dynamics modelling of the early cycles. Part 2: Persistent slip markings and micro-crack nucleation. *Philosophical Magazine*, 86(1), 79-97. doi: 10.1080/14786430500341250. cited By 47.

Déprés, C., Fivel, M. & Tabourot, L. (2008). A dislocation-based model for low-amplitude fatigue behaviour of face-centred cubic single crystals. *Scripta Materialia*, 58(12), 1086-1089. doi: http://dx.doi.org/10.1016/j.scriptamat.2008.02.027.

Dvorak, G., Bahei-El-Din, Y. & Wafa, A. (1994). The modeling of inelastic composite materials with the transformation field analysis. *Modelling and Simulation in Materials Science and Engineering*, 2(3A), 571.

Eberl, F. (1999). *Second Order Heterogeneities in a Multicrystal: Experimental Developments using X-Ray Diffraction and Comparison with a Finite Element Model*. (Thesis, Ecole Nationale Supérieure des Arts et Métiers).

Eshelby, J. D. (1957). *The Determination of the Elastic Field of an Ellipsoidal Inclusion, and Related Problems*. doi: 10.1098/rspa.1957.0133.

Evrard, P., Aubin, V., Degallaix, S. & Kondo, D. (2008a). Formulation of a new single crystal law for modeling the cyclic softening. *Mechanics Research Communications*, 35(8), 589 - 594. doi: https://doi.org/10.1016/j.mechrescom.2008.06.001.

Evrard, P., Aubin, V., Pilvin, P., Degallaix, S. & Kondo, D. (2008b). Implementation and validation of a polycrystalline model for a bi-phased steel under non-proportional loading paths. *Mechanics Research Communications*, 35(5), 336 - 343. doi: https://doi.org/10.1016/j.mechrescom.2008.01.006.

Fatemi, A. & Socie, D. F. (1988). A critical plane approach to multiaxial fatigue damage including out-of-phase loading. *Fatigue & Fracture of Engineering Materials & Structures*, 11(3), 149–165.

Forest, S., Cailletaud, G., Jeulin, D., Feyel, F., Galliet, I., Mounoury, V. & Quilici, S. (2002). Introduction au calcul de microstructures. *Mecanique et Industries*, 3(5), 439-456.

doi: http://dx.doi.org/.

Frederick, C. & Armstrong, P. (2007). A Mathematical Representation of the Multiaxial Bauscinger Effect. *Materials at High Temperatures*, 24, 1-26. doi: 10.3184/096034007X207589.

Fritzen, F. (2011). *Microstructural Modeling and Computational Homogenization of the Physically Linear and Nonlinear Constitutive Behavior of Micro-heterogeneous Materials*. KIT Scientific Publ.

Fritzen, F. & Böhlke, T. (2010). Three-dimensional finite element implementation of the nonuniform transformation field analysis. *International Journal for Numerical Methods in Engineering*, 84(7), 803–829.

Galvanetto, U. & Aliabadi, M. (2010). *Multiscale Modeling in Solid Mechanics: Computational Approaches*. Imperial College Press.

Gavazzi, A. C. & Lagoudas, D. C. (1990). On the numerical evaluation of Eshelby's tensor and its application to elastoplastic fibrous composites. *Computational Mechanics*, 7(1), 13-19. doi: 10.1007/BF00370053.

Gérard, C. (2008). *Field measurements and identification of crystal plasticity models*. (Theses, Université Paris-Nord - Paris XIII). Consulted at https://tel.archives-ouvertes.fr/tel-00315792.

Germain, L., Gey, N., Humbert, M., Bocher, P. & Jahazi, M. (2005). Analysis of sharp microtexture heterogeneities in a bimodal IMI 834 billet. *Acta Materialia*, 53(13), 3535 - 3543. doi: https://doi.org/10.1016/j.actamat.2005.03.043.

Gilbert, E. N. (1962). Random Subdivisions of Space into Crystals. *Ann. Math. Statist.*, 33(3), 958–972. doi: 10.1214/aoms/1177704464.

Groeber, M., Haley, B., Uchic, M., Dimiduk, D. & Ghosh, S. (2006). 3D reconstruction and characterization of polycrystalline microstructures using a FIB–SEM system. *Materials Characterization*, 57(4), 259 - 273. doi: https://doi.org/10.1016/j.matchar.2006.01.019.

Guerchais, R., Morel, F. & Saintier, N. (2017). Effect of defect size and shape on the high-cycle fatigue behavior. *International Journal of Fatigue*, 100, 530 - 539. doi: https://doi.org/10.1016/j.ijfatigue.2016.12.010. Multiaxial Fatigue 2016: Experiments and Modeling.

Guery, A., Hild, F., Latourte, F. & Roux, S. (2016). Slip activities in polycrystals determined by coupling DIC measurements with crystal plasticity calculations. *International Journal of Plasticity*, 81, 249 - 266. doi: https://doi.org/10.1016/j.ijplas.2016.01.008.

Guilhem, Y. (2011). *Étude numérique des champs mécaniques locaux dans les agrégats polycristallins d'acier 316L sous chargement de fatigue*. (Thesis, École Nationale Supérieure des Mines de Paris, Paris).

Guilhem, Y., Basseville, S., Curtit, F., Stephan, J.-M. & Cailletaud, G. (2010). Investigation of the effect of grain clusters on fatigue crack initiation in polycrystals. *International Journal of Fatigue*, 32(11), 1748-1763.

Guilhem, Y., Basseville, S., Curtit, F., Stephan, J.-M. & Cailletaud, G. (2013). Numerical investigations of the free surface effect in three-dimensional polycrystalline aggregates. *Computational Materials Science*, 70, 150-162.

Haboussa, D. (2014). *Mono and polycrystalline behaviors elastoviscoplastic - Code_Aster documentation R5.03.11* (Report n°R5.03.11). France: Code_Aster - EDF R&D. Consulted at https://www.code-aster.org/doc/v14/en/man_r/r5/r5.03.11.pdf.

Hashin, Z. & Shtrikman, S. (1963). A variational approach to the theory of the elastic behaviour of multiphase materials. *Journal of the Mechanics and Physics of Solids*, 11(2), 127-140. doi: http://dx.doi.org/10.1016/0022-5096(63)90060-7.

Hemery, S., Nait-Ali, A., Gueguen, M. & Villechaise, P. (2018). Mechanical study of crystalline orientation distribution in Ti-6Al-4V: An assessment of micro-texture induced load partitioning. *Materials and Design*, 137, 22-32. doi: https://doi.org/10.1016/j.matdes.2017.10.011.

Hertzberg, R., Vinci, R. & Hertzberg, J. (2012). *Deformation and Fracture Mechanics of Engineering Materials, 5th Edition*. Wiley.

Hesselbarth, H. W. & Göbel, I. R. (1991). Simulation of recrystallization by cellular automata. *Acta Metallurgica et Materialia*, 39(9), 2135-2143. doi: http://dx.doi.org/10.1016/0956-7151(91)90183-2.

Hill, R. (1965a). Continuum micro-mechanics of elastoplastic polycrystals. *Journal of the Mechanics and Physics of Solids*, 13(2), 89-101. doi: http://dx.doi.org/10.1016/0022-5096(65)90023-2. SC.

Hill, R. (1965b). A self-consistent mechanics of composite materials. *Journal of the Mechanics and Physics of Solids*, 13(4), 213-222. doi: http://dx.doi.org/10.1016/0022-5096(65)90010-4.

Hill, R. (1963). Elastic properties of reinforced solids: some theoretical principles. *Journal of the Mechanics and Physics of Solids*, 11(5), 357–372.

Huntington, H. (1958). The Elastic Constants of Crystals. *Solid State Physics*, 7, 213-351. doi: 10.1016/S0081-1947(08)60553-6.

Jasiuk, I., Sheng, P. & Tsuchida, E. (1997). A spherical inclusion in an elastic half-space under shear. *Journal of applied mechanics*, 64(3), 471–479.

Kanit, T., Forest, S., Galliet, I., Mounoury, V. & Jeulin, D. (2003). Determination of the size of the representative volume element for random composites: statistical and numerical approach. *International Journal of Solids and Structures*, 40(13–14), 3647-3679. doi: http://dx.doi.org/10.1016/S0020-7683(03)00143-4.

Kanit, T. (2003). *Notion of representative volume element for heterogeneous materials: statistical and numerical approach*. (Thesis, École Nationale Supérieure des Mines de Paris).

Klemenc, J. & Fajdiga, M. (2012). Estimating S–N curves and their scatter using a differential ant-stigmergy algorithm. *International Journal of Fatigue*, 43, 90 - 97. doi: https://doi.org/10.1016/j.ijfatigue.2012.02.015.

Kocks, U. F., Tome, C. N. & Wenk, H. R. (1999). *Texture and Anisotropy. Preferred Orientations in Polycrystals and Their Effect on Material Properties*. Cambridge: Cambridge University Press.

Kröner, E. (1961). Zur plastischen verformung des vielkristalls. *Acta Metallurgica*, 9(2), 155-161. doi: http://dx.doi.org/10.1016/0001-6160(61)90060-8. SC.

Krupp, U. (2007). *Fatigue Crack Propagation in Metals and Alloys: Microstructural Aspects and Modelling Concepts*. Wiley.

Kumar, S., Kurtz, S. K. & Agarwala, V. K. (1996). Micro-stress distribution within polycrystalline aggregate. *Acta Mechanica*, 114(1), 203-216. doi: 10.1007/bf01170404.

Lahellec, N. & Suquet, P. (2007a). On the effective behavior of nonlinear inelastic composites: I. Incremental variational principles. *Journal of the Mechanics and Physics of Solids*, 55(9), 1932 - 1963. doi: https://doi.org/10.1016/j.jmps.2007.02.003.

Lahellec, N. & Suquet, P. (2007b). On the effective behavior of nonlinear inelastic composites: II: A second-order procedure. *Journal of the Mechanics and Physics of Solids*, 55(9), 1964 - 1992. doi: https://doi.org/10.1016/j.jmps.2007.02.004.

Lahellec, N. & Suquet, P. (2013). Effective response and field statistics in elasto-plastic and elasto-viscoplastic composites under radial and non-radial loadings. *International Journal of Plasticity*, 42, 1 - 30. doi: https://doi.org/10.1016/j.ijplas.2012.09.005.

Lalanne, C. (2002). *Fatigue Damage*. Taylor & Francis.

Largenton, R., Michel, J.-C. & Suquet, P. (2014). Extension of the Nonuniform Transformation Field Analysis to linear viscoelastic composites in the presence of aging and swelling. *Mechanics of Materials*, 73, 76 - 100. doi: https://doi.org/10.1016/j.mechmat.2014.02.004.

Lebensohn, R. A. (2001). N-site modeling of a 3D viscoplastic polycrystal using Fast Fourier Transform. *Acta Materialia*, 49(14), 2723 - 2737. doi: https://doi.org/10.1016/S1359-6454(01)00172-0.

Lebensohn, R. A., Liu, Y. & Ponte Castañeda, P. (2004). On the accuracy of the self-consistent approximation for polycrystals: comparison with full-field numerical simulations. *Acta Materialia*, 52(18), 5347-5361. doi: http://dx.doi.org/10.1016/j.actamat.2004.07.040.

Lebensohn, R. A. & Needleman, A. (2016). Numerical implementation of non-local polycrystal plasticity using fast Fourier transforms. *Journal of the Mechanics and Physics of Solids*, 97, 333 - 351. doi: https://doi.org/10.1016/j.jmps.2016.03.023. SI:Pierre Suquet Symposium.

Lebensohn, R. A., Kanjarla, A. K. & Eisenlohr, P. (2012). An elasto-viscoplastic formulation based on fast Fourier transforms for the prediction of micromechanical fields in polycrystalline materials. *International Journal of Plasticity*, 32-33, 59 - 69. doi: https://doi.org/10.1016/j.ijplas.2011.12.005.

Lee, Y.-G., Zou, W.-N. & Ren, H.-H. (2016). Eshelby's problem of inclusion with arbitrary shape in an isotropic elastic half-plane. *International Journal of Solids and Structures*, 81, 399 - 410. doi: https://doi.org/10.1016/j.ijsolstr.2015.12.024.

Lemaitre, J., Chaboche, J., Benallal, A. & Desmorat, R. (2009). *Mécanique des matériaux solides - 3ème édition*. Dunod.

Lin, H., Binoniemi, R. R., Fett, G. A., Woodard, T., Punch, E. F., Tyne, C. V., Taylor, B. C. & Matlock, D. K. (2006, apr). Investigation of the Effect of Sample Size on Fatigue Endurance Limit of a Carburized Steel. *SAE 2006 World Congress & Exhibition*. doi: https://doi.org/10.4271/2006-01-0539.

Liu, Z., Bessa, M. A. & Liu, W. K. (2016). Self-consistent clustering analysis: An efficient multi-scale scheme for inelastic heterogeneous materials. *Computer Methods in Applied Mechanics and Engineering*, 306, 319-341. doi: 10.1016/j.cma.2016.04.004.

Liu, Z., Kafka, O. L., Yu, C. & Liu, W. K. (2018). Data-driven self-consistent clustering analysis of heterogeneous materials with crystal plasticity. In *Computational Methods in Applied Sciences* (vol. 46, pp. 221-242). Springer Netherland. doi: 10.1007/978-3-319-60885-3-11.

Man, J., Obrtlík, K., Blochwitz, C. & Polák, J. (2002). Atomic force microscopy of surface relief in individual grains of fatigued 316L austenitic stainless steel. *Acta Materialia*, 50(15), 3767 - 3780. doi: https://doi.org/10.1016/S1359-6454(02)00167-2.

Mareau, C. & Berbenni, S. (2015). An affine formulation for the self-consistent modeling of elasto-viscoplastic heterogeneous materials based on the translated field method. *International Journal of Plasticity*, 64, 134 - 150. doi: https://doi.org/10.1016/j.ijplas.2014.08.011.

Martin, G., Ochoa, N., Sai, K., Hervé-Luanco, E. & Cailletaud, G. (2014). A multiscale model for the elastoviscoplastic behavior of Directionally Solidified alloys: Application to FE structural computations. *International Journal of Solids and Structures*, 51(5), 1175–1187.

Masson, R., Bornert, M., Suquet, P. & Zaoui, A. (2000). An affine formulation for the prediction of the effective properties of nonlinear composites and polycrystals. *Journal of the Mechanics and Physics of Solids*, 48(6), 1203 - 1227. doi: https://doi.org/10.1016/S0022-5096(99)00071-X.

McDowell, D. L. (2004). Basic issues in the mechanics of high cycle metal fatigue. *International Journal of Fracture*, 80(2), 103. doi: 10.1007/BF00012666.

McDowell, D. L. (2007). Simulation-based strategies for microstructure-sensitive fatigue modeling. *Materials Science and Engineering: A*, 468-470, 4 - 14. doi: https://doi.org/10.1016/j.msea.2006.08.129. The McEvily Symposium: Fatigue and Fracture of Traditional and Advanced Materials, TMS 2006.

McDowell, D. & Dunne, F. (2010). Microstructure-sensitive computational modeling of fatigue crack formation. *International Journal of Fatigue*, 32(9), 1521 - 1542. doi: https://doi.org/10.1016/j.ijfatigue.2010.01.003. Emerging Frontiers in Fatigue.

Meakin, P. (1998). *Fractals, Scaling and Growth Far from Equilibrium*. Cambridge University Press.

Meng, C., Heltsley, W. & Pollard, D. D. (2012). Evaluation of the Eshelby solution for the ellipsoidal inclusion and heterogeneity. *Computers & Geosciences*, 40, 40 - 48. doi: https://doi.org/10.1016/j.cageo.2011.07.008.

Mercier, S., Jacques, N. & Molinari, A. (2005a). Validation of an interaction law for the Eshelby inclusion problem in elasto-viscoplasticity. *International Journal of Solids and Structures*, 42(7), 1923 - 1941. doi: https://doi.org/10.1016/j.ijsolstr.2004.08.016.

Mercier, S., Jacques, N. & Molinari, A. (2005b). Validation of an interaction law for the Eshelby inclusion problem in elasto-viscoplasticity. *International Journal of Solids and Structures*, 42(7), 1923 - 1941. doi: https://doi.org/10.1016/j.ijsolstr.2004.08.016.

Michel, J. C., Moulinec, H. & Suquet, P. (1999). Effective properties of composite materials with periodic microstructure: a computational approach. *Computer Methods in Applied Mechanics and Engineering*, 172(1–4), 109-143. doi: http://dx.doi.org/10.1016/S0045-7825(98)00227-8.

Michel, J. & Suquet, P. (2003). Nonuniform transformation field analysis. *International Journal of Solids and Structures*, 40(25), 6937 - 6955. doi: https://doi.org/10.1016/S0020-7683(03)00346-9. Special issue in Honor of George J. Dvorak.

Michel, J.-C. & Suquet, P. (2009). Nonuniform transformation field analysis: a reduced model for multiscale nonlinear problems in solid mechanics. In Galvanetto, U. & Aliabadi, F. (Eds.), *Multiscale Modelling in Solid Mechanics - Computational Approaches* (pp. 159-206). Imperial College Press, London. Consulted at https://hal.archives-ouvertes.fr/hal-00367772.

Michel, J.-C. & Suquet, P. (2016). A model-reduction approach to the micromechanical analysis of polycrystalline materials. *Computational Mechanics*, 57, 483-508. doi: 10.1007/s00466-015-1248-9.

Mika, D. P. & Dawson, P. R. (1998). Effects of grain interaction on deformation in polycrystals. *Materials Science and Engineering: A*, 257(1), 62 - 76. doi: https://doi.org/10.1016/S0921-5093(98)00824-7.

Miner, M. (1945). Cumulative Damage in fatigue. *Journal of Applied Mechanics*, 12, 159-164.

Monchiet, V., Charkaluk, E. & Kondo, D. (2006). Plasticity-damage based micromechanical modelling in high cycle fatigue. *Comptes Rendus Mécanique*, 334(2), 129 - 136. doi: https://doi.org/10.1016/j.crme.2005.12.002.

Monnet, G. & Vincent, L. (2011). Loi de comportement en plasticité cristalline pour acier à basse température. *Mechanics & Industry*, 12(03), 193-198. doi: doi:10.1051/meca/2011107.

Montheillet, F. & Gilormini, P. (1996). Predicting the mechanical behavior of two-phase materials with cellular automata. *International Journal of Plasticity*, 12(4), 561-574. doi: http://dx.doi.org/10.1016/S0749-6419(96)00020-4.

Mori, T. & Tanaka, K. (1973). Average stress in matrix and average elastic energy of materials with misfitting inclusions. *Acta Metallurgica*, 21(5), 571-574. doi: http://dx.doi.org/10.1016/0001-6160(73)90064-3.

Moschovidis, Z. A. & Mura, T. (1975). Two-Ellipsoidal Inhomogeneities by the Equivalent Inclusion Method. *Journal of Applied Mechanics*, 42(4), 847-852. doi: 10.1115/1.3423718.

Moulinec, H. & Suquet, P. (1998a). A numerical method for computing the overall response of nonlinear composites with complex microstructure. *Computer Methods in Applied Mechanics and Engineering*, 157(1), 69 - 94. doi: https://doi.org/10.1016/S0045-7825(97)00218-1.

Moulinec, H. & Suquet, P. (1998b). A numerical method for computing the overall response of nonlinear composites with complex microstructure. *Computer Methods in Applied Mechanics and Engineering*, 157(1–2), 69-94. doi: http://dx.doi.org/10.1016/S0045-7825(97)00218-1.

Moulinec, H. & Suquet, P. (2003). Intraphase strain heterogeneity in nonlinear composites: a computational approach. *European Journal of Mechanics-A/Solids*, 22(5), 751–770.

Mounounga, T., Abdul-Latif, A. & Razafindramary, D. (2011). Damage induced anisotropy of polycrystals under complex cyclic loadings. *International Journal of Mechanical Sciences*, 53(4), 271 - 280. doi: https://doi.org/10.1016/j.ijmecsci.2011.01.008.

Méric, L., Poubanne, P. & Cailletaud, G. (1991). Single Crystal Modeling for Structural Calculations: Part 1—Model Presentation. *Journal of Engineering Materials and Technology*, 113(1), 162-170. doi: 10.1115/1.2903374. 10.1115/1.2903374.

Mughrabi, H. (1999). On the life controlling microstructural fatigue mechanisms in ductile metals and alloys in the gigacycle regime. *Fatigue & Fracture of Engineering Materials & Structures*, 22, 633 - 641. doi: 10.1046/j.1460-2695.1999.00186.x.

Mughrabi, H. (2006). Specific features and mechanisms of fatigue in the ultrahigh-cycle regime. *International Journal of Fatigue*, 28(11), 1501 - 1508. doi: https://doi.org/10.1016/j.ijfatigue.2005.05.018. Third International Conference on Very High Cycle Fatigue (VHCF-3).

Mura, T. (1987). *Micromechanics of Defects in Solids*. Martinus Nijhoff Publishers.

Musienko, A., Tatschl, A., Schmidegg, K., Kolednik, O., Pippan, R. & Cailletaud, G. (2007). Three-dimensional finite element simulation of a polycrystalline copper specimen. *Acta Materialia*, 55(12), 4121 - 4136. doi: https://doi.org/10.1016/j.actamat.2007.01.053.

Navarro, A. & De Los Rios, E. (1988). Short and long fatigue crack growth: a unified model. *Philosophical Magazine A*, 57(1), 15–36.

Nemat-Nasser, S. & Hori, M. (1999). *Micromechanics: Overall Properties of Heterogeneous Materials*. Elsevier.

Newman, J. (2015). Fatigue and Crack-growth Analyses under Giga-cycle Loading on Aluminum Alloys. *Procedia Engineering*, 101, 339 - 346. doi: https://doi.org/10.1016/j.proeng.2015.02.041. 3rd International Conference on Material and Component Performance under Variable Amplitude Loading, VAL 2015.

Nicholas, T. (2006). *High Cycle Fatigue: A Mechanics of Materials Perspective*. Elsevier Science. Consulted at https://books.google.ca/books?id=owuYRq4mz74C.

Osterstock, S., Robertson, C., Sauzay, M., Degallaix, S. & Aubin, V. (2007). Prediction of the Scatter of Crack Initiation under High Cycle Fatigue. *Key engineering materials*, 363-366. doi: 10.4028/www.scientific.net/KEM.345-346.363.

Othmani, Y., Delannay, L. & Doghri, I. (2011). Equivalent inclusion solution adapted to particle debonding with a non-linear cohesive law. *International Journal of Solids and Structures*, 48(24), 3326 - 3335. doi: https://doi.org/10.1016/j.ijsolstr.2011.08.002.

Papadopoulos, I. (1994). A new criterion of fatigue strength for out-of-phase bending and torsion of hard metals. *International Journal of Fatigue*, 16(6), 377 - 384. doi: https://doi.org/10.1016/0142-1123(94)90449-9.

Paris, P. & Erdogan, F. (1963). A critical analysis of crack propagation laws. *Journal of basic engineering*, 85(4), 528-533.

Park, J. & Nelson, D. (2000). Evaluation of an energy-based approach and a critical plane approach for predicting constant amplitude multiaxial fatigue life. *International Journal of Fatigue*, 22(1), 23 - 39. doi: https://doi.org/10.1016/S0142-1123(99)00111-5.

Pilvin, P. (2010). *SiDoLo Version 2.5298*.

Pilvin, P. (1994). The contribution of micromechanical approaches to the modelling of inelastic behaviour of polycrystals [Conference Paper].

Pourian, M., Pilvin, P., Bridier, F. & Bocher, P. (2014). Heterogeneous elastic behavior of HCP titanium polycrystalline aggregates simulated by cellular automaton and finite element. *Computational Materials Science*, 92, 468-475. doi: 10.1016/j.commatsci.2014.05.068. cited By 6.

Pourian, M., Bridier, F., Pilvin, P. & Bocher, P. (2016). Prediction of crack initiation sites in alpha Ti-alloys microstructures under dwell-fatigue using Cellular Automaton simulation method. *International Journal of Fatigue*, 85, 85-97. doi: 10.1016/j.ijfatigue.2015.12.010. cited By 12.

Prakash, A. & Lebensohn, R. A. (2009). Simulation of micromechanical behavior of polycrystals: finite elements versus fast Fourier transforms. *Modelling and Simulation in Materials Science and Engineering*, 17(6), 064010.

Przybyla, C., Prasannavenkatesan, R., Salajegheh, N. & McDowell, D. L. (2010). Microstructure-sensitive modeling of high cycle fatigue. *International Journal of Fatigue*, 32(3), 512 - 525. doi: https://doi.org/10.1016/j.ijfatigue.2009.03.021. Symposium on Competing Failure Modes and Variability in Fatigue.

Qu, J. (1993). Eshelby tensor for an elastic inclusion with slightly weakened interface. *TRANSACTIONS-AMERICAN SOCIETY OF MECHANICAL ENGINEERS JOURNAL OF APPLIED MECHANICS*, 60, 1048–1048.

Quey, R. (2019, June). Neper: polycrystal generation and meshing [Format]. Consulted at http://neper.sourceforge.net/.

Robert, C., Saintier, N., Palin-Luc, T. & Morel, F. (2012a). Micro-mechanical modelling of high cycle fatigue behaviour of metals under multiaxial loads. *Mechanics of Materials*, 55, 112 - 129. doi: https://doi.org/10.1016/j.mechmat.2012.08.006.

Robert, C. & Mareau, C. (2015). A comparison between different numerical methods for the modeling of polycrystalline materials with an elastic–viscoplastic behavior. *Computational Materials Science*, 103, 134 - 144. doi: https://doi.org/10.1016/j.commatsci.2015.03.028.

Robert, C., Saintier, N., Palin-Luc, T. & Morel, F. (2012b). Micro-mechanical modelling of high cycle fatigue behaviour of metals under multiaxial loads. *Mechanics of Materials*, 55, 112–129.

Rocha, M., Bruehwiler, E. & Nussbaumer, A. (2015). Microstructural influence on the scatter in the fatigue life of steel reinforcement bars. *International Journal of Fatigue*, 75, 205–212.

Roters, F., Eisenlohr, P., Hantcherli, L., Tjahjanto, D. D., Bieler, T. R. & Raabe, D. (2010). Overview of constitutive laws, kinematics, homogenization and multiscale methods in crystal plasticity finite-element modeling: Theory, experiments, applications. *Acta Materialia*, 58(4), 1152-1211. doi: http://dx.doi.org/10.1016/j.actamat.2009.10.058.

Roters, F., Eisenlohr, P., Bieler, T. & Raabe, D. (2011). *Crystal Plasticity Finite Element Methods: in Materials Science and Engineering*. Wiley.

Sackett, E. E., Germain, L. & Bache, M. R. (2007). Crystal plasticity, fatigue crack initiation and fatigue performance of advanced titanium alloys. *International Journal of Fatigue*, 29(9), 2015-2021. doi: https://doi.org/10.1016/j.ijfatigue.2006.12.011.

Sanchez-Palencia, E., Zaoui, A. & Sciences, I. C. f. M. (1987). *Homogenization Techniques for Composite Media: Lectures Delivered at the CISM International Center for Mechanical Sciences, Udine, Italy, July 1-5, 1985*. Springer-Verlag.

Sangid, M. D., Maier, H. J. & Sehitoglu, H. (2011). The role of grain boundaries on fatigue crack initiation – An energy approach. *International Journal of Plasticity*, 27(5), 801 - 821. doi: https://doi.org/10.1016/j.ijplas.2010.09.009.

Santecchia, E., Hamouda, A. M. S., Musharavati, F., Zalnezhad, E., Cabibbo, M., El Mehtedi, M. & Spigarelli, S. (2016). A Review on Fatigue Life Prediction Methods for Metals. *Advances in Materials Science and Engineering*, 2016, 26. doi: 10.1155/2016/9573524.

Sauzay, M. (2007). Cubic elasticity and stress distribution at the free surface of polycrystals. *Acta Materialia*, 55(4), 1193-1202. doi: http://dx.doi.org/10.1016/j.actamat.2006.09.035.

Shodja, H. & Sarvestani, A. (2001). Elastic fields in double inhomogeneity by the equivalent inclusion method. *Journal of Applied mechanics*, 68(1), 3–10.

Shodja, H., Rad, I. & Soheilifard, R. (2003). Interacting cracks and ellipsoidal inhomogeneities by the equivalent inclusion method. *Journal of the Mechanics and Physics of Solids*, 51(5), 945 - 960. doi: https://doi.org/10.1016/S0022-5096(02)00106-0.

Shoemake, K. (1992). Uniform random rotations. In *Graphics Gems III* (pp. 124-132). Academic Press Professional, Inc.

Simmons, G. & Wang, H. (1971). *Single crystal elastic constants and calculated aggregate properties: a handbook* (ed. 2d ed.). Cambridge, Mass., M.I.T. Press: The M.I.T. Press.

Solas, D., Thebault, J., Rey, C. & Baudin, T. (2010). Dynamic Recrystallization Modeling during Hot Forging of a Nickel Based Superalloy. *Materials Science Forum*, Vols. 638-642, 2321-2326.

Stinville, J. C., Vanderesse, N., Bridier, F., Bocher, P. & Pollock, T. M. (2015). High resolution mapping of strain localization near twin boundaries in a nickel-based superalloy. *Acta Materialia*, 98, 29-42. doi: https://doi.org/10.1016/j.actamat.2015.07.016.

Stinville, J. C., Echlin, M. P., Texier, D., Bridier, F., Bocher, P. & Pollock, T. M. (2016a). Sub-Grain Scale Digital Image Correlation by Electron Microscopy for Polycrystalline Materials during Elastic and Plastic Deformation. *Experimental Mechanics*, 56(2), 197-216. doi: 10.1007/s11340-015-0083-4.

Stinville, J. C., Lenthe, W. C., Miao, J. & Pollock, T. M. (2016b). A combined grain scale elastic–plastic criterion for identification of fatigue crack initiation sites in a twin containing polycrystalline nickel-base superalloy. *Acta Materialia*, 103, 461-473. doi: https://doi.org/10.1016/j.actamat.2015.09.050.

Sun, J., Hensel, J., Klassen, J., Nitschke-Pagel, T. & Dilger, K. (2019). Solid-state phase transformation and strain hardening on the residual stresses in S355 steel weldments. *Journal of Materials Processing Technology*, 265, 173 - 184. doi: https://doi.org/10.1016/j.jmatprotec.2018.10.018.

Suquet, P. (1997). Effective properties of nonlinear composites. In *Continuum micromechanics* (pp. 197–264). Springer.

Sweeney, C. A., Dunne, F., McHugh, P. E., Leen, S. et al. (2015). Micro-scale testing and micromechanical modelling for high cycle fatigue of CoCr stent material. *Journal of the mechanical behavior of biomedical materials*, 46, 244–260.

Tabourot, L., Fivel, M. & Rauch, E. (1997). Generalised constitutive laws for f.c.c. single crystals. *Materials Science and Engineering: A*, 234–236, 639-642. doi: http://dx.doi.org/10.1016/S0921-5093(97)00353-5.

Tan, H., Huang, Y., Liu, C. & Geubelle, P. H. (2005). The Mori–Tanaka method for composite materials with nonlinear interface debonding. *International Journal of Plasticity*, 21(10), 1890–1918.

Thomson, W. (1887). On the division of space with minimum partitional area. *Acta Mathematica*, 11(1-4), 121-134. doi: 10.1007/BF02418046.

Tulloue, G. (2015). Les angles d'Euler [Format]. Consulted at http://www.sciences.univ-nantes.fr/sites/genevieve_tulloue/Meca/Cinematique/euler1.html.

Weibull, W. (1952). The statistical aspect of fatigue failure and its consequences. In *Fatigue and fracture of metals* (vol. 4, pp. 182-196). W. M. Murray.

Wirsching, P. H. (1983). Statistical summaries of fatigue data for design purposes. *NASA Contractor Report 3697*, pp. 1-59.

Wolfram, S. (2002). *A new kind of science*. Wolfram Media.

Wu, W., Owino, J., Al-Ostaz, A. & Cai, L. (2014). Applying periodic boundary conditions in finite element analysis. *SIMULIA Community Conference, Providence*, pp. 707-719.

Yaguchi, M. & Busso, E. P. (2005). On the accuracy of self-consistent elasticity formulations for directionally solidified polycrystal aggregates. *International Journal of Solids and Structures*, 42(3–4), 1073-1089. doi: http://dx.doi.org/10.1016/j.ijsolstr.2004.07.009.

Yang, S., Dirrenberger, J., Monteiro, E. & Ranc, N. (2019). Representative volume element size determination for viscoplastic properties in polycrystalline materials. *International Journal of Solids and Structures*, 158, 210 - 219. doi: https://doi.org/10.1016/j.ijsolstr.2018.09.011.

Zghal, J., Gmati, H., Mareau, C. & Morel, F. (2016). A crystal plasticity based approach for the modelling of high cycle fatigue damage in metallic materials. *International Journal of Damage Mechanics*, 25(5), 611-628. doi: 10.1177/1056789516650247.

Zhang, K., Yang, K. V., Huang, A., Wu, X. & Davies, C. H. J. (2015). Fatigue crack initiation in as forged Ti–6Al–4V bars with macrozones present. *International Journal of Fatigue*, 80, 288-297. doi: https://doi.org/10.1016/j.ijfatigue.2015.05.020.

Zhao, Y., Billings, S. A. & Coca, D. (2009). Cellular automata modelling of dendritic crystal growth based on Moore and von Neumann neighbourhoods. *International Journal of Modelling, Identification and Control*, 6(2), 119-25. doi: 10.1504/IJMIC.2009.024328. AC-Origines.

Zhong, X., Dabrowski, M. & Jamtveit, B. (2018). Analytical solution for the stress field in elastic half-space with a spherical pressurized cavity or inclusion containing eigenstrain. *Geophysical Journal International*, 216(2), 1100-1115. doi: 10.1093/gji/ggy447.

Zhou, K., Hoh, H. J., Wang, X., Keer, L. M., Pang, J. H. L., Song, B. & Wang, Q. J. (2013). A review of recent works on inclusions. *Mechanics of Materials*, 60, 144-158. doi: http://dx.doi.org/10.1016/j.mechmat.2013.01.005.

Zouaghi, A., Velay, V., Soveja, A., Pottier, T., Cheikh, M. & Rézaï-Aria, F. (2016). A multi-scale approach to investigate the nonlinear subsurface behavior and strain localization of X38CrMoV5-1 martensitic tool steel: Experiment and numerical analysis. *International Journal of Plasticity*, 87, 130 - 153. doi: https://doi.org/10.1016/j.ijplas.2016.09.007.